Distribution Categories:
Magnetic Fusion Energy (UC-20)
MFE—Plasma Systems (UC-20a)
MFE—Magnetic Systems (UC-20b)
MFE—Reactor Materials (UC-20c
MFE—Fusion Systems (UC-20d)

ANL/FPP/TM-178

ANL/FPP/TM--178

DE84 007094

ARGONNE NATIONAL LABORATORY
9700 South Cass Avenue
Argonne, Illinois 60439

TOKAMAK BURN CYCLE STUDY:
A DATA BASE FOR COMPARING LONG PULSE AND STEADY-STATE POWER REACTORS

by

D. A. Ehst, J. N. Brooks, Y. Cha, K. Evans, Jr., A. Hassanein, S. Kim, S. Majumdar, B. Misra, and H. C. Stevens

Fusion Power Program

DISCLAIMER

November 1983

TABLE OF CONTENTS

TABLE OF CONTENTS (Contd.)

LIST OF FIGURES

LIST OF FIGURES (Contd.)

LIST OF FIGURES (Contd.)

LIST OF FIGURES (Contd.)

LIST OF FIGURES (Contd.)

LIST OF FIGURES (Contd.)

LIST OF FIGURES (Contd.)

LIST OF FIGURES (Contd.)

LIST OF TABLES

ACKNOWLEDGMENT

We would like to express our appreciation to Cyrilla Hytry for the typing and final assembly of this report.

TOKAMAK BURN CYCLE STUDY: A DATA BASE FOR COMPARING LONG PULSE AND STEADY-STATE POWER REACTORS

D. A. Ehst, J. N. Brooks, Y. Cha, K. Evans, Jr., A. Hassanein, S. Kim, S. Majumdar, B. Misra, and H. C. Stevens

Fusion Power Program

ABSTRACT

Several distinct operating modes (conventional ohmic, noninductive steady state, internal transformer, etc.) have been proposed for tokamaks. Our study focuses on capital costs and lifetime limitations of reactor subsystems in an attempt to quantify sensitivity to pulsed operation. Major problem areas considered include: thermal fatigue on first wall, limiter/divertor; thermal energy storage; fatigue in pulsed poloidal field coils; out-of-plane fatigue and eddy current heating in toroidal field coils; electric power supply costs; and noninductive driver costs. We assume a high availability and low cost of energy will be mandatory for a commercial fusion reactor, and we characterize improvements in physics (current drive efficiency) and engineering (superior materials) which will help achieve these goals for different burn cycles.

Chapter 1. INTRODUCTION AND OVERVIEW

Historically, most plasma experiments have created dense, hot plasmas for relatively short periods, and only a few concepts (mirrors, EBT) were felt to potentially offer steady-state operation. The tokamak was originally envisioned to provide the basis for potential fusion reactor which would operate on a pulsed cycle, albeit at high duty factor. Design studies over the years have identified many perceived shortcomings for operation of a pulsed tokamak reactor. These issues are concerned with the costs of thermal and electric energy storage, thermal fatigue in the blanket, first wall, and other high temperature components, and mechanical fatigue associated with oscillating magnetic fields.

There was a measure of enthusiasm, therefore, when it was recently discovered that tokamaks can be operated in a purely steady-state mode, via continuous wave (CW) rf heating and current drive. The STARFIRE tokamak reactor study capitalized on the advantages of CW operation to demonstrate that such a fusion power plant could be economically competitive in producing electricity.

The principal concern with CW tokamak operation is the efficiency of generating the toroidal current by noninductive means. If a 10-MA toroidal current requires much more than 100 MW of auxiliary power absorbed in the plasma this may represent an unacceptable circulating power fraction and an unacceptably large capital cost for the driver. In fact, the STARFIRE design, based solely on theoretical predictions for a lower hybrid wave driver, achieved acceptable driver power only by resorting to an unorthodox (hollow) current density profile. Moreover, experiments (e.g., PLT/ALCATOR C) are confirming the theoretical predictions for lower hybrid waves; scaling from present-day results, we would expect centrally peaked current density generation in a reactor with an efficiency of only $\gamma \sim 0.01$ A/W.

There are several proposals to improve this situation. Alternative drivers such as the compressional Alfven wave are theoretically superior to the lower hybrid wave, and one goal of our study is to quantify how large γ must be in order to make CW operation attractive. Another suggestion is to use noninductive drive only during low density periods, when the ratio of current to driver power, I/P_d, is large. (For all noninductive drivers $I/P_d \propto \gamma/\bar{n}_e$,

where $\bar{n}_e$ is the electron density.) One possibility here is to initiate the full current at low density via noninductive means and then sustain the discharge with an external transformer during high density fusion operation. This extends the burn relative to the conventional ohmic operating mode since transformer volt-seconds are not consumed in establishing the poloidal fields. An alternative suggestion, called internal transformer operation, would eliminate the external transformer, allowing the current I to resistively decay a small amount during a short period of high density operation and then repeating this cycle. Finally, a hybrid cycle was proposed in which I remains constant, driven at high density during the fusion burn by an external transformer, and at low density by a noninductive driver while the transformer is reset. The sundry burn cycles considered in our study are described in more detail in Chap. 2, but we will summarize here qualitatively the results of our preliminary comparison. A more quantitative comparison is made in Chap. 7.

The internal transformer (IT) cycle appears least attractive due to the exceedingly large number of cycles it requires over the life of the reactor. This stems from the desire to limit the current oscillation, ΔI, to a reasonable fraction of the average value, I. Burn periods considerably less than 10^3 s are likely, resulting in unacceptable fatigue damage to the first wall and limiter. Likewise, frequent cycling of the equilibrium (EF) magnetic field will cause large increases in magnet costs to withstand mechanical fatigue. In addition, the duty factor is lowest of all the cycles. One advantage is that the toroidal current remains nearly full value at all times, which may reduce the likelihood of disruptions. There also appear to be modest cost savings in the electrical and thermal energy transfer system (ETS) in comparison with conventional ohmic operation. Finally, the IT cycle requires no ohmic heating coil (OHC), representing a direct cost savings and permitting the design of a more compact tokamak with smaller major radius.

The ohmic burn (OH) cycle is more attractive. At the expense of rather large major radius it is possible to design an OHC which delivers burn periods of $\gtrsim$1 h. This reduces the thermal and mechanical fatigue problems. However, the ETS is a very large cost penalty for pulsed operation; for the OH cycle the direct ETS capital cost can exceed several hundred million dollars. Due to these cost penalties the OH cycle would appear economical only if current

drive efficiencies were $\gamma \lesssim 0.01$ A/W, assuming a noninductive driver were to cost on the order of a dollar per watt.

The hybrid cycle provides quantitative improvements relative to the OH cycle. For the same major radius and burn time as the OH reactor, the hybrid would require a less expensive OHC and a less expensive ETS. Alternatively, for the same cost as an OH reactor this burn cycle could provide a longer fusion burn period, resulting in a higher duty factor (more net power) and fewer lifetime cycles (less fatigue and more reliability). Potentially large savings in the toroidal field coil structural costs are projected, since the EF fluctuations are relatively small. Additionally, the ability to maintain I at constant values for long periods may reduce the probability of major disruptions. We infer that this cycle is competitive for $0.01 \text{ A/W} \lesssim \gamma \lesssim 0.1 \text{ A/W}$.

If $\gamma \gtrsim 0.10$ A/W the CW cycle is by far most attractive. Thermal and magnetic fatigue is practically eliminated since steady-state fusion operation is possible for months at a time. Thermal energy storage is not required between burns, and the poloidal magnets can be energized over long periods, so electric power supplies are very inexpensive. The complete ETS costs are estimated to be ~\$10 M, which is negligible compared to the systems for pulsed cycles. The absence of changing plasma conditions may augur for the nonexistence of plasma disruptions. Furthermore, the prospect of truly steady-state operation promises to increase system reliability in myriad small subsystems which have not been studied or even invented to date.

The comparisons presented herein should be viewed as a preliminary study of problems and advantages associated with specific burn cycles. System availability is impossible to truly estimate in the advanced devices we are considering. Since availability as well as capital cost determine the economics of power generation we can only discern general trends from the data presented. More consistent integrated designs of systems optimized for different burn cycles will be necessary in order to better quantify the advantages of long pulse tokamak operation.

Chapter 2. MODELS FOR BURN CYCLE ANALYSIS

This study aims to compare cost and performance of tokamak reactors operating under different burn cycle assumptions. To clarify differences among the cycles it is desirable to hold as many characteristics as possible constant. Thus we select certain reference systems and analyze performance sensitivity as one parameter is varied independently from others. This chapter briefly describes the reference models used.

2.1 Reference Reactor Systems

Two basic tokamaks were considered in our study. The "7-m reactor" has a major radius R_0 = 7.0 m and has a plasma quite similar to that in the STARFIRE reactor.[1] This device, with parameters given in Table 2-1, has a small "hole in the doughnut" and cannot be driven inductively, since a practical transformer would have too few volt-seconds to ramp the plasma current up to its full value. This tokamak serves as a model for burn cycles (continuous and internal transformer) which have no external transformer. The second tokamak, the "8-m reactor", was selected to characterize performance of burn cycles with inductive current drive (ohmically heated and hybrid cycle). This tokamak, with R_0 = 8 m and other parameters given in Table 2-2, is by no means an optimized design but is merely indicative of the size needed to obtain fusion burns $\gtrsim 10^3$ s with inductively driven current. Both basic tokamaks were selected with a similar minor radius, so the 8-m reactor has a larger aspect ratio, A. Beta was scaled as $\bar{\beta}_t = 0.24/A$, with a vertically elongated plasma, $\kappa = 1.6$. The plasma cross section has mild triangularity, d = 0.2; as noted in Chap. 5, if a more highly shaped plasma were specified this would aggravate the difficulties of designing the magnets for the transformer-driven reactors. For this study a low safety factor ($q_{axis} = 1.0$, $q_{lim} = 2.5$) equilibrium was selected with a centrally peaked current density.

Accurate calculations of the plasma parameters were done with the TRAC-II code by specifying impurity levels and the confinement parameter $n\tau$. Figure 2-1 shows the performance of the 7-m reactor with the maximum toroidal field (at the inboard magnet leg) set at B_M = 11.1 T, for various plasma temperatures. For $\bar{T} \gtrsim 10$ keV the fusion power drops roughly as $P_f \propto \bar{T}^{-1}$. However,

TABLE 2-1

7-m Reference Reactor

A	= 3.6	$\bar{T}_e$	= 12 keV
κ	= 1.6	T_i	= 13.9 keV
d	= 0.2	$\bar{n}_D \tau_D^{\varepsilon}$	$\equiv 1.2 \times 10^{21}$ s/m^3
$\bar{\beta}_t$	= 0.067, $\beta^* = 0.0854$	λ^{P}_i	= 0.11
α_p	= 1.4	λ^{ε}_i	= 1.0
q	= 1.0-2.5	λ^{ε}_e	= 0.26
β_p^{ANL}	= 1.59	$\bar{n}_{Be}/\bar{n}_D$	= 0.08
α_F	=1.5510	R_α	= 0.75
a_J	= 0.4764	$\bar{n}_{Xe}/\bar{n}_D$	$= 28.6 \times 10^{-5}$
δ	= 0.0770	$\bar{n}_e$	$= 1.90 \times 10^{20}$ m^{-3}
		$\bar{n}_D$	$= 0.696 \times 10^{20}$ m^{-3}
R_0	= 7.0 m	$\bar{n}_\alpha/\bar{n}_D$	= 0.200
a	= 1.94 m	Z_{eff}	= 1.80
Δ_{BS}^{i}	= 1.2 m		
Δ_v	= 0.2 m	P_f	= 4230 MW
A_w	= 769 m^2	P_n	= 3380 MW
V_p	= 320 m^3	P_α	= 846 MW
B_M	= 11.2 T	P_{rad}	= 704 MW
B_0	= 5.35 T	P_{lim}	= 145 MW
I_0	= 14.8 MA	P_d	= 0 MW
B_0^{EF}	= 0.689 T	P_Ω	= 0.601 MW
σ_{TFC}^{SS}	= 80 ksi	W_n	= 4.40 MW/m^2
Δ_{TFC}	= 0.94 m	W_{rad}	= 0.917 MW/m^2
Δ_{SUP}	= 0.42 m	P_{th}	= 4699 MW
R_1	= 3.19 m	P_g	= 1689 MW
R_2	= 13.02 m	P_{net}	= 1604 MW
$t_f = t_I$	$= 8.5 \times 10^6$ s = 98 d	L	= 14.1 μH
t_{off}	$= 2.0 \times 10^6$ s = 24 d	R	= 2.74 nΩ
$N_f = N_I$	= 120	$I_0 L$	= 209 V-s
a_n	= 0.3	$I_0 R_{Spitzer}$	= 0.041 V
α_T	= 1.1		

TABLE 2-2

8-m Reference Reactor

$A = 4.0$	$a_n = 0.3$
$\kappa = 1.6$	$\alpha_T = 1.1$
$d = 0.2$	$\bar{T}_e = 10$ keV
$\bar{\beta}_t = 0.060$, $\beta^* = 0.0767$	$\bar{T}_i = 10.9$ keV
$\alpha_p = 1.4$	$\bar{n}_D \tau_D^{\varepsilon} \equiv 2.0 \times 10^{21}$ a/m^3
$q = 1.0\text{-}2.5$	$\lambda^p_i = 0.11$
$\beta_p^{ANL} = 1.81$	$\lambda^{\varepsilon}_i = 1.0$
$\alpha_F = 1.494$	$\lambda^{\varepsilon}_e = 0.26$
$a_J = 0.5300$	$\bar{n}_{Be}/\bar{n}_D = 0.08$
$\delta = 0.0804$	$R_\alpha = 0.75$
	$\bar{n}_{xe}/\bar{n}_D = 18.6 \times 10^{-5}$
$R_0 = 8.0$ m	$\bar{n}_e = 2.02 \times 10^{20}$ m^{-3}
$a = 2.0$ m	$\bar{n}_D = 0.719 \times 10^{20}$ m^{-3}
$\Delta^1_{BS} = 1.2$ m	$\bar{n}_\alpha/\bar{n}_D = 0.238$
$\Delta_v = 0.2$ m	$Z_{eff} = 1.70$
$A_w = 903$ m^2	
$V_p = 992$ m^3	$P_f = 3900$ MW
$B_M = 9.81$ T	$P_n = 3120$ MW
$B_0 = 5.64$ T	$P_\alpha = 780$ MW
$I_0 = 13.0$ MA	$P_{rad} = 687$ MW
$B_0^{EF} = 0.578$ T	$P_{lim} = 93$ MW
$\sigma^{SS}_{TFC} = 40$ ksi	$P_d = 0$ MW
$\Delta_{TFC} = 1.08$ m	$P_\Omega = 0.624$ MW
$\Delta_{SUP} = 0.35$ m	$W_n = 3.45$ MW/m^2
$\Delta_{OH} = 0.50$ m	$W_{rad} = 0.761$ MW/m^2
$R_{OH} = 2.93$ m (inboard)	$P_{th} = 1.14\ P_n + P_\alpha + P_d = 4337$ MW
$\Delta B^{OH} = 20.0$ T	$P_g = 0.357\ (P_{th} + 33) = 1560$ MW
$R_1 = 4.06$ m	$P_{net} = P_g - 85 - [P_d/0.5] = 1475$ MW
$R_2 = 14.15$ m	$L = 17.2\ \mu$H
	$R = 3.69\ n\Omega$
$t_f = t_I = 8.4 \times 10^3$ s $= 2.3$ h.	$I_0 L = 224$ V-s
$t_{off} = 90$ s	$I_0 R_{Spitzer} = 0.048$ V
$N_f = N_I = 1.22 \times 10^5$ (80% avail.)	

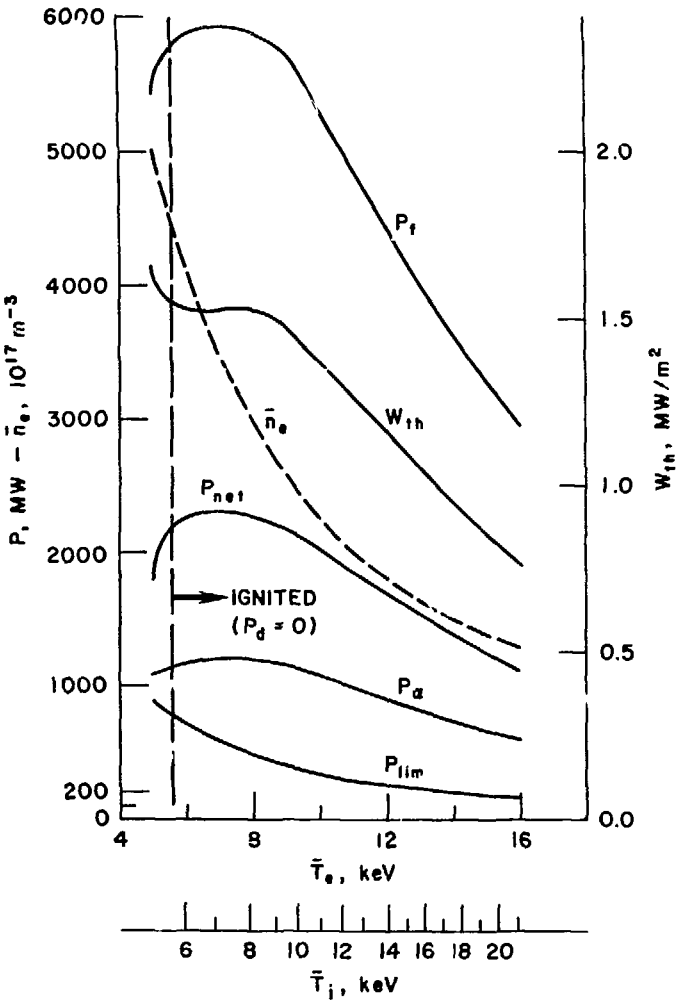

Fig. 2-1. Reactor performance at fixed B_M = 11.1 T; R_0 = 7.0 m, A = 3.6, κ = 1.6, d = 0.2, β_t = 0.067, α = 1.4, α_T = 1.1, $\bar{n}_{DT\tau D}$ = 6.5 × 10^{20} m^{-2}, I_0 = 14.7 MA.

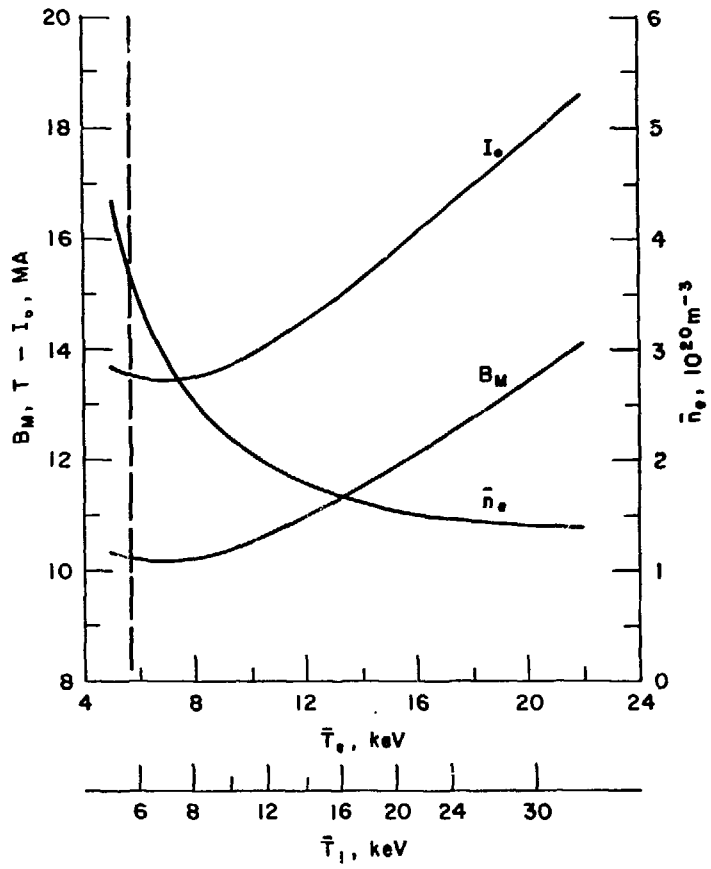

Fig. 2-2. Reactor requirements for fixed P_f = 4230 MW and thermal wall load, W_{th} = 1.1 MW/m^2; A = 3.6, κ = 1.6, d = 0.2, β_t = 0.067, α = 1.4, α_T = 1.1, $\bar{n}_{DT\tau D}$ = 6.5 × 10^{20} m^{-3}, R_0 = 7.0 m.

$\bar{n}_e \propto \bar{T}^{-1}$ also, and low $\bar{n}_e$ is desirable for the 7-m device, which is driven noninductively. Therefore, a trade-off study was done by fixing fusion power, $P_f = 4230$ MW, and neutron wall load, $W_n = 4.4$ MW/m^2, and then finding the required B_M for various $\bar{T}$. The results, shown in Fig. 2-2, indicate that B_M is minimum in the range of 6-10 keV and that $\bar{n}_e$ is nearly minimized for $\bar{T}_e \gtrsim 8$ keV. In order to better quantify the effect of plasma parameters on the noninductively driven 7-m reactor, several models of noninductive current drive were considered.

One class of current drive techniques adds momentum or energy to the electrons at suprathermal velocities. This method, which we dub high-speed drive, is exemplified by lower-hybrid and high-speed magnetosonic waves, electron cyclotron heating, and relativistic electron injection, and is characterized by a current drive efficiency[2] $j/p = 1.0 \times 10^{18} (T_e/n_e) (\hat{j}/\hat{p})$. This ratio maximizes at relativistic velocities, for which $\hat{j}/\hat{p} \to 2(c/v_e^2)$. Substituting this optimistic limit, we integrate the absorbed driver power, $p(r)$, over a density profile $n_e(r) = (1 + \alpha_n)\bar{n}_e[1 - (r/\tilde{a})^2]^{\alpha_n}$. For a current density $j(r) = (1 + a_j)\bar{j}[1 - (r/\tilde{a})^2]^{\alpha_j}$, we find the ratio of driver power to toroidal current

$$\frac{P_d^{(0)}}{I_0} = \frac{\pi R_0 (1 + \alpha_n)(1 + \alpha_j)\bar{n}_e}{5.11 \times 10^{20}(1 + \alpha_n + \alpha_j)},$$

where

$$I_0 \equiv \pi \tilde{a}^2 \bar{j} .$$

For typical values $\alpha_n = 0.3$ and $\alpha_j = 1.0$ we get

$$\frac{I_0}{P_d^{(0)}} = \gamma^{(0)} \left[\frac{1 \times 10^{20}\ \text{m}^{-3}}{\bar{n}_e}\right]\left[\frac{7.0\ \text{m}}{R_0}\right],$$

with $\gamma^{(0)} = 0.21$ A/W in the best theoretical case (the relativistic limit). Roughly speaking then, driver power is proportional to $\bar{n}_e I_0$ for high-speed current drive. We have replotted our data in Fig. 2-3 to show how B_M and $P_d^{(0)}$

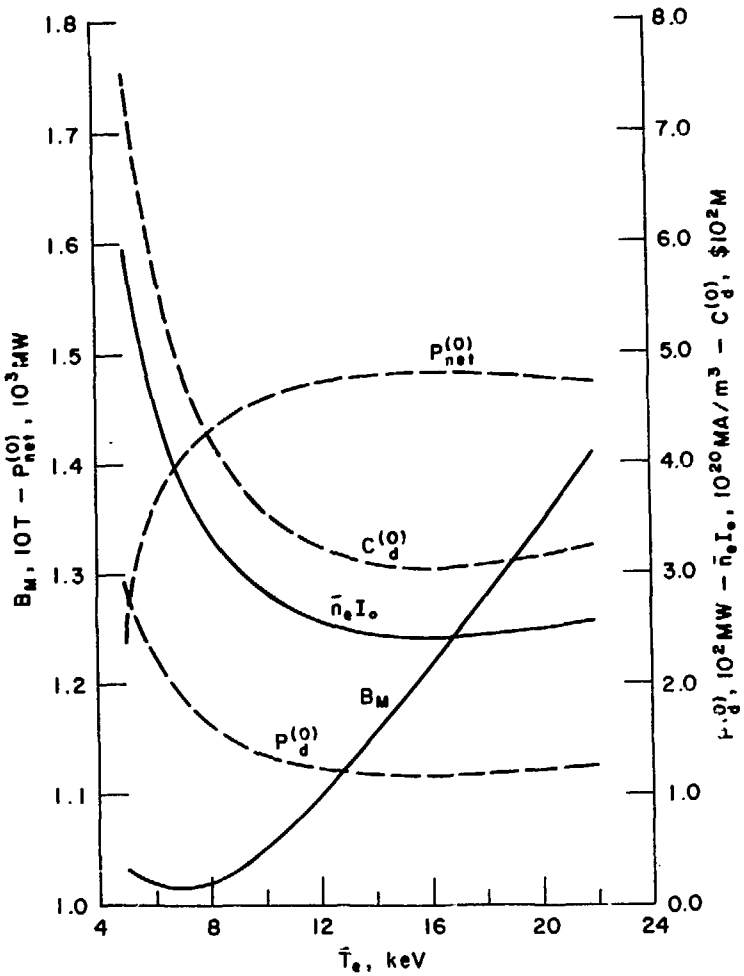

Fig. 2-3. Best theoretical high-speed current drive: $\gamma^{(0)} = 0.21$ A/W with $I_0/P_d^{(0)} = \gamma^{(0)}[10^{20}\ \text{m}^{-3} \times 7.0\ \text{m}]/[\bar{n}_e R_0]$; A = 3.6, $\beta_t = 0.067$, $P_f = 4230$ MW, $W_{th} = 1.1$ MW/m^2, $P_{net}^{(0)} = 0.357\left[P_d^{(0)} + 1.1\ P_f\right] - 73$ MW $- [P_d^{(0)}/0.7]$; $C_d^{(0)} = (\$2.6/\text{W}) \times P_d^{(0)}$.

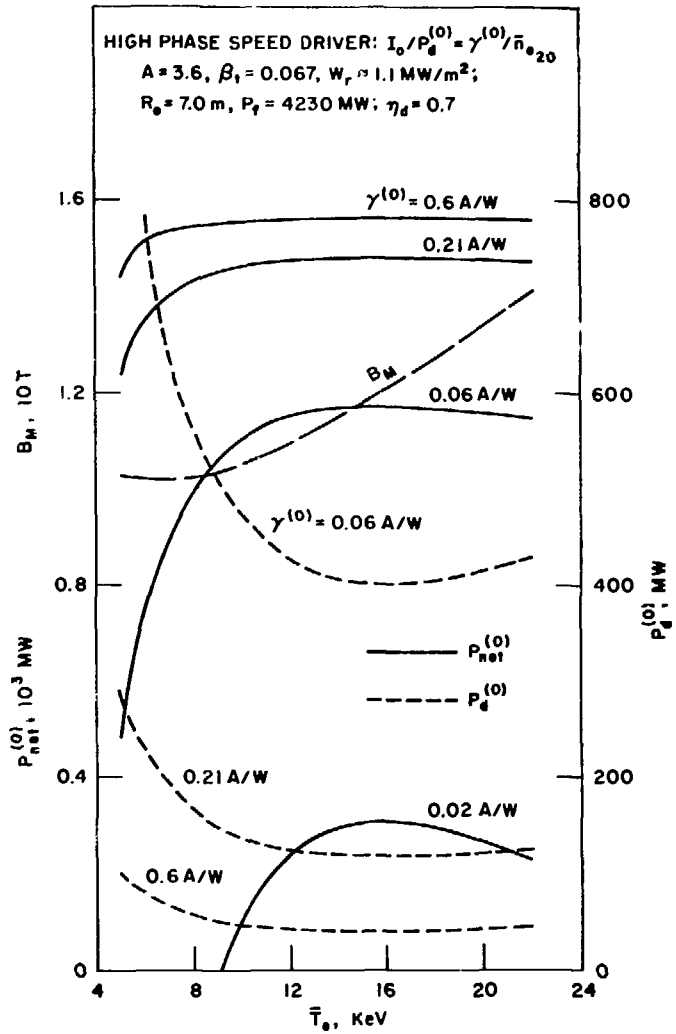

Fig. 2-4. High-speed curent drive for various $\gamma_d^{(0)}$, required driver power, $P_d^{(0)}$, net electric output, $P_{net}^{(0)}$, and magnetic field, B_M.

vary with $\bar{T}_e$. The net electric power production, P_{net}, is estimated as $P_{net} = 0.357\ P_{th} - 73\ MW - [P_d^{(0)}/0.7]$, where the thermal power is due to alpha heating, the driver power absorbed, and neutron heating with blanket enchancement: $P_{th} = P_\alpha + P_d^{(0)} + 1.14\ P_n$. For illustration we costed the driver hardware as $C_d^{(0)} = \$2.6 \times P_d^{(0)}$ (Watts), typical of rf systems.[2,3] From the figure we see net power is insensitive to $\bar{T}_e$ as long as $\bar{T}_e \gtrsim 6$ keV, but the capital cost for driver equipment is very large (>\$300 M) so there will be incentive to operate at $\bar{T}_e \gtrsim$ 10-12 keV, which minimizes $C_d^{(0)}$. However, for $\bar{T}_e \gtrsim 12$ keV B_M quickly exceeds 11 T, and the credibility and reliability of such very high field superconducting magnets is called to question.

Present-day experiments with lower hybrid current drive obtain significantly lower efficiencies than the relativistic limit. We display $P_{net}^{(0)}$ and $P_d^{(0)}$ in Fig. 2-4 for other values of $\gamma^{(0)}$. Net power drops dramatically for $\gamma^{(0)} \lesssim 0.04$ A/W, but more significant is the huge investment in the driver system $[P_d^{(0)} \gtrsim 200$ MW, $C^{(0)} \gtrsim \$400$ M$]$ for $\gamma^{(0)} \lesssim 0.1$.

Low-speed wave drivers (compressional Alfven, low-speed magnetosonic, and ion-cyclotron minority heating) as well as neutral beams are characterized by a maximum in $\hat{j}/\hat{p}$ occurring at subthermal electron speeds. In the best case (Alfven waves) $\hat{j}/\hat{p} \approx 130$.[2] If we substitute this value of $\hat{j}/\hat{p}$ and integrate, assuming $T_e(r) = (1 + \alpha_T)\bar{T}_e[1 - (r/a)]^{\alpha_T}$, we find

$$\frac{P_d^{(1)}}{I_0} = \pi R_0 \frac{(1 + \alpha_n)(1 + \alpha_j)}{(1 + \alpha_T)\ 6.5 \times 10^{19}} \frac{\bar{n}_e}{\bar{T}_e} \frac{1}{(a_n + \alpha_j - \alpha_T)} .$$

For $\alpha_n = 1.1$, $\alpha_j = 0.5$, and $\alpha_T = 0.3$, we obtain

$$\frac{I_0}{P_d^{(1)}} = \gamma^{(1)} \left[\frac{\bar{T}_e}{10\ keV}\right] \left[\frac{1.0 \times 10^{20}\ m^{-3}}{\bar{n}_e}\right] \left[\frac{7.0\ m}{R_0}\right] ,$$

with $\gamma^{(1)} = 0.16$ A/W. Now we find driver power is proportional to $\bar{n}_e I_0/\bar{T}_e$. This factor and $P_d^{(1)}$ are shown varying in Fig. 2-5. Capital costs for the driver and net electric power are shown using the same algorithms as before. Once again net power and driver costs suffer for $\bar{T}_e \lesssim$ 12-14 keV, but unreasonably large B_M is needed to operate at $\bar{T}_e \gtrsim 16$ keV. Figure 2-6 expands these results to include other values of $\gamma^{(1)}$.

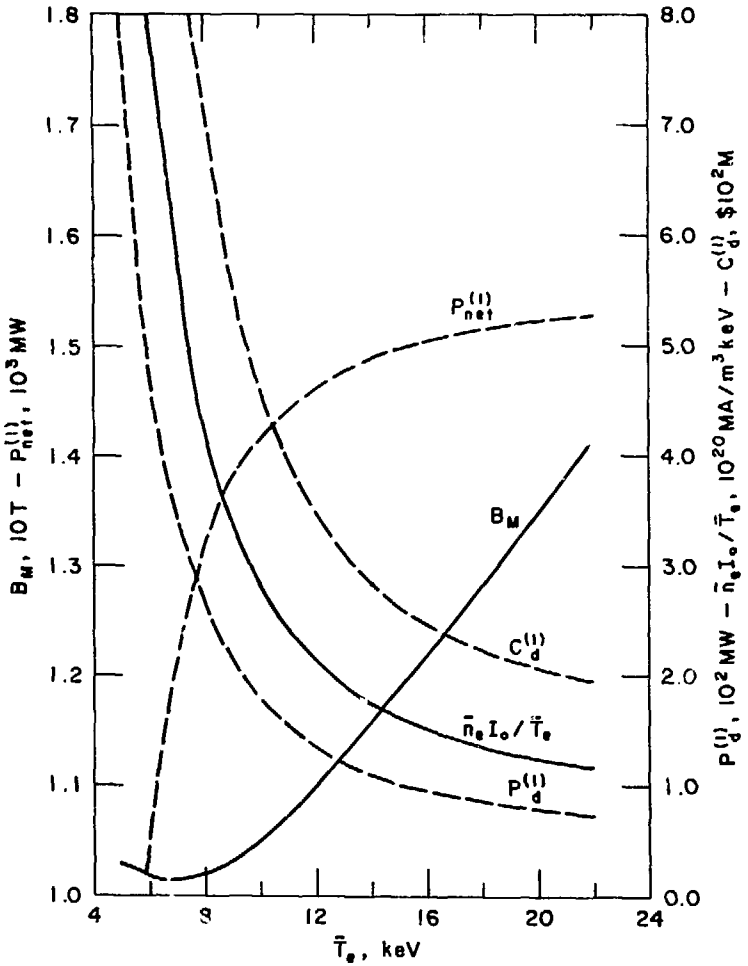

Fig. 2-5. Best theoretical low-speed current drive: $\gamma^{(1)} = 0.16$ A/W with $I_0/P_d^{(1)} = \gamma^{(1)}[10^{20}\ \text{m}^{-3} \times 7.0\ \text{m}/10\ \text{keV}]/[\bar{n}_e R_0/\bar{T}_e]$.

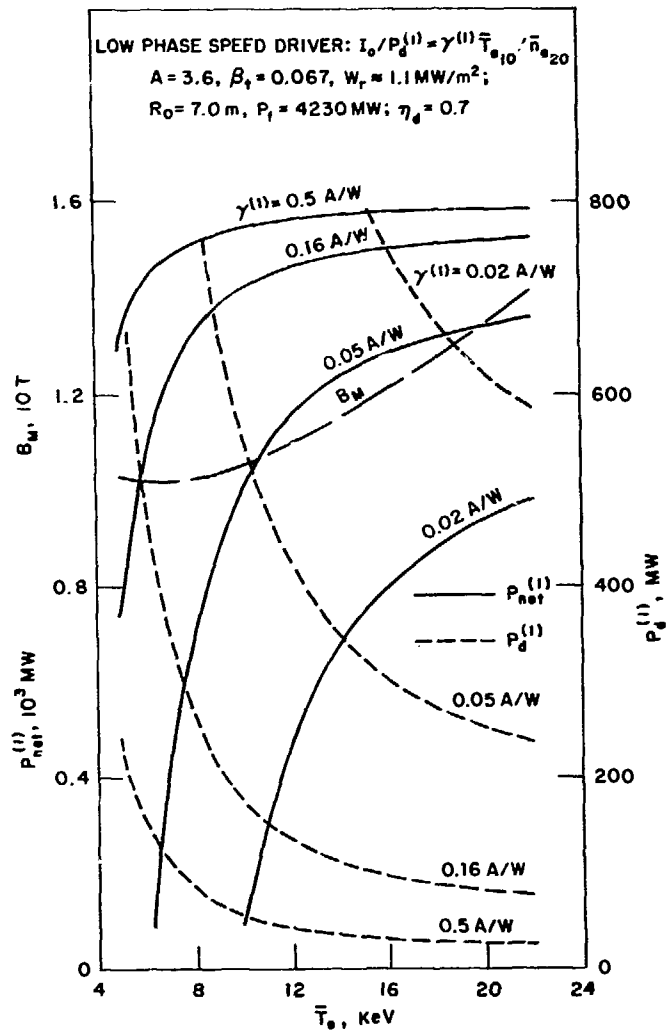

Fig. 2-6. Low-speed current drive for various $\gamma^{(1)}$.

From these trade-off studies several general conclusions are evident for continuous noninductive current drive. First, there is strong incentive to obtain $\gamma \gtrsim 0.1$ A/W in a reactor. Additionally it is highly desirable to hold driver capital costs as low as possible, hopefully in the range \$1/W. Finally, the penalties of noninductive current drive are minimized by operating at high $\bar{T}_e$, which requires increasingly strong magnetic fields. For our study we assume the maximum practical fields are those obtained in the STARFIRE design,[1] $B_M \approx 11$ T. The parameters in Table 2-1 are based on this choice.

The 8-m reactor was sized under a slightly different set of constraints. Since this device is the basis for inductively driven reactors it is specified to produce less gross power than the 7-m tokamak, which is assumed to need $\gtrsim$100 MW of circulated power to drive the plasma current. Additionally, a smaller wall load may be desirable for the 8-m reactor since it is a pulsed machine, and a fluctuating thermal load is expected to be more damaging than a constant heat load. Figure 2-7 shows the required toroidal field B_M at various $\bar{T}_e$ to produce P_f = 3900 MW and $W_n = 3.5$ MW/m^2. As in the previous calculations, Z_{eff} denotes the level of impurities needed to obtain thermal power balance in the plasma: $P_\alpha + P_d + P_\Omega = P_{rad} + P_{lim}$. P_α is the fusion-produced power vested in alpha particles, P_d is the externally supplied (current drive) power, P_Ω is the ohmic heating, P_{lim} is the power lost (mostly to the limiter) as particle kinetic energy, and P_{rad} is the power loss as photons, which is a strong function of Z_{eff}.

The selection of an optimum operating temperature for an ohmically driven tokamak involves the issue of burn length. Assuming plasma resistance drops with T_e we seek high-temperature operation to maximize the burn length. However, the larger B_M needed to keep P_f constant as T_e increases beyond ~8 keV implies larger plasma curent, I_0, to maintain MHD equilibrium. In addition, Z_{eff} increases at higher T_e and, roughly speaking, plasma resistance $\propto Z_{eff}$. Hence the loop voltage scales as the product $I_0 Z_{eff}/\bar{T}_e^{3/2}$. As shown in Fig. 2-8, this factor decreases rapidly until $\bar{T}_e \gtrsim 12$ keV and only slowly at higher $\bar{T}_e$. Countering this drop in loop voltage is a decrease in volt-seconds stored $\bar{T}_e$ (TFC) become thicker since B_M is getting larger. The result is a reduction in the size of the hole in the doughnut, R_{OH}. The figure shows R_{OH} versus $\bar{T}_e$, and the burn length, t_f, can be estimated by

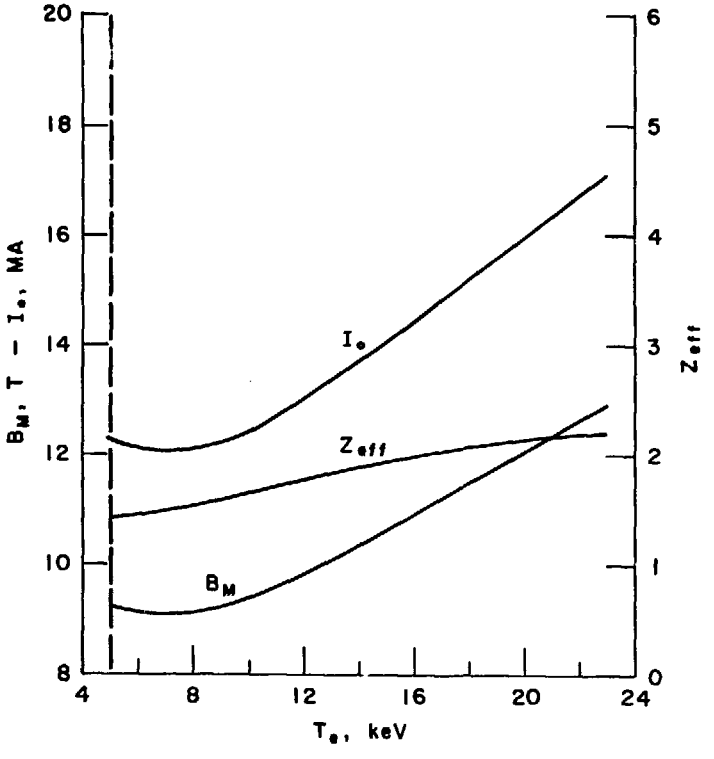

Fig. 2-7. Plasma current, required field, and Z_{eff} for power balance in 8-m reactor: P_f = 3900 MW, W_n = 3.5 MW/m^2.

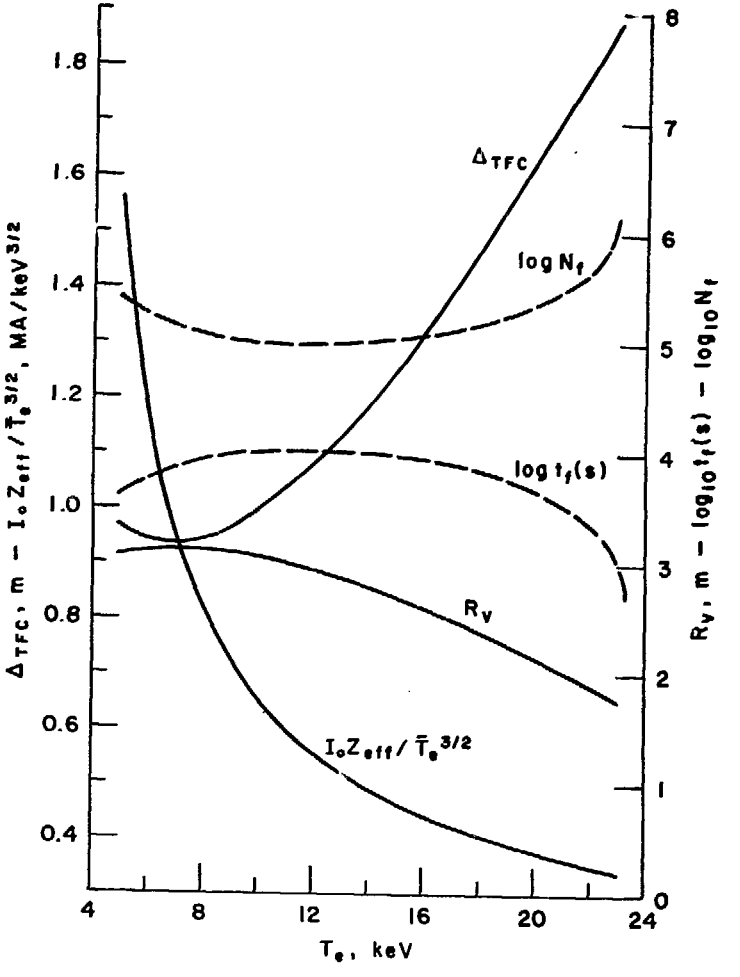

Fig. 2-8. Ohmic reaccor performance; higher B_M increases magnet build, Δ_{TFC}, decreasing the hole in the solenoid, $R_{OH} \equiv R_V$, and reducing volt-seconds. Volt-seconds assume ΔB_{OH} = 2 × 10 T; fusion period, t_f, is based on (Spitzer) loop voltage, $V_\ell = 2.2\ n\Omega \times I_0 Z_{eff}[10\ keV/\bar{T}_e]^{3/2}$.

$$t_f = \frac{\pi R_{OH}^2 \Delta B^{OH} - 25 \text{ V-s} - 1/2 \, LI_0}{I_0 R} ,$$

where ΔB^{OH} is the field swing in the transformer, L is the plasma self-inductance, R is the toroidal resistance, and 25 V-s is assumed for startup losses. For illustration we assume a double-swing transformer with $\Delta B^{OH} = 2 \times 10$ T and a resistance close to Spitzer,

$$R = 2.2 \text{ n}\Omega \times Z_{eff} [10 \text{ keV}/\bar{T}_e]^{3/2} .$$

The result, shown in Fig. 2-8, is that t_f is a broad maximum, nearly 10^4 s, for 8 keV $\lesssim \bar{T}_e \lesssim$ 16 keV. In order to reduce the demands on the TFC we choose to operate at the lower end of this range, where B_M is relatively small. Our reference design, described in Table 2-2, operates at $\bar{T}_e = 10$ keV with $B_M = 9.8$ T, substantially lower than for the 7-m tokamak. The number of fusion cycles in 40 yr of operation at 80% availability is over 10^5.

2.2 Reference Burn Cycles

Noninductive current drive introduces considerable flexibility in designing tokamak burn cycles. For our study we have identified five alternative burn cycles, which are qualitatively distinct:

- **Conventional ohmically driven (OH) cycle.** This cycle is shown schematically in Fig. 2-9. The toroidal current is driven by a transformer, and once the volt-seconds are consumed the current decays and the fusion burn is extinguished. Both the current pulse, t_I, and fusion power period, t_f, are the same, ~10^3–10^4 s. Thermal loads and magnetic fields (ohmic heating and equilibrium) oscillate with the same periodicity. The figure illustrates single swing transformer action (plasma current and equilibrium field always in one direction), but double swing operation is also possible. Neutron power, P_n, and fusion thermal power, P_α, are zero when the plasma density, n, and temperature drop; during this down period, t_{off}, thermal power must be extracted from auxiliary storage units to supply the steam generators. Previous studies[4,5,6] of the OH cycle have addressed some issues related to the burn length.

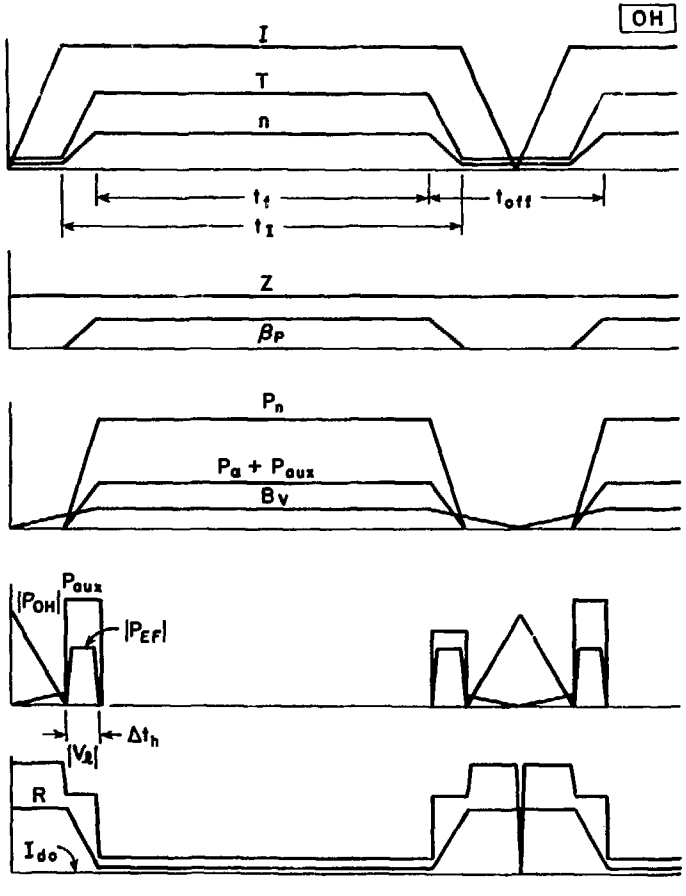

Fig. 2-9. Schematic OH burn cycle.

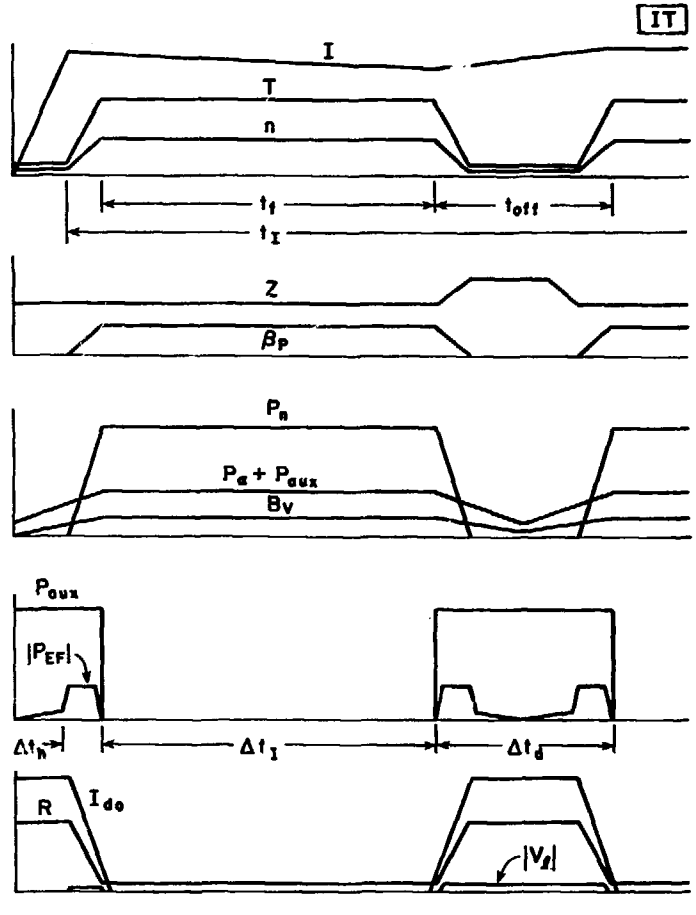

Fig. 2-10. Schematic IT burn cycle.

- **Noninductive assisted startup.** The wave forms for this cycle are similar to the OH cycle. However, during the low density phase of startup, noninductive current generation is utilized.[7] The advantage of this technique is the avoidance of large loop voltages, V_ℓ, which would otherwise be needed to initiate inductive current during the low temperature, high resistance (R) phase of the burn cycle. This elimination of large loop voltages may facilitate the design of a conducting first wall around the plasma. In addition, noninductive current initiation may permit better control over the current density profile early in the discharge when disruptions are particularly virulent.

- **Internal transformer (IT) operation.** This mode of operation[8-10] requires no external transformer. Instead, noninductive current drive is used during periodic low density phases to boost toroidal current by a small increment ΔI. Between current drive periods the density is increased for full fusion power production, and the current decreases resistively for a burn length $t_f \approx \Delta t_I \approx (\Delta I/I_0)(L/R)$. In order to keep the toroidal current nearly constant ($\Delta I \ll I_0$), the burn is limited to a relatively short period ($\sim 10^2$ s), and this mode will result in many times more total fusion cycles in the reactor lifetime than the OH cycle. The fusion power oscillations lead to thermal cycling, as in the OH cycle. The equilibrium field, B^{EF} will also fluctuate; even though toroidal current is nearly steady, poloidal beta, β_p, fluctuates from density cycling, and we note

$$B^{EF} \approx \frac{\mu_0 I_0}{4\pi R_0} \left[\ell n(8A) + \beta_p - 1.5\right] .$$

Roughly speaking we can expect B^{EF} variations on the order of half the full field value, for a typical IT cycle. This cycle is shown schematically in Fig. 2-10. A possible advantage of this cycle is that the current density might be kept fairly constant, in a safe regime which does not permit major disruptions.

- **Hybrid transformer operation.** A variation from the IT cycle, this would use an external transformer to maintain I_0 during the fusion burn and then keep I_0 at full value with low density noninductive current drive while the transformer is quickly recharged.[10] As with the IT, both thermal and

magnetic fluctuations occur, but the fusion period is much longer, resulting in fewer lifetime cycles. Compared to the OH cycle this mode benefits from keeping I_0 constant: equilibrium field power, P_{EF}, may be smaller, downtime (t_{off}) may be shorter, periodic purging and plasma breakdown is avoided, and disruptive regimes might be circumvented. Of course, an external transformer is a necessary system for this reactor cycle and represents additional cost and complexity.

- **Continuous (CW) operation.** This mode was the postulated mode used by STARFIRE (Refs. 1 and 11) and is shown schematically in Fig. 2-11. This technique is only practical if noninductive current drive is sufficiently efficient during high density fusion operation that the circulating power, P_{aux}, is a small fraction of the fusion power. With this proviso, however, reactor operation is possible in principle for very long periods (months), until reactor maintenance forces shutdown. Fatigue is expected to be of minor concern

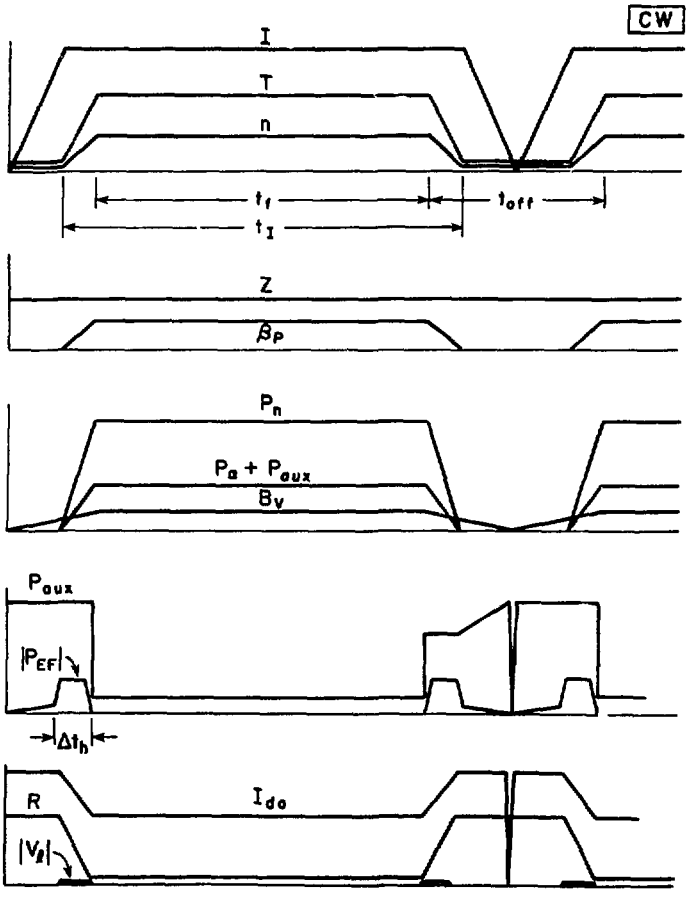

Fig. 2-11. Schematic CW burn cycle.

since only a few hundred thermal and magnetic cycles occur in the reactor lifetime. Thermal storage is eliminated, slow current and power ramps minimize the cost of startup power supplies, disruptions may be very infrequent, and additional design latitude (e.g. low aspect ratio[12]) derives from eliminating the external transformer. The main drawbacks are circulating power and the capital cost of the noninductive driver hardware.

Our study focuses on the effects of cyclic operation on the following reactor subsystems: first wall; limiter/divertor; blanket; thermal energy storage; electric power supplies; ohmic heating (OHC) transformer; equilibrium field (EFC) coils; and toroidal field (TFC) coils. In our assessment we fix most reactor parameters as given in Tables 2-1 and 2-2 and study subsystem sensitivity to a range of operating conditions for a single critical design driver. As an example, we expect thermal storage costs to be closely dependent on downtime, t_{off}, between fusion burns but relatively insensitive to such parameters as fusion burn length, t_f, and neutron wall load, W_n. Table 2-3 lists the range of operating conditions relevant to the spectrum of burn cycles described above. The lifetime number of fusion burns, N_f, is found by dividing t_f into 1.01×10^9 s, the total operating life (40 y at 80% availability).

2.3 Tokamak Subsystem Models

The design of tokamak reactors is the object of our present investigation; we have included multiple concepts for most subsystems in order to reflect the uncertainty of future technology.

In the case of the limiter structure we have studied two basic alternatives. One system, representative of near-term technology, uses a copper alloy for the heat sink structure and is water cooled (4 MPa, 130°C, flowing at 8 m/s with an interface conductivity 5.684 W/cm^2-K). A more advanced alternative has a vanadium alloy heat sink with liquid lithium coolant (4 MPa, 210°C, ~2 m/s, laminar flow with interface conductivity 3.45 W/cm^2-K). The actual geometry is that proposed and analyzed in the STARFIRE study.[1] The front face of the limiter (that portion closest to the plasma, nearly tangential to the magnetic field) is modeled as a flat slab with a thermal load, W_{ff} = 1.5-3.5 MW/m^2. The leading edge (farthest recessed into the limiter

TABLE 2-3

Burn Cycle Operating Windows

Parameters	Range of Values	Reactor/Cycle
Fusion period (s):		
t_f =	9×10^6 $(N_f \sim 120)$	CW
	9×10^4 $(N_f \sim 1 \times 10^4)$	OH (daylong burn)
	8×10^3 $(N_f \sim 1 \times 10^5)$	OH reference
	2×10^3 $(N_f = 5 \times 10^5)$	OH
	600 $(N_f = 1 \times 10^6)$	IT
	60 $(N_f = 1 \times 10^7)$	IT
Low power period (s):		
t_{off} =	400	IT
	90	OH reference
	4	IT
Maximum limiter heat load (MW):		
P_{lim} =	150	CW
	93	OH reference
	75	
Maximum radiation first wall load (MW/m^2):		
W_{rad} =	1.0	CW
	0.76	OH reference
	0.50	
Maximum neutron first wall load (MW/m^2):		
W_n =	4.40	CW
	3.45	OH reference
	2.00	
Minimum power levels and wall loads during downtime =	0 (nonzero levels possible for IT and hybrid models)	

shidow, where the poloidal magnetic field appears almost normal to the surface) is analyzed as a cylinder. Careful design of the limiter geometry is expected to result in leading edge thermal loads smaller than those on the front face; we consider $W_{\ell e}$ = 0.75-1.75 MW/m^2. For this study we assume the entire limiter is laminated with a surface material specifically designed to reduce sputtering poisoning of the plasma. The high plasma temperature at the front face constrains our choice to a small class of options, and we pick beryllium as a typical coating. Near the leading edge the plasma temperature is lower, and a larger number of options are possible. In this region we consider both beryllium and tungsten as coatings.

The first wall is treated as a simple bank of cooling tubes.[14] One option is water cooled (15 MPa, 300°C) with prime candidate alloy (PCA) for the tube structure. We use 20% cold worked Type 316 stainless steel to model the PCA properties. At these high pressures a thin wall tube requires a small inner radius, and we consider r_i = 3-10 mm. The more advanced design utilizes liquid lithium (2 MPa, 350°C) as a coolant and vanadium as the structure. The low pressure permits relatively large radius piping; r_i = 25 cm is chosen. The surface heat load, W_{rad} = 0.5-1.0 MW/m^2, is assumed normal to the pipe surface. Away from the limiter this heating is due mainly to photon radiation, and the first wall is thus assumed to be bare structure. (In the vicinity of the limiter charge-exchange sputtering may be significant and would require a special surface coating. This region was not studied in our present first wall lifetime analysis.)

Electrically the first wall is considered to be a good conductor, since this feature is deemed desirable for disruption control. The resistive time constant for a circular toroidal shell is[7] $\tau_s = 1.3\ a\ d\ \eta_w^{-1}$, where τ_s is in seconds and a is the minor radius in meters, d is the shell thickness in centimeters, and η_w is the shell resistivity in μΩ-cm. For the first wall model with water coolant we find $\tau_s \approx 20$ ms for bare PCA tubes. However, a 1.0-mm beryllium coating on the tube panel surface adds an additional 20 ms to the time constant. Most importantly, this first wall concept is frequently suggested in combination with a solid lithium blanket and ~5.0 cm of beryllium neutron multiplier directly behind the first wall. This beryllium layer increases the total τ_s to ~1000 ms. For the alternative first wall model, vanadium with lithium coolant, we note that vanadium has a lower resistivity than

PCA and that lithium has an even lower value than vanadium. Considering in addition the large volume of lithium flowing in the first wall (and blanket) we find $\tau_s \gtrsim 1000$ ms is also reasonable for this design concept.

One consequence of a highly conducting first wall is the possibility that inductive startup of the toroidal current is made more difficult. For a continuous toroidal first wall the wall's circuit resistance is related to τ_s by $R_w = 1.3 \times 10^{-6} R_0/\tau_s$, in MKS units. For reactors we are considering, R_w = 10 μΩ - 100 μΩ for τ_s in the range 1000 ms to 100 ms. A previous study[15] has shown that the current ramp is delayed for $R_w \lesssim 25$ μΩ and that currents $\gtrsim 1$ MA are generated in the first wall for periods of order 1 s.

Two models have been selected for the blanket and thermal storage analysis. One is similar to the STARFIRE design.[1] It has PCA structure with a mass of solid lithium breeding compound (Li_2O), which is penetrated by many water-filled coolant tubes. The alternative blanket design assumes a liquid lithium breeder, which is also the primary coolant, and vanadium structure. Thermal storage is accomplished in former case with a high pressure water system and with liquid sodium in the latter case.

Electric power supplies are needed to transfer energy to magnets. The systems in this study are based on standard equipment, using present-day technology, since this was found to be the least expensive option. The equilibrium field coils (EFC) are powered through silicon controlled rectifiers from a motor-generator-flywheel set. A similar power train is used to reset the ohmic heating coil (OHC) between fusion burns of the ohmically driven and hybrid burn cycles. A third power system is needed for the ohmic burn cycle in order to supply high loop voltage for startup; this power supply dumps considerable energy from the OHC through a resistor. The dump resistor operates with very high power transients but is relatively inexpensive.

The pulsed superconducting magnets (the OHC and EFC) as well as the toroidal field coils (TFC) utilize the multifilament cable described in the STARFIRE design.[1] Separate designs were developed for the OHC with maximum fields of 8, 10, and 12 T, and a performance comparison was pursued. Only niobium-titanium was considered for the OHC since the pulsed nature of its operation would make Nb_3Sn a poor alternative. Both 4.2 K and 1.8 K cooling were examined. A large number of EFC configurations were developed; all EFC designs used niobium-titanium at 4.2 K. In all cases a pumped limiter is

assumed for impurity control, so the EFC does not have to provide a poloidal divertor field.

The TFC model is a critical input to this burn cycle study since the TFC is a very expensive system and is sensitive to fatigue from out-of-plane bending. Our current focus is on one particular TFC design, described in the STARFIRE study.[1] This model calls for Nb_3Sn in the high field region and niobium-titanium elsewhere. The superconductor is housed in a helium vessel at 4.2 K which is suspended by thin struts (of low thermal conductivity) from an enclosing room temperature vacuum tank. Both vessels are constructed from Type 316 LN stainless steel (annealed). The overturning moments on the TFC are resisted by the steel support cylinder (inboard) and shear panels (outboard). This leaves unsupported free spans, along the top and bottom legs of each TFC, which are restrained from gross bending by the stiffness of the vacuum tank. (An alternative TFC model,[13] not considered in the present study, would utilize cryogenic intercoil support structures at the top and bottom and no shear panels outboard. The advantage would be better outboard access and possibly less structure, but a disadvantage would be the extra refrigerator power needed to extract eddy current heat from the larger volume of cryogenic structure.)

2.4 Operating Conditions, Variables, and Lifetime Analysis

In order to facilitate this study we have fixed certain parameters and set limits to others. We briefly describe these operating conditions in what follows.

The first wall and limiter/divertor experience large surface heating, and we must thoughtfully examine maximum permissible temperatures in these materials. Our temperature limits reflect the conclusions of previous fusion materials studies.[16-18] Both candidate surface coatings are limited by radiation induced swelling, beryllium to 700°C, and tungsten to 600°C. Structural alloys are limited in temperature more due to thermal creep since they must be fail-safe against mechanical stress. We limit PCA to ~500°C and vanadium to ~600°C. Copper alloys are not well characterized for a fusion environment, but extrapolating from very limited data (radiation swelling, tensile strength, and ductility) we are compelled to limit this heat sink material to ~250°C.

Our study considers only the thermal effects of disruptions (particle and photon energy delivered to the first wall and limiter). Following the logic presented in the INTOR study[17] we assume ~1.5 GJ of energy, equal to the thermal kinetic energy plus one quarter of the electromagnetic energy, may be dumped on portions of the first wall and limiter. The spatial deposition of this thermal dump is presently difficult to predict, except that the limiter is expected to absorb the brunt of the energy density due to its proximity to the plasma. Additional experimental evidence[19] suggests the disruption thermal load is distributed along the limiter surface in proportion to the normal steady-state heating distribution. For our study we consider the following upper limits to thermal loads from disruptions: first wall $\lesssim$800 J/cm^2, limiter leading edge $\lesssim$1200 J/cm^2, and limiter front face $\lesssim$2500 J/cm^2. We note that a reactor plasma has approximately five times the thermal energy as INTOR and roughly twice the first wall/limiter surface area, so these energy densities are approximately two and one-half times the values considered in the INTOR study.

The time scale for disruptions is also subject to much debate. Carreras et al.[20] have developed a theoretical estimate of the disruption growth period, $\Gamma = C(R_0^2 m_i n_i B_0 a^6 V_\ell^{-3})^{1/5}$, where units are MKS and amu with density in 10^{13}/cm^3. This theory assumes nonlinear interaction of the 3/2 and 2/1 tearing modes in an inductively driven discharge without a close fitting conducting wall. Carreras showed close agreement of this scaling with data from many tokamaks if C = 900 μs. For our 8-m OH reactor, with V_ℓ = 0.048 V, we find Γ = 86 ms. A conducting wall, however, may significantly affect tearing mode behavior. Rutherford has argued[21] that the m = 2 mode cannot grow faster than the resistive time τ_s of the conducting shell. As discussed in Sec. 2.3, τ_s may be as long as 1000 ms. Furthermore it was claimed that the 2/1 precursor to the disruption may be stabilized if $\tau_s \gtrsim 0.3\ \tau_{sawtooth}$. This is because the 2/1 mode is stable whenever q(0) < 1.0, as occurs during a sawtooth. For our reactors the sawtooth period is $\tau_{sawtooth} \approx 2.6$ s, so there is indeed hope that disruptions will not occur. In this study we consider disruption times of 20 ms, 100 ms, and 500 ms. These time scales are much longer than those from small tokamak experience, but they reflect the increase in disruption time observed with larger plasma, higher currents, and hotter temperatures.

Also at issue is the question of how frequently disruptions will be experienced in reactors. As our understanding increases on the subject of the causes of disruptions[22] we expect the likelihood of random disruptions will decrease. Problems occur most frequently during current ramps in ohmic discharges, so one model (which we adopt for our study) is to assign a probability of disruption on each burn cycle. DOUBLET-III has documented[23] disruption frequencies as low as 10^{-2} of the discharges when the limiter q_{lim} = 2.8. In our work we examine frequencies of 10^{-2}, 10^{-3}, and 10^{-4} per burn cycle. In our damage calculations we take the pessimistic assumption that on each disruption the spatial distribution of the thermal dump is identical. We note that for CW current drive this model of disruption frequency may not be appropriate since there are only $\sim 10^2$ discharges in the 40-yr lifetime of the reactor. Additionally we note that tearing mode theory has not been developed for noninductive current drive, so we do not have a good feeling of how to treat disruption frequency in this limit. One model, which should be studied in future work, might be to assume disruptions occur after some arbitrary period of operation (e.g., every 10^4 s or 10^5 s).

Fatigue damage to reactor structure is due to both fluctuating electromagnetic forces and varying thermal expansion and is studied with two distinct methods. Thin structures (steel bands in the magnets) and cooling tubes designed for high static primary pressures are analyzed with smooth sample data curves (see Appendix A) which show the number of cycles to failure versus the strain variation per cycle. The limiter constraints are modeled in the manner of the INTOR configuration.[17] Thick structural members (in the TFC system), on the other hand, are assumed to have flaws which are initially present but undetected due to the thickness of the structure. Prudent engineering then dictates that a crack propagation analysis be undertaken for estimating lifetime.

Radiation dose is assumed as follows. It is supposed that most of the fusion alpha power leaves the plasma as photons, in order to reduce the charged particle heat load on the limiter as much as possible. The first wall heat load is thus taken as $W_{rad} \approx (1/4) \times W_n$, where W_n is the neutron wall load. In the thermal hydraulic analysis of structure and cladding we use the following nuclear bulk heating rates, normalized to $W_n = 1.0$ MW/m^2: beryllium

= 7.8 W/cm^3; tungsten = 23 W/cm^3; PCA = 10.8 W/cm^3; vanadium = 7.4 W/cm^3; and copper = 14.7 W/cm^3. Radiation damage to structural materials is difficult to gauge due to a paucity of data. It is felt, however, that radiation-induced creep is less damaging than thermal creep, and values as high as 5% are assumed acceptable in our thermal stress analysis. Based on a survey of swelling and ductility measurements under neutron and charged particle radiation we assign the following life limits for neutron fluence to structural materials: copper = 4 MW-yr/m^2; PCA = 12 MW-yr/m^2; and vanadium = 24 MW-yr/m^2. These limits assume the temperature constraints on these materials, given previously, are not violated.

Sputtering erosion of surfaces exposed to plasma is not explicitly calculated in this study. We note, however, that sputtering may be the most severe life limitation to the limiter, calculations suggest cladding erodes at rates as large as 10 cm/yr.[17] We assume in situ recoating techniques will be developed. In the lifetime analysis, though, we acknowledge that some structure (e.g., the limiter) may be replaced during annual maintenance periods. We likewise note that sputtering depends strongly on the plasma edge temperature, which cannot presently be predicted. Thus, the suitability of limiter coatings, such as tungsten and beryllium, depends on information which is not presently known.

Our study ignores synergistic effects on material aging. As an example, the thermo-physical properties of structural alloys are not degraded with time in our fatigue cycle lifetime analysis. Nor is structural thinning from disruptions or sputtering considered in the fatigue analysis. Likewise, surface crack initiation from disruptions is not considered in the analysis of fatigue.

The total number of fusion cycles in the reactor lifetime is based on a 40-yr assumed lifetime and 80% availability, which yields 1.0×10^9 s of operation. Our philosophy is that all burn cycles must achieve this high availability to be of interest to a utility. We attempt to calculate design requirements and system capital costs needed to approach these goals. Except where noted, all costs are in 1983 dollars. An accurate estimate of subsystem reliability, mean time to replace failed components, and system availability is obviously not possible at present. However, the data base presented here provides a useful comparison of the relative attractiveness of the various burn cycles to different reactor subsystems.

REFERENCES FOR CHAPTER 2

1. C. C. BAKER et al., "STARFIRE, A Commercial Tokamak Power Plant Study," ANL/FPP/80-1, Argonne National Laboratory (1980).

2. M. ABDOU et al., "A Demonstration Tokamak Power Plant Study - Interim Report," ANL/FPP/TM-154, Argonne National Laboratory (1982).

3. "A Design Analysis of Supplemental Heating Systems, Final Report," TRW, Inc. (1981)

4. R. L. REID et al., "Large Aspect Ratio Study," Proc. 8th Symp. on Engineering Problems of Fusion Research, Vol. I, p. 427 (1979).

5. L. BROMBERG et al., "A Modular Commercial Tokamak Reactor with Day-Long Pulse," J. Fusion Energy 3, 63 (1983).

6. J. N. BROOKS and R. L. KUSTOM, "Power Supply Requirements for a Tokamak Fusion Reactor," ANL/FPP/TM-119, Argonne National Laboratory (1979).

7. Y-K. PENG et al., "FED-A," ORNL/FEDC-83/1, Oak Ridge National Laboratory (1983).

8. R. A. BOLTON et al., "New Techniques for Inducing Plasma Current in Large Tokamak Devices," in Proc. 3rd Top. Mtg. on Technology of Controlled Nuclear Fusion, CONF-780508, Vol. II, p. 824 (1978).

9. C. E. SINGER et al.,"Continuous Tokamak Operation with an Internal Transformer," PPPL-1936, Princeton Plasma Physics Laboratory (1982).

10. N. J. FISCH, "Current Generation in Toroidal Plasma in Heating in Toroidal Plasma," Proc. 3rd Joint Grenoble-Varenna Intern. Symp. on Heating on Toroidal Plasmas, Grenoble, France (1982).

11. D. A. EHST et al., "Lower Hybrid Heating and Current Drive System for a Tokamak Reactor," J. Fusion Energy 2, 83 (1982).

12. D. A. EHST, "Wave Driver Options for Low Aspect Ratio Steady-State Tokamak Reactors," J. Fusion Energy 1, 357 (1981).

13. C. A. FLANAGAN et al., "FED", ORNL/TM-7948, Oak Ridge National Laboratory (1981).

14. D. L. SMITH et al., "Fusion Reactor Blanket/Shield Design Study," ANL/FPP/79-1, Argonne National Laboratory (1979), Chap. 7.

15. J. N. BROOKS, in "Recent Contributions to Fusion Reactor Design," ANL/FPP/TM-103, Argonne National Laboratory (1978), p. 1.

16. R. F. MATTAS and D. L. SMITH, "Model for Life Limiting Properties of Fusion Reactor Structural Materials", Nucl. Technol. 39, 186 (1978).

17. "FED/INTOR Critical Issues," USA FED-INTOR/82 (1982).

18. R. F. MATTAS, "Fusion Component Lifetime Analysis," ANL/FPP/TM-160, Argonne National Laboratory (1982).

19. T. S. TAYLOR, in "Annual Report to DOE of the General Atomic Company Fusion Pogram for Fiscal 1981," T. Ohkawa and J. C. Wesley (eds.), GA-A16816, General Atomic Company (1981), p. 27ff.

20. B. CARRERAS, B. V. WADDEL, and H. R. HICKS, "Analytical Model for the Nonlinear Interaction of Tearing Modes of Different Pitch in Cylindrical Geometry," , ORNL/TM-6175, Oak Ridge National Laboratory (1978).

21. Y-K. PENG et al., "FED-A", ORNL/FEDC-83/1, Oak Ridge National Laboratory (1983).

22. R. B. WHITE AND D. A. MONTICELLO, "Causes of Major Tokamak Disruptions," PPPL-1674, Princeton Plasma Physics Laboratory (1980).

23. J. WESLEY, General Atomic Co., personal communication (1981).

Chapter. 3. FIRST WALL/LIMITER/DIVERTOR

Twenty per cent of the fusion power in a deuterium-tritium (D-T) reactor is deposited on the surfaces of the first wall and the limiter or divertor neutralizer plates during normal operation. Thus thermal fatigue is expected to play an important role in these structures for any burn cycle with a large number of pulses. In addition, surface erosion is anticipated due to both continuous sputtering and occasional large thermal dumps during plasma disruptions. Another life limit is imposed by neutron damage to these structures. The goal of this chapter is to identify the burn cycle conditions which maximize component lifetime, considering all these constraints simultaneously. The capital cost for the first wall/limiter system is not large (~$4 M in the STARFIRE design) compared to the overall power plant. However, the impact on reactor operations is tremendous if these structures require frequent replacement. The STARFIRE study estimated, for example, that a week to ten days would be needed to remotely remove and replace a blanket sector and its first wall structure. Such long periods for reactor maintenance appear uneconomical to an electric utility, and we thus feel there is a strong motivation for achieving lifetimes of many years for these components.

This chapter is organized as follows. The damage to surfaces exposed to plasma disruptions is calculated first for a variety of assumptions. This data serves as input to the lifetime analysis which follows. In the next section the limiter is studied. The temperature profiles through the limiter are calculated for various conditions, and then a stress analysis is done to assess fatigue damage. The lifetime analysis of the limiter identifies the optimum thickness for surface coatings to maximize lifetime against disruptions, fatigue, radiation damage, etc. Finally, the fatigue life of bare first wall coolant tubes is studied. Again an analysis is done to find the optimum tube thickness for maximum first wall life. Our results are then related to the burn cycle parameters in order to indicate the length needed for a fusion burn in order to approach the benefits of purely steady-state thermal operation.

3.1 Disruptions

Disruptions can limit the lifetime of the limiter, divertor, and first wall. The surfaces of these components are subject to melting and vaporization resulting from the deposition of plasma energy in a relatively short time. Induced current will result in forces and torques within the melt layer which give rise to instabilities that can result in melt layer removal.[1]

The primary disruption parameters are the energy deposition per unit area, the disruption time, and the frequency of disruptions. A discussion of the energy density range and deposition times considered in this analysis is presented in Chap. 2. The reference disruption time is assumed to be 100 ms and the range of energy densities vary as whether first wall, leading edge, or the front face of the limiter is considered. The maximum energy density deposited on the first wall is 800 J/cm^2 and for the limiter the maximum is 2500 J/cm^2. Two materials are investigated as potential first wall candidates, i.e. stainless steel and vanadium. For the limiter also two coating materials are considered: beryllium and tungsten. The thermal response and the resulting vaporization losses and melt layer thickness are computed with the A*THERMAL computer code.[2] The code solves the heat conduction equation with temperature varying thermal properties and uses the surface temperature to compute the evaporation rate. Moving boundary conditions are used to account for surface recession from evaporation and also for solid-liquid interface. For a review of the models used to calculate the evaporation see Ref. 2. No vapor shielding has been accounted for in this analysis.[3]

Figure 3-1 shows the total material erosion as a function of disruption energy density for 100-ms disruption time (reference case), for both first wall and limiter materials. Vanadium as a first wall material results in much less erosion than stainless steel. At these energies the main material erosion is from melting. For limiter materials, beryllium shows much higher erosion than tungsten. The threshold energy density to induce melting in beryllium is near 350 J/cm^2 while for tungsten it is about five times higher. This is mainly because of the very high melting point of tungsten.

The variation of the melting zone thickness and vaporization losses with energy density for different disruption times is shown for beryllium in Figs.

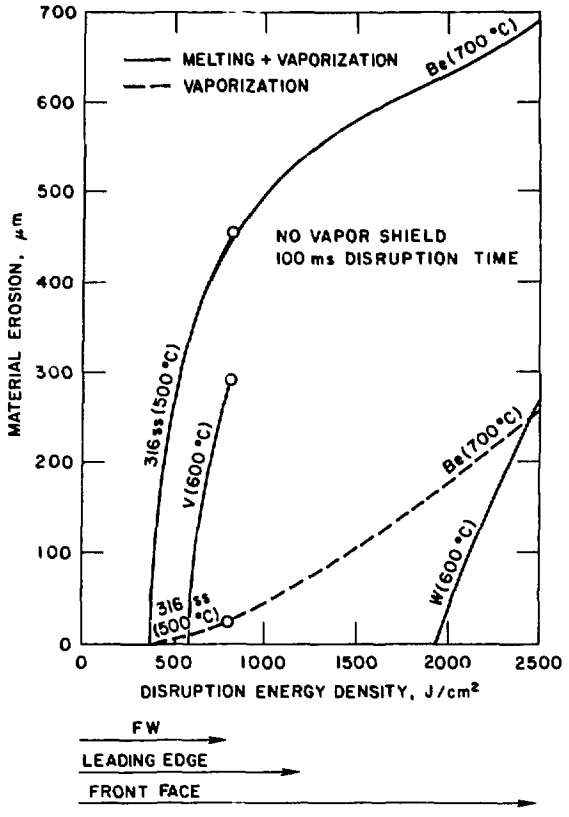

Fig. 3-1. Disruption damage for 100-ms thermal dump.

3-2 and 3-3, respectively. Shorter disruption times always lower the threshold energy density required to induce melting and cause significant vaporization. Longer disruption times usually result in larger melting zone thickness and smaller vaporization losses while shorter disruption times result in higher vaporization and less melting. This is mainly because for shorter disruption times there is not enough time for the energy to be conducted away into the material and the resulting higher surface temperature produces more evaporation and consequently less energy to be conducted to cause melting. For the case with 2500 J/cm^2 deposited in 500 ms on beryllium surface, a melt layer thickness of ~1.0-mm thickness is developed. If this melt layer is unstable under the various forces existing in the reactor cavity, as is assumed in this study, a complete loss of the limiter coating material can occur after a few disruptions. The total material erosion (including melting) is usually less for shorter disruption times at higher energy densities.

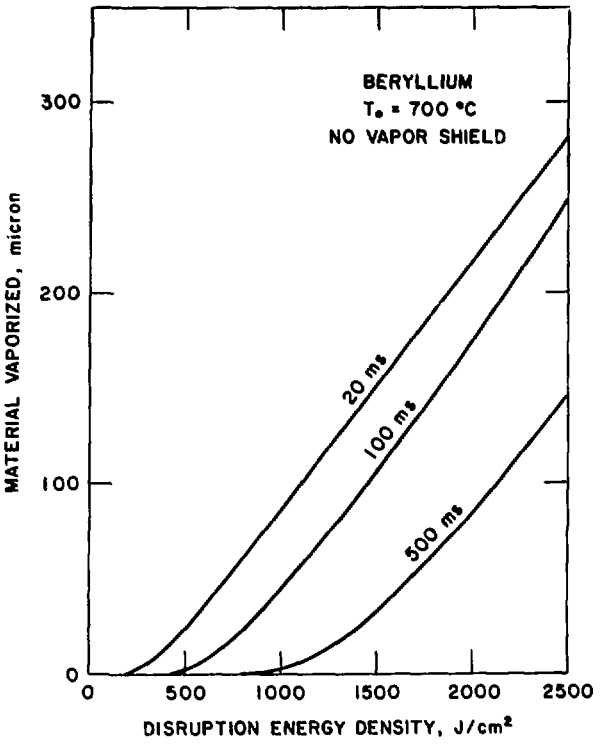

Fig. 3-2. Beryllium melting for various disruption times.

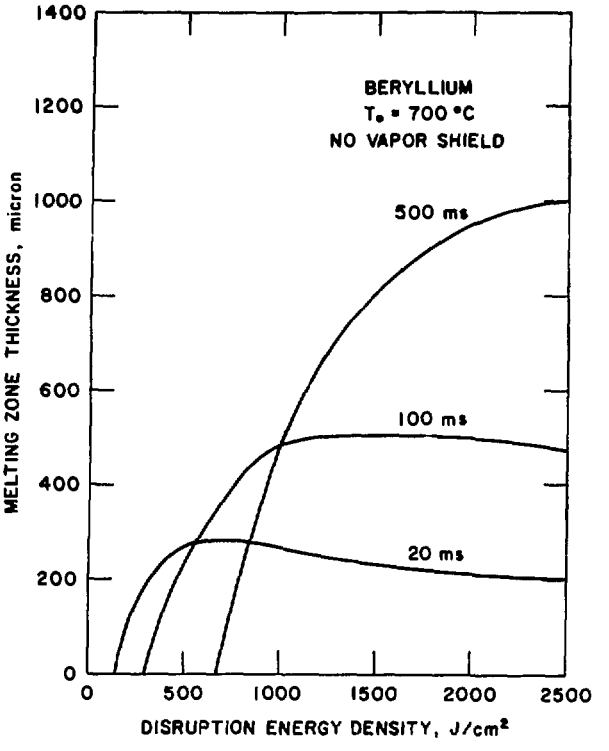

Fig. 3-3. Beryllium vaporization for various disruption times.

3.2 Limiter

The "mushroom"-shaped limiter experiences qualitatively differing heat flow at the front face and at the leading edge. The front face is tangential to the poloidal magnetic field and is analyzed as a slab. Normal heating and disruptive loads are assumed to be twice as large on the front face as on the leading edge. However, the cylindrical geometry of the leading edge aggravates the heat removal problem as the surface coating becomes thicker. The constraints on the heat sink and surface coatings (tiles) also depend on these differences in geometry. Here we compute temperature profiles in the first subsection, and this is followed by a fatigue analysis. Finally, at the end of this chapter, a lifetime study is performed in order to set fusion burn goals for pulsed burn cycles.

3.2.1 Limiter Temperature Profiles

The objective of the thermal-hydraulics analysis is to provide temperature distribution in the coating and structural materials of the limiter.

These temperature distributions will be used as input for stress analysis, and will also be used to determine if the temperatures are within the acceptance levels. One-dimensional steady-state analyses are carried out for both the front surface and the leading edge of the limiter. A list of materials, coolants, and parameter ranges covered in this study is provided in Table 3-1.

TABLE 3-1

Materials, Coolants, and Parameter Ranges
Employed in the Thermal-Hydraulic Calculations

Coating material	Beryllium and tungsten[a]
Structural material/coolant	Copper alloy/water and vanadium alloy/lithium
Structural material thickness (mm)	1.5
Coating material thickness (mm)	1-20
Neutron wall loading (MW/m^2)	3.45
Surface heat flux:	
Leading edge	0.75, 1.25, and 1.75
Front surface	1.5, 2.5, and 3.5

[a]Leading edge only.

Analyses and results of the front surface and the leading edge of the limiter are described in the following sections.

3.2.1.1 Analyses

The limiter front surface is modeled with a slab geometry shown in Fig. 3-4, where q_s is the surface heat flux, Q is the nuclear heating rate, T is temperature, k is the thermal conductivity of the material, is the thickness of the material, x is the coordinate in the direction of the surface heat flux, T_f is the mean bulk temperature of the coolant, and subscripts 1 and 2 refer to the structural and coating materials, respectively. Under steady-state condition, the temperature distribution in the coating material is:

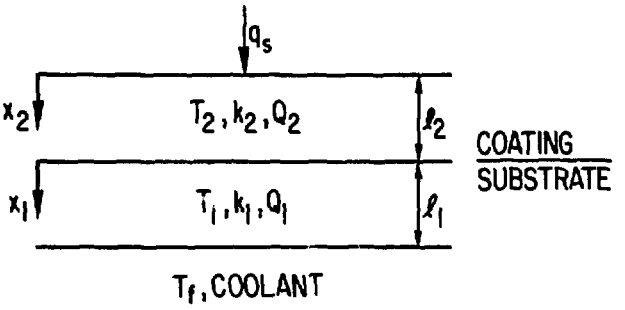

Fig. 3-4. Slab geometry for the front surface of a limiter.

$$T_2 - T_{12} = \frac{q_s}{k_2}(\ell_2 - x_2) + \frac{Q_2}{2k_2}(\ell_2^2 - x_2^2) , \tag{3-1}$$

where T_{12} is the temperature at the interface between the coating and the is:

$$T_1 - T_w = \frac{q_{12}}{k_1}(\ell_1 - x_1) + \frac{Q_1}{2k_1}(\ell_1^2 - x_1^2) , \tag{3-2}$$

where q_{12} is the heat flux at the interface between the coating and the structural material, and T_w is the structural temperature at the structure/coolant interface. The heat fluxes at the two interfaces are given by:

$$q_{12} = q_s + Q_2\ell_2 \tag{3-3}$$

$$q_{1f} = q_{12} + Q_1\ell_1 = q_s + Q_1\ell_1 + Q_2\ell_2 , \tag{3-4}$$

where q_{1f} is the heat flux at the structure/coolant interface. In addition, T_w is related to q_{1f} by:

$$q_{1f} = h(T_w - T_f) , \tag{3-5}$$

where h is the heat transfer coefficient between the structure and the coolant.

If it is assumed that perfect contact (brazed condition) exists between the coating and the structural materials, then the temperature is continuous across this interface. The interface temperature T_{12} can be obtained by letting $x_1 = 0$ in Eq. (3-2):

$$T_{12} - T_w = \frac{q_{12}}{k_1} \ell_1 + \frac{Q_1 \ell_1^2}{2k_1} . \qquad (3\text{-}6)$$

For given h, t_f, q_s, ℓ_1, ℓ_2, Q_1, Q_2, and k_1, k_2, Eqs. (3-1) through (3-6) can be used to calculate the temperature distributions in the coating (T_2) and the structural (T_1) materials for the front surface of the limiter.

At the leading edge, the effect of curvature should be included if the thickness of the coating material is not small compared to the radius of curvature at the leading edge. Figure 3-5 shows the geometry at the leading edge

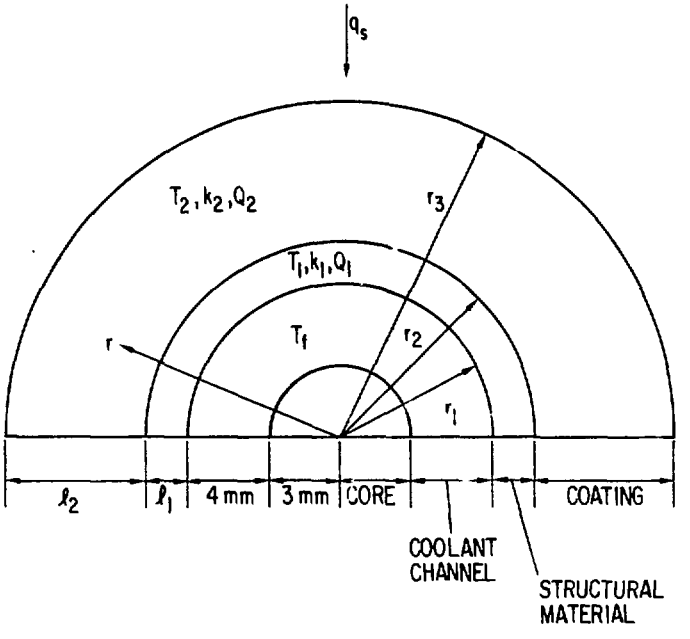

Fig. 3-5. Cylindrical geometry at the leading edge of a limiter.

of the limiter. The nomenclature in Fig. 3-5 is defined in the same manner as those shown in Figs. 3-4 for the front surface except the radial coordinates r_1, r_2, and r_3 now replace x_1 and x_2. The steady-state temperature distribution in the coating material is:

$$T_2 - T_{12} = \frac{Q_2}{4k_2} (r_2^2 - r^2) + \left(\frac{Q_2 r_3^2}{2k_2} + \frac{q_s r_3}{k_2} \right) \ln \left(\frac{r}{r_2} \right), \qquad (3\text{-}7)$$

and the structural temperature distribution is:

$$T_1 - T_W = \frac{Q_1}{4k_2}(r_1^2 - r^2) + \left(\frac{Q_1 r_2^2}{2k_1} + \frac{q_{12} r_2}{k_1}\right) \ell n \left(\frac{r}{r_1}\right), \qquad (3\text{-}8)$$

where q_{12} is again the heat flux at the coating/structure interface. The following approximate energy balance is employed to determine the interfacial heat flux q_{12}:

$$2\pi r_2 q_{12} = 2\pi(r_3 - r_2)(r_2 + r_3)(Q_2/2) + 2\pi r_3 q_s$$

or

$$q_{12} = \frac{q_s r_3 + Q_2(r_3^2 - r_2^2)/2}{r_2} . \qquad (3\text{-}9)$$

Similarly, the heat flux at the structure/coolant interface is given by:

$$q_{1f} = \frac{q_{12} r_2 + Q_1(r_2^2 - r_1^2)/2}{r_1} . \qquad (3\text{-}10)$$

The interfacial heat flux q_{1f} is related to the interface wall temperature T_w by:

$$q_{1f} = h(T_w - T_f) , \qquad (3\text{-}11)$$

and the interface temperature T_{12} is obtained by letting $r = r_2$ in Eq. (3-8) and by assuming perfect contact between the coating and the structural materials,

$$T_{12} - T_w = \frac{Q_1}{4k_2}(r_1^2 - r_2^2) + \left(\frac{Q_1 r_2^2}{2k_1} + \frac{q_{12} r_2}{k_1}\right) \ell n \left(\frac{r_2}{r_1}\right) \qquad (3\text{-}12)$$

For given q_s, h, T_f, Q_1, Q_2, k_1, k_2, and r_1, r_2, r_3, Eqs. (3-7) through (3-12) can be used to calculate the temperature distributions in the coating (T_2) and the structural (T_1) materials.

Table 3-2 lists some values of the material properties used in the calculations. The heat transfer coefficient (h) needs to be determined.

TABLE 3-2

Values of Some Material Properties
Used in the Calculations

Material	Thermal Conductivity (W/m-K)	Nuclear Heating Rate (W/cm^3)
Beryllium	100	27
Tungsten	130	79
Copper alloy	120	51
Vanadium alloy	28	25

For water, the Dittus-Boelter correlation for fully developed turbulent flow can be used. $h = 5.66 \times 10^4$ W/m^2-K was used for water, which corresponds to a velocity of 11.7 m/s. For liquid lithium, the heat transfer coefficient cannot be determined easily. It is known that the magnetic field suppresses turbulence in liquid-metal flows. Thus, the flow in the limiter is likely to be laminar. It is also known that the velocity profile of liquid-metal flow in a transverse magnetic field is very sensitive to geometry and the orientation of the field. For the present study, it is conservatively assumed that the heat transfer coefficient is equal to that of laminar, fully developed flow in a rectangular duct. The actual value of h used for liquid lithium turns out to be in the same order of magnitude as the h for water. Thus, a value of $h = 5.66 \times 10^4$ W/m^3-K is also used for liquid lithium.

3.2.1.2 Results

Figure 3-6 shows the variation of the maximum coating temperature for various surface heat fluxes at the front surface of the limiter. The corresponding variation of maximum structural temperature with coating thickness is shown in Fig. 3-7. In both Figs. 3-6 and 3-7, the coating material is beryllium and the structural material is copper alloy. The coolant used is pressurized water and the mean bulk fluid temperature is assumed to be 130°C. It can be observed that maximum coating temperature increases almost linearly with coating thickness while maximum structural temperature is almost independent of the coating thickness. Both maximum coating and structural temperatures increase with surface heat flux. Similar results are obtained for using

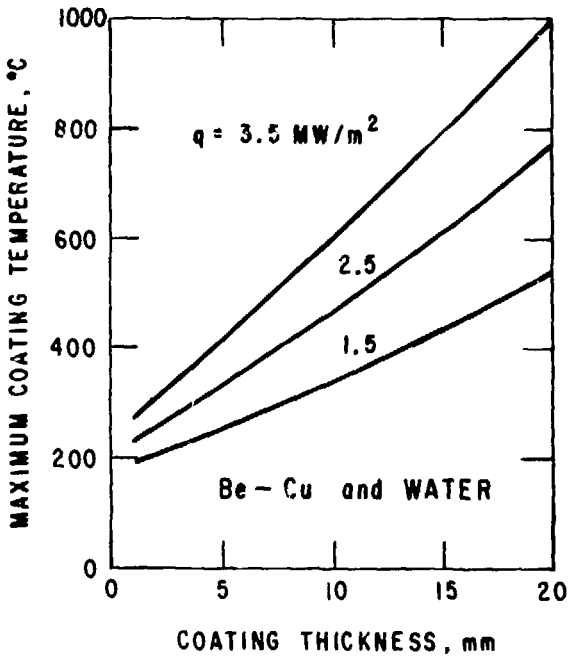

Fig. 3-6. Maximum coating temperature versus coating thickness for various surface heat fluxes at the front surface of a limiter.

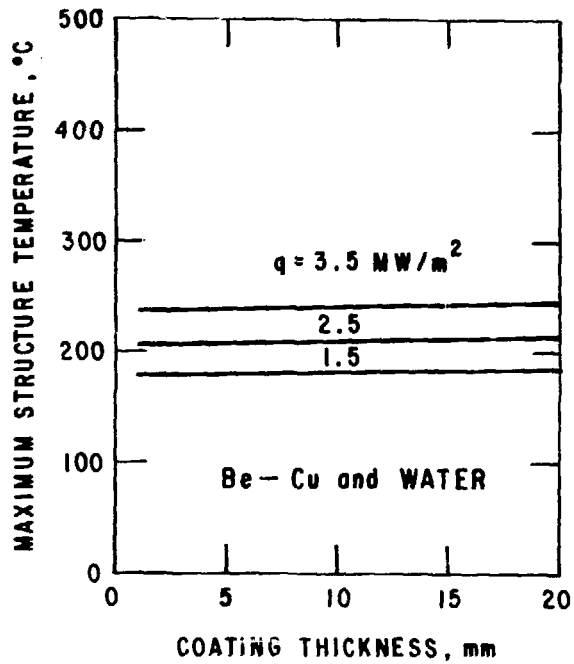

Fig. 3-7. Maximum structure temperature versus coating thickness for various surface heat fluxes at the front surface of a limiter.

lithium as coolant and vanadium alloy as structural material, and these results are shown in Figs. 3-8 and 3-9. The only difference betweem using water and lithium as coolant is the bulk fluid temperature. A maximum bulk temperature of 210°C is assumed for liquid lithium. This plus the relatively low conductivity of vanadium alloy resulted in much higher structural temperature compared to the case of using water as coolant and copper alloy as structural material. However, this does not mean copper is superior to vanadium since the acceptable temperature level for vanadium is higher than that of copper.

The choice of 210°C for lithium bulk temperature is on the low side. Lithium has a melting point of ~180°C. The inlet temperature of lithium should be, say 50°C above the melting point in order to avoid operating too close to the solidification limit. This plus some additional temperature rise through the limiter could make the maximum lithium temperature higher than 210°C assumed here. However, it should be noted that the trend of the results will not be affected by the choice of the bulk lithium temperature. A choice of a higher lithium temperature will shift all the temperatures upward by the same amount. The slopes of the temperature profiles remain unaffected.

Figures 3-10 and 3-11 show the results at the leading edge with water as coolant and beryllium/copper as coating/structure materials. It can be observed that both maximum coating and structural temperatures increase with coating thickness. The increase in structural temperature with coating thickness at the leading edge is the result of reduction in heat transfer area radially towards the coolant channel as shown in Fig. 3-5. Similar results, shown in Figs. 3-12 and 3-13, are obtained with tungsten/copper as coating/-structure materials. Tungsten has a higher thermal conductivity than beryllium, but it also has a higher nuclear heating rate compared to beryllium (Table 3-2). When surface heat flux is controlling (high heat flux and relatively thin coating), the difference in maximum temperature between tungsten and beryllium is relatively insignificant. When nuclear heating is controlling (relatively low surface heat flux and thick coating), the difference in temperature between tungsten and beryllium becomes more pronounced. In the latter situation, the tungsten temperatures are appreciably higher than the

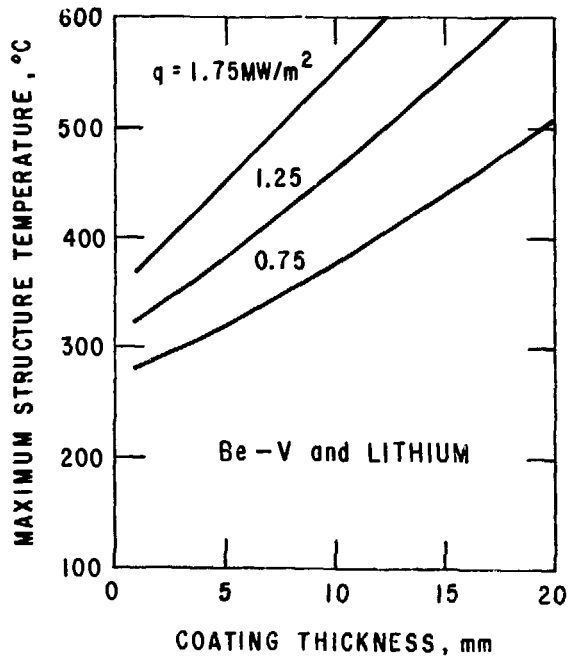

Fig. 3-8. Maximum coating temperature versus coating thickness for various surface heat fluxes at the front surface of a limiter.

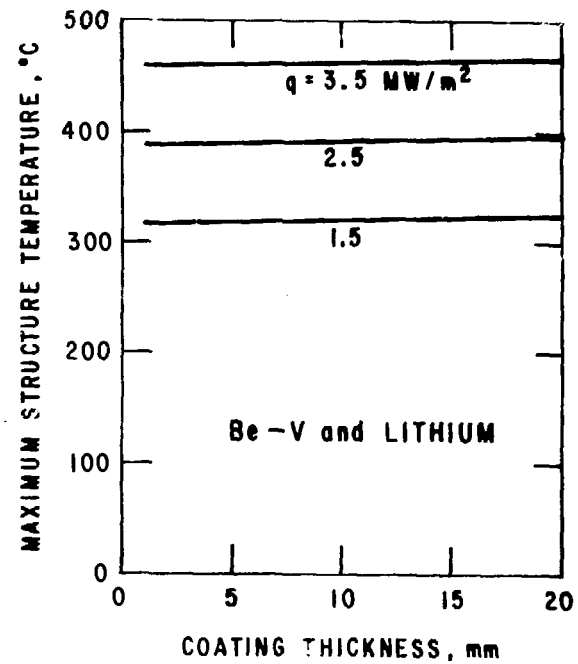

Fig. 3-9. Maximum structure temperature versus coating thickness for various surface heat fluxes at the front surface of a limiter.

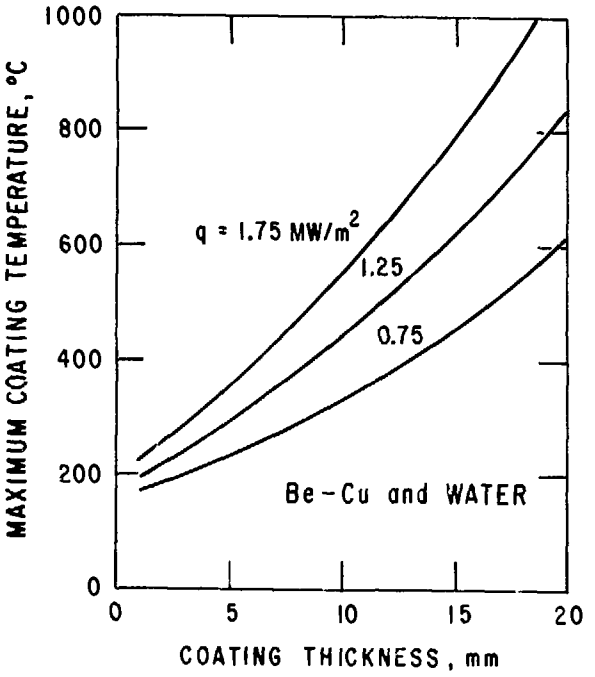

Fig. 3-10. Maximum coating temperature versus coating thickness for various surface heat fluxes at the leading edge of a limiter.

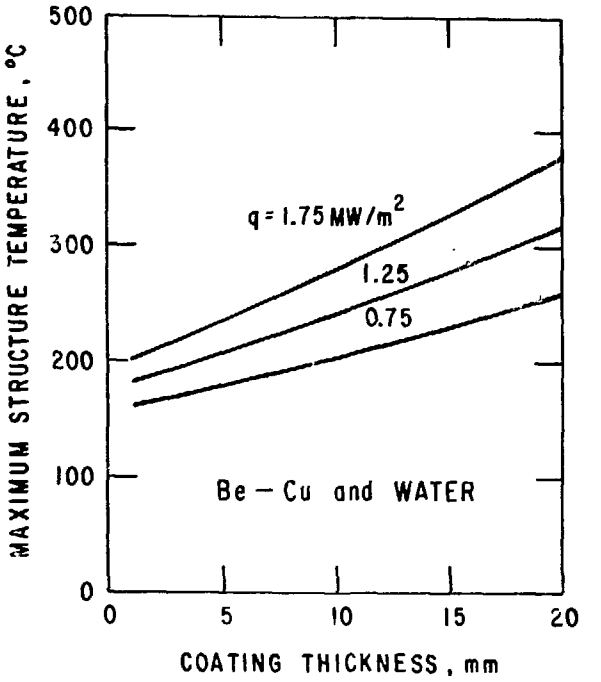

Fig. 3-11. Maximum structure temperature versus coating thickness for various surface heat fluxes at the leading edge of a limiter.

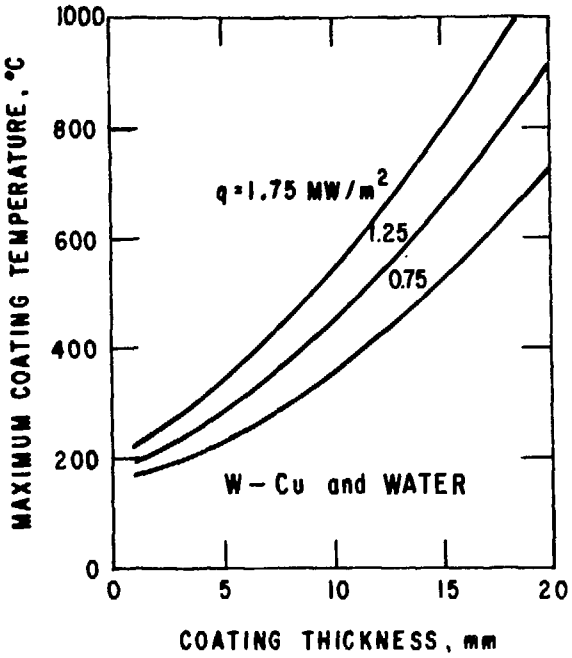

Fig. 3-12. Maxmum coating temperature versus coating thickness for various surface heat fluxes at the leading edge of a limiter.

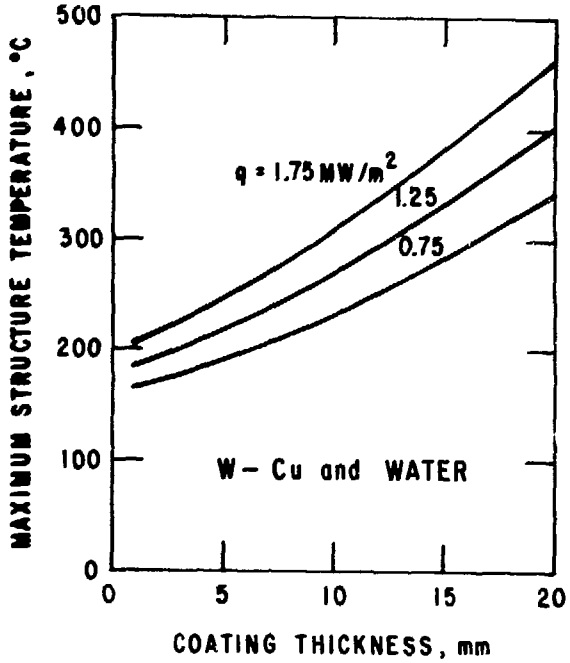

Fig. 3-13. Maximum structure temperature versus coating thickness for various surface heat fluxes at the leading edge of a limiter.

beryllium temperatures for the same surface heat flux and coating thickness. This is also true for the substrate (copper) temperatures. Figures 3-14 through 3-17 show the similar results when lithium is used as coolant and vanadium is the structural material.

Figure 3-18 shows the typical temperature distribution in the coating material at the leading edge. When the coating material is relatively thin, the temperature distribution is very close to linear. When the coating becomes relatively thick, the temperature distribution is no longer linear. This is also true for the temperature distributions in the front surface of the limiter. Figure 3-19 shows the variation of the coating/structure interface temperature with the coating thickness for various surface heat fluxes. The interface temperature increases with coating thickness and surface heat flux almost linearly.

Finally, it should be noted that the results described here are based on the analyses described in Sec. 3.2.1.1. The analyses are limited to one-dimensional, constant property, and conduction-controlled (no thermal radiation) heat transfer problems. Thermal radiation becomes important only when the coating temperature is relatively high. There will be some correction of the coating temperature when it is high, but the correction is likely to be small when the coating temperature is below 1000°C. Neglecting the effect of temperature-dependent property and heat conduction in the direction perpendicular to the surface heat flux may also introduce some error in the results. However, the general trend and the order of magnitude of the temperatures obtained here are not significantly different from that reported in FED/INTOR,[4] where a two-dimensional analysis was performed that included the effects of variable property and thermal radiation. Furthermore, the uncertainties in the temperature calculations described here are probably much smaller than the uncertainties in the calculations of the erosion rates for various coating materials.

3.2.2 Thermal Fatigue of the Limiter

Due to the pulsed nature of a tokamak reactor the limiter will be subjected to cyclic thermal stresses. A possible life limiting mode for the limiter is, therefore, fatigue crack initiation. This section will consider

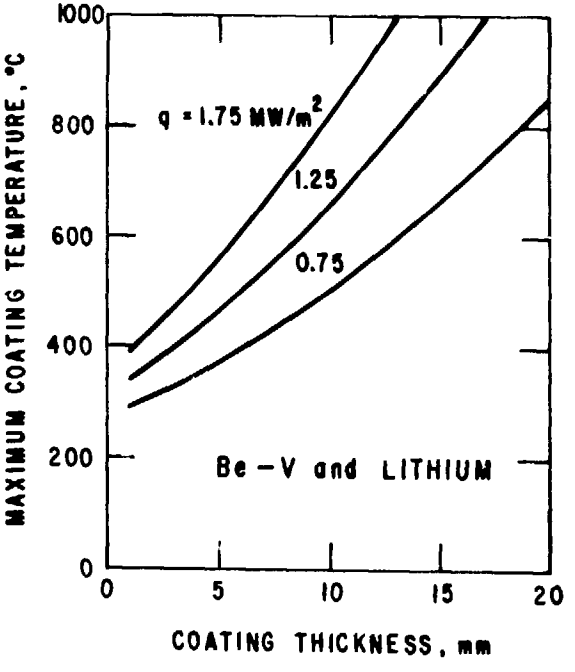

Fig. 3-14. Maximum coating temperature versus coating thickness for various surface heat fluxes at the leading edge of a limiter.

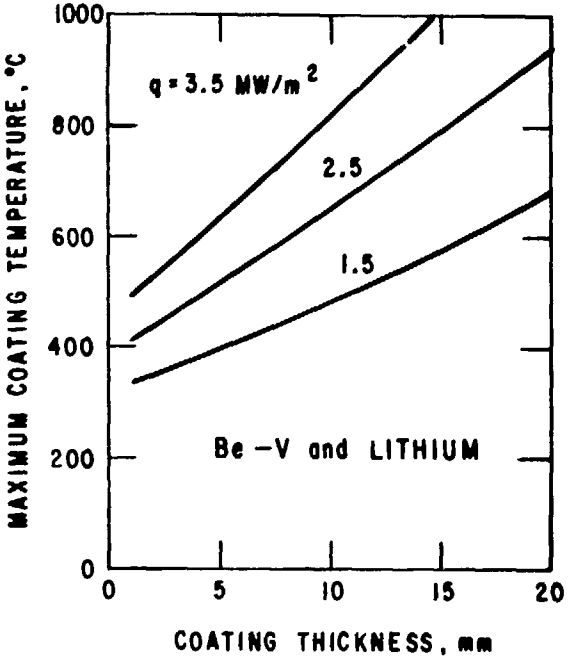

Fig. 3-15. Maximum structure temperature versus coating thickness for various surface heat fluxes at the leading edge of a limiter.

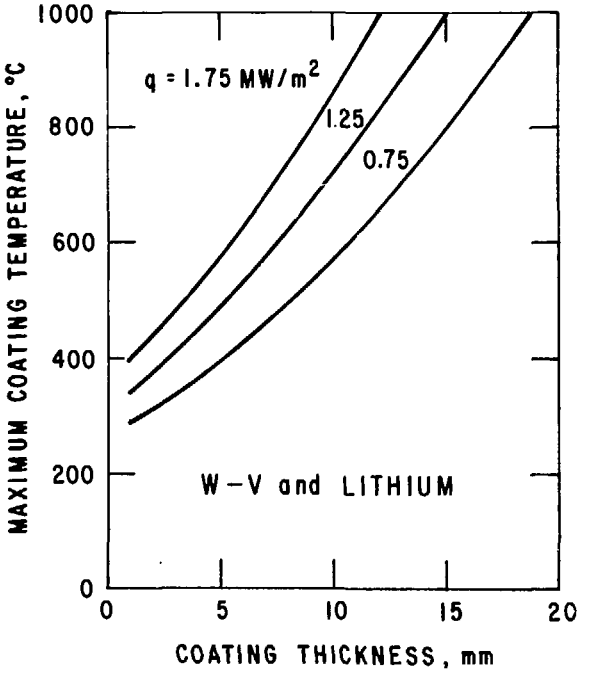

Fig. 3-16. Maxmum coating temperature versus coating thickness for various surface heat fluxes at the leading edge of a limiter.

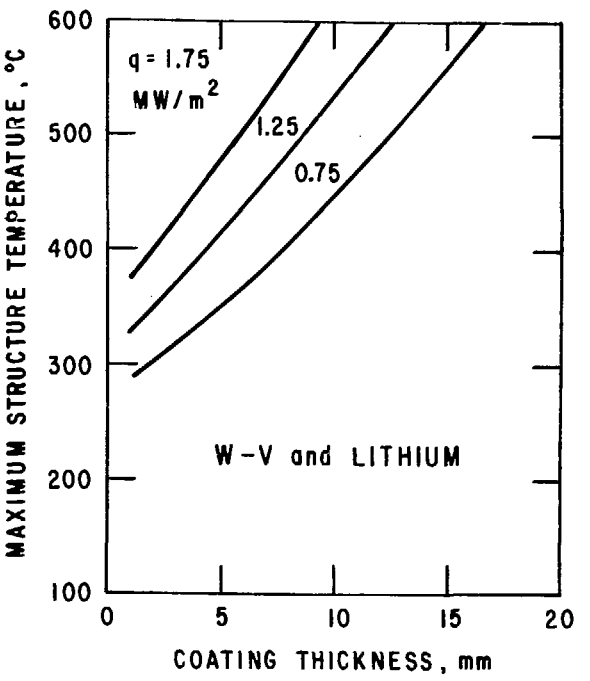

Fig. 3-17. Maximum structure temperature versus coating thickness for various surface heat fluxes at the leading edge of a limiter.

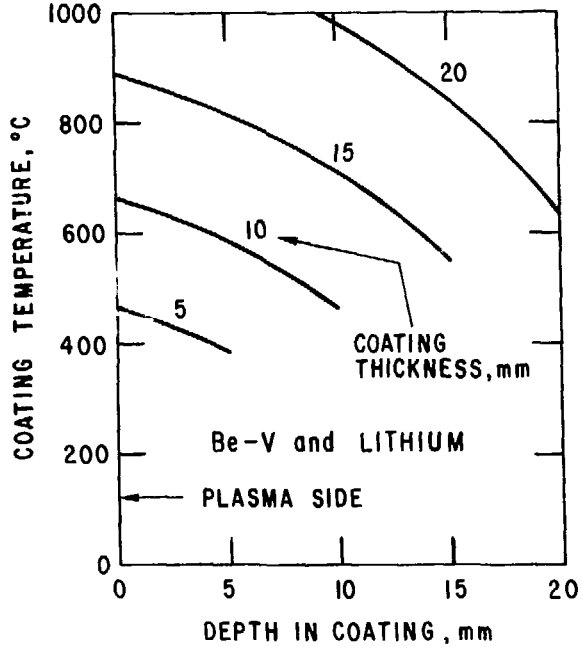

Fig. 3-18. Temperature distribution in the coating material with q = 1.25 MW/m^2; leading edge.

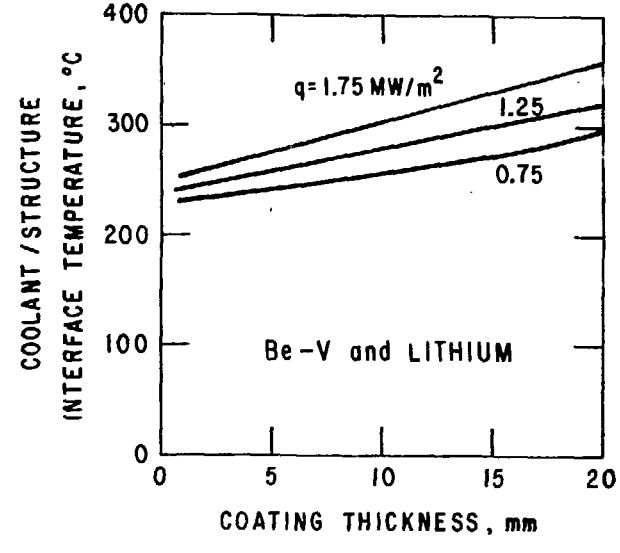

Fig. 3-19. Coating/structure interface temperature versus coating thickness for various surface heat fluxes at the leading edge of a limiter.

the cyclic design life based on fatigue of the limiter for two structural materials (copper and vanadium alloys) and two coating materials (beryllium and tungsten). Water is assumed to be the coolant for the case of copper and lithium for the case of vanadium. Typical fatigue properties of the various structural alloys are shown in Fig. 3-20. For the purposes of design, a safety factor of two on strain range or 20 on life (whichever gives smaller life) is applied on the fatigue curves.

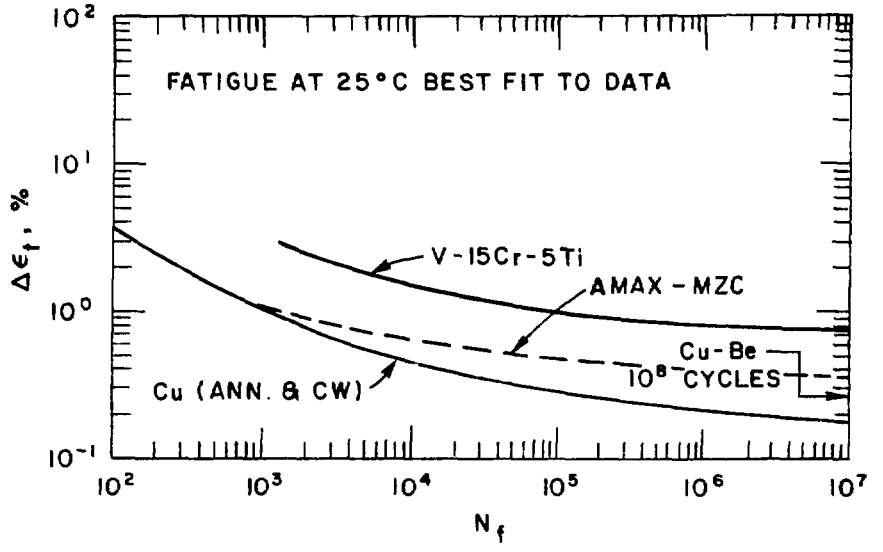

Fig. 3-20. Fatigue for copper and vanadium alloys at room temperature. Dashed lines represent estimated fatigue properties of AMAX-MZC based on very limited data.

3.2.2.1 Leading Edge

The idealized leading edge geometry used for stress analysis is shown in Fig. 3-21. Since the coating, in general, will have finite width (W), an effective thickness of the coating is used for analysis as shown in Fig. 3-22. Figure 3-23 shows the fatigue life of copper as a function of the coating thickness and surface heat flux. In general, the fatigue life decreases with increasing coating thickness and increasing surface heat flux. Beryllium-coated copper has longer life than tungsten-coated copper. For small coating thicknesses ($\leq$1 cm), the use of a stronger copper alloy (e.g. AMAX-MZC) instead of pure annealed copper can increase the design fatigue life significantly. Figure 3-24 shows the fatigue life of V-15Cr-5Ti as functions of

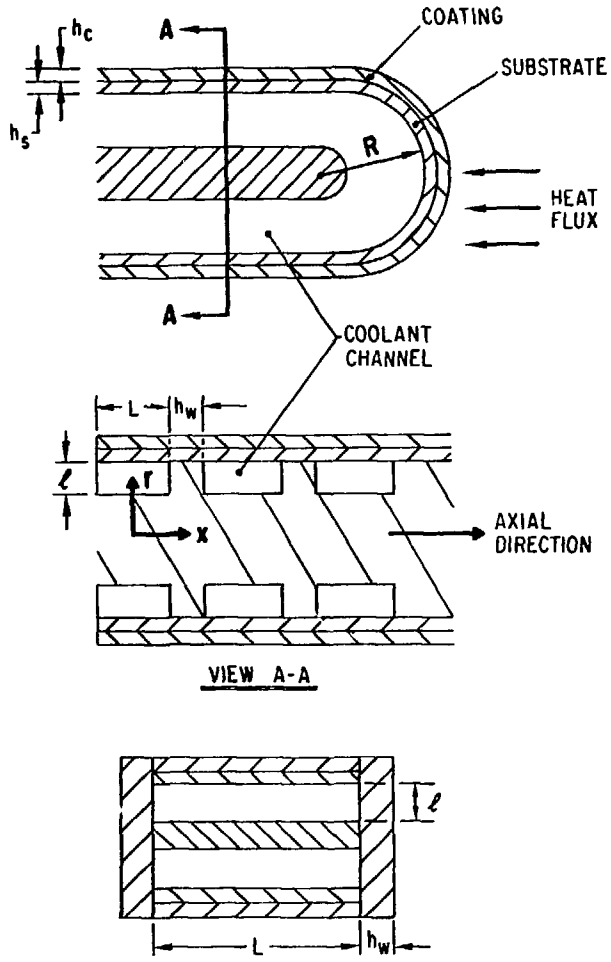

Fig. 3-21. Leading edge geometry used for stress calculations.

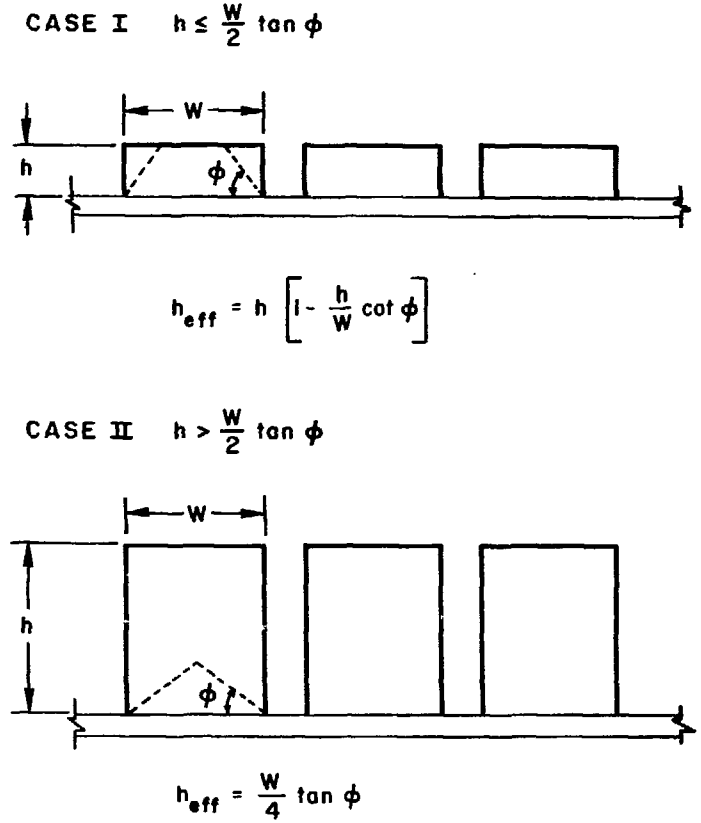

Fig. 3-22. Effective thickness for the coating.

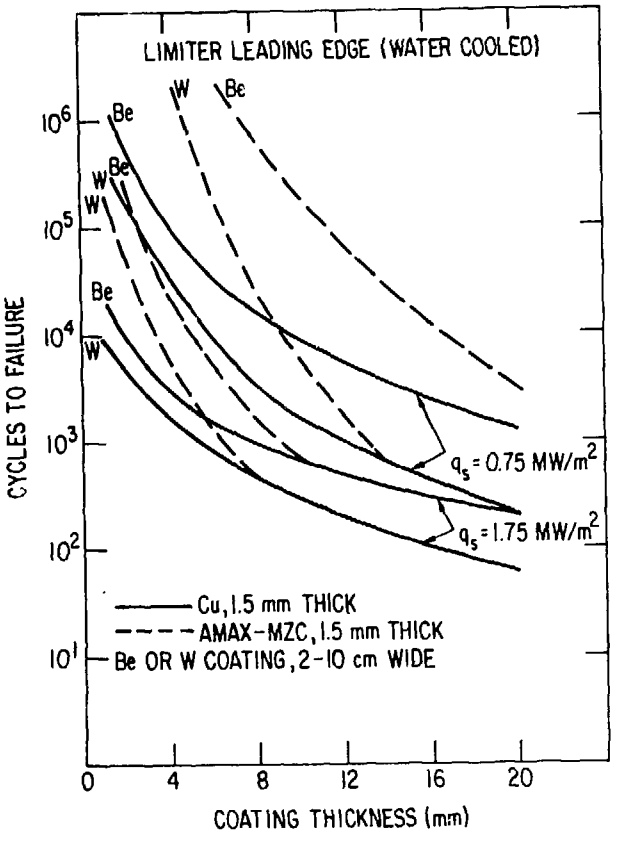

Fig. 3-23. Design fatigue life of the leading edge of the limiter using copper as the structural material and beryllium and tungsten as the coating material.

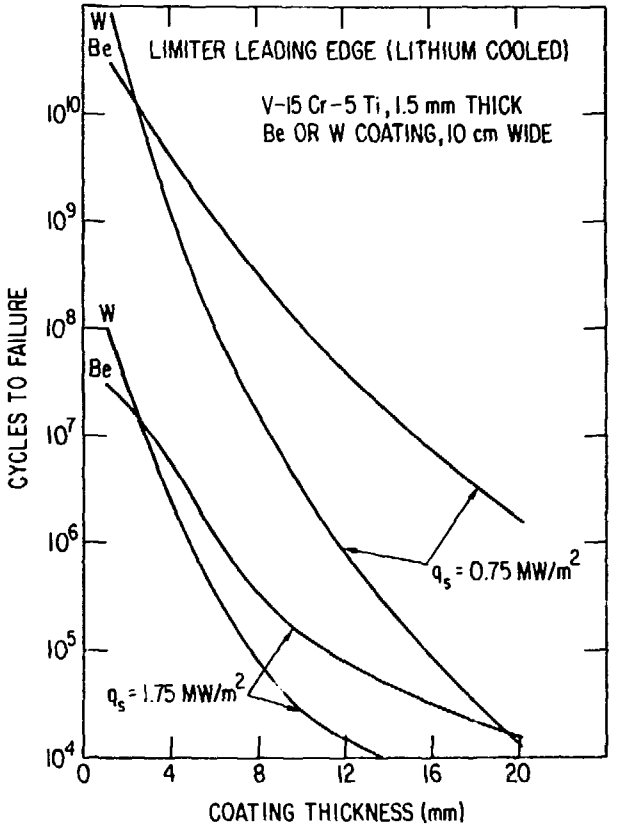

Fig. 3-24. Design fatigue life of the leading edge of the limiter using V-15Cr-5Ti as the structural material and beryllium and tungsten as the coating material.

coating thickness, surface heat flux, and coating material. In general, the fatigue life of vanadium is much greater than for copper.[4] However, in the case of vanadium the fatigue life decreases more rapidly with increasing thickness than in the case of copper. Except for small coating thicknesses ($\leq$2 mm), beryllium-coated vanadium has higher life than tungsten-coated vanadium.

3.2.2.2 Top Surface

The top surface of the limiter is analyzed as a flat plate constrained to deform with the cooler back part of the limiter. Figure 3-25 shows the fatigue life of copper as functions of the coating thickness and surface heat flux. Despite higher surface heating loading, the design life of the top surface is comparable to that of the leading edge. As is the case of the leading edge, the use of a stronger copper alloy like AMAX-MZC significantly increases the design fatigue life. Figure 3-26 shows a similar plot for the cae of V-15Cr-5Ti. Unlike the case of copper, the higher heat flux in the top surface reduces the design fatigue life at the top surface compared to that of the leading edge.

3.3. Thermal Fatigue of First Wall

For the purpose of this study, the first wall has been modeled as an infinitely long annular cylinder of circular cross section. Since the provision of margin against erosion will require a wall thickness which is greater than the needed minimum to contain the internal pressure, significant thermal stresses due to thermal gradient through the wall will be generated during steady-state operation. The cyclic nature of these thermal stresses in a pulsed reactor can potentially limit the useful design life of the first wall because of fatigue. Both PCA (25 CW Type 316 stainless steel) and V-15Cr-5Ti have been considered in this study as potential structural materials for the case of water-cooled and lithium-cooled reactors, respectively. Although the surface heat flux will be distributed nonuniformly in the circumferential direction, for simplicity the analysis is based on an axisymmetric temperature and stress distribution. The design fatigue curve for Type 316 stainless steel is shown in Fig. 3-27. Fatigue curves for the vanadium alloy have already been given in Fig. 3-20.

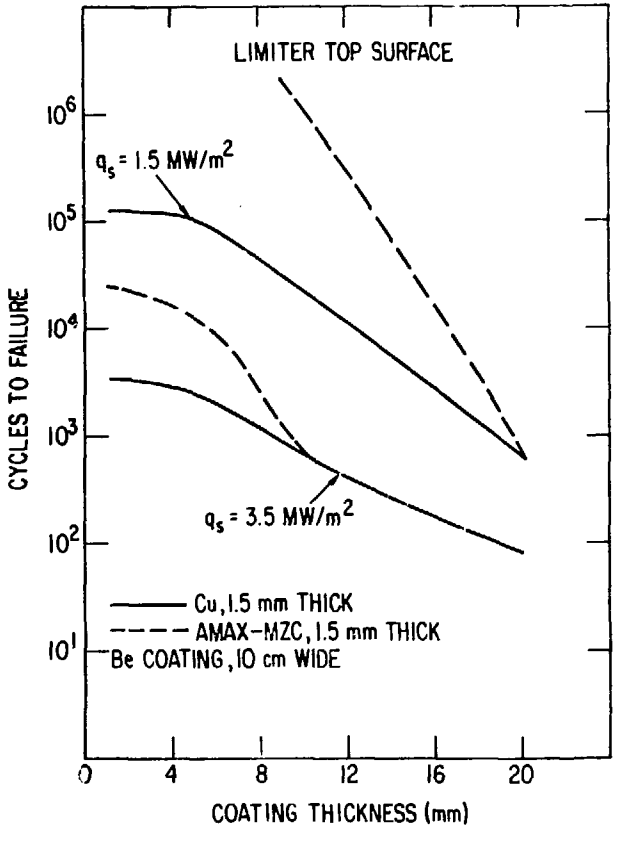

Fig. 3-25. Design fatigue life of the top surface of the limiter using copper as the structural material and beryllium as the coating material.

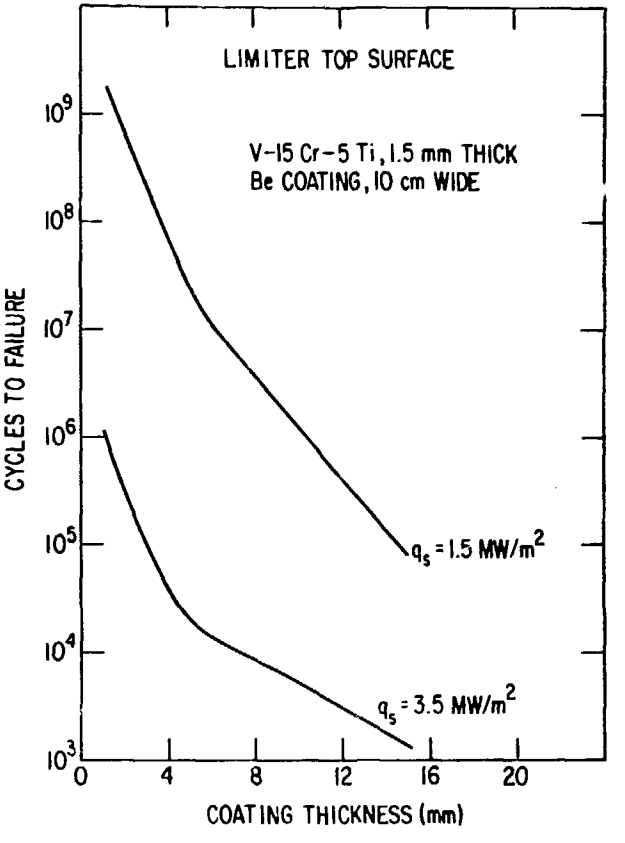

Fig. 3-26. Design fatigue life of the top surface of the limiter using V-15-Cr-5Ti as the structural material and beryllium as the coating material.

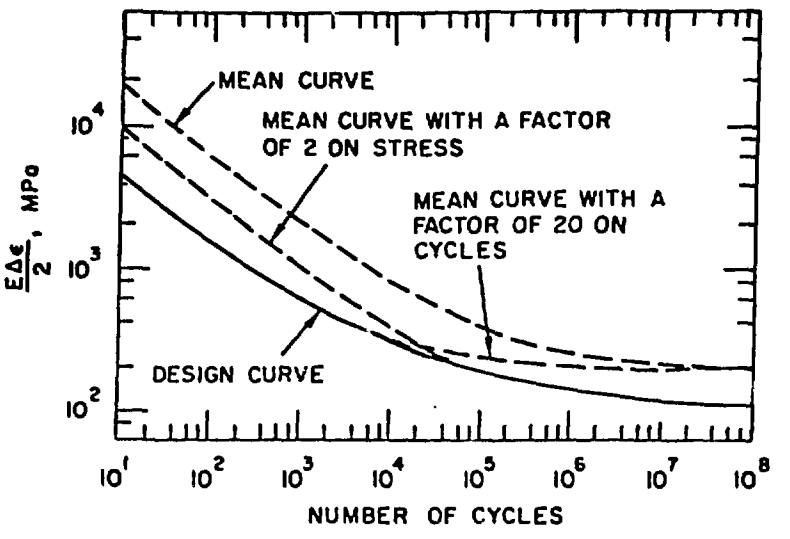

Fig. 3-27. Fatigue design curve for Type 316 stainless steel.

The analysis shows that the critical location for fatigue is at the inner diameter surface where the axial and hoop thermal stresses are given by

$$\sigma_z = \sigma_\theta = \frac{r_o^2 E\alpha}{1-\nu}\left\{-\frac{Q_n}{8k}\left(1-\frac{r_i^2}{r_o^2}\right)+\left(\frac{Q_n}{2k}+\frac{q_s}{r_o k}\right)\left[\frac{\ell n(r_o/r_i)}{1-(r_i^2/r_o^2)}-\frac{1}{2}\right]\right\},$$

where

r_o, r_i = outer and inner radius of the tube

E, ν = elastic constants

α = coefficient of thermal expansion

k = thermal conductivity

Q_n = bulk heating rate

q_s = surface heat flux

The general primary membrane stress intensity is

$$P_m = \frac{p_c r_i}{(r_o - r_i)},$$

where

p_c = coolant pressure.

Figure 3-28 shows the plot of wall thickness versus maximum allowable surface heat flux for various fatigue lives of a tube of Type 316 stainless steel with an inner radius of 5 mm. Also shown in this figure (by dashed lines) are the maximum surface heat flux corresponding to a maximum allowable metal temperature of 500°C and 430°C. The fatigue curves and the maximum temerature limit curves give upper bounds to the wall thickness for a given surface heat flux. A lower bound for the wall thickness is set by the primary tress criterion, $P_m \leq S_{mt}$.

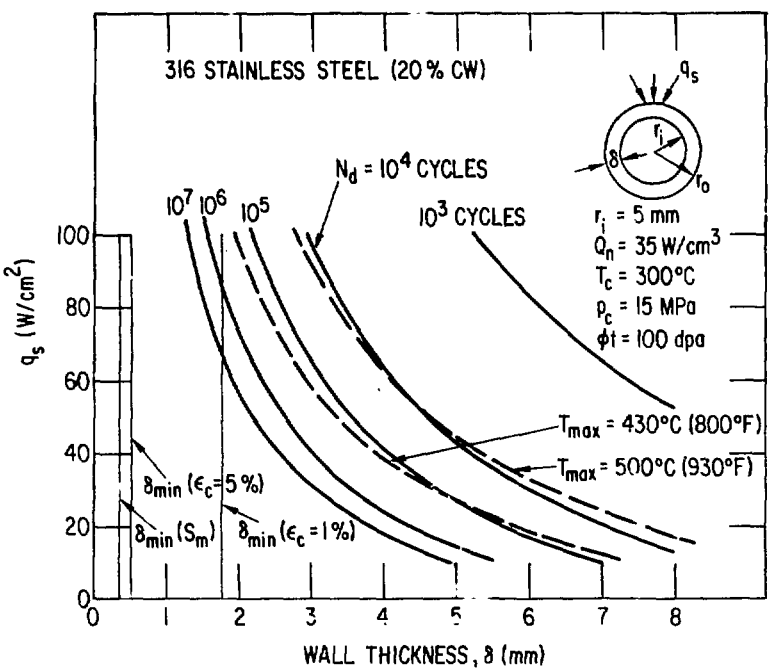

Fig. 3-28. Allowable wall thickness for a given surface heat flux on a Type 316 stainless steel tube of 5-mm inside radius.

The figure shows minimum thickness corresponding to a time-independent-stress limit, S_m, and to time-dependent stress limits S_{mt} corresponding to maximum radiation induced creep strains of 1% and 5%. Since radiation-induced creep is considered nondamaging, a 5% creep strain limit may be reasonable. The difference between the lower bound and the upper bound for thickness may

be considered as the margin against erosion. Figures 3-29 and 3-30 show similar plots for tubes with inner radii of 10 mm and 3 mm respectively. Note that in all three cases the limit for a maximum structural temperature of 500°C almost coincides with the limits for a design fatigue life of 10^4 cycles. In other words, if for any given surface heat flux, a fatigue life greater than 10^4 cycles is required, then the maximum wall thickness must be reduced such that the maximum metal temperature is less than 500°C. For example, a maximum wall temperature of 430°C guarantees a design fatigue life of 10^5 cycles.

Figure 3-31 shows a similar plot for the case of V-15Cr-5Ti with a tube of radius 25 cm. In contrast to the case of Type 316 stainless steel, the maximum metal temperature limit of either 600°C or 700°C sets an upper bound for the wall thickness for fatigue life of up to 10^6 cycles. Also note that because of the superior thermal properties vanadium tubes can have significantly larger wall thickness than Type 316 stainless steel tubes.

3.4 Lifetime Analysis and Burn Goals

We begin by considering the limiter's leading edge, and we first consider the copper heat sink with water coolant and a beryllium coating. Reference to Fig. 3-11 shows an upper limit to the coating thickness δ_{Be} if we restrict the substrate to 250°C, as proposed in Chap. 2: $\delta_{Be} \leq 18$ mm at a surface heat load $W_{\ell e} = 0.75$ MW/m^2 and $\delta_{Be} \leq 7$ mm at $W_{\ell e} = 1.75$ MW/m^2. We find the temperature limits to the beryllium coating are less stringent (cf. Fig. 3-10) since this coating can be permitted to reach 700°C. Taking these limits to δ_{Be} into account we have replotted the fatigue curves (Fig. 3-23) for the AMAX-MZC copper heat sink (see Fig. 3-32).

As the figure shows, fatigue life increases with thinner coatings. However, thinner coatings are more easily eroded by repeated disruptions. From Fig. 3-1 we might expect up to 539 μm of beryllium removal per disruption near the upper limits of leading edge thermal loads (~1200 J/cm^2). Hence the beryllium can be removed in the worst case after a number of cycles $N = \delta_{Be}[f \times 0.54\ \text{mm}]^{-1}$, where f is the average frequency (probability) of disruptions per burn cylce. Figure 3-32 displays N versus δ_{Be} for $f = 10^{-3}$ (one disruption per thousand burn cycles) and two different coating removal rates. The optimum coating thickness is the intersection of fatigue and disruption curves.

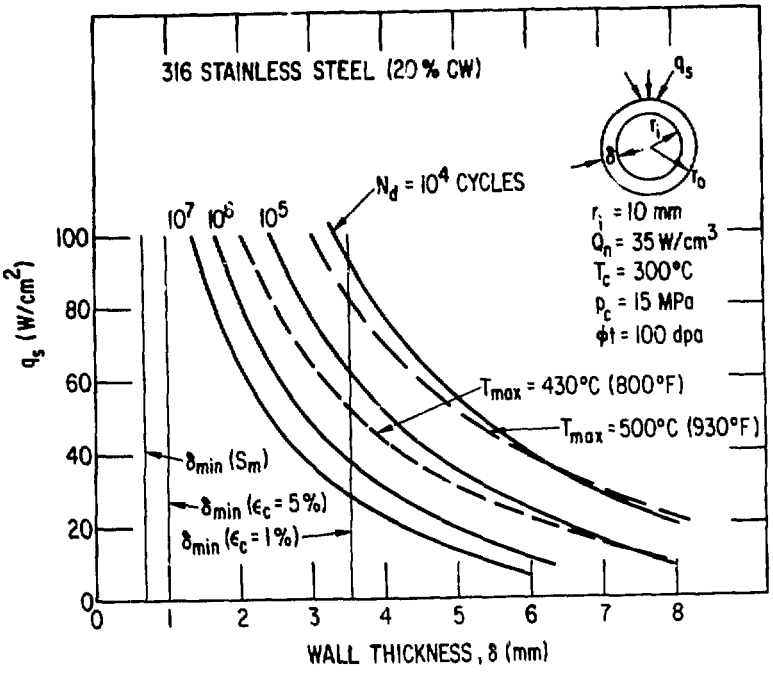

Fig. 3-29. Allowable wall thickness for a given surface heat flux on a Type 316 stainless steel tube of 10-mm inside radius.

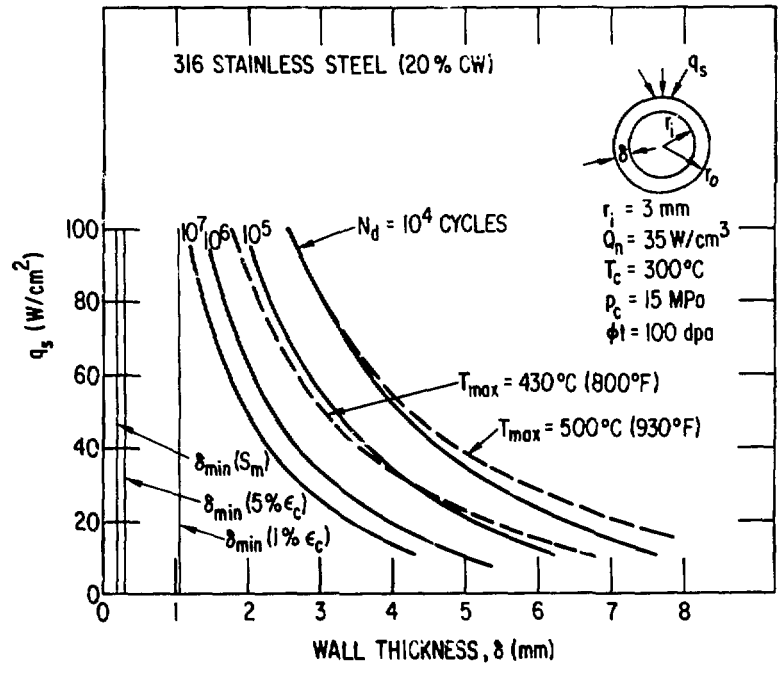

Fig. 3-30. Allowable wall thickness for a given surface heat flux on a Type 316 stainless steel tube of 3-mm inside radius.

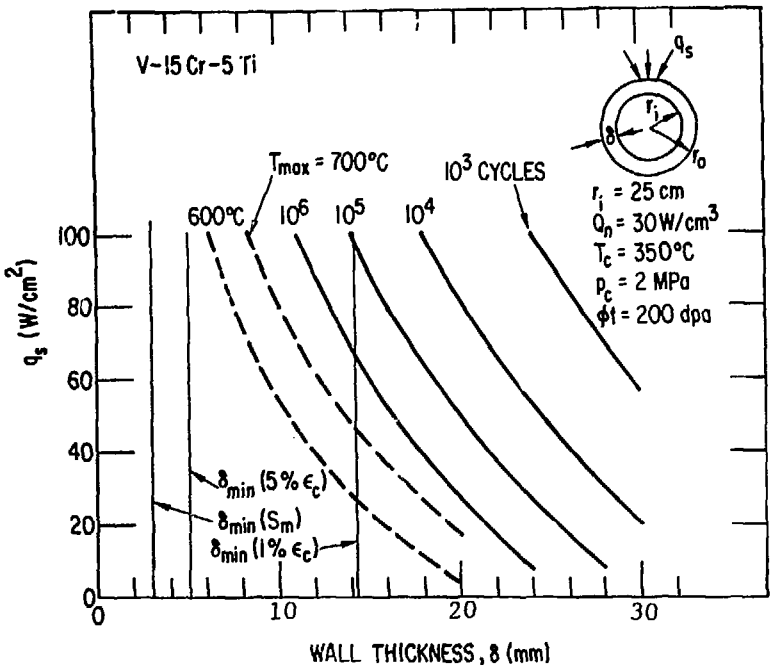

Fig. 3-31. Allowable wall thickness for a given surface heat flux on a V-15-Cr-5Ti tube of 25-cm inside radius.

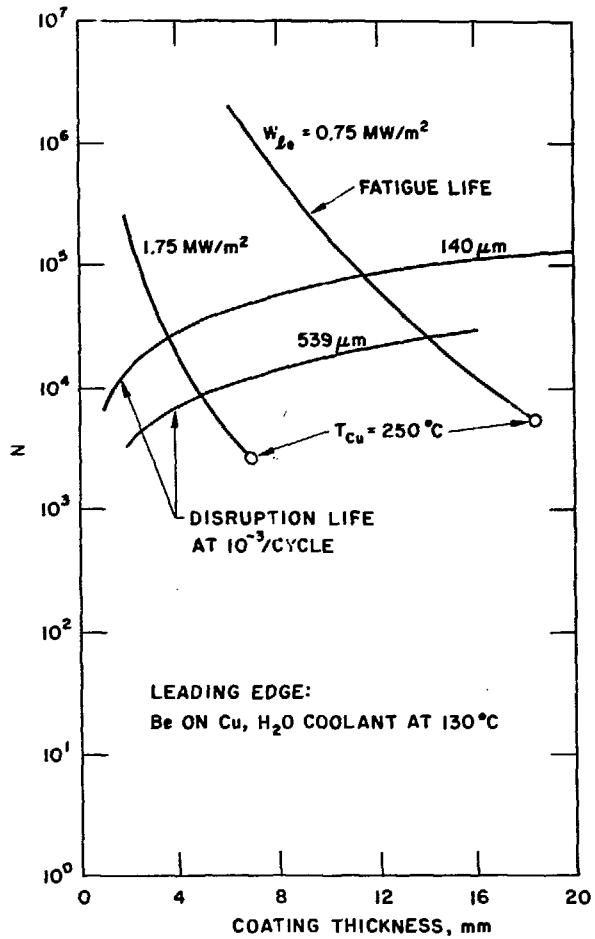

Fig. 3-32. Cyclic lifetime of leading edge.

For example, for high leading edge heating, 1.75 MW/m^2, and mild disruption damage, 140 μm lost per disruption, the maximum lifetime is to be expected for δ_{Be} = 3.6 mm, which results in a survival time of N = 2.7×10^4 burn cycles.

Finally we fold into our analysis the radiation life limit for the heat sink. Our philosophy will be that the fusion burn length, t_f, should be long enough that the cycle life, N, is at least as long as the radiation life, L_{rad}. Thus, we compute the minimum, $t_f = (0.8 \times L_{rad} \times N^{-1}) - t_{off}$. As an illustration, the copper heat sink is believed to have poor radiation resistance, and one might expect to require its replacement every L_{rad} = 2 yr. Then, at 80% availability, a fusion period $t_f = 1.8 \times 10^3$ s would be needed in order for a cyclic lifetime N = 2.7×10^4 to equal the radiation lifetime. (We will usually assume the period between fusion burns to be t_{off} = 100 s.) Figure 3-33 shows these burn goals for the beryllium/copper leading edge under different conditions. In the case of severe disruption damage there is a strong motivation to achieve $t_f \gtrsim 2$ h at $W_{\ell e} \approx 2.0$ MW/m^2. The motivation for long burns diminishes for more mild disruptions. In fact, according to Fig. 3-1, disruptions do no damage at thermal loads <300 J/cm^2, so very thin coatings with negligible fatigue could be selected in this limit. The first lesson we have learned is that $t_f \approx 1$ h may be adequately long to eliminate fatigue as a life-limiting consideration if the limiter leading edge has a heat sink with poor radiation resistance. This set of circumstances might typify a near-term tokamak constructed with conventional technology (water-cooled copper heat sink).

It may well be that a commercial reactor would be designed with more radiation resistant materials in order to extend the period between limiter repairs. As an example we consider a vanadium heat sink at the leading edge, clad with beryllium. In this case the 600°C temperature limit on vanadium is less restrictive than the 700°C limit on the beryllium coating, and, by reference to Figs. 3-14 and 3-15, we limit δ_{Be} to 8 mm and 16 mm at $W_{\ell e}$ = 1.75 MW/m^2 and 0.75 MW/m^2, respectively. These limits and the fatigue life (Fig. 3-24) are shown in Fig. 3-34, along with the disruption life for the beryllium coating, as calculated previously. The superior fatigue resistance of vanadium results in a much longer cyclic life than the copper heat sink. For moderate damage rates, disruptions are the life-limiting concern, so δ_{Be} should be maximized to the temperature limit, given above. The corresponding number

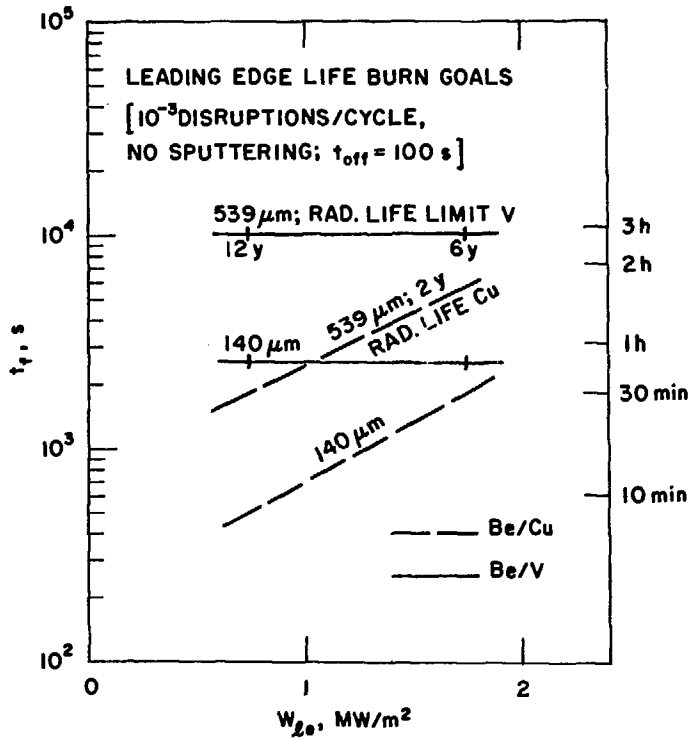

Fig. 3-33. Required t_f for equality of cyclic lifetime and radiation damage lifetime of leading edge.

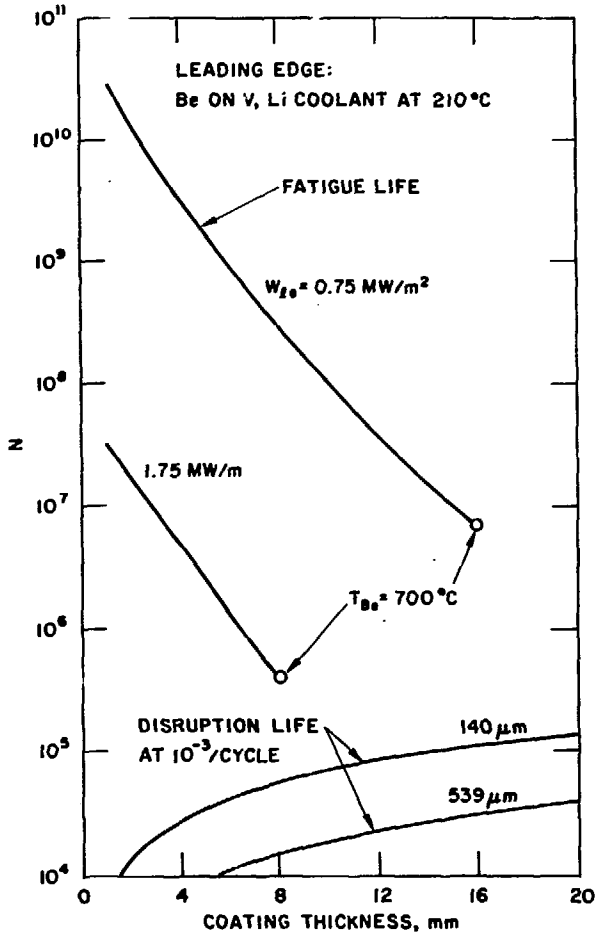

Fig. 3-34 Cyclic lifetime of leading edge.

of burn cycles can again be converted to a burn length such that the cycle lifetime at least equals the radiation lifetime. For vanadium, however, radiation resistance is believed to be much better than for copper -- we take $L_{rad} = (24\ MW\text{-}y/m^2)/W_n$, and, for the sake of illustration, we assume $W_n = (8/3)\ W_{\ell e}$. The results are shown in Fig. 3-33. Compared to a copper heat sink there is strong motivation to achieve longer burns. For severe disruptions burn times approaching 3 h are desired. These slightly longer burns are needed in order to achieve the full potential radiation life of the limiter, in the six- to twelve-year range.

As we have seen, the requisite burn length decreases as disruption damage becomes less severe. In the desirable situation where disruptions can be completely eliminated from tokamak reactors we must consider sputtering as an erosion mechanism. We have seen that temperature constraints limited the beryllium coating to 1 to 2-cm thickness. Thus net erosion rates $\dot{\delta}_{Be} \gtrsim 1$ cm/yr would require limiter replacement or recoating at intervals approaching 1 yr. Any shorter intervals would likely be intolerable due to unacceptable reductions in reactor availability. We assume that net erosion can be controlled, and for the sake of illustration, we examine burn cycle implications for $\dot{\delta}_{Be} = 1$ cm/yr. Since sputtering life is so short, radiation damage does not concern us in this limit. The beryllium coating is increased to the temperature limit to maximize life against erosion, and the number of acceptable fatigue cycles is found (cf. Figs. 3-32 and 3-34). For the copper heat sink N is now smaller than for the cases dominated by disruptions so a longer t_f ($\gtrsim$2 h) is needed to obtain a 1-2 yr lifetime of the leading edge; see Fig. 3-35. On the other hand, for the vanadium substrate N is now larger, so a shorter t_f ($\lesssim$100 s) is permissible.

Tungsten has also been proposed as a limiter coating at the leading edge. If the plasma temperature exceeds ~50 eV at the leading edge the high self sputtering of tungsten will preclude its use. However, at lower temperatures this appears to be an ideal coating. Sputtering is then low and redeposition is very effective due to the short mean free path of tungsten ions. In addition, disruptions do little damage to a tungsten coating since, at the leading edge, the thermal load is likely to be less than the threshold for melting and vaporization; see Fig. 3-1. Hence, at such low temperatures erosion may not be significant for tungsten coatings. A thin tungsten cladding,

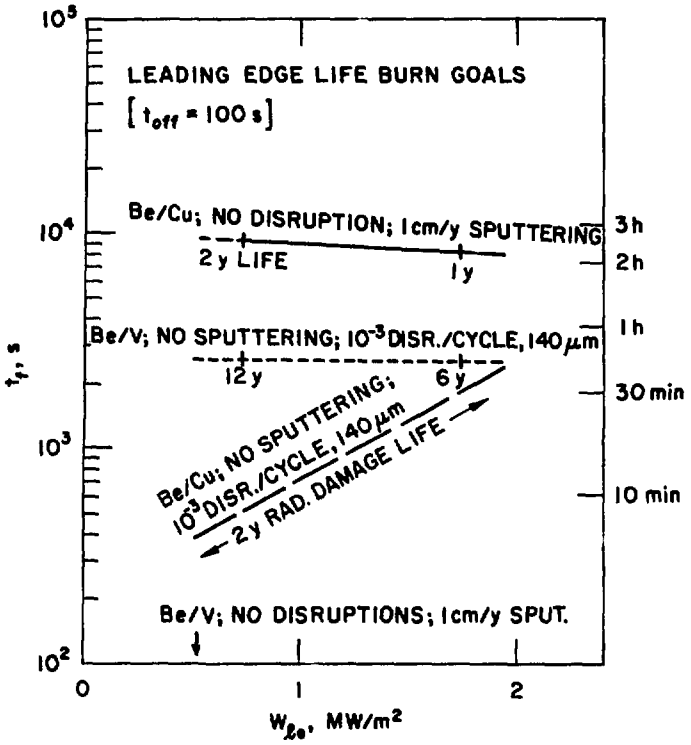

Fig. 3-35. Required t_f for equality of cyclic lifetime and radiation damage lifetime of leading edge.

δ_W, would be specified. Since our fatigue calculations showed very large cycle lifetimes for either copper or vanadium substrates with $\delta_W \leq 1$ mm we find that fatigue may not be an issue for the leading edge whenever a tungsten cladding can be used.

Using the fatigue curves in Figs. 3-24 and 3-25 an identical lifetime analysis was done for the front face of the limiter. The beryllium coating was assumed to be removed at 690 μm and 170 μm per disruption, representing the worst case and more typical disruption damage (2500 J/cm^2 and 500 J/cm^2, respectively). The optimum δ_{Be} was inferred for a disruption probability f = 10^{-3} to obtain the maximum cycle lifetime, and the minimum fusion burn, t_f, was calculated such that the cyclic lifetime was equal to the radiation life of the heat sink (24 MW-yr/m^2 for vanadium and 4 MW-yr/m^2 for copper). The results are displayed in Fig. 3-36. Our first observation is that $t_f \lesssim 1$ h is adequate for the front face with a copper heat sink, even with the worst disruption damage. However, the one- to two-year radiation life of copper is so

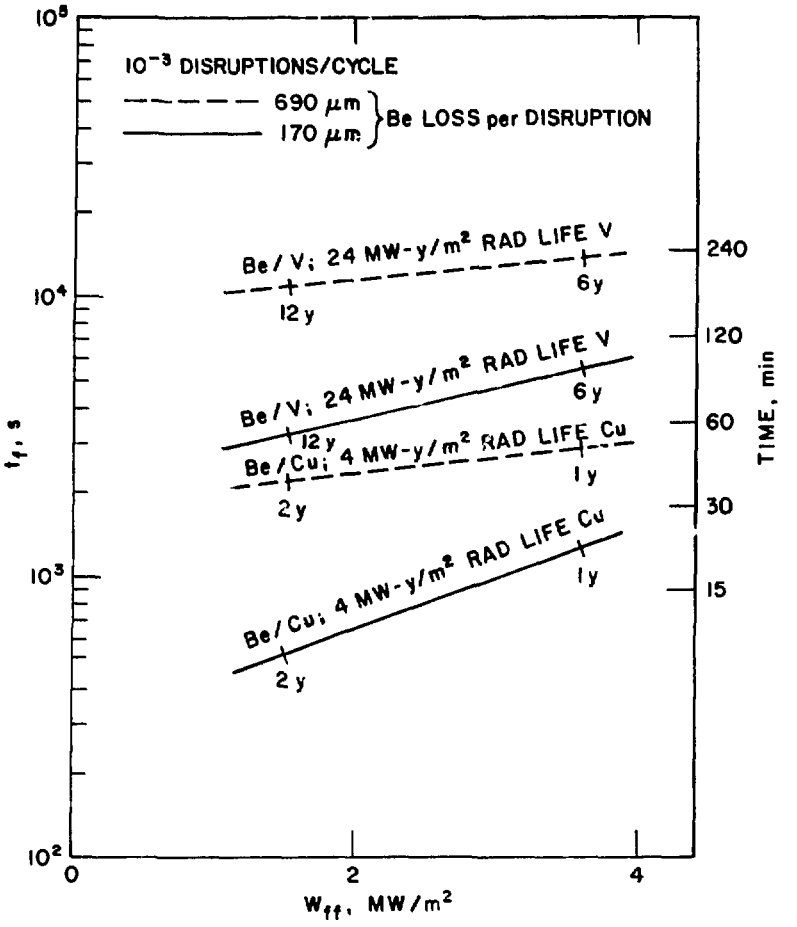

Fig. 3-36. Required t_f for equality of cyclic lifetime and radiation damage lifetime of front face.

short that there will be great incentive to consider materials such as vanadium. Then we find, in order to achieve the six-fold increase in limiter life, the burn length must be extended, so as not to aggravate the fatigue problem. For moderate disruptions we need $t_f \sim$ 1-1.5 h. Of course, if the frequency of disruptions were $f << 10^{-3}$ then thinner beryllium coatings, with resulting longer fatigue life for the substrate, would be appropriate. In the extreme where sputtering erosion limits the lifetime to ~1 to 2 yr the burn length would need to be only 15-30 min in order to eliminate thermal fatigue as a concern with a vanadium substrate.

We next analyze the first wall lifetime, starting with the bare PCA water-cooled tubes. The fatigue cycles versus coolant tube thickness (see Figs. 3-27 through 3-30) is replotted for three thermal wall loads, W_{FW} = 0.5,

0.75, and 1.0 MW/m^2 in Figs. 3-37 through 3-39. In addition, we display the cycle lifetime against disruptions for f = 10^{-3} and 10^{-4}, assuming modest thermal energies in the disruption (380 J/cm^2 removing 70 μm of PCA). The tubing is assumed to fail once disruptions thin the wall to $\delta_{PCA} = \delta_{min}$. Here δ_{min} is the minimum wall thickness required to withstand the coolant pressure (15 MPa) with a specified amount of creep. For neutron-induced damage we might permit 5% creep. Thus, for 70 μm loss per disruption we find a disruption controlled cycle lifetime of $N = (\delta_{PCA} - \delta_{min})(f \times 0.07 \text{ mm})^{-1}$.

As with the limiter we select the intersection of the fatigue and disruption curves to find the δ_{PCA} which yields the maximum cycle life, N. Our results are insensitive to tube radius, r_i, and we consider r_i = 5.0 mm from now on in our analysis; r_i = 5.0 mm was the STARFIRE specification. Next we compute the fusion burn period needed for the cycle lifetime to equal the radiation life, which we take to be $L_{rad} = (12 \text{ MW-yr/m}^2)/W_n$, with $W_n \approx 4 \times W_{FW}$. The results, shown in Fig. 3-40, indicate that relatively short burns, t_f < 1 h, suffice to eliminate the cycling factor from concern when there are infrequent or mild disruptions. Moreover, if first wall replacement is undertaken before 12 MW-yr/m^2 is absorbed, then proportionally shorter burns are acceptable.

It is conceivable that the disruption damage could be more troublesome, however. If, for example, neutron radiation proved to be more damaging such that creep would be limited to 1%, then δ_{min} would exceed the values in Figs. 3-37 through 3-39; fewer disruptions could be tolerated before the tubes failed. In some cases t_f would have to double in order to still achieve the radiation life limit of the first wall; this is illustrated in Fig. 3-41 for the PCA tubes with 70-μm erosion at f = 10^{-3} and the two cases of 5% and 1% creep. Even more serious is the consequence of slightly larger thermal dumps. Merely increasing the energy deposition from 380 J/cm^2 to 700 J/cm^2 multiplies the melting and vaporization loss by a factor of six for PCA (see Fig. 3-1). This motivates a design goal for much longer fusion burns; as shown in Fig. 3-41, $t_f \sim 4$ h is needed to realize the full radiation life potential in this case.

Finally, we consider the burn goals needed to achieve the full benefits of radiation resistant structure such as vanadium. In this exercise we use

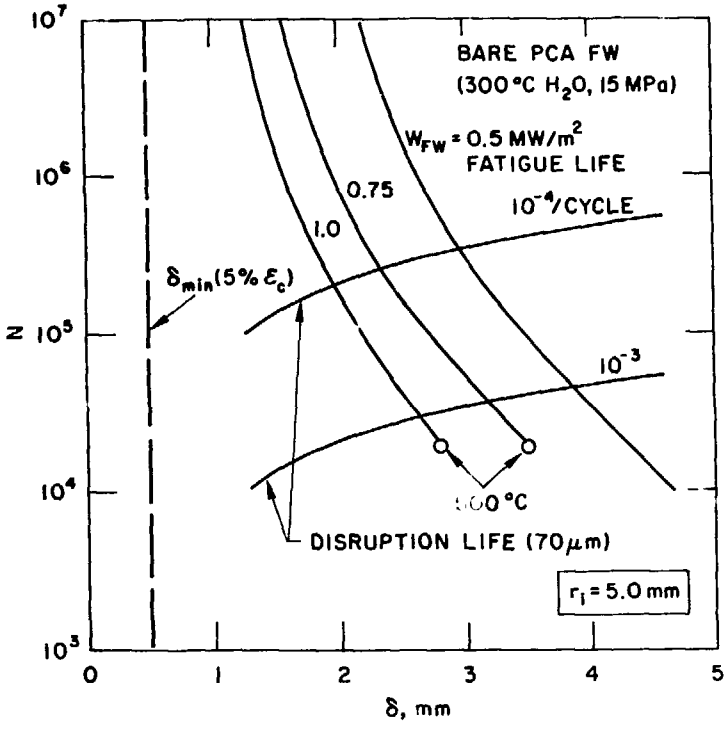

Fig. 3-37. Cyclic lifetime of first wall; tube radium = 5.0 mm.

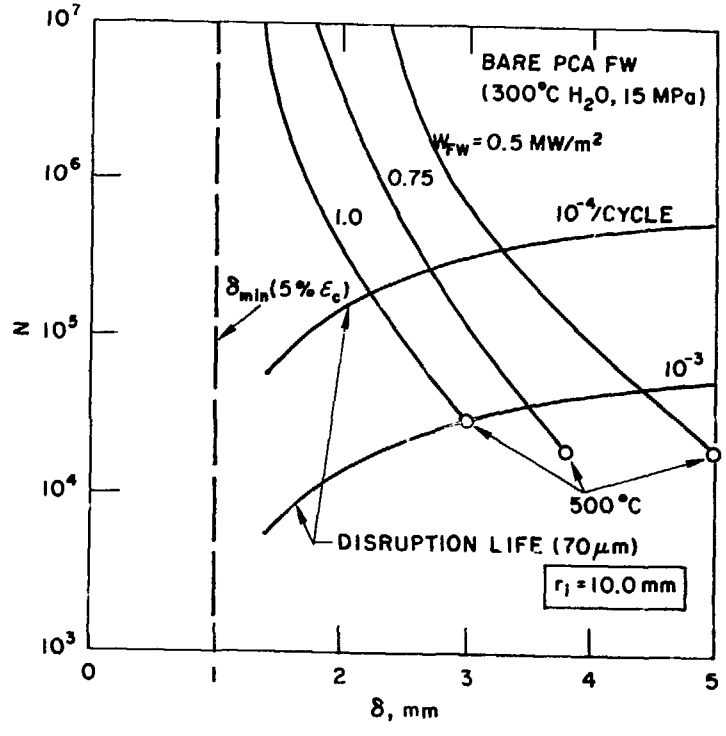

Fig. 3-38. Cyclic lifetime of first wall; tube radius = 10.0 mm.

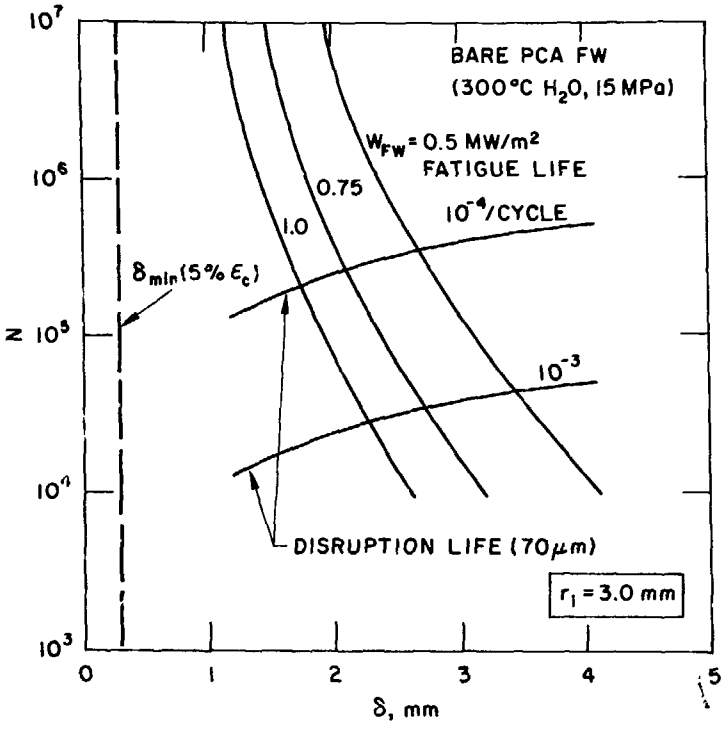

Fig. 3-39. Cyclic lifetime of first wall; tube radius = 3.0 mm.

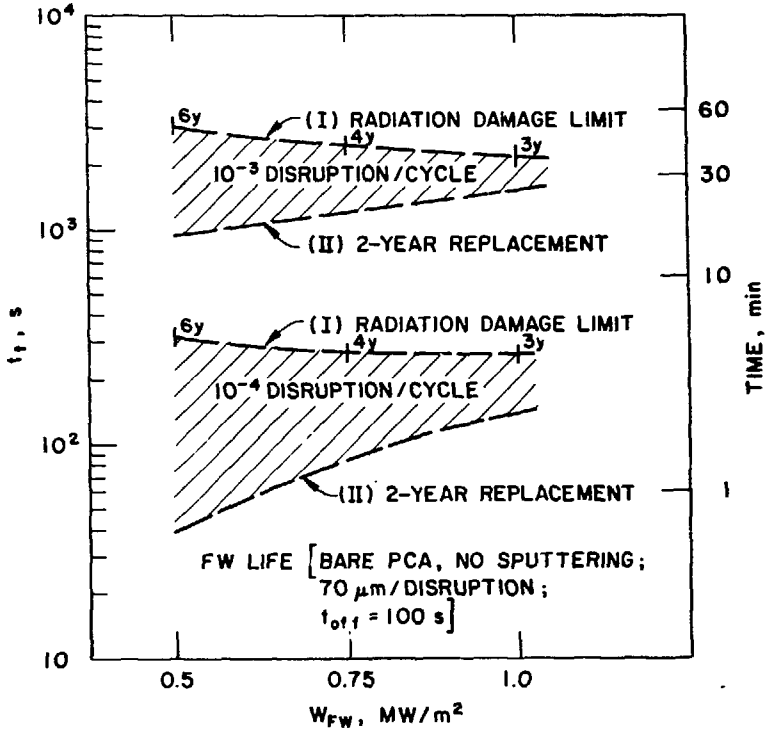

Fig. 3-40. Required t_f for the first wall cyclic lifetime equal to 2 yr and to the radiation damage lifetime (12 MW-yr/m² for PCA); radiation creep of 5% allowed.

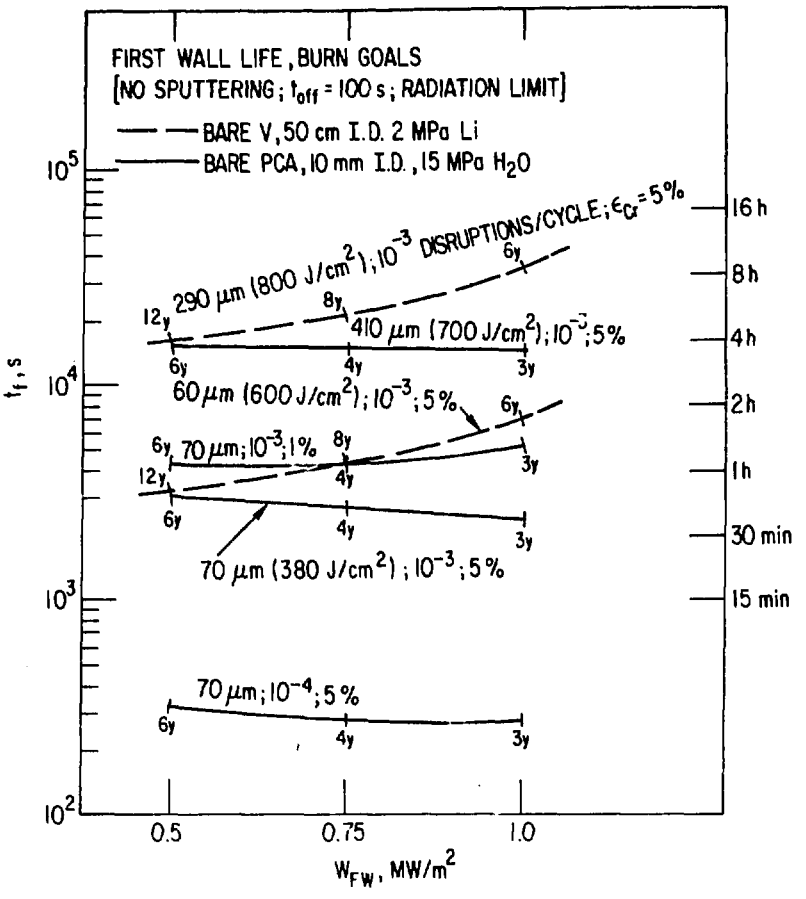

Fig. 3-41. Required t_f for equality of cyclic lifetime and radiation damage lifetime of first wall.

the fatigue and disruption data developed earlier (see Figs. 3-1 and 3-31), and we calculate burn lengths needed for an assumed lifetime of 24 MW-yr/m^2. The 600°C limit on vanadium constrains δ_V to $\lesssim$10 mm, and we find disruption erosion dominates fatigue as a consideration. Our results, displayed in Fig. 3-41, show that t_f will be at least as long as required for the PCA first wall in order to achieve twice the in-reactor lifetime (6-12 yr versus 3-6 yr). In the pessimistic disruption scenario depicted we find $t_f \sim 8$ h is desirable at high wall loads.

We conclude this chapter with some general observations. Our results typically show that "near-term" structures such as copper limiters and a steel first wall can tolerate relatively short fusion burns because their radiation life is thought to be short. In order to take full advantage of advanced

materials, such as vanadium, with longer radiation life it will be necessary to arrange for longer burns. This will be possible, for example, with noninductive current drive or with very large major radius reactors with high volt-second ohmic transformers. On the other hand, reactors with short burns ($t_f \sim$ 100 s), operating in the internal transformer mode, will not be attractive unless disruption frequency is $f \lesssim 10^{-5}$ and sputtering erosion is $\dot{\delta} \lesssim 1$ cm/yr.

Generally speaking the higher wall and limiter thermal loads are more demanding on our designs. In the first place this is because we have assumed the higher thermal loads are associated with higher neutron damage and therefore shorter in-reactor life. In the second place these higher thermal loads exacerbate the fatigue problem and generally require longer burns in order to not surpass the limit on cycle lifetime.

Finally, we repeat that our results only display general trends. Reactor availability should improve with several factors: use of more radiation and fatigue resistant materials; reduction in the frequency and severity of disruptions; reduction in net sputtering erosion; selection of disruption resistant materials (e.g. tungsten, if low plasma temperatures can be obtained); operation at lower wall loads; and operation with longer fusion burns. At this point it is not possible to specify a unique goal for the burn length since it depends on a variety of operating characteristics, as we have shown.

REFERENCES FOR CHAPTER 3

1. W. G. WOLFER and A. M. HASSANEIN, "On Melt Layer Stability Following a Plasma Disruption," J. Nucl. Mater. 111/112, 580 (1982).

2. A. M. HASSANEIN, Ph.D. Thesis, "Thermal Effects and Erosion Rates Resulting from Intense Deposition of Energy in Fusion Reactor First Walls," UWFDM-465, University of Wisconsin (1982).

3. A. M. HASSANEIN, G. L. KULCINSKI and W. G. WOLFER, "Vaporization and Melting of Materials in Fusion Devices," J. Nucl. Mater. 103/104, 321 (1981).

4. M. A. ABDOU, et al., "Impurity Control and First Wall Engineering," Chapt. VII of FED-INTOR Activity and the U.S. Contribution to the International Tokamak Reactor, Phase-2A Workshop, Vienna, Austria, IAEA, USA FED-INTOR/82-1 (1982).

Chapter 4. THERMAL HYDRAULIC AND THERMAL STORAGE SYSTEM ANALYSIS

4.1 Introduction

The current efforts on the Blanket Comparison and Selection Study[1] indicates that the two most viable breeding blankets are (1) a solid breeder blanket cooled either by pressurized water or helium; and (2) a liquid breeder blanket consisting of either lithium-lead eutectic (17Li-83Pb) or liquid lithium. Blanket designs such as the STARFIRE (Ref. 2) and DEMO/STARFIRE (Ref. 3) that operate under steady state are less complex compared with pulsed reactors, although the majority of the design and operating problems such as tritium permeation and recovery, heat transport, thermal energy conversion system, safety, etc., are common to both types. However, from the standpoint of power conversion, pulsed mode operation has significant impact on the balance of the plant design, since during the low- or non-power producing part of the reactor operation, a means must be provided to generate power at a constant rate within certain limits. Hence, one of the primary requirements for a pulsed reactor is that it must have a thermal storage system along with the associated auxiliary equipment.

4.2 Description of Breeding Blankets

To assess the thermal storage requirements and the thermomechanical effects of pulsed operation, detailed burn cycle analyses were carried out for a Li_2O breeding blanket. For the self-cooled liquid lithium blanket only an overall analysis based on thermal storage requirements was performed. A brief description of the two blanket designs is presented below.

4.2.1 Solid Breeder Blanket

A schematic of the water-cooled Li_2O breeder blanket is shown in Fig. 4-1. The solid breeder material is in the form of sphere-pak (a mixture of three different spherical particles varying in sizes from 1300 μm in diameter to 300 μm in diameter which produces a packed bed with bulk density greater than 85% TD (see Ref. 1 for details). The toroidally oriented coolant tubes

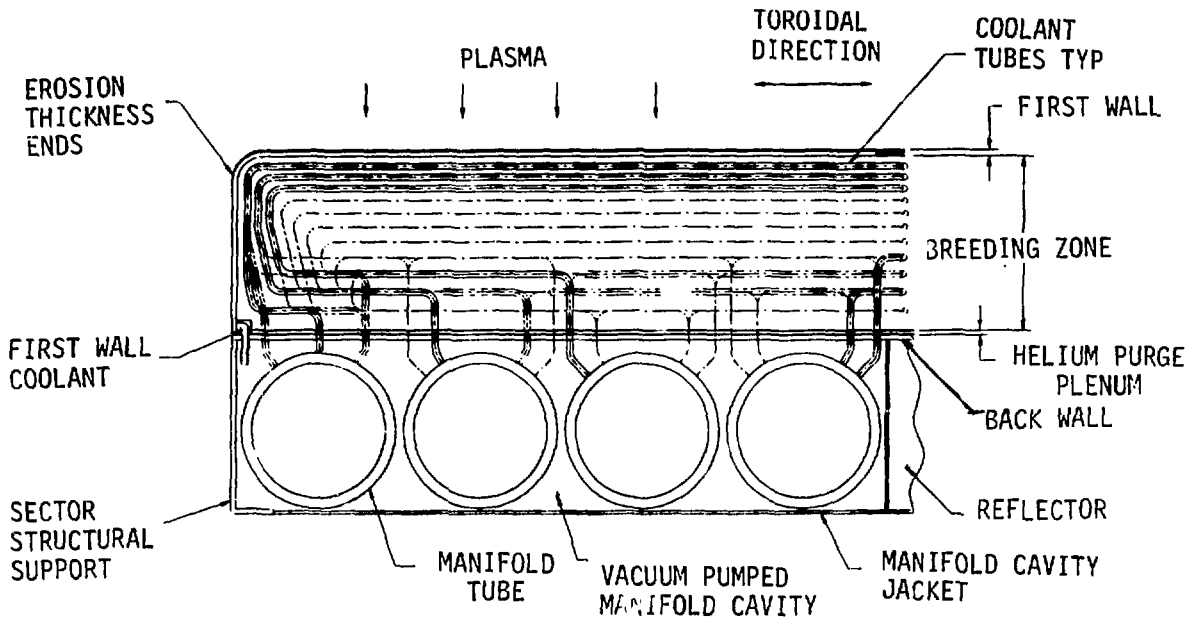

Fig. 4-1. Li_2O/H_2O blanket concept preliminary reference design.

in the breeder zone are arrayed in banks; each coolant tube makes a single pass through the breeder. The coolant tubes are U-shaped and terminate in the inlet and outlet manifolds located immediately behind the back wall. This blanket concept is referred to as a breeder outside coolant tube (BOT) design. Several inlet and outlet header arrangements are shown in Fig. 4-2. In simplest terms this design concept may be described as blanket modules consisting of a box of breeder material in which the coolant-carrying tubes are embedded. The spacing of the coolant tubes in the radial (depthwise) direction of the blanket conform to the exponentially decaying nuclear power field so that the solid breeder material is maintained within the operating temperature window (i.e., within the upper- and lower-temperature limits).

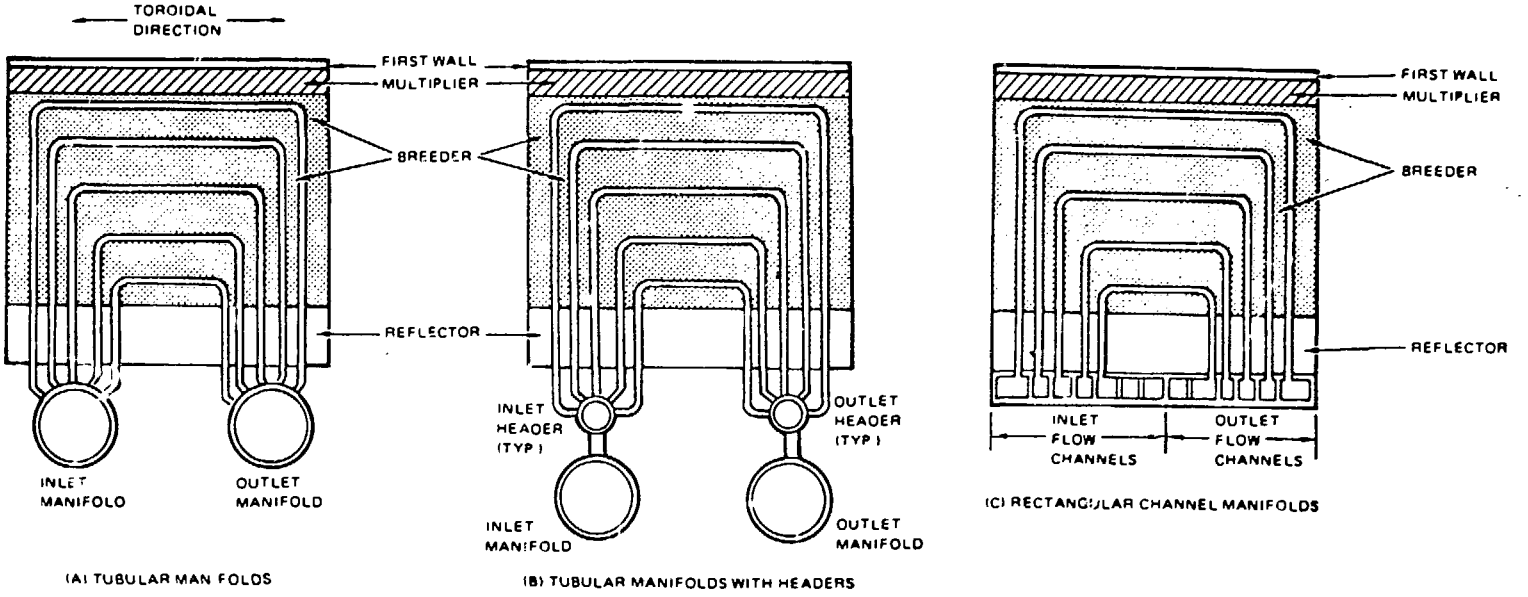

Fig. 4-2. Coolant header arrangement - Li_2O blanket.

4.2.1.1 Design and Operating Conditions

For a given neutron wall loading the primary design considerations are the operating conditions for the coolant, breeding material, and structural material. The operating conditions for the heat transport system is essentially similar to those in current pressurized water reactors. A detailed discussion of the operating temperature window (i.e., the upper and lower temperature limits) for Li_2O is given in Ref. 1. The thermal hydraulic analysis is based on the following data and operating conditions:

Structural material	PCA (prime candidate alloy)
Breeding material (sphere-pak)	Li_2O (85% TD)
Breeder density (g/cm^2)	1.71
Li_2O heat capacity (J/g-K)	2.76
Neutron wall loading (MW/m^2)	3.4
Coolant	Pressurized water
Coolant inlet/outlet temperature (°C)	280/320
Breeder temperature window (°C)	850/410
Surface heat flux on the first wall (W/cm^2)	10-100
Average thermal conductivity of Li_2O at the operating temperature range (W/m-K)	3.4
Blanket module size, length and width (m)	3 × 2
Coolant tube (mm)	
inside diameter	10.0
outside diameter	12.5
Thermal barrier between coolant channel and breeder material	Stainless steel felt, helium, Li_2ZrO_3

Since the lower temperature limit for the Li_2O breeder is significantly higher than the coolant temperature, it is necessary to provide a thermal barrier between the coolant tubes and the breeder in order to maintain the breeder within the operating temperature limits. Thermal analysis presented herein assumes the presence of a thermal barrier either in the form of a ceramic coating (e.g., Li_2ZrO_3) or stainless steel felt sleeves over the coolant tubes. For the design and operating conditions given in the previous section, thermal hydraulic analysis shows that for a ~0.5 m blanket, there will be ten rows of coolant tubes in the radial (depthwise) direction of the blanket.

4.2.2 Liquid Breeder Blanket

For the liquid breeder blanket, only the self-cooled blankets (i.e., the coolant serves both as the heat transfer medium as well as the tritium breeder) were considered. Because of the electrical conducting nature of the liquid metal coolants (either lithium or 17Li-83Pb) flowing through strong magnetic fields, the coolant flow direction and the size of the coolant channels (wall thickness, cross-sectional area) are very critical. A schematic of the toroidal/poloidal flow liquid lithium blanket is shown in Fig. 4-3. The blanket modules consist of slightly slanted poloidal manifolds and relatively small toroidal channels. Each manifold supplies coolant to a number of toroidal channels. In simplest terms, the poloidal flow blanket may be thought of as a vertical straight duct with constant cross-sectional area. Since this design is still in the early stages of development, no transient analysis of this design has been undertaken during the scope of the current burn cycle analysis. However, an overall thermal analysis was carried out to size the thermal storage requirements and to compare the relative cost of thermal systems for the two types of breeding blankets.

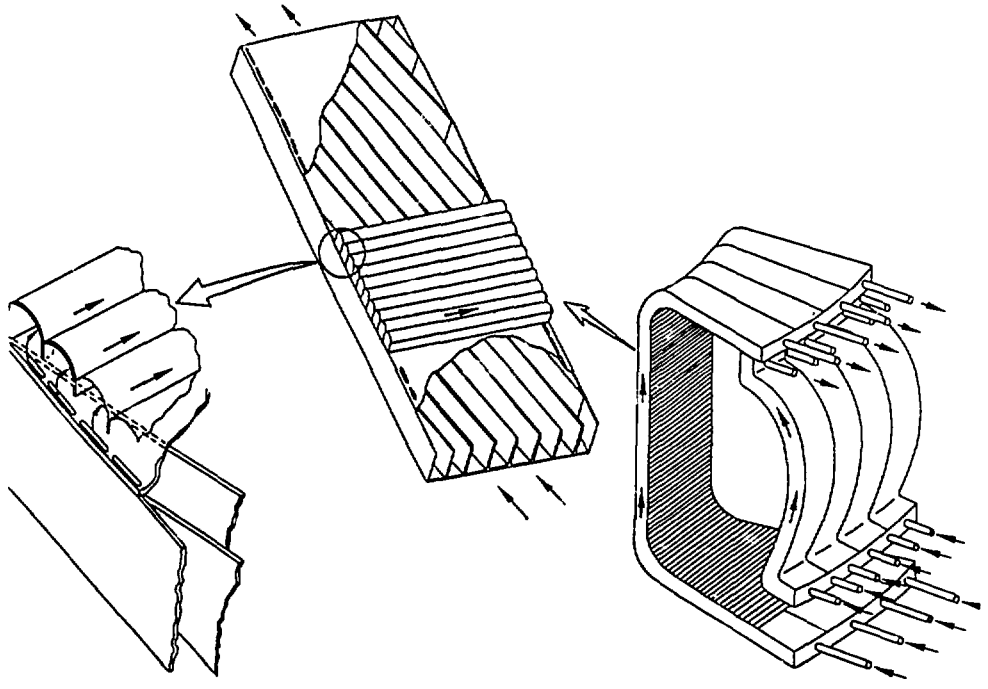

Fig. 4-3. Schematic of lithium blanket.

4.3 Burn Cycle

A discussion of the pulsed modes of operation is presented in Chap. 2. The transient thermal hydraulic and thermomechanical analysis is based on a reactor power profile such as shown in Fig. 4-4. For simplicity, the startup and the shutdown ramps have been assumed to be linear, although inclusion of any startup and shutdown power profile does not present any mathematical difficulty. The following burn cycle scenarios have been used in the transient analysis:

	Time (s)
Startup time (zero power to full power)	10
Steady-state time (operation at full power)	3600
Shutdown time (full power to zero power)	10
Dwell or pumpdown time (operation at zero power)	0,30,90,200

Dwell time of 0 s represents a limiting case for a pulsed power reactor, and the minimum economic penalty associated with pulsed mode operation.

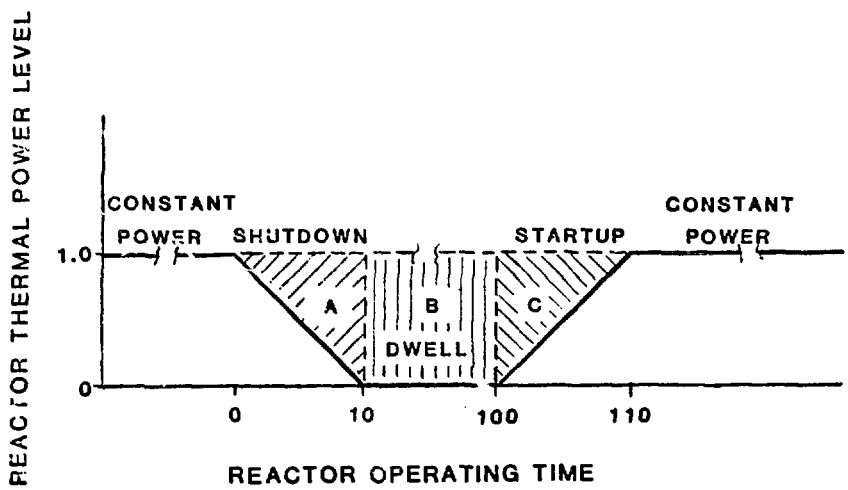

Fig. 4-4. Reactor power profile.

4.4 Thermal Storage System

The analysis of the thermal storage system may be divided into two parts. The first part is associated with the energy deficiency that occurs during the shutdown, dwell, and startup periods of reactor operation. Hence, consideration of the amount of supplemental energy requirements is independent

of the type of breeding blanket. The second part consists of transient temperature response of the entire reactor system and, in particular, the mixed mean temperature of the coolant that enters the energy conversion segment of the power reactor.

For the Li_2O breeder blanket corresponding to neutron wall loading of 3.4 MW/m^2, analyses show that there will be ten breeder regions representing ~0.50-m thick blanket as indicated earlier. Hence, the mixed mean temperature from the ten breeder regions will dictate the sizing of the thermal storage components such as the steam drums, pipes, valves, pumps, heat exchangers, turbines, flow controllers, and numerous other auxiliary equipment. Experience gained from the study of the thermal storage requirements for WILDCAT (Ref. 4) indicate that an acceptable assessment of the thermal storage system can be carried out with analytical data based on only three representative blanket regions. Hence, for the analysis presented herein only three blanket regions, as listed below, were used (note: 100% region refers to blanket regions near the first wall and 5% region refers to blanket region near reflector/shield) as listed below were used:

	Region		
	1 (100%)	2 (25%)	3 (5%)
Nuclear heating rate, (W/cm^3)	41.1	10.3	2.06
Coolant tube, i.d. (mm)	10	10	10
Module length (m)	3	3	3
Coolant velocity (m/s)	5.0	2.9	1.7
Breeder region radius (mm)	13.69	20.14	34.43
No. of coolant tubes	73	50	29

4.5 Transient Temperature Response

The analysis of three blanket regions covering four burn cycle scenerios constitute 12 cases. The transient temperature responses due to cyclic operation were calculated for blanket modules corresponding to the coolant exit locations. The transient calculations include the temperature response of coolant, cladding, and the Li_2O breeder blanket. For the Li_2O breeder, only the maximum and the minimum (and thus the temperature gradient across the

breeder) are included in this analysis. Since the initial temperature of the reactor is not known *a priori*, the transient temperature response during the first few cycles is not meaningful. Hence, the temperature response during the second and the subsequent cycles were considered in this analysis. Table 4-1 summarizes the minimum temperatures that occur during the zero power period. Since the volume of the blanket region associated with each coolant channel in an exponentially decreasing nuclear power field increases as the blanket regions are located further and further away from the first wall, the thermal inertia of regions in the radial direction (depthwise) increases. This effect can be observed from data shown in Table 4-1 where, for example, Region 3 temperatures do not decrease as much as the corresponding temperatures either in Region 2 or in Region 1. Similarly, the temperature differences across blanket regions away from the first wall are larger.

As expected, the changes in the coolant outlet temperatures and temperature gradients in the Li_2O blanket increase as the dwell times increase. If the dwell times are sufficiently long, the temperature of components are expected to decrease to the coolant inlet values. This condition is in contrast to a large number of short pulses where the temperature of the components reach some quasi-steady-state values after a few pulses. From the data presented in Table 4-1, it may be observed that the dwell times have to be greater than 200 s for all of the components to cool down to inlet temperature (assuming the decay heat to be small). When the dwell times are of the order of 200 s, only Region 1 cools down to the inlet temperatures.

The transient temperature response of the coolant, cladding, T_{min} and T_{max} for several cases are shown in Figs. 4-5 through 4-16. As expected, the maximum variation in temperatures occurs for Region 1 due to its having the least volume of material (least thermal inertia). Since Region 1 has the least thermal inertia, its temperature recovers most rapidly during pulsed operation. Similarly the recovery of coolant temperatures is directly related to the breeder volumes. It may be observed from Figs. 4-13 to 4-16 that it takes almost 3000 s for Region 3 to fully recover from the cyclic operation. The time/temperature response for dwell time of 0, 30, and 200 s are included in Appendix B.

TABLE 4-1

Minimum Temperature (°C) During Cyclic Operation of Li_2O Breeding Blanket

Region:	1				2				3			
Dwell time (s):	0	30	90	200	0	30	90	200	0	30	90	200
Coolant	312	297	287	280	316	310	303	292	319	317	315	311
Cladding[a]	345	315	294	281	349	333	320	303	352	338	335	329
T_{min}	394	342	304	282	402	382	357	323	409	391	388	377
T_{max}	807	586	398	287	840	773	659	491	850	829	810	759

[a]Temperature in cladding node (midpoint of cladding thickness).

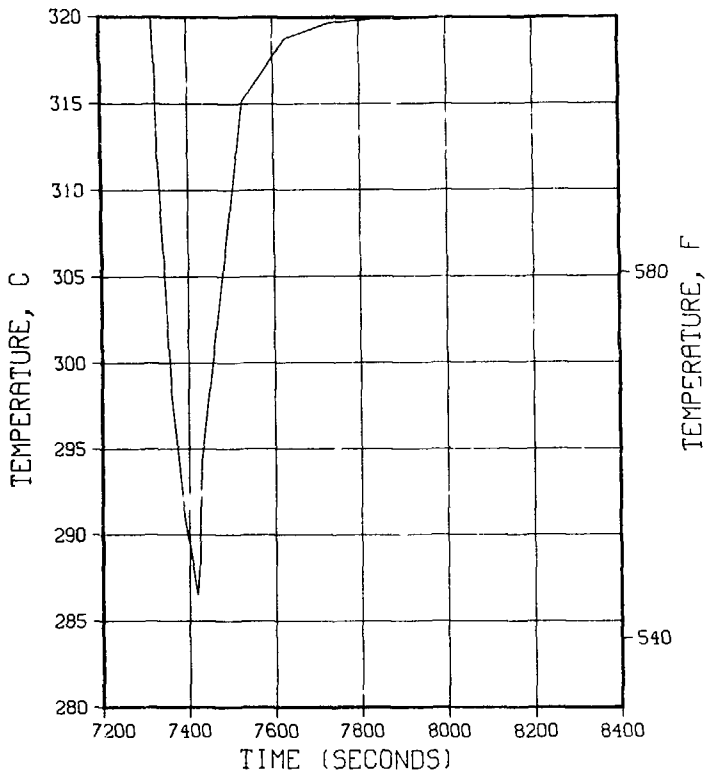

Fig. 4-5. Coolant temperature response: 90-s dwell/region 1.

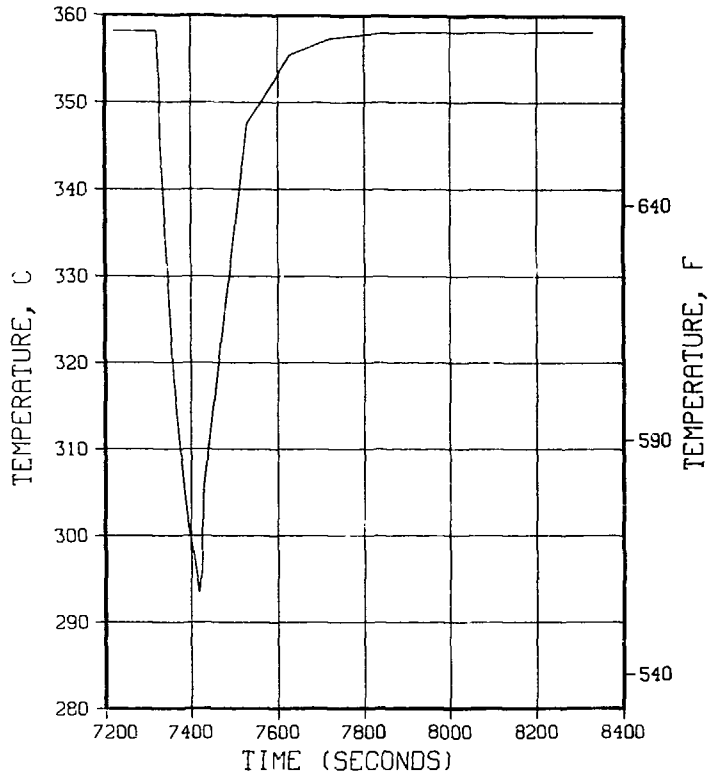

Fig. 4-6. Cladding temperature response: 90-s dwell/region 1.

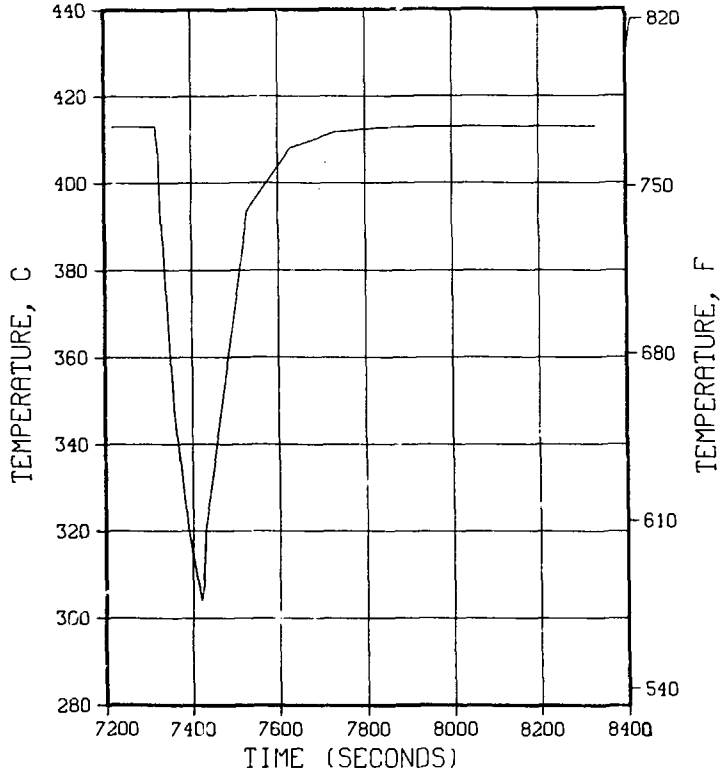

Fig. 4-7. Breeder minimum temperature response: 90-s dwell/region 1.

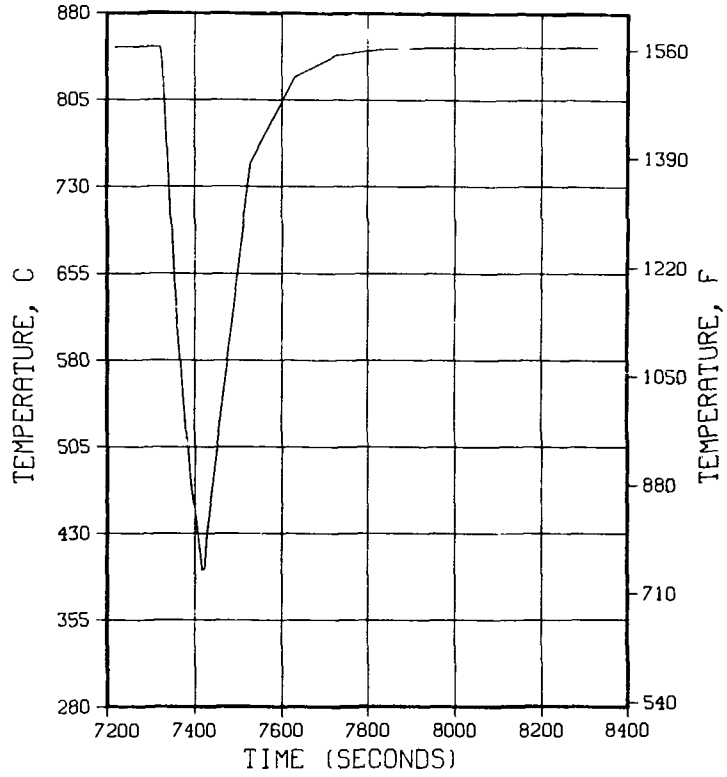

Fig. 4-8. Breeder maximum temperature response: 90-s dwell/region 1.

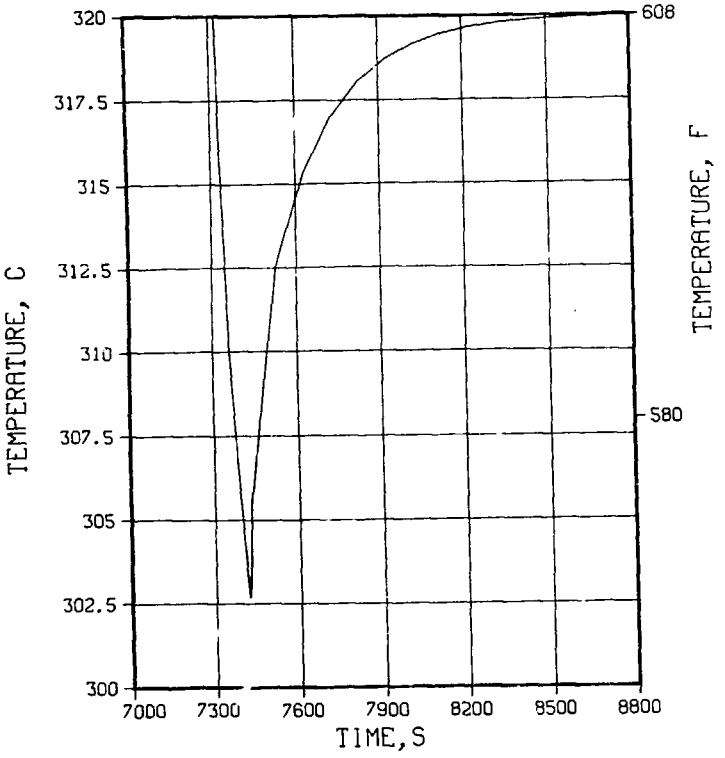

Fig. 4-9. Coolant temperature response: 90-s dwell/region 2.

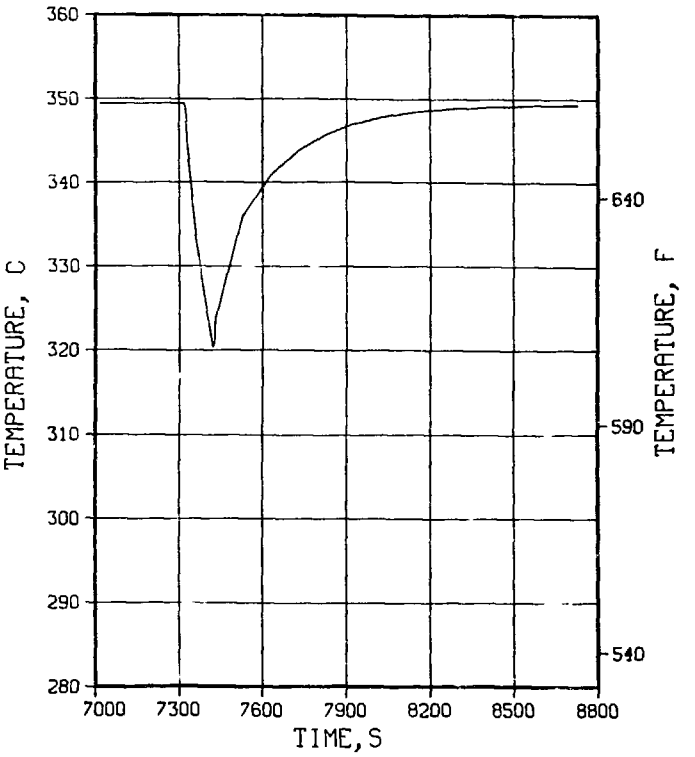

Fig. 4-10. Cladding temperature response: 90-s dwell/region 2.

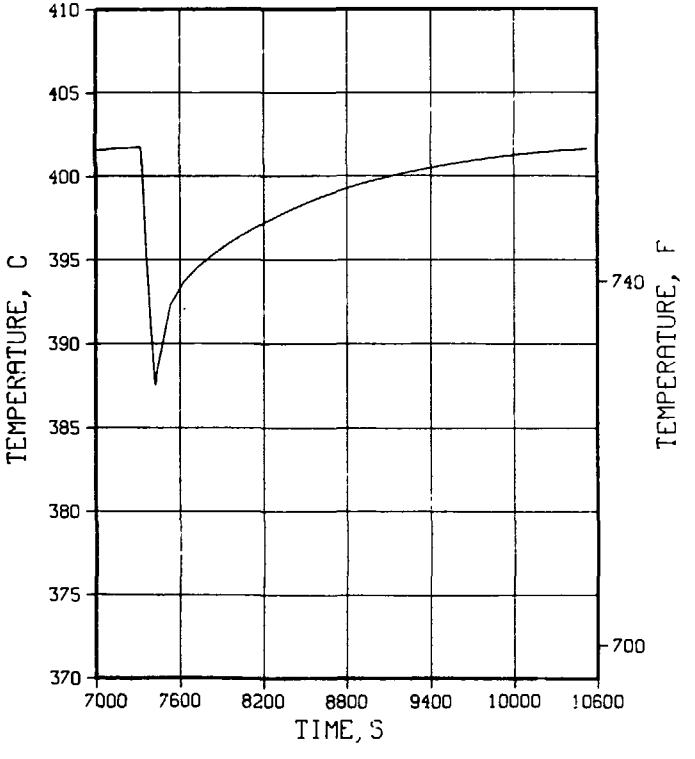

Fig. 4-11. Breeder minimum temperature response: 90-s dwell/region 2.

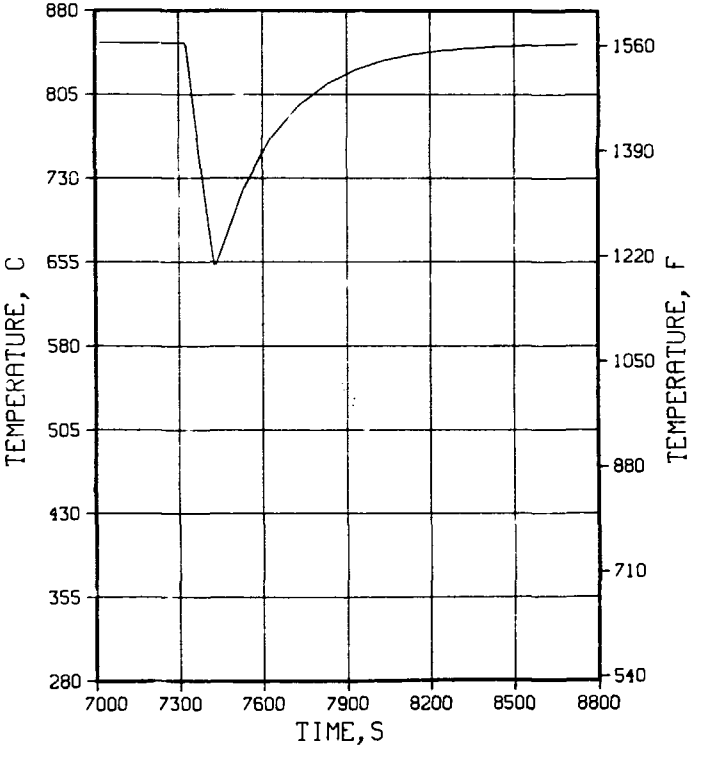

Fig. 4-12. Breeder maximum temperature response: 90-s dwell/region 2.

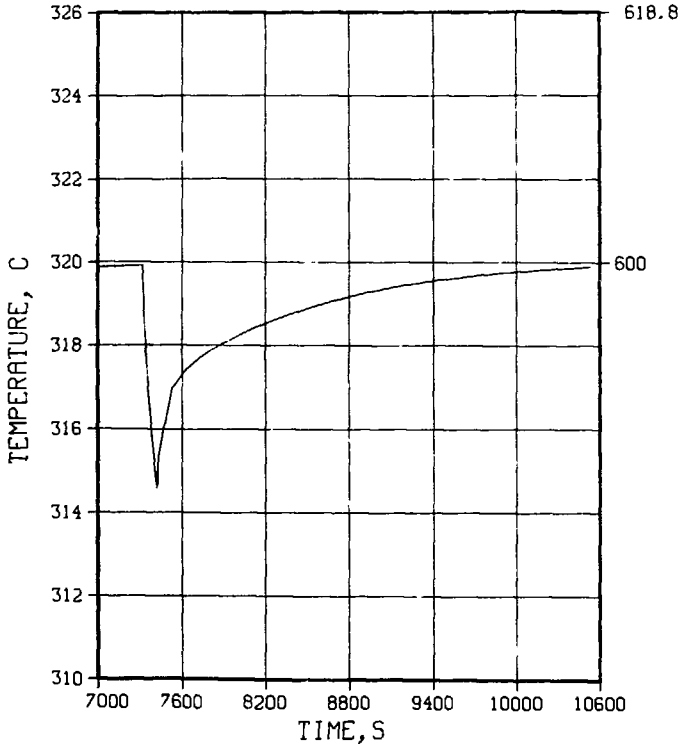

Fig. 4-13. Coolant temperature response: 90-s dwell/region 3.

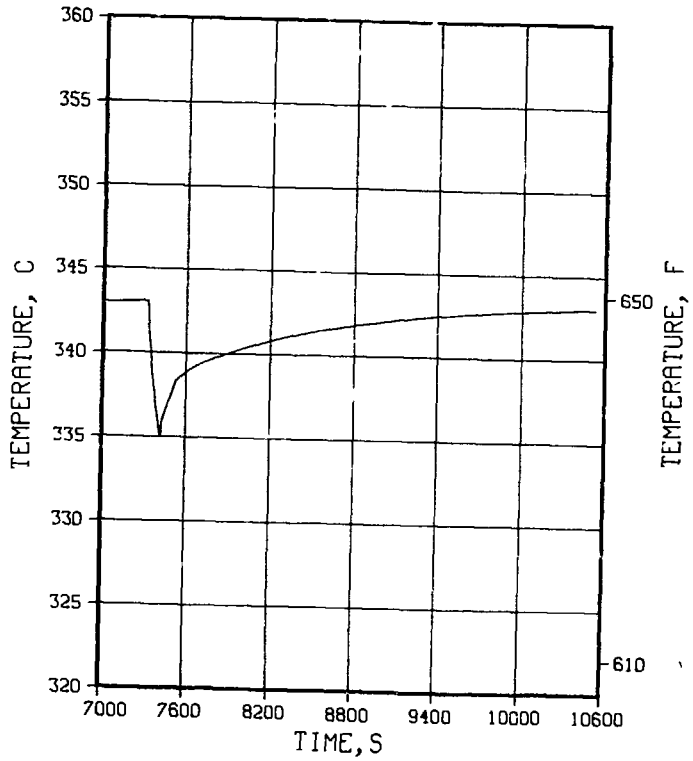

Fig. 4-14. Cladding temperature response: 90-s dwell/region 3.

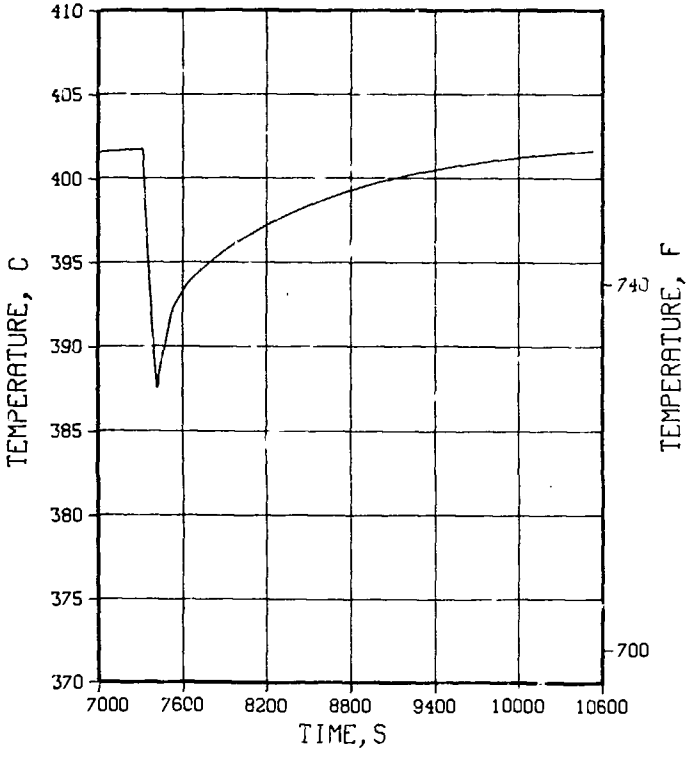

Fig. 4-15. Breeder minimum temperature response: 90-s dwell/region 3.

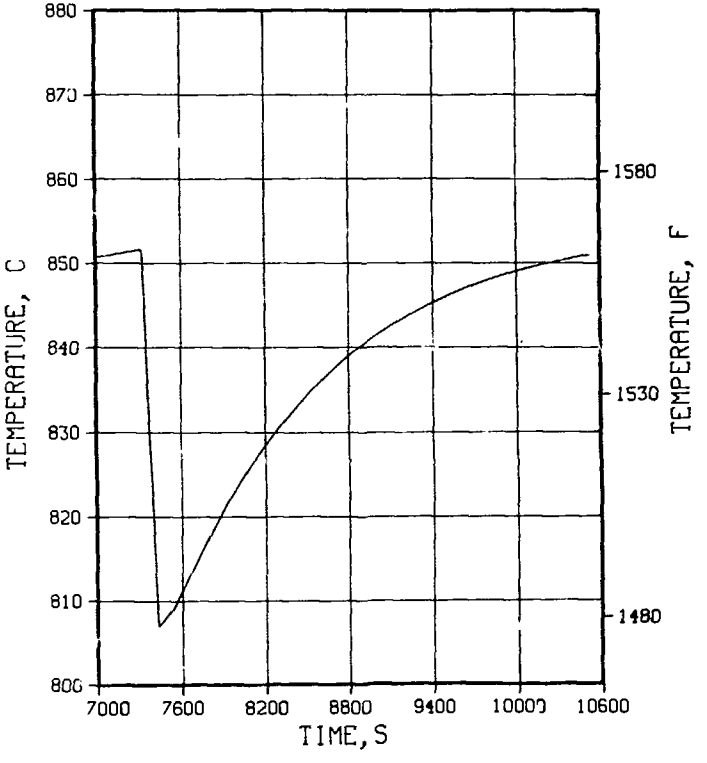

Fig. 4-16. Breeder maximum temperature response: 90-s dwell/region 3.

4.6 Thermal Storage Requirements

As indicated earlier (1) the size of the thermal storage system depends on the energy deficiency that occurs during shutdown, dwell, and startup phases of the power reactor; and (2) the characteristics of the thermal storage system are dictated by the bulk average temperature of the coolant leaving the blanket modules. Hence, for a given burn cycle, the energy storage requirement for a solid breeder blanket or a liquid breeder blanket would be the same, although the same thermal storage system may not be appropriate for two entirely different blanket concepts.

For the solid breeder blanket, the bulk average temperature of the coolant was estimated by:

$$T_{avg} = \frac{\sum_{i=1}^{i=N} W_i T_i n_i}{\sum_{i=1}^{i=N} W_i n_i},$$

where

T_{avg} = Volumetric average temperature of the coolant at blanket exit

W_i = coolant flow rate for Region i

T_i = Coolant exit temperature for Region i

N = Total number of blanket regions.

n_i = Number of coolant tubes in Region i.

For analytical simplicity, only three regions (representing the whole blanket modules) were analyzed. The time/temperature history of the mixed coolant for the four burn cycles are shown in Figs. 4-17 through 4-20.

The integral of the power curve in Fig. 4-17 (as an example; also see Fig. 4-4) determines the total energy deficiency during the shutdown/dwell/startup phases. The actual time/temperature response of the mixed mean coolant will dictate the design details of the thermal storage and control systems. It can be observed from Figs. 4-17 through 4-20 that as the dwell time increased from 0 to 200 s, the mixed coolant temperature decreases from 313°C

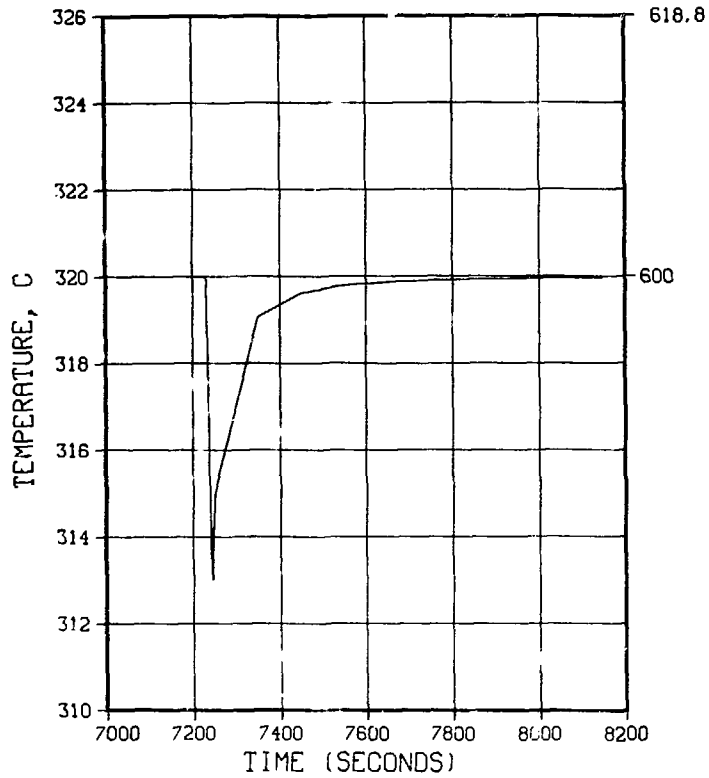

Fig. 4-17. Volumetric average temperature response: 0-s dwell.

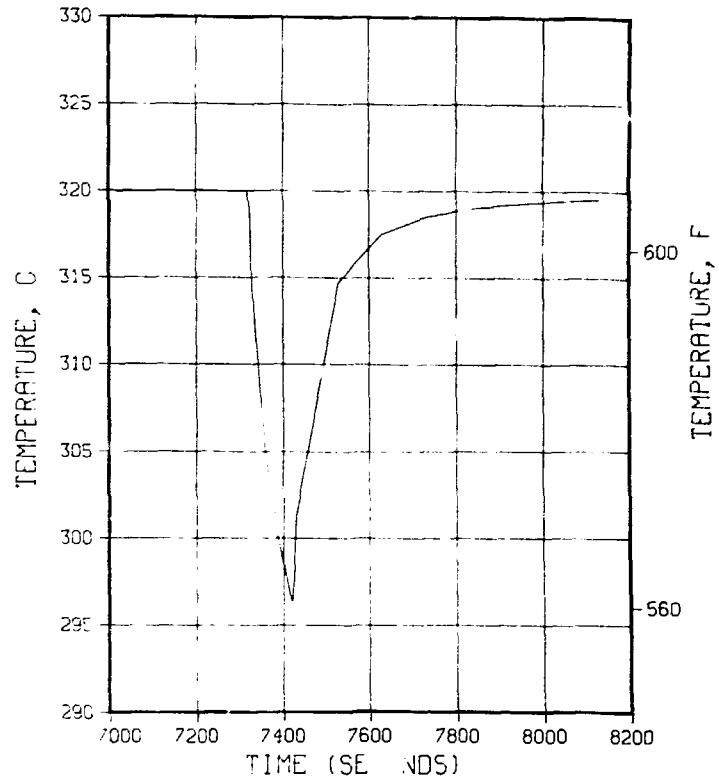

Fig. 4-18. Volumetric average temperature response: 90-s dwell.

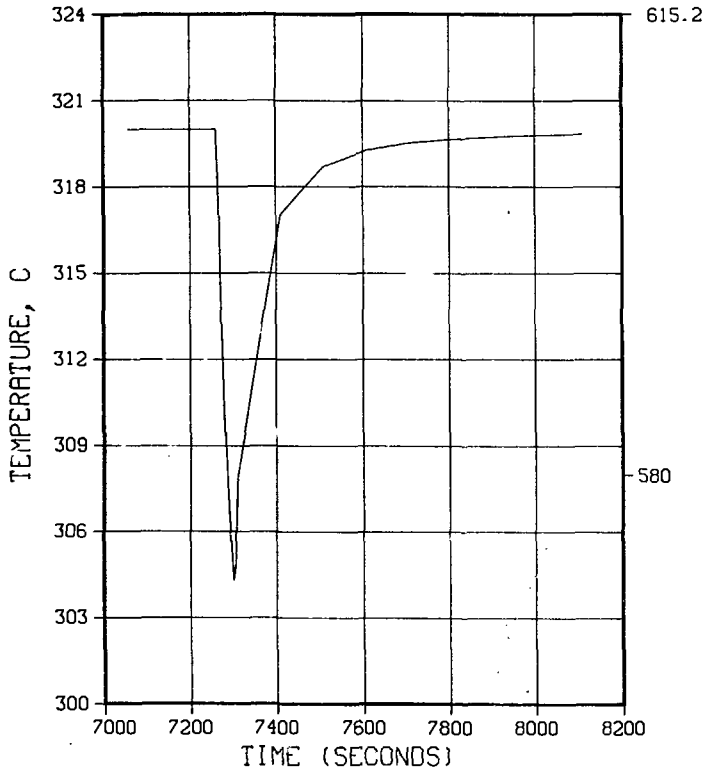

Fig. 4-19. Volumetric average temperature response: 30-s dwell.

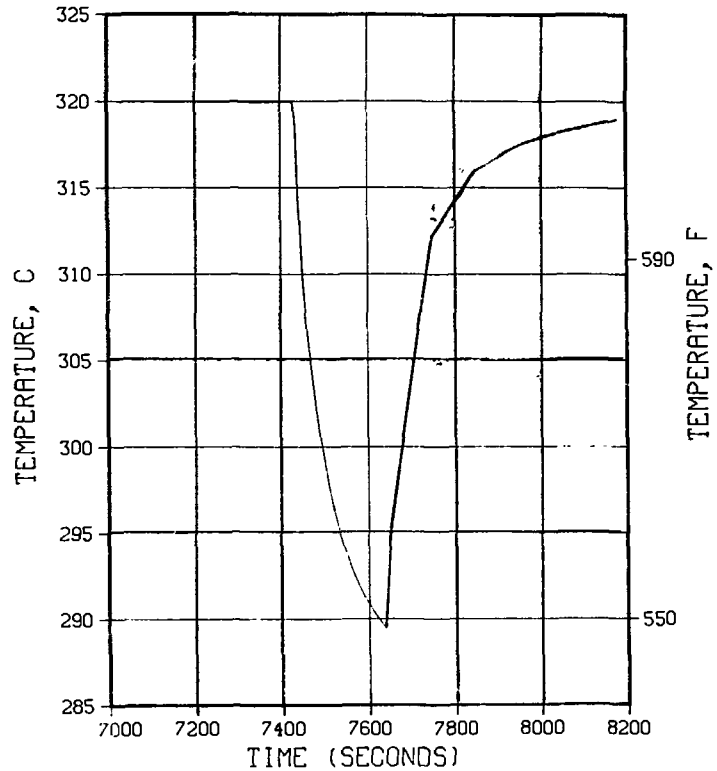

Fig. 4-20. Volumetric average temperature response: 200-s dwell.

to ~290°C, and it takes progressively longer time to approach the steady state as dwell time increases. It should be noted that the power conversion system (heat exchangers/evaporators, steam turbines, condensers, feedwater heaters, etc.) is based on coolant outlet temperatures of 320°C. The power conversion system can no longer be kept in operation when the coolant outlet temperature drops below 290°C. Hence, the necessity of a thermal storage system arises.

For a 4000-MWt reactor, the energy deficiency, assuming linear startup and shutdown ramps, varies from 11 MWh to over 230 MWh. The above quantity of energy must be supplied in a matter of a few hundred seconds in order to operate the power conversion system in a stable manner. Several thermal storage systems, such as packed columns of metals or ceramics and chemicals, were considered for energy storage. However they did not appear to be practical if the thermal energy is to be withdrawn in a relatively short period of time. Energy storage in pressurized water, which can be withdrawn as steam by flashing, or energy storage in a high temperature liquid metal which can be fed into a heat exchanger/evaporator unit appear to be practical, although such systems are considered to be at the upper end of the existing technology. Analyses have shown that pressurized water/steam system is suitable for the solid breeder blanket, and hot sodium reservoir would be practical for the liquid lithium blanket. A brief description of the two systems and the corresponding cost analyses are presented below.

4.6.1 Pressurized Water/Steam System

Figure 4-21 schematically shows the pressurized water/steam thermal storage and power conversion system, which consists of heat exchanger/evaporator units, high pressure and low pressure steam turbines, condenser and condensate storage vessels, feedwater heaters, condensate return (high pressure and low pressure) pumps, generators, and the control system. During the steady-state period, steam flows from the primary steam generator/evaporator unit to the low-pressure turbines. The turbine exhaust after condensation is returned to the evaporators through the feedwater heaters. A bypass stream of blanket coolant flows into the thermal storage units. During shutdown, dwell, and storage periods, as the blanket coolant temperature drops below the steady-state value (v.z., below 320°C), steam is withdrawn from the high-pressure thermal storage units by flashing. The high-pressure steam drives the high-

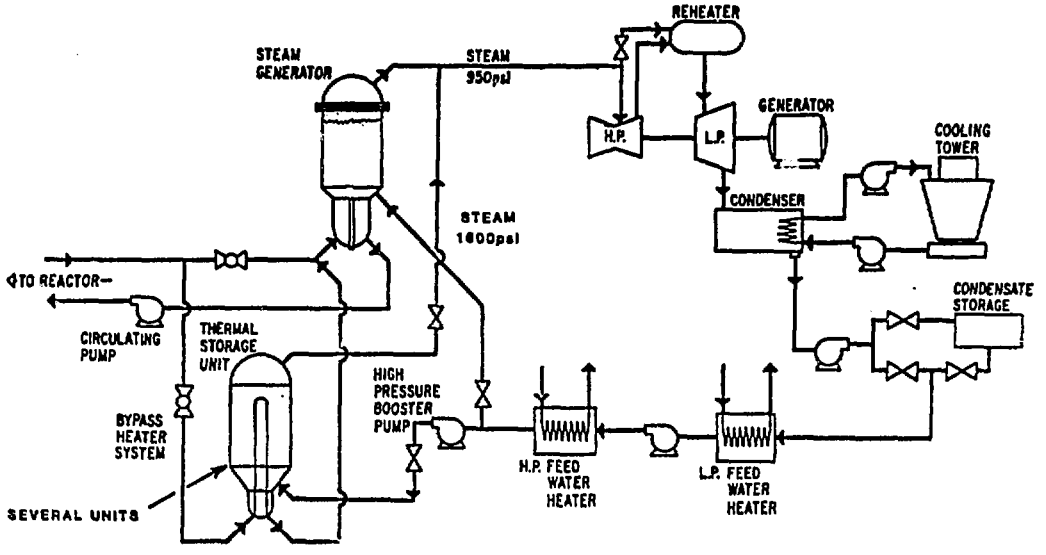

Fig. 4-21. Schematic of thermal storage system for water-cooled Li_2O blanket.

pressure turbine, and mixes with the low-pressure steam from the regular steam generator/evaporator units via the reheater and flows through the low pressure turbines. A portion of the condensate after passing through the feedwater heaters is fed back into the thermal storage unit via booster pumps. The major components, except the control system as discussed above, are shown in Fig. 4-21. During the next phase of this study, an assessment of the control system design details of the auxiliary equipment will be made.

4.6.1.1 Cost Estimate

The cost analysis is divided into two parts. In the first part, cost analysis is carried out based on zero dwell time and 10 s each for startup and shutdown times. Hence, the first part represents the minimum cost of the thermal storage system and the economic penalty for a pulsed reactor. In the second part, a cost estimate is made based on additional components that would be necessary to supplement the thermal storage system for the 10-s dwell or other nonpower generating periods. Table 4-? lists an approximate cost of the thermal storage system.

TABLE 4-2

Cost[a] of Thermal Storage System: Water-Cooled Li_2O Breeder

	Basic Cost	Cost of Additional Components for 10-s Dwell
High pressure vessels (@ $14 M each)	28	28
Charging pumps	10	
Piping	5	1
Valves	8	
Condensate storage	5	1
Instrumentation and control	5	1
Building and structures (incremental)	4	2
Installation	8	4
Total	71	37

Hence, the cost of the thermal storage system may be estimated by:

Total cost = 71 + 3.7 × dwell time (s).

Cost for:		
	0 s dwell time	≈$71
	30 s dwell time	≈$182
	90 s dwell time	≈$404
	200 s dwell time	≈$811

[a](1983) $M.

4.6.2 Liquid-Metal Breeder/Coolant

The liquid-metal blanket and heat transport system consists of a self-cooled lithium blanket, sodium reservoirs, lithium-to-sodium intermediate heat exchangers, and sodium/water steam generator/evaporator units (similar to liquid-metal-cooled fast breeder reactor). The operating conditions for this breeder blanket are as follows:

	°C
Lithium inlet temperature	300
Lithium outlet temperature	500
Sodium inlet temperature	290
Sodium outlet temperature	490
Steam temperature	455

Figure 4-22 schematically shows the major components of the thermal storage system. It consists of lithium-to-sodium heat exchangers; heat accumulators; sodium-to-water evaporator/superheaters; turbine-generator; sodium and lithium circulating pumps; clean-up and purification systems (cold traps) for sodium; inert-gas pressurization systems; and a safety release system. The principle of operation of this system is based on storing thermal energy in the sodium vessels which are designed to accumulate hot sodium. During the low power or nonpower producing period of the reactor operation, energy is withdrawn at a constant rate (i.e., at the same rate as during the steady-state power phase) from the sodium vessels via the intermediate heat exchangers. The amount of energy (i.e., the volume of hot sodium) that is withdrawn during the low/zero power period is made up during the steady-state operation through a side stream of hot lithium supplied from the reactor blanket.

4.6.2.1 Cost Estimate

As in the previous case, the cost of the thermal storage units is divided into two parts. The first part represents the minimum cost of the thermal storage units for zero dwell time. The second part is based on cost of the thermal storage system per each 10-s dwell time. Table 4-3 shows the cost of this system.

4.7 Comparison of Costs

Examination of the cost of the thermal storage units for the two systems indicates that the costs for the liquid-lithium breeder are significantly lower. The primary reason for the low cost of the liquid-metal system is due to low-pressure operation of the thermal storage systems (200 psia liquid-metal breeder versus ~2000 psia for water-cooled solid breeder). It should be noted, however, the added cost of tritium containment such as double-wall

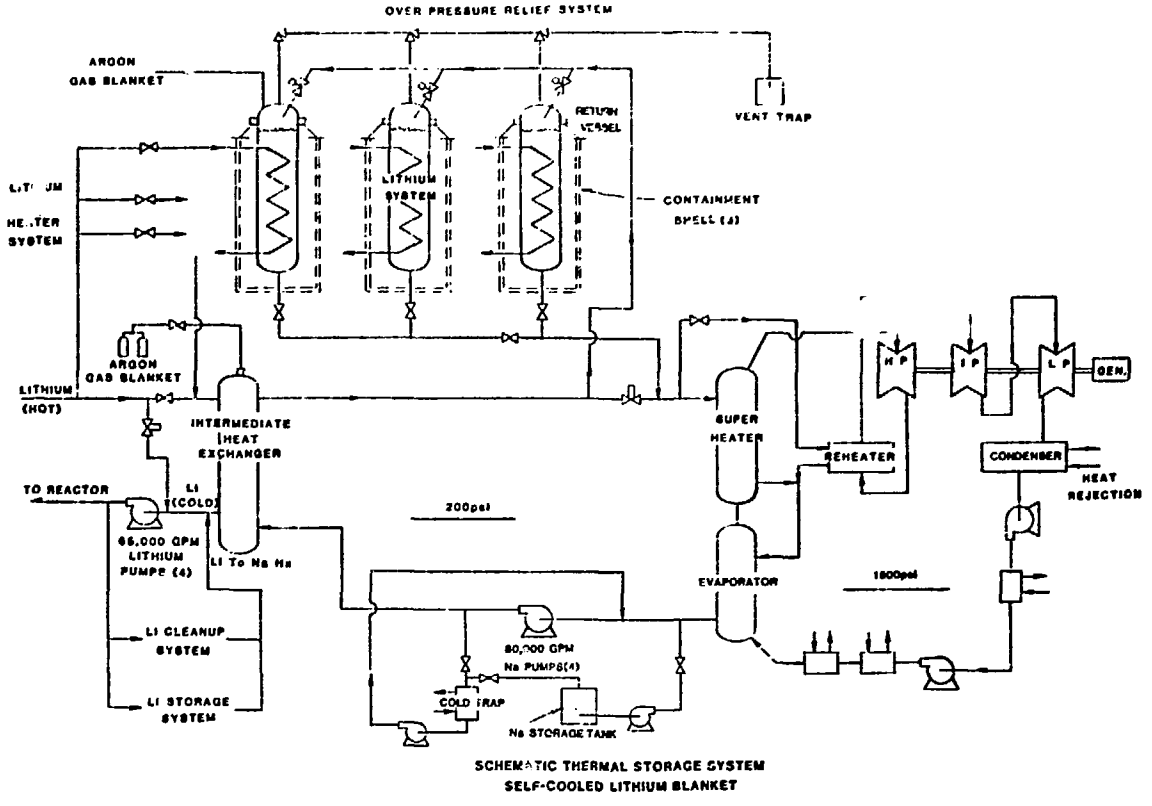

Fig. 4-22. Schematic of thermal storage system for self-cooled lithium blanket.

TABLE 4-3

Cost[a] of Thermal Storage System: Self-Cooled Lithium Blanket

	Basic Unit	Cost of Components for Each 10-s Additional Dwell
Storage vessels	6.5	6.5
Sodium charge	0.3	0.3
Piping	3.6	1.8
Valves	7.1	4.0
Building and structures (incremental)	2.6	1.5
Gas blanket and emergency venting	1.2	0.6
Sodium cleanup system	2.0	0.6
Instrumentation controls	3.0	1.2
Installation	4.0	1.5
Miscellaneous	2.0	1.0
Total	32.3	19.0

Hence, the total cost of the thermal storage system may be estimated by:

Total cost = 32 + 1.9 x dwell time (s).

Cost for:		
	0 s dwell	$32
	30 s dwell	$89
	90 s dwell	$203
	200 s dwell	$412

[a](1983) $M.

pipes, penalty for heat exchangers due to added thermal resistance across double-wall pipes, tritium cleanup, and recovery systems have not been included in this analysis. Although tritium-related costs could significantly increase the cost of the thermal storage systems for the liquid lithium-cooled reactors, it is expected that due to low-pressure operation the cost of the thermal storage for the liquid-metal blanket will still be lower than the cost of the pressurized water-cooled blankets. Additionally, they would be much simpler to operate.

4.8 Thermo-mechanical Analysis

For the design and operating conditions given in Sec. 4.2.1.1, the heat flux over the coolant tubes varies from a maximum of ~100 W/cm^2 to $\leq$10 W/cm^2. The maximum thermal stresses induced by the temperature gradients across the coolant channels is $\leq$5 MPa. However, the primary stress due to high pressure (~15 MPa) water is the order of 55 MPa. During cyclic operation the temperature gradients across the coolant tubes are not significantly larger than the steady-state values. Hence, thermal stresses in the coolant tubes due to cyclic operation is not considered to be a problem for the solid breeder blankets.

4.9 Discussion of Results

Transient analysis of a Li_2O solid breeder blanket corresponding to neutron wall loadings of 3.4 MW/m^2 indicate that the breeder regions near the first wall will cool down to approximately the coolant inlet temperature when the dwell times exceed 200 s. While large temperature variations across the breeder may not adversely affect the integrity of the breeder of sphere-pak design, cooldown of the breeder below the lower operating temperature limit may have significant impact on tritium recovery. The induced thermal stresses across the coolant tubes during transient operation is low; no severe degradation of blanket life due to cyclic operation is anticipated.

Cyclic operation has a severe cost penalty. For zero dwell time alone the thermal system will cost 20 to 70 M$. The preliminary cost analysis shows that the thermal storage system for self-cooled lithium blanket to be less than that for the solid breeder blankets. However, the cost associated with tritium containment and recovery has not been included in these analyses. Detailed cost analysis of both systems is necessary before definitive conclusions can be made. The penalty in terms of adverse thermo-mechanical effects on major components appears to be minimal. The results of the cost analysis indicate that systems with greater than 100 s dwell may not be economically viable.

The results of this chapter are based on the desire to supply constant steam conditions in the turbine, and all costs are based on conventional equipment for the steam cycle. In future work we will determine to what

extent thermal storage costs may be reduced. This question involves several issues: the blanket design should be better optimized for pulsed cycles; additional heat capacity in the coolant, piping, and heat exchangers might be identified; turbine blade tolerances (fatigue, erosion) should be quantified regarding variations in steam quality and temperature; and permissible generator ripple must be determined.

REFERENCES FOR CHAPTER 4

1. M. A. ABDOU et al., "Blanket Comparison and Selection Study," ANL/FPP/TM-177, Argonne National Laboratory (1983).

2. C. C. BAKER et al., "STARFIRE, A Commercial Tokamak Power Plant Study,: ANL/FPP-80-1, Argonne National Laboratory (1980).

3. M. A. ABDOU et al., "A Demonstration Tokamak Power Plant Study (DEMO)," ANL/FPP/82-1, Argonne National Laboratory (1982).

4. K. EVANS et al., "WILDCAT: A Catalyzed D-D Tokamak Reactor," ANL/FPP/TM-150, Argonne National Laboratory (1981).

Chapter 5. MAGNETS

Substantial differences, both quantitative and qualitative, occur among the magnetic systems for various burn cycles. All reactors experience magnetic field variations, from as few as ~200 cycles in the life of a CW reactor to over 10^7 cycles for the internal transformer mode, and this determines the cost of structure needed to survive fatigue associated with large stress fluctuations. On the other hand, cost savings may be realized in certain burn cycles (CW and internal transformer) due to the elimination of a complete subsystem, the ohmic heating coil (OHC) and its attendant power supplies. This chapter presents the performance and cost variations of the three main magnet systems: the OHC, the equilibrium field coils (EFC), and the toroidal field coils (TFC), as a function of the burn cycle parameters. The division of topics is somewhat arbitrary, as the design of one system affects the design of the other coil systems.

5.1 Ohmic Heating Coil

A reference OHC design was developed for the 8-m reactor, and several variations were studied in order to address the following issues:

- What coil configuration maximizes the transformer volt-seconds for inductive current drive?
- What is the practical maximum field swing, ΔB^{OH}, in the OHC?
- How much energy, U^{OH}, must the OHC power supply deliver to charge the OHC?
- What is the fringing field, due to the OHC, at the other magnets and the plasma?
- What is the cost of the OHC, and how does it vary with the number of cycles?

5.1.1 Reference Design

The basic solenoid for the OHC system has a winding thickness, Δ_{OH} = 0.64 m, centered at a radius, R_{OH} = 2.72 m, with a half-height, H_{OH} = 7.7 m. It

consists 2602 turns of 50-kA cable. The average current density is 13.2 MA/m^2. Using the infinite solenoid approximation the field is:

$$\bar{B}_{OH} = \mu J \Delta_{OH} = (4\pi \times 10^7)(13.2 \times 10^6)(0.64) = 10.6 \text{ T}$$

and the volt-seconds are:

$$\Delta\phi_{OH,P} = \pi \bar{R}_{OH}^2 \bar{B}_{OH} = \pi(2.72)^2(10.6) = 246 \text{ V-s} .$$

More accurate calculations, modeling the solenoid as 12 circular coils of radius 0.361 m above the midplane with their mirror images below the midplane and the plasma as several hundred current filaments from the MHD equilibrium calculation indicate the coupling is only 166 V-s. Past experience indicates the circular coil approximation is accurate if the cross-sectional area of all the circular coils equals that of the solenoid, and the infinite-solenoid result is, in fact, produced if the solenoid is sufficiently long (≈20 times longer).

A better design can be obtained by flaring the ends of the solenoid, making it higher, and providing individual trim coils at larger major radii to help channel the flux. The reference design is the best combination of these improvements among those investigated. The field in the plasma is less than the error field of the EF coils. The configuration is shown as modeled in Fig. 5-1 and has parameters:

Stored energy:	18.7 GJ
Total current:	163 MAT
Coil volume:	259 m^3
$\Delta\phi_{OH,P}$:	-235 V-s
Current density:	13.2 MA/m^2
B^{OH}:	10.6 T

5.1.2 ΔB^{OH} Influence; Cost and Lifetime

Several designs were studied for the basic central solenoid: with B_{OH} = 8 T and 10 T at 4.2-K cooling and also with B_{OH} = 10 T and 12 T at 1.8-K operation. As B_{OH} increases from 8 T to 12 T (a 50% increase in field) the volt-second rating increases at a slower rate, by only 27%. This is due to the increased thickness, Δ_{OH}, of the solenoid at higher fields, which decreases

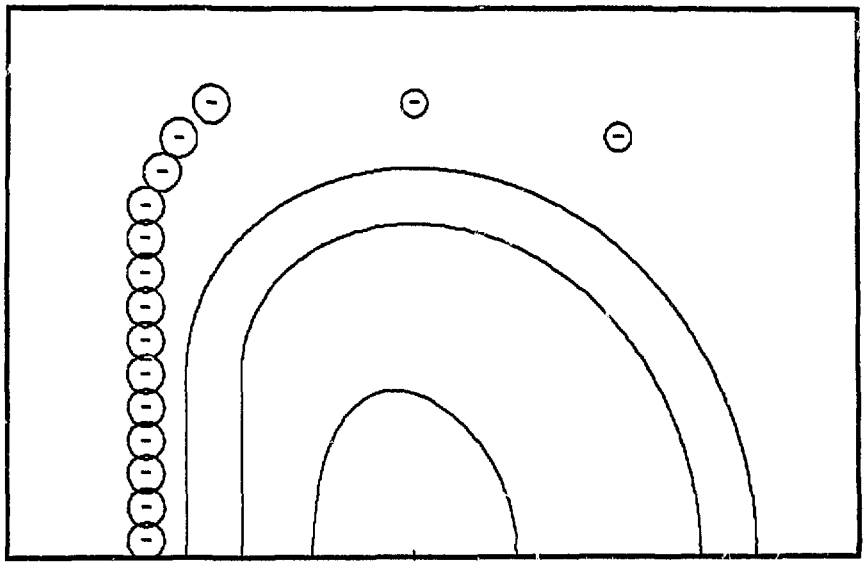

Fig. 5-1. Final design, OHC for 8-m reactor.

the mean radius of the coil, R_{OH}. Considering the increased costs and lower critical current densities near the 12-T range, we feel a practical field goal for the solenoid is thus about 10 T. Significant benefits (high current density) accrue from selecting 1.8 K cooling at 10 T, rather than 4.2 K, and we therefore choose the 1.8-K design.

The amounts of conductor and structural materials are estimated based on specific conductor designs and are listed in Table 5-1. The reference cable configuration for the central OHC uses a helium-II (1.8 K) pool-boiling coil made of niobium-titanium with a copper stabilizer. This choice has an adequate thermal stability margin and acceptable current density in the superconductor. For the outer trim coil, which is in relatively low fields (7.6 ~ 2.8 T), the cable configuration uses helium-I (4.2 K) pool-boiling coils.

To have low ac losses the cables are composed of multistrand subcables. The diameter of the superconducting composite is 0.7 mm; the superconducting filament diameter is 10 μm; the twist pitch length is 18 mm, and the magnetic diffusion time constant is 10 ms.

Data on fatigue properties of niobium-titanium composite and multi-strand cables are not available. It can be assumed that the resistivity increase of the copper stabilizer due to the work hardening and degradation of the superconducting properties of niobium-titanium could be restored by annealing dur-

TABLE 5-1

Reference Ohmic Heating Coil

[B_{OH} = 10 T, 1.8 K; single swing; t_{OH} = 15 s, t_{reset} = 40 s, 1-h cycle]

	Central OHC	Outer Ring OHC
Temperature (K)	1.8	4.2
Niobium-titanium current density (kA/cm^2)	80	38 ~ 110
50-kA cable dimension (cm x cm)	9.56 x 1.06	11.6 x 1.29
Niobium-titanium cross section (cm^2)	0.625	1.313
Copper cross section (cm^2)	4.406	5.25
Total cable length (km)	44.5	27.9
Niobium-titanium weight (Mg)	16.8	12.3
Copper weight (Mg)	175.5	101.2
Hysteresis losses at 4.2 K (kJ/pulse)	950	25.2
Pulsing field losses at 4.2 K (kJ/pulse)	791	21.0
Refrigeration load for the ac losses at 300 K (kw)	169	4.5
Type 316 stainless steel strap (Mg)	595	336

ing the warm-up period of the machine. The support structure most sensitive to the number of burn cycles would be the stainless steel strap used to absorb the hoop stress of the coil.

Variations of the magnetic (volt-second) flux of the central (10 T) OHC and the cost of the stainless steel strap as a function of the number of burn cycles are shown in Table 5-2 and Fig. 5-2. A safety factor of 20 on the allowed number of cycles over that from stainless steel fatigue data is used to determine the maximum strain amplitude. For the number of cycles N less than 2.5×10^4, the stress limit of the strap is constrained by a safety factor of one-third of the ultimate strength of the material. For N ≈ 10^6, where the strain amplitude of the strap is less than 10^{-3}, the magnetic flux and the cost of the strap may be insensitive to the number of cycles.

To have a radial distance of 12.5 cm between the TFC and the OHC for the OHC structure and helium vessel, the outer radius of the central OHC winding is chosen to be 3.04 m. Mainly due to the thickness increase of the strap,

TABLE 5-2

OHC Performance and Cost Versus Cyclic Fatigue

N	$\Delta\varepsilon$	σ (MPa)	Δ_{OH} (m)	R_{OH} (m)	$\pi R_{OH}^2 B_{OH}$ (V-s)	316 SS Strap (Mg)	Cost of SS at \$14K/Mg (\$M)
2.5×10^4	0.0020	407	0.725	2.68	225	931	13.0
5×10^4	0.0017	349	0.789	2.65	220	1086	15.2
2×10^5	0.0011	226	1.036	2.52	199	1677	23.5
2.5×10^5	0.001	205	1.107	2.49	194	1848	25.9
5×10^5	0.0008	164	1.30	2.39	179	2310	32.3

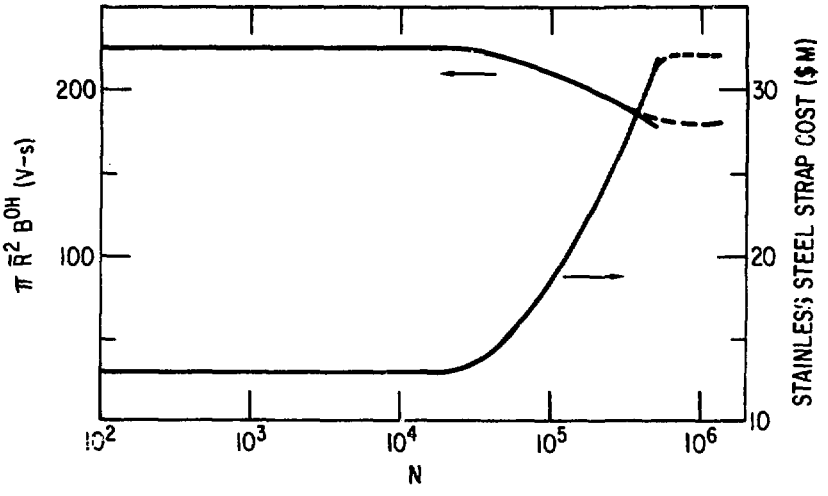

Fig. 5-2. Transformer structure cost and volt-seconds versus OHC cyclic life requirement.

the thickness of the central OHC is increased from 0.725 m to over 1.3 m as the number of cycles increased to 10^6. This reduces the magnetic flux by over 20%. If the cost of the coil fabrication is 1.5 times that of the materials listed in Table 5-3, then the cost increase of the strap is 15% of the OHC cost.

TABLE 5-3

Cost of OH Magnets

	Central OHC ($M)	Outer Ring OHC ($M)
Niobium-titanium ($239/kg)	4.01	2.94
Copper ($10.3/kg)	1.81	1.04
Cable processing ($87/kg)	16.73	9.87
Stainless steel strap for $N < 2.5 \times 10^4$ ($14/kg)	8.33	4.70
Coil winding (1.5 times the material)	46.35	27.9
Total	77.25	46.5

5.2 Equilibrium Field Coils

The equilibrium field coil (EFC) system is necessary to any tokamak to maintain the equilibrium of the toroidal discharge. The presence or absence of an OHC and the time variation of the EFC currents will place important constraints on the EFC design and affects the interaction of the EFC with other magnets. Six principal characteristics of the EFC are significant in comparing burn cycles:

- The conductor volume, V_{EFC}, influences the EFC cost.
- The magnetic energy, U^{EF}, stored by the EFC affects the reactor power supply requirements.
- The fields from the EFC may reduce the current density in the superconductor of the toroidal field coils (TFC).
- The EFC fields produce eddy-current heating in the TFC when they are varied during the burn cycle.
- The EFC fields produce out-of-plane forces on the TFC which may lead to fatigue damage after a certain number of cycles.
- Cyclic stresses influence the design and cost of the EFC itself.

In what follows we first develop reference EFC configurations for both the 8-m and the 7-m reactors. This is followed by a study of design sensitivity to variations in the EFC locations and then by a cost and performance assessment of the EFC systems for the various burn cycles.

5.2.1 Reference Designs

The EFC system is described first for the 8-m reactor. It is required to be decoupled from the OHC system. A number of configurations were investigated and the resulting design, Fig. 5-3, is the best of these. The outboard coils are in positions similar to those in WILDCAT (Ref. 1), since the triangularity, d, is the same and the position of these coils depends most on d. It can be noted that the outboard coils are in the way of a shield door of the type on STARFIRE. For the lower d they need to be where they are, implying the coils would have to be moved if such a door were removed.

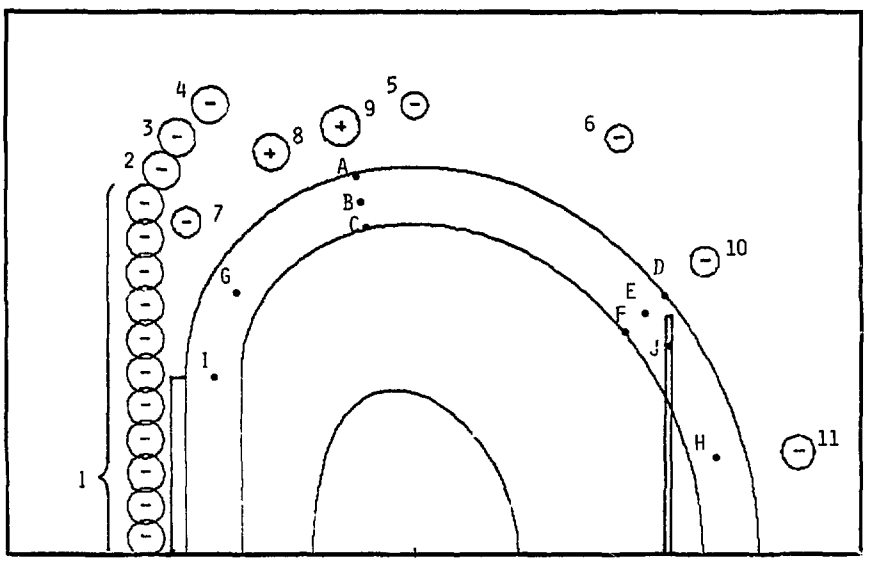

Fig. 5-3. Reference 8-m reactor EFC, decoupled from OHC.

The major parameters are:

Stored energy:	6.36 GJ
Total current:	49.3 MAT
Coil volume:	177 m^3
$\Delta\phi_{EF,P}$:	-71.2 V-s
Current density:	15 MA/m^2

When considering the differences among burn cycles we note that noninductive current drive eliminates the need for an OHC, and this removes two constraints on the EFC design: the need for decoupling from the OHC and the need to prohibit EF coils in the center hole. To assess the impact of eliminating these constraints we made two designs for the 7-m reactor.

The first design has no inboard EF coils while the second design does have. In both cases a number of coil configurations were examined and the design described is the best obtained using a small number of coils (five in both cases). More coils, especially in the outboard region, would somewhat reduce the stored energy. These designs are shown in Figs. 5-4 and 5-5.

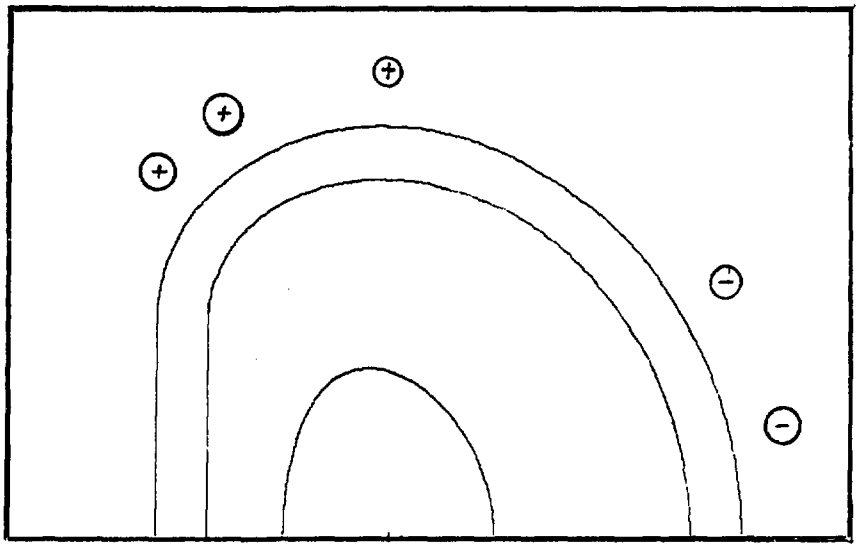

Fig. 5-4. EFC for 7-m reactor, without coils in central hole.

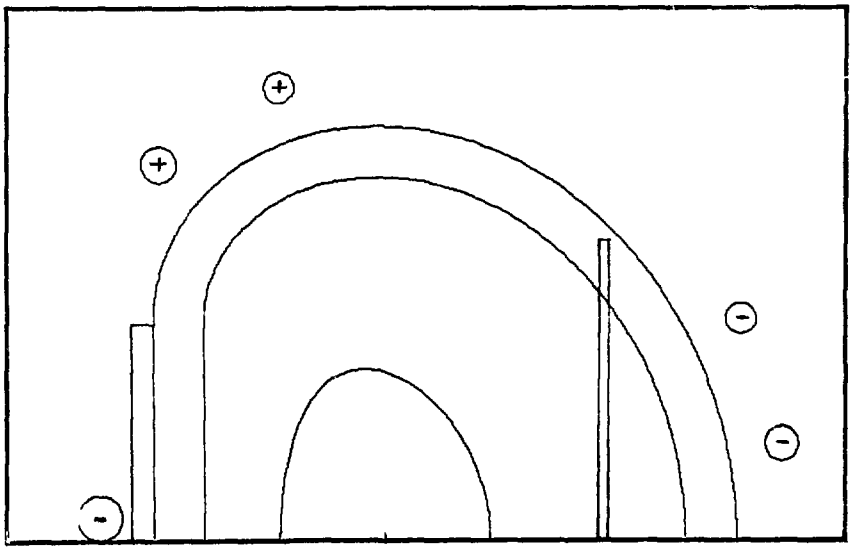

Fig. 5-5. Reference 7-m reactor EFC, including support cylinder and shear panel

The design with inboard coils was selected as the reference system for the 7-m reactor, due to the lower stored energy and coil volume and higher

volt-seconds compared to the alternative without inboard coils. The two EFC systems are described by:

	Inboard Coils	No Inboard Coils
Stored energy, GJ	5.61	6.25
Total current, MAT	50.5	51.6
Coil volume, m^3	136	159
$\Delta\phi_{EF,P}$, V-s	-94.9	-66.2
Current density, MA/m^2	15.0	15.0

Comparing the reference EFC systems for the 8-m reactor (with OHC) and the 7-m reactor (without OHC) we see the quantitative advantages of the latter configuration. The net advantages are not large, however, since the 7-m reactor has the higher plasma current. The advantages of inboard coil placement would be greatly magnified, though, if a more highly shaped ($d \gtrsim 0.3$, or "bean" shaped) equilibrium is desired. The strong increase of stored energy with triangularity is well known.(2)

5.2.2 EFC Design Sensitivity

Since the EFC designs contain several decisions which are a matter of judgment, the sensitivity of the design to these decisions has been studied.

The following cases portray the effects of decoupling and inboard coil placement. Relatively large numbers of coils are used to eliminate bias due to choice of coil placement.

Case A.

Eighteen coil pairs, equally spaced all around, were included, and the system was not decoupled from the OHC.

Case B.

The EFC was not decoupled from the OHC but coil pairs were prohibited in the inboard (OHC) region, eliminating five of the above coil pairs.

Case C.

The EFC/OHC were decoupled and inboard EFC pairs were prohibited, using the coil locations of Case B.

In all three cases the EF coils are separated by one meter from the TFC case.

The results are given in Table 5-4. Case A is most attractive but may be unrealistic due to control problems when the OH and EF systems must be independently driven. Case B again shows the penalty in stored energy if coils are prohibited from the "hole in the doughnut". Case C indicates the substantial penalty in stored energy if the EF/OH systems are decoupled.

The following cases indicate the sensitivity of the EFC system to the number of coil pairs and to the distance, $\delta_{TF/EF}$, of the EF coils from the TFC. All of these cases used a set of model coils equally spaced about the TFC, but with centers not extending into the region $R < R_1 - (\Delta_{TFC}/2)$, the location of the inboard edge of the TFC. The EFC and OHC were decoupled in all cases and the results are included in Table 5-4.

Case D: 20 coil pairs, $\delta_{TF/EF}$ = 0-2 m

(For $\delta_{TF/EF} \gtrsim 2$ m, the model EFCs interfere with the flared part of the solenoid.)

Case E: 10 coil pairs, $\delta_{TF/EF}$ = 0-2 m

The trends are the same as for 20 coil pairs, but the stored energy runs higher, as expected. In Case D and Case E the stored energy and winding volume, both strong cost drivers, increase rapidly as the separation between EFC and TFC increases, so there is a strong motivation to decrease this standoff distance, $\delta_{TF/EF}$. The trends of U^{EF} and V^{EF} for the model with 10 equally spaced coil pairs is displayed in Fig. 5-6.

Case F: 5 coil pairs, $\delta_{TF/EF}$ = 0-2 m

These cases most nearly match the pulsed reference design. The five coils are moved toward the TFC along radii from the plasma centerline. This procedure should maintain the coils in optimized positions, although only the coil locations for the reference case were specifically optimized. This case is included since the effects (to be studied below) of the EF field on the TFC should be larger for the fewer coils with correspondingly larger currents.

TABLE 5-4

EFC Sensitivity (J = 15.0 MA/m^2)

Case	$\delta_{TF/EF}$ (m)	N	U (GJ)	MAT	$\phi_{EF,P}$ (V-s)	V^{EF} (m^3)
A	1.0	18	4.25	45.7	-65.1	150
B	1.0	13	4.60	41.0	-89.0	157
C	1.0	13	5.71	54.3	-71.6	204
D	0.0	20	3.03	32.3	-69.3	126
	0.5	20	4.07	40.6	-71.0	159
	1.0	20	5.58	53.6	-71.7	203
	1.5	20	7.28	64.8	-72.8	245
	2.0	20	9.10	72.6	-70.5[a]	275
E	0.0	10	3.20	32.2	-69.5	126
	0.5	10	4.30	41.1	-71.1	160
	1.0	10	5.87	53.4	-71.7	200
	1.5	10	7.74	64.8	-71.4	237
	2.0	10	9.63	73.8	-70.6[a]	271
F	0.0	5	3.64	28.1	-68.3	117
	0.5	5	4.71	36.4	-70.1	143
	1.0	5	6.36	49.3	-71.2	177

[a]Inner EFC is quite close to solenoid flare.

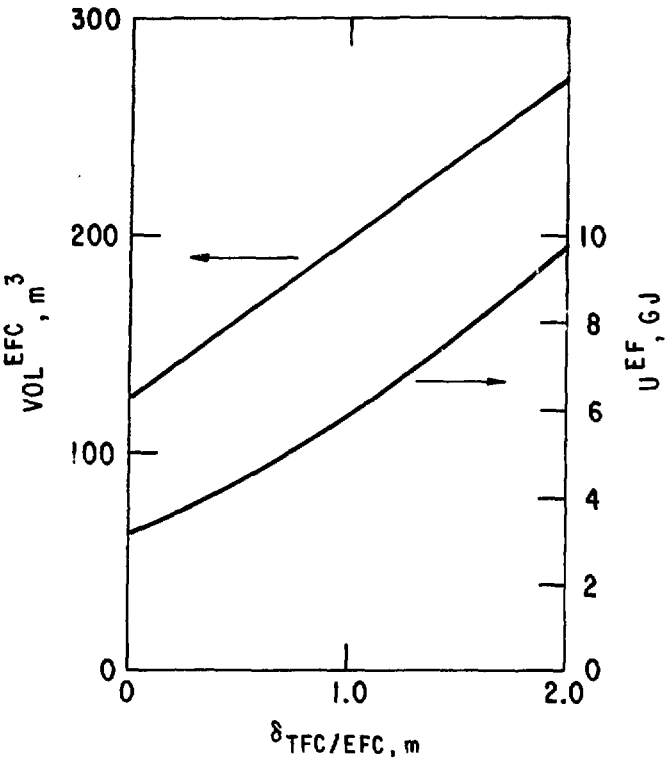

Fig. 5-6. EFC volume and stored energy versus distance from TFC; Case E: 10 EFC pairs equally spaced, decoupled from OHC.

The penalty for locating the EFC closer to the TFC is that the local poloidal field will degrade the TFC performance in three ways: the EF coil fields may reduce the superconductor current density; eddy current heating will be larger, especially for frequently pulsed cycles; and out-of-plane stress fatigue may increase for the TFC structure. These specific problems are addressed in Secs. 5.2.3 and 5.3 for Case F. The reference configuration is shown in Fig. 5-3 and the other two Case F configurations are shown in Figs. 5-7 and 5-8. Note from the figures that it is likely a four-coil pair design is possible if $\delta_{TF/EF}$ is sufficiently small. This EFC design would have attractions due to low U^{EF} and small V^{EF} but may well be prohibited due to fringing effects on the TFC.

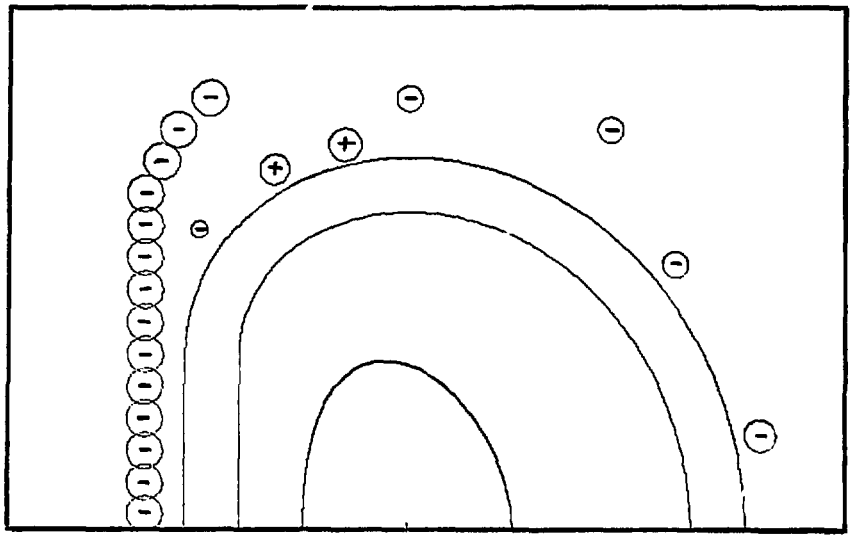

Fig. 5-7. Case F: $\delta_{TF/EF}$ = 0.5 m.

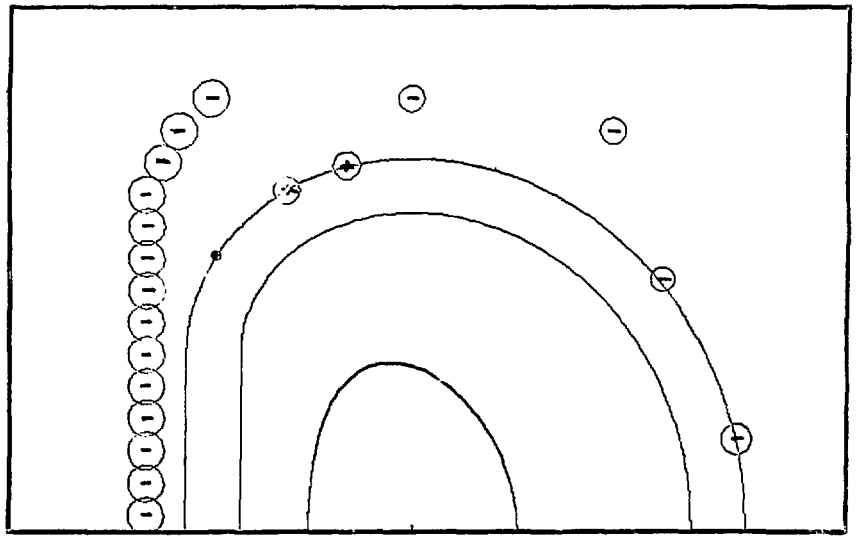

Fig. 5-8. Case F: $\delta_{TF/EF}$ = 0.0 m.

5.2.3 Poloidal Field at the TFC

The poloidal field, B_p, was calculated at several locations within the TFC for several variations of the EFC configuration from the 8-m reactor reference EFC design.

The first study was to compute the poloidal field contributions from the OHC and EFC currents separately. The reference coil set (Fig. 5-3) was used for this study. The OHC contribution to B_p within the TFC structure is typically less than 20% of that due to the EFC, and in all cases it is less than 0.3 T. The small OHC field is a result of the effort expended to make the OH field nearly zero in the plasma.

Next, B_p was computed versus position transversely across the TFC. The B_p gradient is largest directly beneath individual EF coils. For example, in Fig. 5-3, B_p = 1.84 T, 1.36 T, and 1.05 T at points A, B, and C, respectively, due to the EFC set alone. Points A, B, and C represent the highest B_p values as well as the largest B_p variation throughout the TFC. For example, B_p = 1.1 T, 0.93 T, and 0.87 T at points D, E, and F of Fig. 5-3. If the TFC design is similar to that of STARFIRE, then the TFC can operate with B = 5.0 T on the outer windings, and at B ≈ 11 T on the inner windings. The combined poloidal and toroidal fields are less than these values everywhere for the reference design.

The B_p value was computed on the surface of the finite-sized EF coils in Fig. 5-3. At coil No. 7 B_p = 1.7 T and at coil No. 8 B_p = 4.5 T. In all cases $B_p < 5$ T at the EFC outer surfaces, so these coils could be placed directly on top of the TFC structure without exceeding the critical field for the outer windings of the TFC. We note, in addition, from Figs. 5-7 and 5-8, that the EF coils carry even smaller currents and have lower B_p values if they are moved closer to the TFC. The center of the TFC winding is probably more sensitive to B_p since B_t is substantial there. At the center of the TFC winding the diminution of the EFC currents is countered by the increasing nearness of the EFC currents as $\delta_{TF/ET} \to 0$. Thus we computed B_p along the center of the TFC winding for the three configurations in Case F with $\delta_{TF/EF}$ = 1.0, 0.5, and 0.0 m using a line current model for the five EF coils. In addition, the 13-MA plasma current and OHC currents were included to accurately model the full poloidal field. The OH and EF currents were selected near the end of

the burn cycle, when the transformer field, B^{OH}, is completely reversed, since this time corresponds to the largest B_p effects on the TFC. Figure 5-9 shows only slight increases in B_p at point B (from 1.1 T to 1.3 T, at ℓ = 8.2 m) and at point H (from 1.1 T to 1.9 T, at ℓ = 17.6 m) as the EF coils are moved inward. At point G (ℓ = 5.26 m) the B_p strength actually decreases (from 0.82 T to 0.71 T) as $\delta_{TF/EC} \to 0$. In view of the relatively large B_t component along the coil centerline it seems unlikely that a reduction of $\delta_{TF/EF}$ would significantly degrade the TFC performance, provided the conductor along the centerline is designed for operation in the 5-7 T range. There are, thus, indications the EF coils could be moved closer to the TFC, reducing their stored energy and other requirements. Such a design would necessitate further study, however.

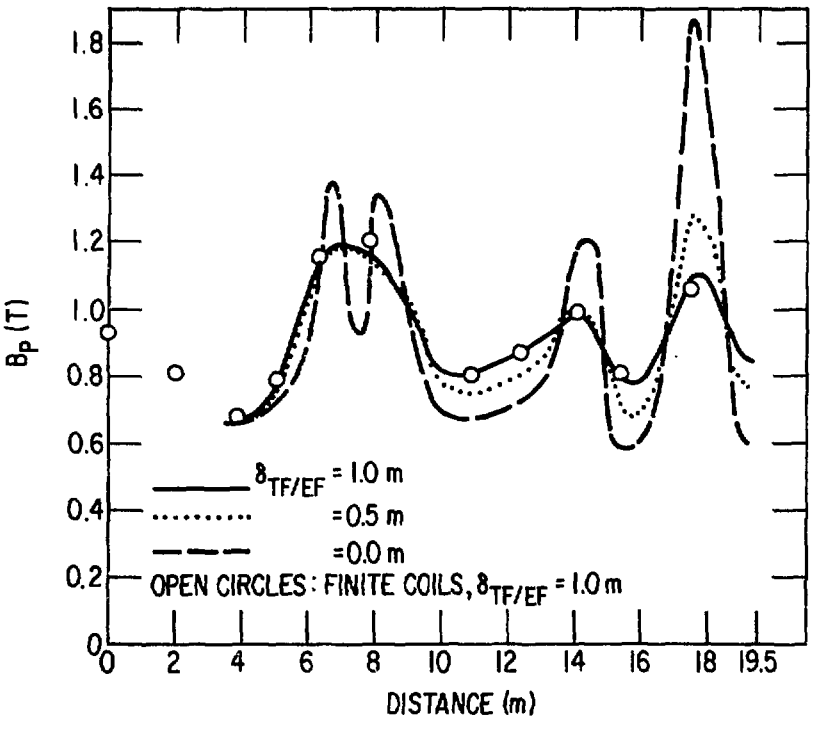

Fig. 5-9. Poloidal field along TFC midline at end of burn; reference OH cycle (8-m reactor). The abscissa is the distance, ℓ, along the coil starting from the inboard midplane.

The remaining issue for the design of the pulsed EFC is the impact of $\delta_{TF/EF}$ on out-of-plane forces and eddy current heating in the TFC. To study this question it is necessary to model the structural components of the TFC, and this topic will be addressed in Sec. 5.3.

5.2.4 EFC Cost and Lifetime

As in the case of OHC, the cost of the conductor and structural materials for the EFC is estimated from a 50-kA cable design. Since the fields on the EFC conductors are in the range of 3.2-5.0 T, the cable configuration is assumed to be helium-I (4.2 K) pool-boiling coils with niobium-titanium with copper stabilizer (same as the OHC outer ring coils). Important parameters and a cost estimate are listed in Table 5-5.

TABLE 5-5

EFC Parameters and Cost Estimate

[8.0 m reactor; single swing vertical field, t_{EF} = 30 s (up and down), 1-h cycle.]

Temperature (K)	4.2
Niobium-titanium current density (kA/cm^2)	110
Total 50-kA cable length (km)	53.3
Niobium-titanium weight (Mg)	14.7
Copper weight (Mg)	170
Hysteresis losses at 4.2 K (kJ/pulse)	12.7
Pulsing field losses at 4.2 K (kJ/pulse)	46.4
Refrigeration load for the ac losses at 300 K (kW)	5.9
Stainless steel strap (Mg)	846
Niobium-titanium cost ($M)	3.51
Copper cost ($M)	1.75
Cable processing ($M)	16.1
Stainless strap cost ($M)	11.84
Coil winding cost ($M), (1.5 times the materials cost)	49.8
Total cost ($M)	83

In Fig. 5-10 the estimated stainless steel strap cost for the hoop stress support is shown as a function of the number of burn cycles. For the OH operation the strap cost is increased by a factor of 1.5 for $N \approx 10^6$. This increase is about 20% of the coil cost ($83 M).

The stress amplitude in the hybrid operation is one-half of that in the OH operation. Therefore, the variation of the stainless steel strap cost for hybrid operation is very insensitive to the number of burn cycles as shown in Fig. 5-10. The increase of the strap cost is less than 4% of the coil cost.

5.3 Toroidal Field Coil

Reference designs for the toroidal field coil (TFC) systems were developed for both the 8-m and the 7-m reactors. In the present study the support structure was based on the STARFIRE concept, with room temperature shear panels and a double box construction for the coil cases. The selection of a

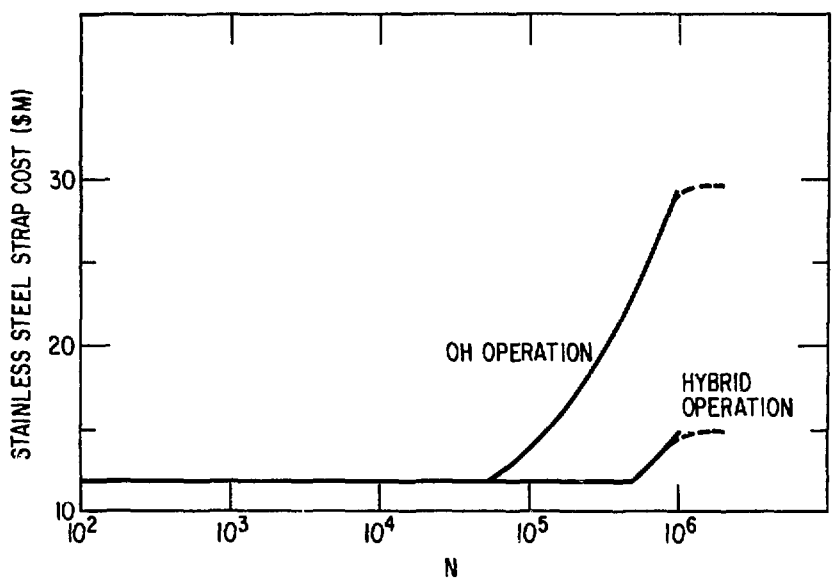

Fig. 5-10. EFC structure cost versus cyclic life requirement.

specific design concept enables us to study the relative effects of pulsed burn cycles on TFC performance, but we caution that our conclusions will change quantitatively if a different design approach (e.g. DEMO/FED/INTOR,

with 4 K intercoil structure) is considered. The main issues we have studied include:

- How do cyclic stresses affect the lifetime of the TFC components due to mechanical fatigue?
- How much (eddy current) heat is introduced into the TFC system when the vertical fields are pulsed?
- How do the TFC capital costs and refrigeration costs depend on the choice of a burn cycle?

5.3.1 Reference Designs

The portions of superconductor, copper stabilizer, and co-wound steel support which comprise the TFC winding pack were computed with the TRAC-II code, using algorithms previously developed[3] for modeling studies. As discussed in Chap. 2, the 8-m reactor has a lower peak toroidal field, B_M = 9.81 T, than the 7-m reactor which, like STARFIRE, has B_M = 11.2 T. Preliminary concerns that pulsed operation of the 8-m reactor would lead to fatigue failure in the windings led us to specify a lower stress limit, σ, for the co-wound steel in the 8-m reactor (σ = 276 MPa versus σ = 552 MPa in the 7-m device). As a consequence the TFC radial thickness, Δ_{TFC}, is larger for the 8-m reactor, despite its lower field. A detailed picture of the cabling, taken from the STARFIRE design, is exemplified in Figs. 5-11 through 5-13.

The inboard legs of the TFC, at $R = R_1$, were located as close as possible to the plasma, consistent with an inboard blanket/shield plus scrape-off width of $\Delta^i_{BS} + \Delta_V$ = 1.4 m. The outboard legs, at $R = R_2$, allowed a clearance from the plasma of $\Delta^0_{B/S} + \Delta_v + \Delta_d$ = 3.4 m, where Δ_d permits an access gap; for both reactors this results in similar toroidal field ripple. The number of coils, N_{TFC}, was chosen as 12 for both reactors, and a standard, constant-tension shape was selected using the Moses and Young approximation.[4] The magnet parameters are illustrated in Fig. 5-14, and the dimensions for the two reference designs are given in Table 5-6. Note that the smaller reactor has a significantly smaller winding volume. As detailed in Table 5-6, this is mainly due to the smaller amount of steel required in the winding pack.

Considering pulsed operating modes, we find the largest TFC cost differences to arise from the different out-of-plane forces generated by the OHC and

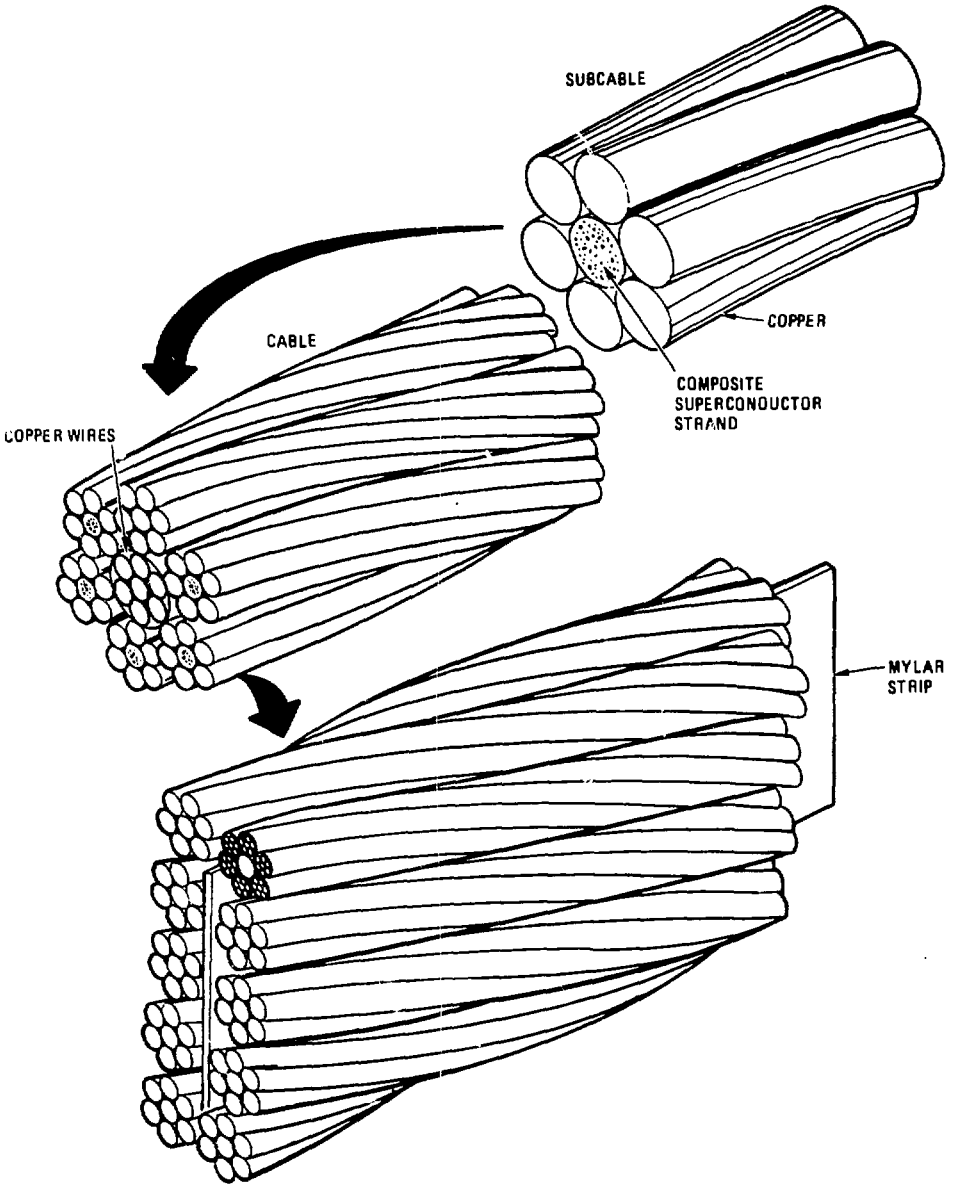

Fig. 5-11. Three-level cabled conductor.

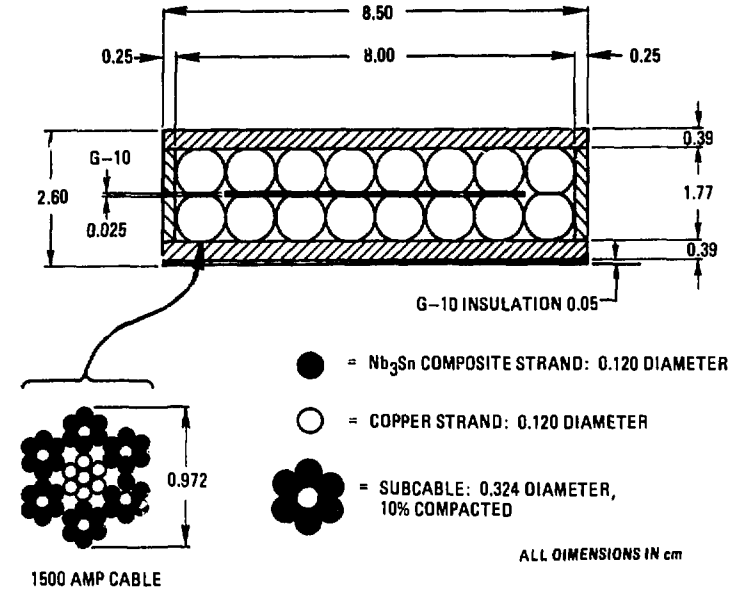

(a)

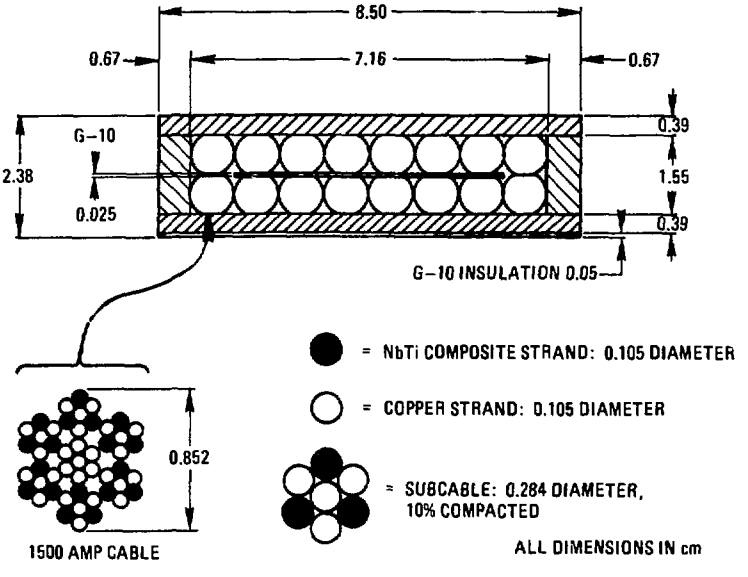

(b)

Fig. 5-12. 24-kA conductor/support module: (a) high field region (9-11 tesla); and (b) 7-9 tesla field region.

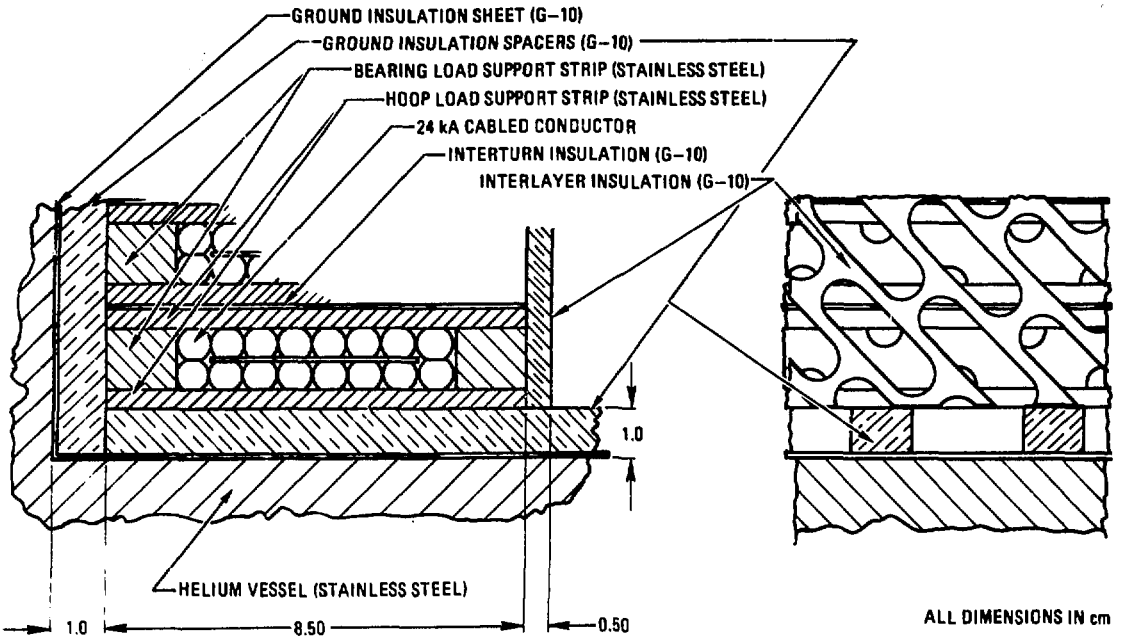

Fig. 5-13. Coil detail: inner radius conductor region.

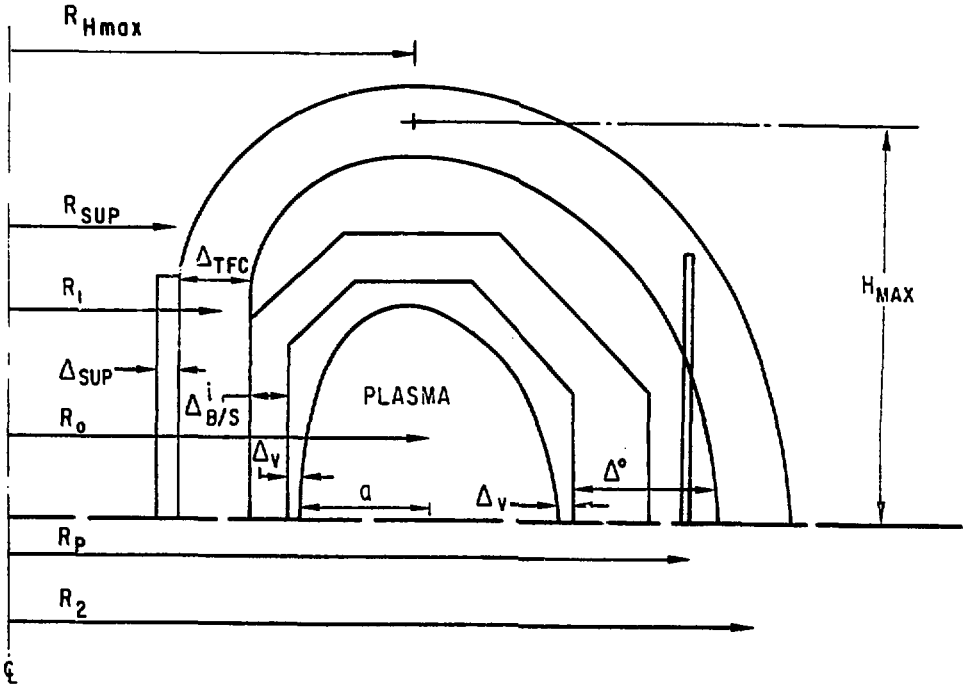

Fig. 5-14. TFC geometry.

TABLE 5-6

TFC Dimensions

Item	Variable	Values	
		8-m Reactor	7-m Reactor
Maximum field	B_M	9.81 T	11.2 T
Major radius	R_0	8.0 m	7.0 m
Inboard leg	R_1	4.06 m	3.19 m
Outboard leg	R_2	14.15 m	13.02 m
Thickness (helium vessel)	Δ_{TFC}	1.08 m	0.94 m
Number of coils	N_{TFC}	12	12
Half straight leg	H_{R1}	3.52 m	4.02 m
Half height	H_{max}	6.90 m	7.06 m
Radius of H_{max}	$R_{H_{max}}$	7.98 m	6.73 m
Full perimeter	L	39.03 m	39.34 m
Winding volume	$2\pi R_1 \Delta_{TFC} L$	1075 m^3	741 m^3
Copper stabilizer		2.22×10^6 kg	2.13×10^6 kg
Niobium-titanium		57.0×10^3 kg	45.6×10^3 kg
Nb_3Sn		2.00×10^3 kg	4.60×10^3 kg
Co-wound steel		3.59×10^6 kg	1.66×10^6 kg
Helium vessel width	$2\ b_t$	2.13 m	1.67 m
Helium vessel thickness	t_{He}	0.04 m	0.04 m
Shear panel radius	R_p	12.57 m	11.94 m
Shear panel height × width	h × w	9.61 × 4.00 m	9.63 × 4.05 m

EFC current variations in the modes of operation considered. Our assessment of these forces utilizes one specific model for structural support, based on the STARFIRE design. As illustrated in Fig. 5-15, the conductor is housed in a helium container which, as in STARFIRE, is steel of thickness t_{He} = 4.0 cm. The helium vessel, at 4.2 K, is nested in a room temperature vacuum tank dewar and supported by criss-crossing struts of G-10. The thickness, t_v, of this steel vacuum tank is a variable in our study and is selected in order to provide adequate stiffness of the free span of the TFC against out-of-plane bending. The net overturning force on the TF coils is resisted by keys in the in-

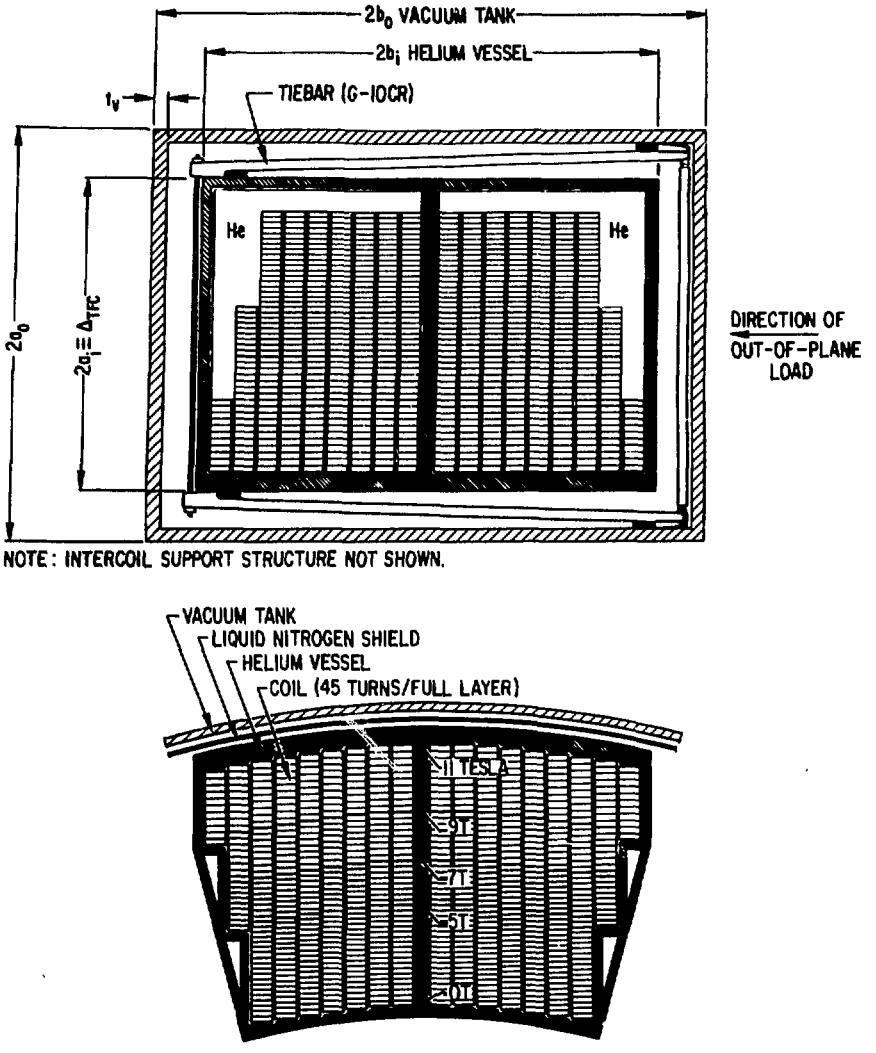

Fig. 5-15. Section through one coil in centerpost and outer regions: double swing OH cycle requires crossed tiebars, in alternating direction, to accommodate oscillating out-of-plane load.

board support cylinder and by shear panels which are wedged between the outboard legs. The straight support cylinder lies against the straight section of the inboard leg, and the shear panel is at a radius R_p which places it beyond the outboard shield. In our study the shear panel thickness is chosen such that this panel alone adequately supports the TFC against turning moments.

5.3.2 Fatigue Due to Out-of-Plane Stress

The moment of inertia for a hollow rectangular box beam was calculated for the bending analysis of the unsupported free span of the TFC. For outer dimensions 2b by 2a (see Fig. 5-15) and a wall thickness t, the moment of inertia is

$$I = \frac{4tb^3}{3} + \frac{4(a - t)}{3}\left[b^3 - (b - t)^3\right] .$$

The helium vessel (inner box) has $I_h = 0.151\ m^4$ and $0.0768\ m^4$ for the 8-m and 7-m reactors, respectively. The outer (vacuum vessel) box moment, I_v, was computed similarly, and the total moment, $I = I_h + I_v$ was used in our stress analysis. We assume that the G-10 struts can be situated such that the composite structure behaves as a rigid unit. In addition we neglect any stiffness associated with the winding pack. This treatment becomes increasingly accurate at large vacuum vessel wall thickness, t_v, where the outer box dominates the total moment of inertia. Figures 5-16 and 5-17 display I versus t_v; in this range we see roughly $I \propto t_v$.

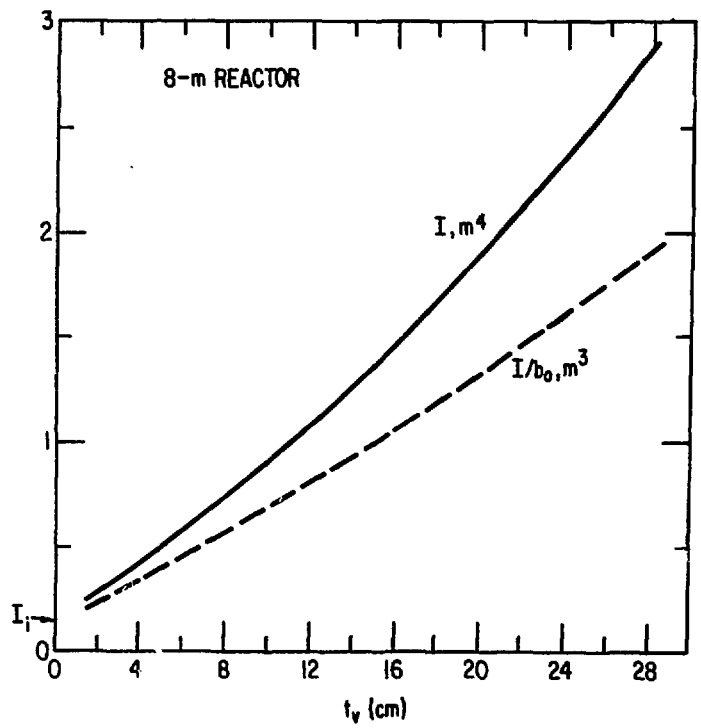

Fig. 5-16. TFC moment of inertia, 8-m reactor.

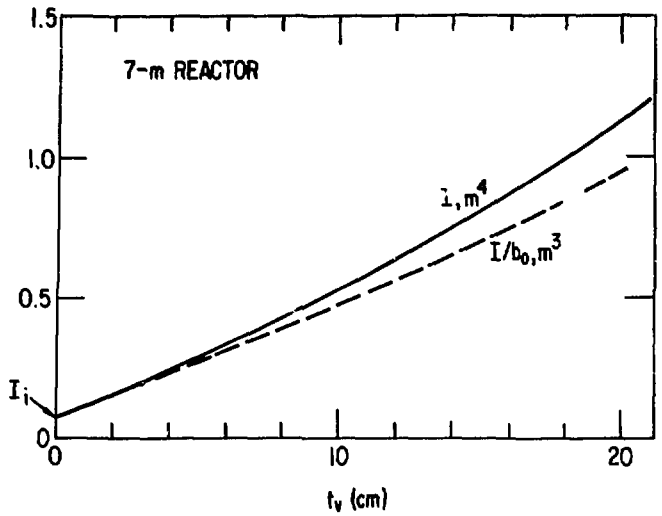

Fig. 5-17. TFC moment of inertia, 7-m reactor.

The current wave forms for the reference OHC/EFC set for the 8-m reactor are shown in Fig. 6-4 of Chap. 6 for the conventional ohmic drive burn cycle. Calculations showed the peak out-of-plane force, due to the poloidal field interaction with 18.8 MA carried in each TFC, is a maximum at the end of the burn, when the EF currents are full value and the OH currents are fully reversed. Of course, since the OHC fringing field is so low, the forces are nearly static throughout the whole period when the EFC and plasma currents are at full value, from 30 s onwards in the burn cycle in the Fig. 6-4.

The running force along the TFC perimeter is displayed in Fig. 5-18 for the 8-m reactor. As shown in Fig. 5-3, the free span runs between the support cylinder (point I) at ℓ = 3.52 m and the shear panel (point J) at ℓ = 15.40 m, a distance of 11.85 m. The forces are large, as high as 21 MN/m, but in opposing directions along this beam. We treat this free span as if it were a straight beam with moment of inertia I to calculate the bending moment, M(ℓ) along its length. M was calculated for various boundary conditions (simple supports both ends; clamped both ends; inboard clamped and outboard simply supported). Testing our code results with the finite element analysis performed for the STARFIRE design, we found good agreement if we selected simple supports for both ends of the beam, so these boundary conditions were adopted for the remainder of our study.

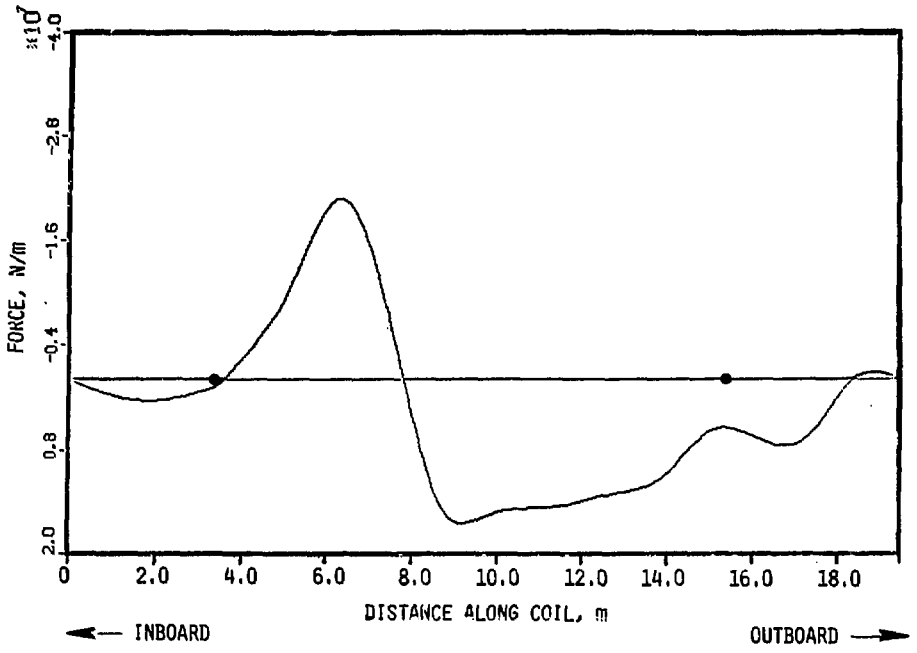

Fig. 5-18. Force of poloidal coils on toroidal coil, 8-m reactor.

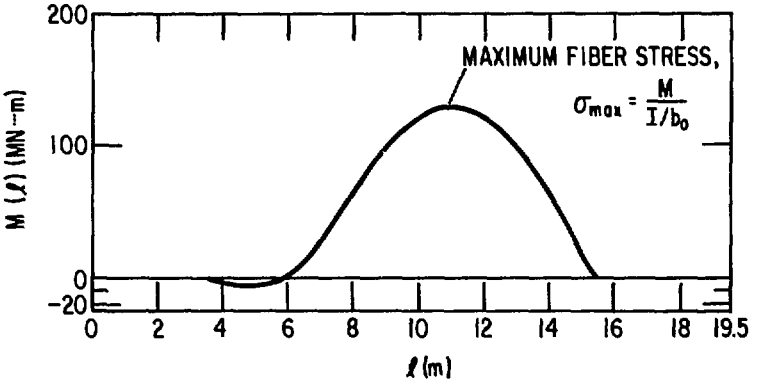

Fig. 5-19. Bending moment along TFC; 8-m reactor, $\delta_{TF/EF}$ = 1.0 m; OH burn cycle.

The bending moment is shown in Fig. 5-19; and the maximum fiber stress, σ, at a position ℓ is on the outer surface, where $\sigma = M(\ell)b_0/I$. The deflection of the beam is found by staightforward means[5] and is a function of I and Young's modulus, E. Figure 5-20 displays a typical result [t_v = 4.2 cm, I = 0.445 m^4, b_0 = 1.26 m, E = 185 GPa (316 LN at 300 K)] for which σ = 371 MPa and with a maximum deflection of 1.9 cm out of the plane.

The same calculations were done for the 7-m reactor and the reference EFC configuration (Fig. 5-4). The free span runs from the support cylinder (ℓ =

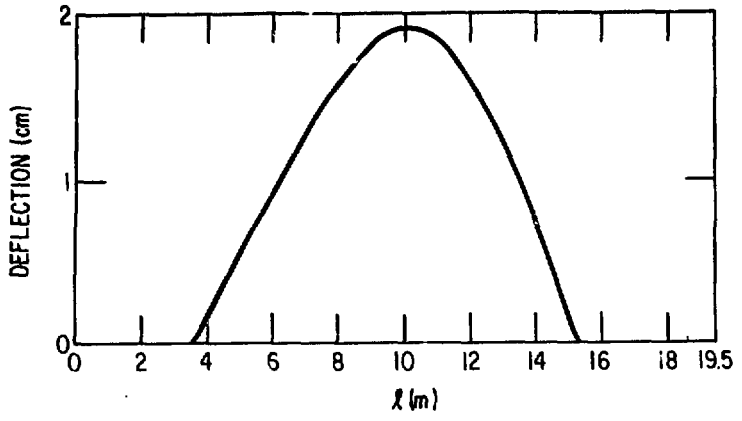

Fig. 5-20. Deflection of TFC out of plane; 8-m reactor, $\delta_{TF/EF}$ = 1.0 m; I/b_0 = 0.353 m^3.

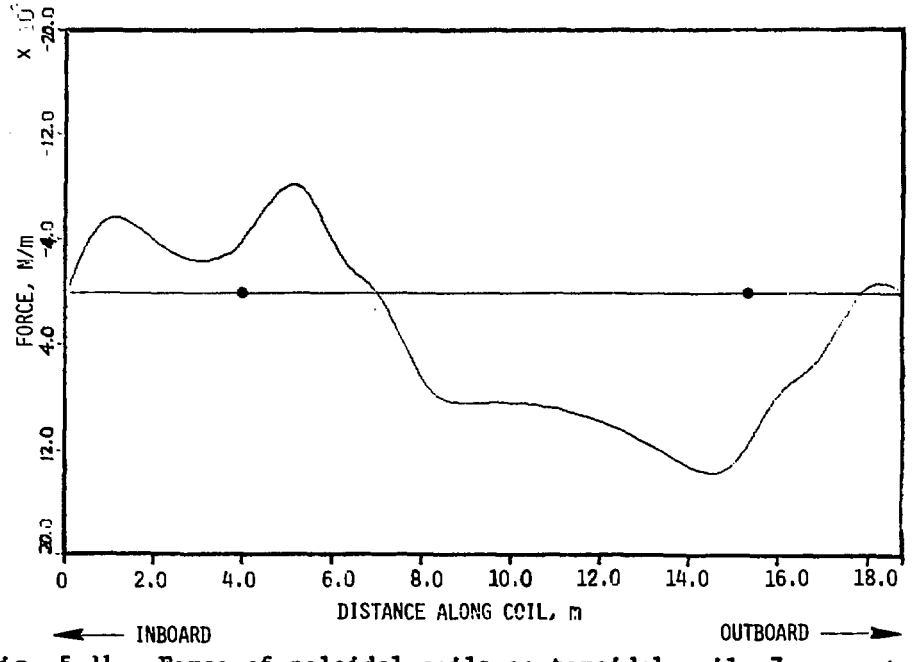

Fig. 5-21. Force of poloidal coils on toroidal coil, 7-m reactor.

4.0 m) to the shear panel (ℓ = 11.9 m), a distance of 11.39 m. Reference to Fig. 5-21 shows significant advantages of the 7-m EFC system compared to the 8-m system. The forces are lower, only reaching 14 MN/m. Also, the loading is concentrated away from the middle of the free span and more towards the support cylinder and shear panel, where the loads are most easily supported. It should be noted that the coil placements were not chosen to minimize the out-of-plane forces, but such a design philosophy could have benefits, and would likely make a comparison of the loading more meaningful.

In order to select the required thickness of the vacuum tank, t_v, to limit the fiber stress, a crack propagation analysis of the steel case was undertaken. Standard fracture mechanics[6] methods were used to predict the crack width, a, as a function of the number of stress cycles, N. The Paris Law, $da/dN = C_0(\Delta K)^n$, was integrated for an initial crack a_0 using the room temperature properties of Type 316 LN, annealed stainless steel (a typical structural material for the TFC vacuum tanks): $C_0 = 4.41 \times 10^{-10}$, $n = 2.7$, and fracture toughness $K_{IC} = 250$ ksi$\sqrt{\text{in}}$. These constants are used in the Paris Law with a expressed in inches. The variable stress intensity is proportional to the maximum stress during the cycle and to the square root of the crack size:

$$\Delta K = 1.2\ f\ \sigma_M \sqrt{\pi a}\ .$$

The factor f depends on how the stress variation compares to the maximum stress. For example, fully cyclic stress, from $+\sigma_M$ (tension) to an equal but opposite stress, $-\sigma_M$ (compression), is more damaging than cycling between σ_M and zero stress. We use the damage model which characterizes most metals,[7] $f = (1 - \mathcal{R})^{0.6}$, with $\mathcal{R} \equiv \sigma_m/\sigma_M$, σ_m being the minimum stress. Figure 5-22 displays the maximum permissible stress for a given number of cycles to failure for various initial cracks, assuming safety factors of two on stress and four on cycles.

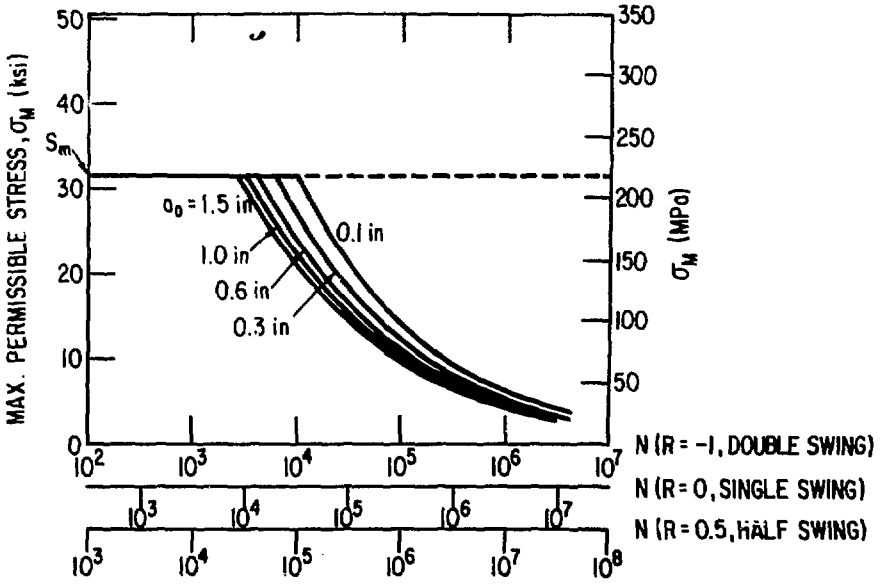

Fig. 5-22. Fracture mechanics limited stress, Type 316 LN (annealed) at 293°K.

Several comments should be made regarding Fig. 5-22. We find that for typical a_0 tens of thousands of cycles to failure occur for $\sigma_M \approx 200$ MPa. Generally, higher σ_M is permissible if a smaller number of cycles is specified. However, in any event the stress should not exceed S_m (the lesser of two-thirds the yield stress or one-third the ultimate stress), which is 217 MPa for this steel. Thus, there are no significant reductions in structural requirements for the TFC once the total number of vertical field cycles is reduced below about ten thousand.

The stress variations are quite different among the tokamak burn cycles we consider. For the hybrid and internal transformer modes the plasma current, I_0, is always maintained near full value, but beta poloidal, β_p, varies from full value to zero as the noninductive driver is in operation, due, for example, to density oscillations. The vertical field due to the EFC is roughly given by

$$B_v^0 = 1 \times 10^{-7} \frac{I_0}{R_0} \left[\ell n(8A) + \beta_p + (\ell_i - 3)/2 \right] .$$

For typical values of internal inductance and with β_p varying between ~1.8 and zero we find B_v^0 varies roughly from full to half value during hybrid or internal transformer operation. This cyclic stress on the TFC is represented by $\mathscr{R} = 0.5$ and is shown on the bottom-most abscissa of Fig. 5-22. Note that each stress period corresponds to one fusion burn period. The conventional ohmic burn cycle has I_0 varying from full to zero each fusion period. If the OHC is reset to the same polarity before each burn, then the toroidal current direction is always in the same sense and the out-of-plane force from the EFC is always in one direction. In this single full swing case $\mathscr{R} = 0$, and the figure shows, from the middle abscissa, that fewer cycles to failure can be tolerated under these conditions compared to the half swing. The worst situation obtains if B_v^0 swings both directions, reversing toroidal current and OHC polarity on alternating fusion periods. Then $\mathscr{R} = -1$, and even fewer stress cycles are tolerable than for single swing operation of the EFC. Note, however, in this mode two fusion burn periods occur for each mechanical stress period.

Considerable controversy exists over what initial crack sizes should be considered for failure analysis. Conservatism dictates the choice of relatively large a_0, since inspection of the fabricated steel structure becomes

expensive and unreliable for small flaws. Moreoever, the failure to detect an initial crack could have serious consequences; even though TFC monitoring is advisable, periodic remote inspection will prove challenging, and replacement of a weakened TFC with a growing crack may prove impractical. On the other hand, inspection techniques may not differentiate between harmless stress risers of dimensions a_0 (for example, bubbles) and true cracks. In this case fracture mechanics could severely underestimate the cycle lifetime of the steel structure. With these caveats in mind we have proceeded to use fracture mechanics with initial crack lengths assumed to be one-tenth the thickness of the vacuum tank, $a_0 = 0.1\ t_v$. (Additional limitations of our model are evident if alternative vacuum tank construction techniques are considered. For example, the dewar could be formed with several laminations of steel plate, preventing through cracking and gross failure. Certain nonmetallic composites could be considered for the structure; these materials might be fabricated such that cracks propagate preferentially along the TFC leg rather than normal to it).

The fusion cycle lifetime, N_f, was inferred from the maximum bending moments of both the 8-m TFC (M_{max} = 130.9 MN-m) and the 7-m TFC (M_{max} = 103.1 Mn-m). The 8-m TFC is the basis for both the double swing ($\mathscr{R} = -1$) and single swing ($\mathscr{R} = 0$) ohmic cycle as well as for the hybrid burn cycle ($\mathscr{R} = 0.5$). The 7-m TFC is used to model the CW burn cycle ($\mathscr{R} = 0$) as well as the internal transformer mode ($\mathscr{R} = 0.5$). The dewar thickness, t_v, was computed versus N_f, and the volume of steel, on the order of hundreds of cubic meters, was determined.

The cost of the vacuum tank, based on \$20/kg (the estimated cost [8] in 1980 dollars) is shown in Fig. 5-23. As expected, the cost is level up to $N_f \sim 10^4$. Hence, a reactor with a day-long burn ($t_f \sim 10^5$ s) has a vacuum tank no more expensive than that of a CW reactor ($N_f \sim 200$, $t_f \sim 3$ months). However, shorter burns accumulate fatigue damage very quickly. For short burns ($t_f \sim$ 1000 s, $N_f \sim 10^6$) the incremental structural costs become prohibitive. We caution, though, that our cost estimates may be too high at large N_f, for the following reasons. At tank costs of \$100 M to \$200 M the steel side walls (Fig. 5-15) are in the range of 20-cm to 30-cm thickness. It may prove impractical to form such large, thick members. The prohibitive costs at this point would drive us to consider alternative structural support. For example, an

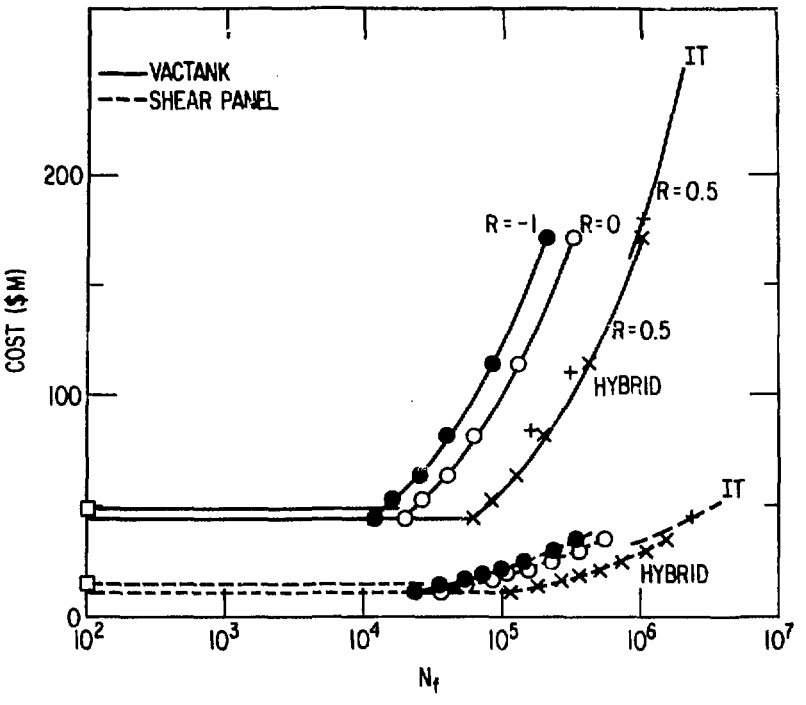

Fig. 5-23. Structure cost for TFC vacuum cases and shear panels.

intercoil support structure[9] could be used in order to drastically shorten the unsupported free spans of the TFC, perhaps reducing costs by large amounts. So we must conclude that the particular model (patterned after STARFIRE) used in our present study may become inappropriate for TFC structure experiencing millions of cycles over its lifetime.

We note that there are large differences among the burn cycles for a fixed N_f. The double-swing ohmic cycle ($\mathscr{R} = -1$) has the largest stress fluctuations and hence requires the most massive structural support. For the same N_f, a single swing ohmic cycle ($\mathscr{R} = 0$) results in cost savings. Even more attractive is the hybrid burn cycle, since the stress fluctuation is so modest ($\mathscr{R} = 0.5$). For internal transformer operation the relatively small stress fluctuations ($\mathscr{R} = 0.5$) are overshadowed by the much larger number of pulses envisioned for the life of the reactor ($N_f > 10^6$), with the net result that this cycle is likely to be the least attractive in terms of TFC structural costs.

Two additional concerns remain with the STARFIRE-type vacuum tank. First, welded joints may be more prone to fatigue damage than the flat steel sheets. More study would be needed to quantify this problem; however, local reinforce-

ment along the welds might compensate for the poorer structural properties of the weld. Due to the small amount of reinforcement which would be required, this is unlikely to affect the TFC cost significantly. A second concern centers on the fatigue resistance of the G-10 struts which center the helium vessel within the vacuum tank. There is presently a very limited fatigue data base characterizing this material, and an assessment of its life expectancy is not possible. We note, however, there may be alternative materials (steel, titanium) which could be used for those struts in the TFC where the local forces are largest. The main penalty in this case would be a slight increase in the heat flow from the room temperature tank to the helium vessel (if the alternate materials are only used for a small number of the struts).

The next support structure considered is the shear panel, which resists the net torque on the TFC. Previous studies have shown that this panel supports most of the torque, and in our calculations we will neglect the small contribution from the central support cylinder. The forces on the shear panel are nearly coplanar, so we neglect bending. The outer TFC legs and carry-through[8] are assumed to be in non-slip contact with the panels. For a permissible shear stress, τ, a rectangle of width w requires a thickness[5]

$$t_s = FP_1/w\tau ,$$

where P_1 is the total force along the upper leg of the TFC from the support cylinder out to the midplane. For the 8-m and 7-m reactors P_1 is 62.08 MN and 79.81 MN, respectively. We set the safety factor, F, to be 2 to allow for stress risers at penetrations, along the edge at the keys and pins, etc. The panel is deflected out of vertical by $d \approx h\tau/G$, where for Type 316 LN stainless, the modulus of rigidity is G = 74.57 GPa. h is the panel height.

As with the vacuum tank, a fracture mechanics life analysis was performed. For a given stress τ the panel thickness is calculated, and the fusion cycle lifetime is inferred from Fig. 5-22, assuming an initial crack $a_0 = 0.1\ t_s$. Although S_m = 217 MPa, we limited the maximum stress to 155 MPa since higher values result in deflections exceeding 2.0 cm. The cost of the shear panels, based on \$16/kg, was found for various burn cycles, and this is also shown in Fig. 5-23. The cost trends exactly parallel those for the vacuum tank, but their magnitude is considerably smaller.

As we have found, the TFC support structure cost is a strong function of the number and type of fusion burn cycles. To place this cost component in the context of the total TFC cost, we have estimated the fixed costs for the 8-m and 7-m reactor TFC systems. The helium vessel is costed at $26/kg, which results in a $29.4 M and $24.2 M expense for the 8-m and 7-m reactors. The conductor winding pack, including fabrication and winding, was estimated to cost $28/kg, $99/kg, $196/kg, and $14/kg, respectively, for copper, niobium-titanium, Nb_3Sn, and stainless steel. Based on the material quantities (Table 5-6) this results in a cost of $120.0 M for the 8-m reactor and $89.9 M for the 7-m reactor.

The total cost of the TFC for various cycle options is shown in Fig. 5-24. We see that a single swing OH cycle operating with a one-hour burn will entail capital costs at least $100 M higher than a reactor operating in the CW mode. This disparity is greatly reduced if the ohmic burn period could be extended to 8 h or more. If neither of these options is available, but low-density current drive permits operation with a hybrid burn cycle, then any fusion cycle period

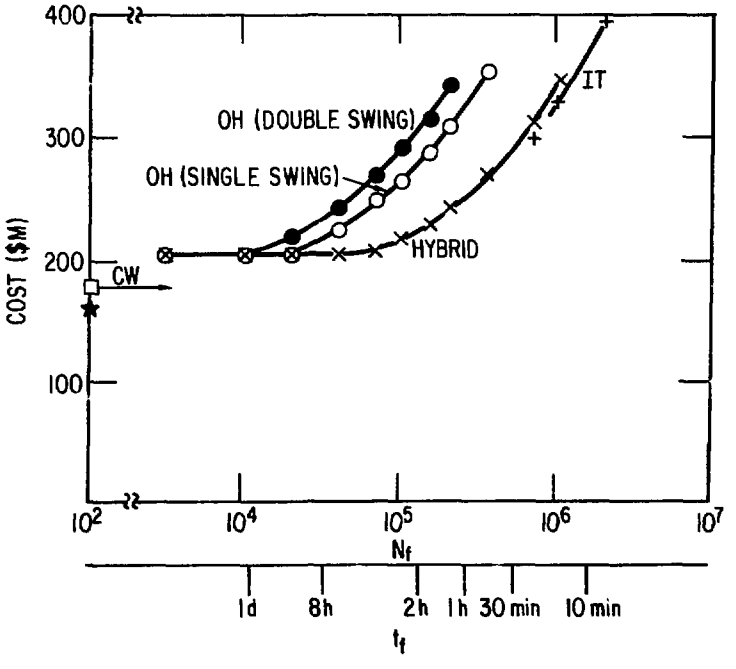

Fig. 5-24. Capital cost of TFC: conductor, steel in winding, helium vessel, vacuum tanks, and shear panels — STARFIRE design concept; Type 316 LN (annealed); initial crack assumed at one-tenth of structural thickness; $1980, per Chap. 22 of ANL/FPP-80-1 (Ref. 8).

exceeding about 30 min becomes competitive. In any event, the internal transformer cycle is unattractive since it has such a tremendously large total number of cycles in the reactor lifetime ($N_f \gtrsim 10^6$). A completely different design philosophy would be required, e.g. inter-coil support structure,[9] to accommodate coil fatigue in such a case.

5.3.3 Eddy Current Heating

Time varying magnetic fields generate heat in superconducting magnets, and we must address this problem for the TFC system. In the winding pack this heat generation has been calculated for past tokamak design studies,[9] and the result is that this contribution is, invariably, very small. Thus we concentrate on eddy current heating of the cryogenic, 4-cm thick, steel helium vessel encasing the winding. (Our model for TFC support assumes the helium vessel is insulated thermally by the G10 struts from the out-of-plane support structure. If an alternative design approach, such as for FED, with cryogenic intercoil supports, were selected, additional eddy heating locations might be introduced.) Moreover, we calculate the heating due to only $\dot{B}_\perp$, the time varying poloidal field component normal to the TFC surface, since this dominates the heat generation due to $\dot{B}_\parallel$.

Following Kalsi's evaluation method,[10] we find that the heating per length along the TFC helium vessel is $dP/d\ell = I_h(\dot{B}_\perp)^2/\rho$, where I_h is the out-of-plane bending moment of inertia for the rectangular helium vessel, and where ρ is the case resistivity (56×10^{-8} Ω-m for Type 316 LN at 4.2 K). The EFC cycle is idealized with a linear ramp at the start and end of the fusion burn, $\dot{B}_\perp = B_{\perp max}/\Delta t_{EF}$, and the heat is constantly removed during a full burn period of $t_f + 2\Delta t_{EF} + 2\Delta t_{OH} + t_{dw}$. (See Chap. 6 for definitions of these terms.) $B_{\perp max}$ was found numerically and the time-averaged power was calculated by

$$\bar{P} = \frac{(2I_i/\rho)\oint B^2_{\perp max} \times N_{TFC}}{\Delta t_{EF}(t_f + 2\Delta t_{EF} + 2\Delta t_{OH} + t_{dw})} .$$

There are three situations which tend to aggravate this heat production. First, any increase in the amount of cryrogenic material, such as increases in the thickness of the helium vessel wall, will tend to increase I_h, and $\bar{P}$

proportionally. More importantly, fast ramps of the vertical field increase the heating, since $\bar{P} \propto \Delta t_{EF}^{-1}$. Finally, shorter fusion cycles tend to increase $\bar{P}$, since there is less time to remove heat generated during the EFC ramps.

Table 5-7 shows $\bar{P}$ for several combinations of Δt_{EF} and fusion burn periods, t_f. The total heat generation is taken roughly to be $\bar{P}_{TOT} = 1.2 \times \bar{P} + 0.1$ kW. The factor 1.2 accounts for $\hat{B}_\parallel$ effects and losses within the coil windings, and the constant, 0.1 kW, is roughly the nuclear heating expected.

TABLE 5-7

Eddy Current Heating in TFC

$(\tau \equiv t_f + 2\ t_{EF} + 2\ t_{OH} + t_{dw})$

Reactor	t_f	t_{dw}	t_{EF}	t_{OH}	τ	$\bar{P}^{kw}$	$\bar{P}^{kw}_{tot}$	$\bar{P}^{MW}_{300^0K}$	C^{FED} ($M)
				Vary t_f					
8-m (OH, hybrid)	3600	30	30	0	3690	0.686	0.923	0.323	0.786
	3600	30	10	10	3670	2.069	2.583	0.904	1.68
	1800	30	10	10	1870	4.061	4.97	1.74	2.74
	900	30	10	10	970	7.83	9.49	3.32	4.42
	7200	30	10	10	7270	1.04	1.35	0.473	1.04
	14400	30	10	10	14470	0.525	0.730	0.255	0.659
7-m (IT)	600	10	10	0	630	3.971	4.87	1.70	2.69
	3600	30	30	0	3690	0.776	0.371	0.130	0.40
	200	10	10	0	230	10.88	13.15	4.60	5.62
	60	10	10	0	90	27.8	33.5	11.7	11.2
				Vary t_{EF}					
8-m (OH, hybrid)	3600	30	20	10	3690	1.03	1.33	0.467	1.03
	3600	30	15	10	3680	1.38	1.75	0.613	1.26
	3600	30	10	10	3670	2.069	2.583	0.904	1.68
	3600	30	5	10	3660	4.15	5.08	1.78	2.78
7-m (IT)	200	0	40	0	280	2.23	2.78	0.973	1.78
	200	0	20	0	240	5.21	6.36	2.22	3.28
	200	0	10	0	220	11.4	13.7	4.81	5.81
	200	0	5	0	210	23.8	28.7	10.04	10.03

The room temperature refrigerator power is $\bar{P}_{300K} = 350\ \bar{P}_{tot}$, and we find this electrical power is almost always negligible in the plant's power balance. The capital cost for the cryogenic refrigeration, in 1981 dollars, is taken as[9]

$$C^{FED}\Big|_{\$} = 10{,}860 \times \left(\bar{P}_{300K}\Big|_{kW}\right)^{0.741} .$$

Again, we find these capital costs are quite small compared to the overall power plant cost. Thus we conclude that burn cycle alternatives, while they affect circulating power and capital costs, have a relatively small effect on the power plant in general.

REFERENCES FOR CHAPTER 5

1. K. EVANS, JR., et al., "WILDCAT: A Catalyzed D-D Tokamak Reactor," ANL/FPP/TM-138, Argonne National Laboratory (1981).

2. K. EVANS, JR., D. A. EHST, and P. MESSERSCHMIDT, "Equilibrium Field Coil Considerations for Tokamak Reactors," Proc. 3rd ANS Top. Mtg. on The Technology of Controlled Nuclear Fusion, CONF-780508, Vol. II, p. 1084 (1978)

3. L. TURNER and M. ABDOU, "Computational Model for Superconducting Tokamak TF Magnets," ANL/FPP/TM-88, Argonne National Laboratory (1977).

4. R. W. MOSES, JR. and W. C. YOUNG, "Analytic Expressions for Magnetic Forces on Sectored Toroidal Coils," Proc. 6th Symp. on Engineering Problems in Fusion Research, IEEE Pub. No. 75CH1097-5-NPS, p. 917 (1981).

5. J. R. ROARK and W. C. YOUNG, Formulas for Stress and Strain, (McGraw-Hill, New York, 1975).

6. R. J. HOOPER and B. L. HUNTER, "Structural Design Procedures for FED Magnets," Proc. 9th Symp. on Engineering Problems in Fusion Research, IEEE Pub. No. 81CH1715-2-NPS, Vol. I, p. 539 (1981).

7. R. MATTAS, "Fusion Lifetime Analysis," ANL/FPP/TM-160, Argonne National Laboratory (1982).

8. C. C. BAKER et al., "STARFIRE, A Commercial Tokamak Power Plant Study," ANL/FPP-80-1, Argonne National Laboratory (1980).

9. C. A. FLANAGAN, et al., "Fusion Engineering Device Design Description," ORNL/TM-7948, Oak Ridge Natonal Laboratory (1981).

10. S. S. KALSI and R. J. HOOPER, "Calculation of Eddy Current Losses in Toroidal Field Coil Casing," Proc. 9th Symp. on Engineering Problems in Fusion Research, IEEE Pub. No. 81CH1715-2-NPS, Vol. I, p. 131 (1981).

Chapter 6. POWER SUPPLY COST, BURN CYCLE EFFECTS

6.1 Burn Cycle and Energy Transfer System

In this chapter burn cycle parameters and the requirements and cost of the energy transfer system are analyzed. The energy transfer system (ETS) consists of the ohmic heating (OH) and equilibrium field (EF) power supplies, and the thermal storage system. A steady-state tokamak reactor does not need thermal storage. Power supply requirements are minimal since startup can be accomplished in a long time, e.g. ~30 min in the case of the STARFIRE conceptual design. In contrast, pulsed tokamaks will have large power supply requirements due to the need to transfer large amounts of energy (~10 GJ) in short times (~10 s). A thermal storage system is needed for pulsed reactors (see Chap. 4) to maintain turbine power and blanket temperatures between burn pulses. These systems are expensive and therefore constitute a key difference between pulsed and steady-state tokamak reactors.

Energy transfer system requirements, and burn cycle parameters, were analyzed for three types of pulsed cycles discussed in Chap. 2: conventional, hybrid, and internal transformer. The 8-m reference reactor design was used in the analysis. The cycles were further subdivided into those having a water coolant or a liquid metal coolant. As discussed in Chap. 4, the liquid metal coolant results in a cheaper thermal storage system.

The key burn cycle parameters, from the standpoint of stress problems, and overall economics, are the length of the burn cycle and the net power produced, and these are compared for the various cycles.

The following general trends were noted in this analysis. For all operating cycles, the energy transfer system costs are highly dependent on cycle parameters — it is important to choose these parameters carefully to minimize cost. The large value of EF stored energy (~6 GJ) precludes the use of very fast startup times, in all cases. No cycle is as good as steady state. For a water-cooled conventional cycle, the cost of the ETS is ~450 M$. A liquid-metal based system is cheaper by ~150 M$. The ETS cost for a hybrid cycle is less than for a conventional one. In addition, the hybrid cycle eliminates the plasma breakdown period and may reduce the number of plasma disruptions.

Although these are not fundamental differences, the hybrid cycle appears to be promising and warrants further study. In contrast, the internal transformer cycle appears to be a poor choice of operating mode due to a combination of short burn time and high ETS cost.

6.2 Conventional Cycle

The burn cycle and the energy transfer system of the reference 8-m reactor were analyzed for a conventional cycle, i.e. one using an OH coil to supply volt-seconds for startup and burn. The analysis used the CTRAN, profile-averaged, time-dependent code[1] to develop the general features of the burn cycle. Based on these results, a simpler parametric model was used for a trade-off study of cost versus cycle parameters. The analysis also made use of results found in an earlier study of power supply requirements for commercial fusion reactors.[2]

A power supply system developed for the conventional cycle is shown in Fig. 6-1. A typical burn cycle using this system is shown in Figs. 6-2 through 6-4. The power supply system, and the burn cycle operation, were chosen to minimize power supply requirements. The emphasis of the analysis is on the startup period since it was found[2] that shutdown imposes no additional requirements except if skin current formation in the then hot plasma proves to be a problem, a subject that remains to be resolved.

As shown in Fig. 6-1 the OH coil is driven by two types of energy transfer devices. (The OH current, over a complete burn cycle, is shown in Fig. 6-2.) A dump resistor is used for startup to ramp down the initially charged OH coil in a time defined as the "ohmic heating time", t_{OH}. For the cycle shown, t_{OH} = 15 s. This resistor could probably be of the nonlinear type, e.g. zinc oxide, or silicon carbide as proposed for the TFTR-OH system.[3] The cost of the resistor (or resistor bank) itself is trivial; all of the cost is essentially in the switch used to connect the resistor to the OH coil. A solid-state switch based on thyristor (SCR) circuitry is probably needed to insure reliability over the tens of thousands of operating cycles. The switch cost, to be discussed later, is still less than any alternative power supply. The resistor was modeled as having an ideal, i.e. constant, voltage drop, when connected. The same resistor is also used for the shutdown. The OH current

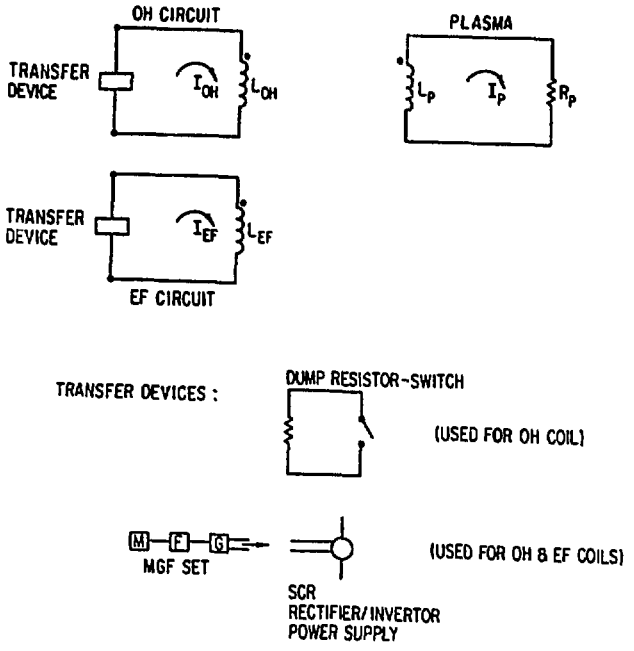

Fig. 6-1. Power supply system for a conventional cycle.

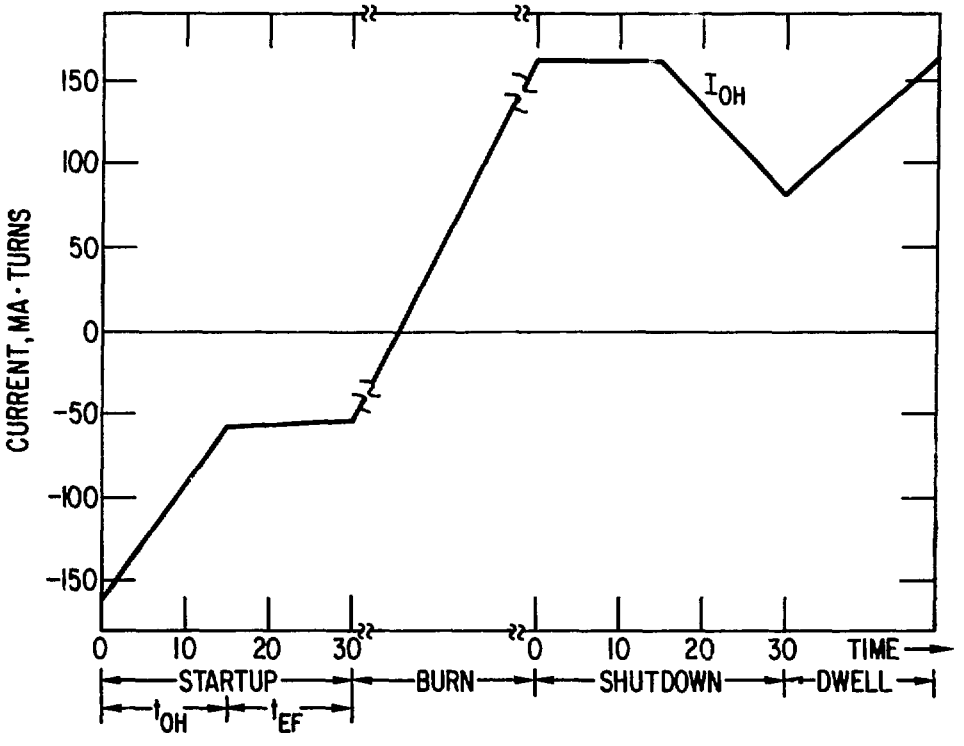

Fig. 6-2. Ohmic heating coil current waveform for a conventional burn cycle.

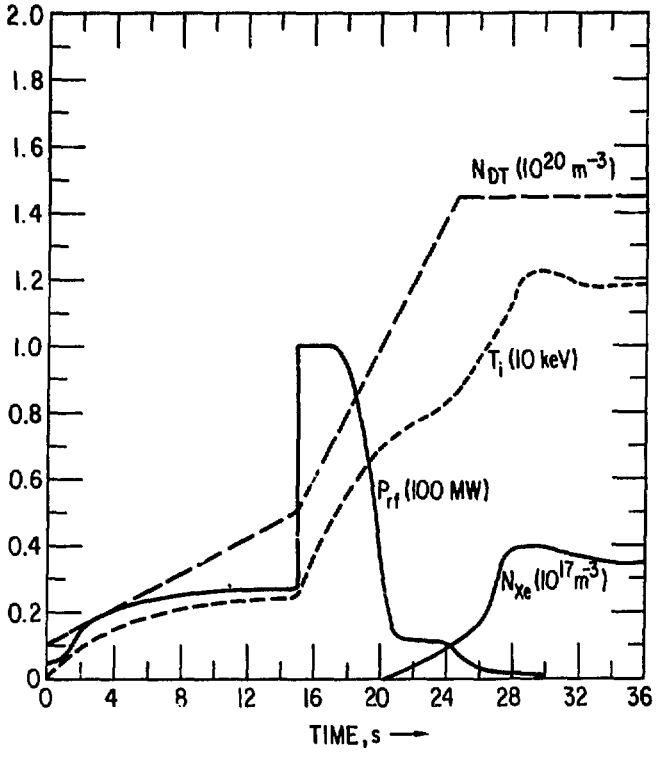

Fig. 6-3. Plasma parameters during startup of conventional cycle.

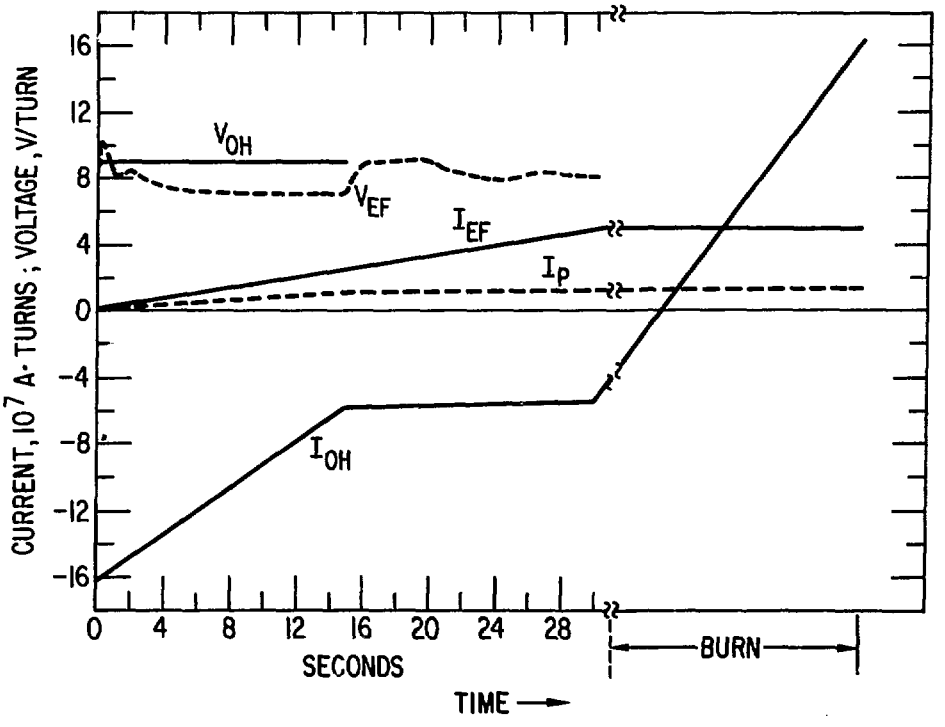

Fig. 6-4. Voltage and current waveforms during startup and burn of conventional cycle.

waveform during shutdown is almost the reverse of the startup except that somewhat less ramp down of I_{OH} is needed. During the burn period the OH current is slowly ramped up to make up for resistive losses in the plasma. The power needed to do this is relatively small, ~15 MVA. Finally, after shutdown, the OH coil must be recocked to the full 10-T value for the next burn pulse. This is done in a "dwell period" with duration t_{DWELL}. During the dwell period the plasma chamber is evacuated and then filled with fresh deuterium-tritium gas for the next burn pulse. The recocking OH power supply is a rectifier/invertor SCR-type supply operating out of an MGF set. The OH coil, for the reference reactor design, has a stored energy content of ~19 GJ at 10-T field. The cheapest way to recock the coil is alternate the direction of induced plasma current every pulse. Thus, in the example shown, I_{OH} is driven from ~80 MA turns to 163 MA turns in the dwell period rather than from ~80 MA turns to -163 MA turns if this strategy were not employed. We note that this alternating current mode aggravates the toroidal magnet fatigue, as discussed in Chap. 5; thus, the power supply cost saving might be offset by the possible need for a more expensive TFC system. Another cost savings technique is to use the same OH recocking SCR supply to drive the EF coil during startup and shutdown and the OH coil during the burn phase. This useage requires that the OH and EF coils have compatible voltage and current requirements. It appears possible to configure the coil windings to do this. The SCR power supply requirements are then set by whatever system, EF or OH, has the maximum power needs.

A low density startup, together with initial rf heating, is used in the cycle shown to minimize resistive volt-second losses. Thus the plasma is kept fairly hot throughout the "ohmic heating" portion of the cycle. For the cycle shown, the resistive volt-second loss during startup is only 5 V-s.

The second phase of the startup is defined as the "EF ramp". During this period the plasma is heated to ignition and the EF current brought to its full value. Throughout the startup the EF current is raised to maintain the plasma in MHD equilibrium. The EF power requirement is given by the product of the maximum EF voltage and the maximum current. In order to minimize the EF voltage during startup, the rf power and hence the heating rate is carefully modulated. The control algorithm used was designed to maintain a fixed rate of net heating power during different portions of the cycle as follows:

$$P_{net} = \begin{cases} 3\ \text{MW}, & t \leq 1\ \text{s} \\ 5\ \text{MW}, & 1 \leq t \leq 15\ \text{s} \\ 67\ \text{MW}, & 15 \leq t \leq 30\ \text{s} \end{cases}, \tag{6-1}$$

where

$$P_{net} = P_{rf} + P_{\alpha} - P_R - P_{TR}\ , \tag{6-2}$$

and P_{rf} is the rf heating power, P_{α} is the alpha-heating power from fusion, P_R is the radiated power, and P_{TR} is the transport loss power. The rf power was varied according to Eqs. (6-1) and (6-2). In addition, xenon was added towards the end of the startup to establish plasma thermal stability. As shown in Fig. 6-4 this rf control algorithm is fairly successful in maintaining a constant EF voltage during startup and is probably typical of the control stategies to be employed. In view of the conceptual nature of this study, it is assumed that a more refined control method could result in a nearly constant value of V_{EF}, and this was assumed for costing purposes.

For the cycle shown, a burn time of ~51 min could be obtained, based on the OH flux swing of 307 V-s available for the burn period and on a plasma loop voltage of ~0.10 V. This loop voltage is based on neoclassical Spitzer resistivity, using an anomaly factor of 2.5 to account for trapped electrons.

Another parameter of interest in comparing burn cycles is the rf power needed for heating to ignition. A feasible steady-state reactor requires on the order of 100 MW input into the plasma for current drive (i.e. much more than this would not be economically feasible). A pulsed reactor requires no current drive power but still needs auxiliary power to reach ignition. In a steady-state reactor the same rf system could hopefully be used for both purposes, i.e. heating and current drive. A study was made, using the CTRAN code, to identify the minimum rf power needed to reach ignition. For the reference reactor this value was found to be ~75 MW. Thus the rf heating power needed for ignition is similar to that needed for current drive, for feasible values of current drive efficiency.

Of course, the power required for current drive is a central issue for the feasibility of steady-state tokamaks. In comparing pulsed to steady-state tokamaks, a heating-only rf system might be cheaper due to relaxed antenna, frequency, and other requirements. However, for the present purposes only differences in the ETS cost were assessed.

6.3 Parametric Analysis

A trade-off study of energy transfer system cost versus burn cycle parameters was performed for a conventional cycle, based on the 8-m reference reactor design. The burn cycle parameters were the OH ramp time, t_{OH}, the EF ramp time, t_{EF}, and the dwell time, t_{DWELL}, as defined in the previous section. The power supply requirements were modeled as follows:

$$P_{OH} = \frac{\Delta\phi_{OH} \times I_{OH}^{max}}{t_{OH}} \tag{6-3}$$

$$P_{OH}^{*} = \frac{0.75\ \Delta\phi_{OH} \times I_{OH}^{max}}{t_{DWELL}} \tag{6-4}$$

$$P_{EF}^{(1)} = \frac{1/2\ U_{EF}}{t_{OH}} \tag{6-5}$$

$$P_{EF}^{(2)} = \frac{U_{EF}}{t_{EF}} \tag{6-6}$$

$$P_{EF} = \begin{cases} P_{EF}^{(2)}, & t_{EF} < t_{OH} \\ P_{EF}^{(1)} + P_{EF}^{(2)}, & t_{EF} \geq t_{OH} \end{cases} \tag{6-7}$$

$$P_{max} = \max\left(P_{OH}^{*}, P_{EF}\right), \tag{6-8}$$

where P_{OH} is the reactive power isolation requirement of the dump resistor/switch, P_{OH}^{*} is the OH recocking requirement, P_{EF} is the EF reactive power requirement, and P_{max} is the reactive power requirement of the SCR supply used for both OH recocking and EF drive. P_{max} is also the requirement of the generator portion of the MGF set. The other parameters are $I_{OH}^{max} = 163 \times 10^{6}$ A, $\Delta\phi_{OH} = 163$ V-s, and $U_{EF} = 6.36$ GJ. The stored energy requirement of the MGF set is approximately constant, at ~30 GJ. Finally, the thermal storage system time requirement is given by:

$$t_{down} = 2\,t_{OH} + t_{EF} + t_{DWELL}\,. \tag{6-9}$$

This "downtime" is approximately equal to the time over one burn cycle when no fusion power is produced, considering the fact that there is some fusion power during the EF ramp-up and ramp-down periods.

The cost algorithms used for the power supplies were obtained by multiplying those used in Ref. 2 by a factor of 2 to approximately escalate them to 1983 dollars. (The original cost estimates were based, in part, on the TFTR experience.) The resulting cost algorithms are as follows:

$$C_{OH} = \$0.016 \times P_{OH} \tag{6-10}$$

$$C_{max} = \$0.1 \times P_{max} + 70\ M\$\ , \tag{6-11}$$

where C_{OH} is the cost of the dump resistor/switch and C_{max} is the combined cost of the SCR supply and the MGF set. The thermal storage system cost is given by:

$$C_{ST} = \begin{cases} 70\ M\$ + 3.70\ M\$\ (t_{down} - 10), & H_2O \text{ system} \\ 30\ M\$ + 2.0\ M\$ \times (t_{down} - 10), & \text{lithium-sodium system,} \end{cases} \tag{6-12}$$

where a minimum downtime of 10 s is used in either case. The total energy transfer system cost is then:

$$C_{ETS} = C_{OH} + C_{max} + C_{ST}\,. \tag{6-13}$$

A range of cycle parameters varying from 5 to 50 s was examined. It was found that a choice of $t_{OH} = t_{EF}$ is about optimum for a fixed value of t_{DWELL}. The resulting ETS cost for this parameterization is shown in Fig. 6-5 for the H_2O system and in Fig. 6-6 for the lithium-sodium system. The results show an interesting tradeoff between the power supplies and the thermal storage system. At short dwell times, $\lesssim$10 s, the recocking supply requirements become very high and dominate the cost. At longer times the increase in thermal storage costs offsets any savings in the power supply. For a given value of t_{OH} there is a broad minimum in cost for a 20- to 30-s dwell time. The total cost for the H_2O system is minimized at $t_{OH} = 5$ s; however, other considerations such as required heating power and control, and density ramp speed limitations may come into play at this relatively short time.

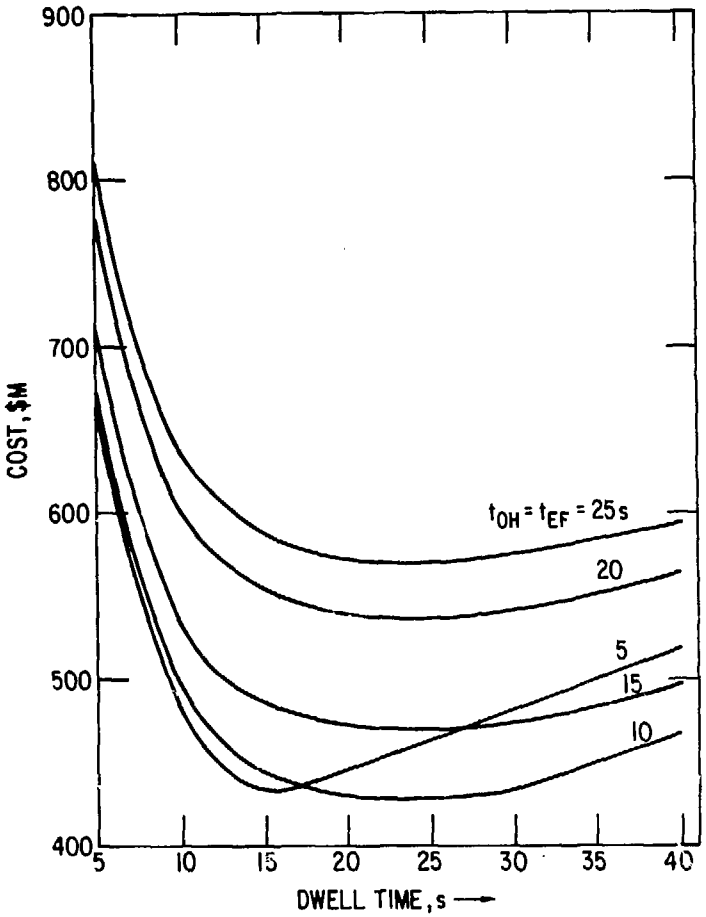

Fig. 6-5. Energy transfer system cost for a conventional cycle as a function of cycle parameters for a water thermal storage system.

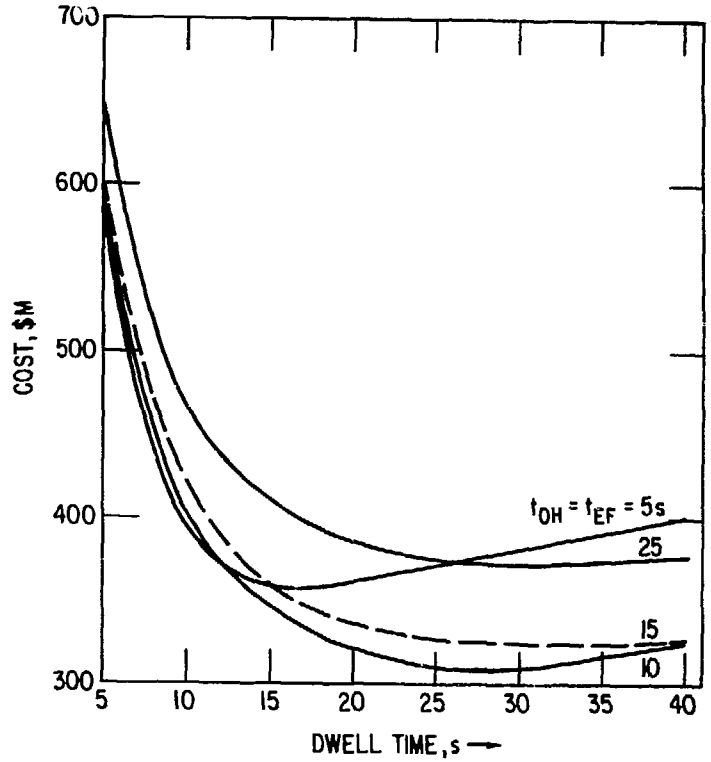

Fig. 6-6. Energy transfer system cost for a conventional cycle as a function of cycle parameters for a liquid metal thermal storage system.

For the typical values of $t_{OH} = t_{EF} = 15$ s and $t_{DWELL} = 30$ s the ETS cost is 475 M$ for the H_2O system. Thus the ETS cost is a substantial fraction of the total capital cost. A liquid-metal-based system costs about 325 M$, a savings of 150 M$ over the water system.

6.4 Hybrid Cycle

As discussed in Chap. 2 the hybrid cycle uses an OH coil to maintain plasma current during the burn, and a current drive system to maintain current during a period of time when the OH coil is recocked. The plasma density is reduced for the recocking period so that the current drive can function efficiently. After recocking, the density is ramped up and fusion power production resumes. Similar types of power supplies are needed for the hybrid cycle as the conventional system except that an OH dump resistor is not needed. The equivalent circuit of a system used for the hybrid cycle is shown in Fig. 6-7.

As with the conventional system the same SCR supply can be used for both OH and EF coils since these coils are pulsed at different times. The current drive source, assumed to be rf, is shown as an equivalent current source in the plasma loop. From Fig. 6-7 the equations for the OH and plasma loop are given by:

$$L_{OH}\frac{dI_{OH}}{dt} - M_{OH,P}\frac{dI_p}{dt} = V_{OH}\,, \tag{6-14}$$

$$R_p\left(I_p - I_{rf}\right) + \frac{d}{dt}\left(L_p I_p\right) = M_{OH,p}\frac{dI_{OH}}{dt} + M_{EF,p}\frac{dI_{EF}}{dt} \tag{6-15}$$

where M's denote the respective mutual inductances and where the fact that $M_{EF,OH} \approx 0$ has been used. During the OH recocking phase $dI_p/dt = 0$ and $dL_p/dt \approx 0$. Also during this phase $dI_{EF}/dt = 0$. The required value of voltage needed to recock the OH coil in a "dwell" time, t_{DWELL} is then given by:

$$V_{OH} = \frac{\Delta\phi_{OH}}{t_{DWELL}}\,, \tag{6-16}$$

where $\Delta\phi_{OH} = L_{OH}\Delta I_{OH}$ is the OH flux swing during the recocking phase.

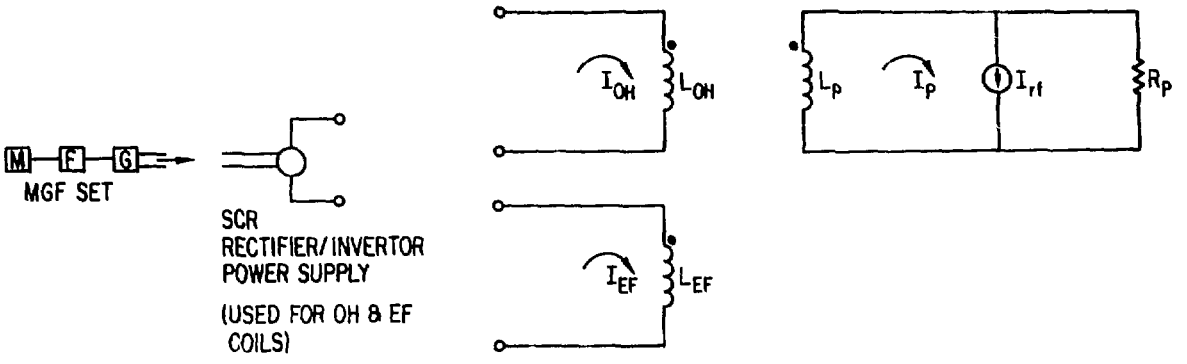

Fig. 6-7. Power supply system for a hybrid cycle.

The OH power required for recocking is given by:

$$P_{OH} = \frac{2U_{OH}^{max}}{\Delta t_{DWELL}} \tag{6-17}$$

where U_{OH}^{max} is the stored energy of the OH coil when fully charged.

From Eq. (6-16) the required value of I_{rf} needed to maintain a constant plasma current during the recocking phase is given by:

$$I_{rf} = I_p - \frac{V_{OH}}{R_p}, \tag{6-18}$$

where the relation $M_{OH,p} \approx L_{OH}$ has been used.

The required rf power, corresponding to this current, is generally believed to have the following form:

$$P_{rf} = \frac{N_{e_{20}} I_{rf}}{\gamma}, \tag{6-19}$$

where $N_{e_{20}}$ is the plasma density, in units of 10^{20} m^{-3}, and γ is the current drive efficiency at $N_{e_{20}} = 1$. Combining the above expressions then gives for

the required rf power in terms of γ and the dwell time:

$$P_{rf} = \frac{N_{e_{20}}}{\gamma}\left[I_p + \frac{|\Delta\phi_{OH}|}{R_p t_{DWELL}}\right] . \qquad (6\text{-}20)$$

Thus the required rf power depends linearly on the density during the recocking phase and also depends strongly on the plasma resistance during this phase. Obtainable values for these parameters as well as the value of γ are uncertain. A brief analysis of various hybrid burn cycles with the CTRAN code show that the following parameters may be $N_{e_{20}} = 0.02$, $R_p = 10^{-7}$ Ω. [A key technique is to keep the plasma temperature fairly low (several keV) during this phase in the injection of xenon.]

A value of $\gamma = 0.02$ A/W was assumed for reference purposes on this basis: if γ were ten times higher, then a steady-state cycle would be chosen, i.e. there would be no need for a hybrid cycle; and if γ were ten times lower, then no form of current drive cycle would work. The effect of different values of γ on the ETS system is discussed in Sec. 6.6.

The value of plasma current during the dwell period is lower than for the burn period. This is so because the reduction in EF current, necessary because of the reduction in plasma β, during the density ramp-down phase, reduces I_p. Conversely when the density is ramped back up, I_{EF} increases and ramps I_p up to its full value. From CTRAN results the value of plasma current during recocking was found to be $I_p = 10$ MA.

The hybrid cycle offers several options in regards to the OH coil design. One option is to design an OH coil to give the same burn time as a conventional cycle. Since the hybrid OH coil is only used to supply burn volt-seconds the OH field strength coil for this option would be lower than for the conventional cycle. This is the approach discussed first. Another option is to use a different value of field to obtain a different burn time -- this is discussed later.

The value of OH field needed to obtain a burn time of 51 min, i.e. the same as for the conventional cycle is $B_{OH} = 6.53$ T. This gives a flux swing capability of $|\Delta\phi_{OH}| = 470(B_{OH}/10\ \text{T}) = 307$ V-s. The stored OH energy at full

field is U_{OH}^{max} = 8.2 GJ, considerably less than the 19.2 GJ needed for the conventional cycle OH coil.

With the above parameters the required rf power is:

$$P_{rf} = 10^7 + \frac{3 \times 10^9}{t_{DWELL}} . \tag{6-21}$$

For a value of t_{DWELL} = 30 s, for example, P_{rf} = 110 MW.

An additional cycle parameter is the EF ramp time, t_{EF}, defined as the time in which the density is ramped down. The density ramp-up phase also takes a time t_{EF}. During the rampdown, the EF current is reduced from the full value to about one-half the full value, as β drops to nearly zero and the plasma current drops by 30%. If the plasma is controlled in an optimum manner, the EF voltage is given by $V_{EF} = L_{EF}(I_{EF}/2)/t_{EF}$. The corresponding EF reactive power requirement, $P_{EF} = V_{EF} \times I_{EF}$ is then:

$$P_{EF} = \frac{U_{EF}}{t_{EF}} . \tag{6-22}$$

The thermal storage system time capacity required for the hybrid cycle is given by:

$$t_{DOWN} = t_{DWELL} + t_{EF} . \tag{6-23}$$

A parametric analysis was performed for the hybrid cycle by varying t_{EF} and t_{DWELL}. The ETS requirements and costs were computed in an analogous manner to the conventional system:

$$P_{OH}^{*} = \frac{32.8 \times 10^9}{t_{DWELL}} , \quad VA \tag{6-24}$$

$$P_{EF} = \frac{6.36 \times 10^9}{t_{EF}} , \quad VA \tag{6-25}$$

$$P_{max} = \max(P_{OH}^{*}, P_{EF}) \tag{6-26}$$

$$C_{max} = 0.1 \times P_{max} + 46 \times 10^6 \ , \quad \$ \tag{6-27}$$

$$C_{ST} = \begin{cases} 70 \times 10^6 + 3.7 \times 10^6 (t_{DOWN} - 10) \ , & \$, \ H_2O \text{ system} \\ 30 \times 10^6 + 2.0 \times 10^6 (t_{DOWN} - 10) \ , & \$, \text{ liquid metal system} \end{cases} \tag{6-28}$$

$$C_{ETS} = C_{MAX} + C_{ST} \ . \tag{6-29}$$

In addition, the incremental cost of the rf system, defined as the difference in cost between the rf system required and a 75-MW system was computed by:

$$P_{rf} = 10 + \frac{3000}{t_{DWELL}} \ , \quad MW \tag{6-30}$$

$$\Delta C_{rf} = 1.5(P_{rf} - 75 \text{ MW}) \ , \quad M\$ \tag{6-31}$$

where a minimum value of $P_{rf} = 75$ MW is used based on the need to heat the plasma to ignition.

The ETS cost of a hybrid system for various values of cycle parameters is shown in Figs. 6-8 and 6-9. The solid curves are C_{ETS} and the dashed curve is $C_{ETS} + \Delta C_{rf}$. The dashed curve indicates that one would expect to pay a high price for recocking in short times, because of the high rf power needed. At long dwell times the costs go up due to increases in the thermal storage system cost.

Reasonable values of hybrid cycle parameters are $t_{DWELL} = 45$ s and $t_{EF} = 15$ s. At these values the ETS cost is 375 M\$ for the H_2O system and ~250 M\$ for the liquid-metal system. This represents a savings of ~60 M\$ over a conventional system. While this is significant it is not a fundamental difference. Cost differences in the current drive system could easily offset ETS system savings. However, the hybrid cycle offers a number of other advantages over the conventional, these being the following: The EF field swing is reduced by about a factor of two for the same number of cycles. This reduces stress on the TF and OH coils (Chap. 5). Secondly, the elimination of the plasma breakdown period, and most of the plasma current swing, may reduce disruptions. Thus, the hybrid cycle may be better than the conventional in a number of important areas.

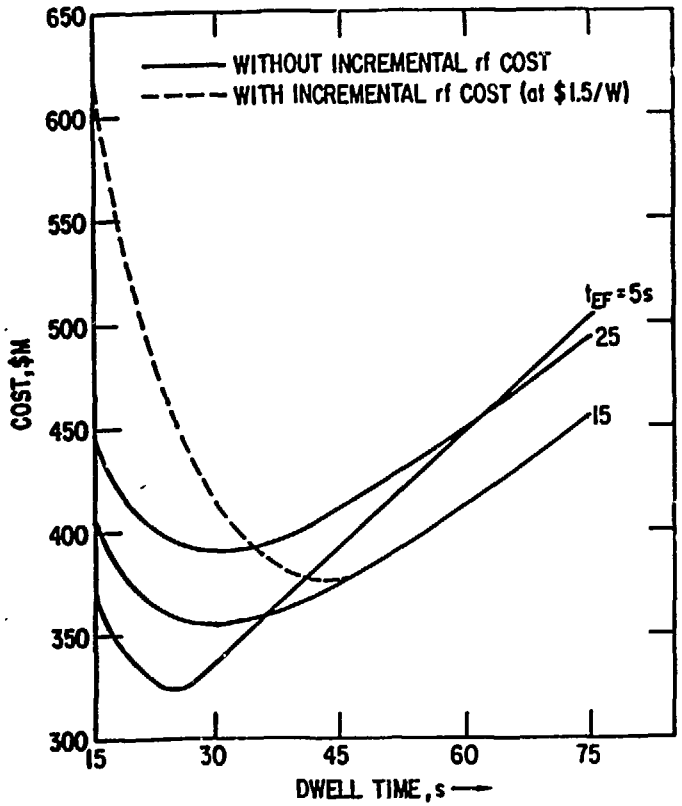

Fig. 6-8. Energy transfer system costs for a hybrid cycle, water system.

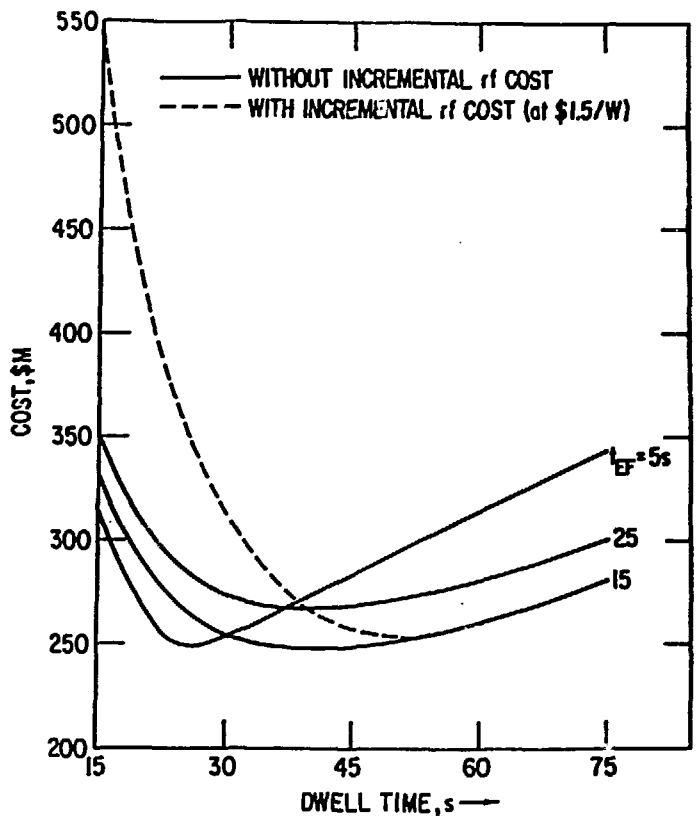

Fig. 6-9. Energy transfer system costs for a hybrid cycle, liquid metal system.

The hybrid cycle using different values of B_{OH} was also analyzed. B_{OH} was varied from 0 to 10 T. For each value of B_{OH} a parametric analysis was performed for the ETS cost. In general, the optimum cycle parameters (t_{EF}, t_{DWELL}) differ substantially over the range of B_{OH}.

For the limiting case of $B_{OH} = 0$, the burn time is zero but there is still a finite cost due to the EF supply and thermal storage systems. For $B_{OH} \gtrsim 3$ T the ETS varies almost linearly with burn time. The maximum burn time obtainable, at $B_{OH} = 10$ T, is about 50% greater than the burn time for a conventional system. These results are discussed in more detail in Sec. 6.6.

6.5 Internal Transformer Cycle

As discussed in Chap. 2, the internal transformer (IT) cycle does not use an OH coil at all but instead relies on overdriving the plasma current with a noninductive driver. This is done during a low density period. The plasma is then brought up to ignition and burns until the current decays to some minimum value. The density is then ramped down and the cycle is repeated.

The energy transfer system for the IT cycle consists of an EF power supply and a thermal storage system. A fundamental parameter for the IT cycle is the plasma current overdrive ratio defined as:

$$\eta = \frac{I_{p_1}}{I_{p_0}} , \tag{6-32}$$

where I_{p_1} is the maximum plasma current induced, and I_{p_0} is the required minimum plasma current. For the IT cycle the plasma current is given by Eq. (6-15) with $M_{OH,p} = 0$. During the burn phase this has the solution

$$I_p = I_{p_1} e^{-t/\tau} ,$$

where τ is the plasma time constant during the burn phase. The burn time is given by the time it takes for I_p to decay to I_{p_0}:

$$t_{BURN} = \tau \log \eta . \tag{6-33}$$

During the current drive period the plasma current is given by:

$$I_p = I_{rf} + (I'_{p_0} - I_{rf})e^{-t/\tau'} ,$$

where τ' is the plasma time constant during the current drive period and I'_{p_0} is the plasma current at the start of the current drive period. I'_{p_0} is somewhat less than I_{p_0} due to the EF rampdown preceeding the current drive period. From the above equation the dwell time necessary to obtain a current I_{p_1} is given by:

$$t_{DWELL} = \tau' \ln\left[\frac{1 - I_{rf}/I'_{p_0}}{\eta - I_{rf}/I'_{p_0}}\right] \qquad (6\text{-}34)$$

The EF ramp period for the IT cycle is the same as for the hybrid. However, the EF stored energy is higher because of the higher plasma current. The EF power requirement was modeled as follows:

$$P_{EF} = \frac{\eta^2 U_{EF_0}}{t_{EF}} , \qquad (6\text{-}35)$$

where U_{EF_0} is the EF energy corresponding to I_{p_0} and where the scaling $B_{EF} \sim I_p$ is employed. (EF power is also needed during the burn phase as I_p decays and where β is assumed constant, but this can be shown to be smaller than given by Eq. (6-35). The MGF set stored energy was also scaled accordingly. A clearly unfavorable scaling of the IT cycle is that while burn time increases only logarithmically with overdrive ratio, the EF power increases as η^2. Also, a higher EF field B_{EF} is required which tends to result in a higher cyclic scress on the TF system. The EF coil system also needs to be bigger, although this may be offset by the elimination of the OH coil. Neither the EF coil design, nor the plasma MHD equilibrium characteristics at higher values of plasma current were assessed for this study, but these may be serious issues for the IT cycle.

The final parameter for the IT cycle is the thermal storage requirement, given by $t_{DOWN} = t_{DWELL} + t_{EF}$. The cost algorithms for the EF supply and thermal storage systems used previously were applied to the IT system. Simi-

lar parameters to the hybrid cycle were used, where applicable. The parameters used were: I_{p_0} = 13 MA, I'_{p_0} = 10 MA, τ' = 171 s, and τ = 2236 s.

A parametric analysis of the IT cycle using a range of overdrive ratios from η = 1 to 2 was performed. Note that a value of η = 2 corresponds to twice the plasma current and four times the plasma magnetic energy needed for the other cycles and this was intuitively felt to be a feasible upper limit. For each value of η a range of t_{EF} from 0-30 s was used. From CTRAN analysis of this subject it was found that a value of t_{EF} = 5 s is probably the minimum possible in which to reduce density by a factor of 50 while still maintaining good control of the EF voltage. In any event, the ETS cost was found to be minimized at larger values of t_{EF}, (15-25 s) in all cases.

The results of the parametric study of the IT system are discussed in the following section.

6.6 Burn Cycle Comparison

Using the models described previously, the cost of the energy transfer system was computed as a function of burn time for a conventional, hybrid, and internal transformer cycle. The costs shown include incremental rf costs at \$1.5/W where applicable. The results are shown in Fig. 6-10 for the water-cooled, 8-m reference reactor. The trends are similar for a liquid metal system with all costs reduced. For the conventional and hybrid cycles the obtainable burn time is varied by varying the OH design field, B_{OH}. For a conventional cycle, B_{OH} varies from ~4 T to 10 T; the minimum value is needed to supply inductive volt-seconds for startup. For the hybrid cycle B_{OH} varies from 0 to 10 T. For both cycles the burn time varies linearly with B_{OH}. For the IT cycle the overdrive ratio, η, is varied from one to two. For the hybrid and IT cycles a broad range of current drive parameter $\gamma/N_{e_{20}}$ was used. Each point on the curves of Fig. 6-10 represents the cheapest ETS cost identified by the parametric analysis. In general, the duty factor and net power produced are about the same for the conventional and hybrid cycles at longer burn times, but are lower for all cycles at short burn times.

For the conventional cycle, the ETS cost increases fairly slowly with burn time. There is probably no point in using less than the maximum burn time of 51 min, corresponding to B_{OH} = 10 T.

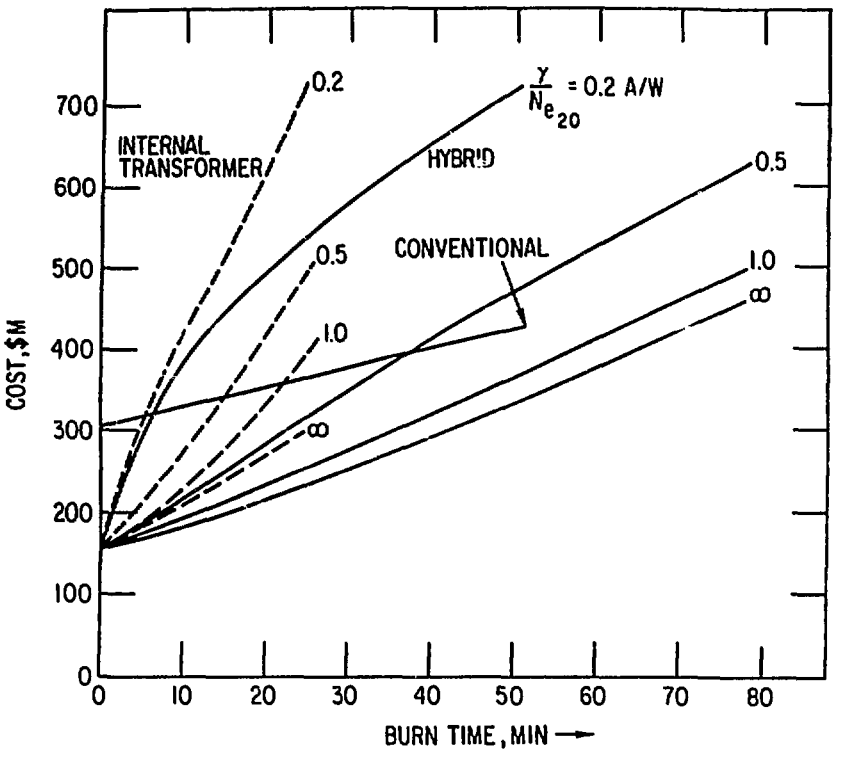

Fig. 6-10. Energy transfer system cost as a function of burn time and cycle type. [Includes incremental rf cost = \$1.5 × $(P_{rf}$ - 75 MW) where applicable.]

As shown, the internal transformer cycle is limited to an ~25-min burn time. This corresponds to an overdrive ratio of two. The cost of the ETS system, for the IT cycle, depends on the current drive parameter. For a value of $\gamma/N_{e_{20}}$ = 0.2 A/W, which appears to be a probably attainable value, the ETS cost for the IT cycle is comparable to the conventional, at a 25-min burn time. For any given value of $\gamma/N_{e_{20}}$, the IT, ETS cost is significantly more than the ETS cost for the hybrid cycle.

The hybrid cycle has the potential of burning about 50% longer than the conventional. For burn time of ~51 min the ETS cost for the hybrid cycle is comparable to the conventional for values of $\gamma/N_{e_{20}} \geq 0.5$. For values of $\gamma/N_{e_{20}} < 0.5$, the hybrid cycle is probably unacceptable.

The burn time of all the cycles is linearly dependent on plasma resistivity during the burn phase. Therefore, uncertainties in the resistivity affect the burn time of all cycles equally.

Table 6-1 summarizes the net electrical power and several other parameters, for the various types of cycles including a steady-state cycle. The number of cycles, N_c, is shown for a 40-yr plant lifetime at 75% availability. Data for the steady-state mode is based on extrapolation from the STARFIRE burn cycle. The ETS system for the steady-state mode is very modest. The net electrical power produced for each cycle type depends on the respective duty factor and the expended current drive energy. For the IT cycle with $\eta = 1.1$, the net power is 10% lower than for the 51-min conventional cycle, a serious deficiency. An overdrive ratio of $\eta = 2$ is necessary to produce about the same power as the conventional. The hybrid cycles of 51 and 77 min produce essentially the same net electrical power as the conventional, since the duty factors approach unity. Calculations for the steady-state cycle were based on a value of 100 MW of input current drive power to the plasma. This results in the net power of 1360 MWe based on STARFIRE values of current generation efficiency, and thermal-to-electrical efficiency.

6.7 Discussion

The results shown in this chapter represent a first cut at comparing cycle types, as regards the ETS requirements, and general burn cycle parameters. There are clearly uncertainties in some of the critical physics issues such as obtainable densities, current requirements, etc. In addition, the cost algorithms used are fairly general ones intended for broad comparison purposes only. In spite of these qualifications, several conclusions can be made. The internal transformer cycle is not an attractive approach because of limited burn time and high ETS cost, to say nothing of possible difficulties with operating the plasma at up to twice the nominal plasma current. However, the IT cycle would look better, in relative terms, for smaller tokamaks than the 8-m design. In contrast, the hybrid approach looks promising although differences between the hybrid and conventional cycles are much less than the difference between both these and a steady-state cycle.

TABLE 6-1

Burn Cycle Parameter and Cost Summary

Cycle Type	Burn Time (min)	Duty Factor	No. of Cycles (N_c)	Energy Transfer System Cost (M$)	Net Electrical Power, P_{net} (MWe)
Internal transformer					
η = 1.1	3.5	0.87	3.9×10^6	178	1280
Internal transformer					
η = 2.0	26	0.95	5.6×10^5	404	1400
Conventional (double swing)					
B_{OH} = 10 T	51	0.97	3.0×10^5	425	1430
Hybrid					
B_{OH} = 6.5 T	51	0.97	3.0×10^5	371	1430
Hybrid					
B_{OH} = 10T	78	0.98	2.0×10^5	493	1445
Steady state					
P_{rf} = 100 MW	6 mo	1.0	~100	~10	1360

REFERENCES FOR CHAPTER 6

1. W. M. STACEY, JR., et al., "Tokamak Experimental Power Reactor Conceptual Argonne National Laboratory (1976).

2. J. N. BROOKS and R. L. KUSTOM, "Power Supply Requirements for a Tokamak Fusion Reactor," Nucl Technol. 46, 61 (1979).

3. F. PETREE and R. L. CASSEL, Proc. 7th Symp. on Engineering Problems of Fusion Research, IEEE Pub. No. 77CH1267-4 NPS, Vol. I, p. 891 (1977).

Chapter 7. INTERIM CONCLUSIONS

For capital intensive power plants the cost of energy will be largely determined by plant availability and initial capital cost. This study of tokamak burn cycles has found certain cost differences among the cycle options and has identified differences in cycle performance which will affect reliability and, hence, availability. Thermal and mechanical fatigue affect component lifetime, which has a tremendous impact on reactor availability. Capital costs are driven by requirements for energy transfer and storage in pulsed reactors, by the need for extra structure to withstand early fatigue failure in pulsed reactors, and by the needs for a noninductive current driver for certain cycles.

The thermal fatigue aging of components such as the limiter or divertor persuades us to derive minimum fusion burn periods, t_f, needed to maximize system lifetime. We view these values of t_f as goals to be met by the various burn cycles. As we show, these goals are strong functions of our assumptions: the severity and frequency of disruptions, the net rate of sputtering erosion, the materials selected for the substrate and plasma-side coating, and the acceptable frequency for replacing failed components. In general, t_f should be sufficiently long that fatigue is less limiting than radiation damage in determining component lifetime.

Consider first the limiter's leading edge, with a beryllium coating. Severe disruptions (removing ~0.54 mm of beryllium) at a frequency of $f = 10^{-3}$ (once per thousand burn cycles) force us to seek $t_f \sim 1.8 \times 10^3 - 2.7 \times 10^3$ s in order to achieve lifetimes of one or two years (~4 MW-y/m^2), the radiation damage limit for a copper heat sink. Such a short replacement interval is unattractive for a reactor, so substrates with superior radiation resistance must be considered. Vanadium-base alloys (~24 MW-y/m^2) promise longer radiation life, 6 to 12 yr, but t_f must be increased such that fatigue is not life-limiting; we find $t_f = 1 \times 10^4$ s is needed for the case of severe disruptions at $f = 10^{-3}$.

In the other extreme when there is no disruption damage, but for which net sputtering is very large, at $\delta_{Be} = 1$ cm/yr, we need $t_f \approx 9 \times 10^3$ s for a

copper heat sink to survive; the superior fatigue resistance of vanadium permits $t_f \ll 10^3$ s. However, temperature limits to the beryllium clad will limit δ_{Be} such that in-reactor life will be limited again to only one or two years with such high sputtering erosion.

It seems likely that net sputtering losses as high as $\dot{\delta} = 1$ cm/yr will not be tolerated, and also it seems likely that disruption damage will be better controlled than cited in the examples above. For negligible sputtering and moderate disruption damage (140 μm lost per 10^5 burn cycles) we need $t_f \geq 2.6 \times 10^3$ s with a beryllium/vanadium duplex, to achieve the full radiation life potential of the leading edge.

Tungsten is an attractive coating for the leading edge, provided the local plasma temperature is below the self-sputtering threshold ($T \lesssim 50$ eV). Disruption damage to tungsten is so minimal that very thin coatings are practical ($\delta_W \leq 1$ mm), and fatigue life is consequently very long, requiring at most $t_f \sim 10^2$ s. For the worst case net sputtering, $\dot{\delta}_W = 1$ cm/yr, a copper heat sink would prematurely fail unless $t_f \approx 10^4$ s, but the superior fatigue properties of vanadium would permit t_f as short as 10^2 s. Again, such severe erosion may not be realistic since it would limit the leading edge life to $\lesssim 2$ yr. Thus, for maximum credible disruptions and negligible net-sputtering ($T \lesssim 50$ eV) the tungsten-clad leading edge will survive for even very short t_f ($\lesssim 10^2$ s).

The front face of the limiter may experience higher energy dumps than the leading edge during major disruptions, and the t_f goals are thus somewhat more ambitious. In the worst case situation (690 μm of beryllium lost with $f = 10^{-3}$) we require $t_f = 2.2 \times 10^3 - 2.9 \times 10^3$ s to achieve full life (1 or 2 yr) with a copper heat sink or $t_f = 1.1 \times 10^4 - 1.4 \times 10^4$ s to achieve full life (6 to 12 yr) with the vanadium heat sink. In the more realistic case with moderate disruptions (170 μm lost with $f = 10^{-3}$) and tolerable sputtering erosion ($\dot{\delta}_{Be} \lesssim 1$ mm/yr) we need $t_f \gtrsim 3.2 \times 10^3 - 5.2 \times 10^3$s to achieve full life potential of the beryllium/vanadium front face.

Sputtering is not a significant factor for the first wall survival; however, disruptions can be a major concern. If we consider bare PCA with severe disruptions (410 μm lost with $f = 10^{-3}$) and permit 5% radiation creep we require $t_f = 1.5 \times 10^4 - 1.3 \times 10^4$ s to attain the 12 MW-yr/m^2 life potential

of the wall (3 to 6 yr). More stringent creep criteria (e.g. 1%) would increase the t_f requirement considerably. A vanadium structure for the first wall is more attractive than PCA since it is expected to have roughly twice the radiation damage life of PCA. For the vanadium structure that we studied (thickness $\delta_V \sim 1$ cm) we found fatigue is not a consideration; instead, temperature concerns limited δ_V and determined lifetime against disruptions. For the severe disruption scenario we require $t_f = 1.6 \times 10^4 - 3.2 \times 10^4$ s to achieve the full radiation life potential (replacement at 12-yr to 6-yr interval). However, for moderate disruption damage (60 μm lost with $f = 10^{-3}$) and allowing 5% radiation creep we need $t_f \geq 3.2 \times 10^3 - 6.4 \times 10^3$ s to achieve full life potential of a vanadium first wall. For even less severe disruptions the fusion burn period ceases to be a factor in the first wall life.

Mechanical stress fatigue is an important consideration for the ohmic heating coil (OHC) for reactors which require an external transformer. The OHC we studied has steel bands which resist the expulsive pressure of the 10-T solenoidal field. For cycle lifetimes exceeding $N \sim 5 \times 10^4$ the thickness of these bands must be increased such that stress levels are reduced appropriately to guarantee survival for the requisite number of cycles. Besides an increase in the OHC capital cost, the main adverse effect is a reduction in the OHC flux (volt-seconds) from the increase in the winding thickness. For $N = 3 \times 10^5$ the total flux is 80% of that at $N = 3 \times 10^4$. In order to achieve the longest discharge period, t_I, we would need a maximum $N \simeq 5 \times 10^4$ cycles, which would require OHC replacement every 10 yr provided we obtain $t_I \simeq 5 \times 10^3$ s. Replacement cost for each new OHC is estimated to be more than $70 M.

Capital cost is expected to play a large role for those systems which are required to survive the full 40-yr life of the reactor. Consider as an example the equilibrium field coil (EFC) system. This system is estimated to cost over $80 M, so it would be undesirable to replace these magnets. In fact, we found that the hybrid and CW burn cycles are unlikely to cause fatigue failure of the EFC whereas OH operation will require roughly a $15 M cost increment to guarantee survival of the EFC. This result stems from the small number of cycles (~200) for CW operation over 40 yr and from the relatively small vertical field swing associated with the hybrid cycle.

In the case of the toroidal field coil (TFC) system, not only is the replacement cost prohibitively expensive, but the replacement procedure would practically require disassembly of the whole tokamak, reducing reactor availability to near zero. Remote inspection and maintenance (reinforcement of weakened structure) may be very difficult, so prudence dictates the use of very conservative fracture mechanics methods to estimate TFC lifetime. Again we conclude that mechanical fatigue is a serious problem unless $t_f \gtrsim 2 \times 10^4$ s. Considering all TFC costs, superconductor, stabilizer, steel banding, helium vessel, vacuum tank, and shear panels, we estimate TFC cost very roughly as: \$200 M - CW ($t_f \gtrsim 10^5$ s); \$230 M-hybrid ($t_f \approx 5 \times 10^3$ s); \$300 M-OH ($t_f \approx 5 \times 10^3$ s); and \$400 M-IT ($t_f \approx 300$ s). These cost differences mainly arise from the increased steel structure required to withstand mechanical fatigue.

For pulsed burn cycles the cost of energy transfer and storage is very large. For short dwell periods between fusion burns the poloidal coils must be charged and discharged quickly, requiring very high power electrical supplies. The need to transfer tens of gigajoules of magnetic energy in tens of seconds implies the use of power supplies rated on the order of ~1000 MVA; typical capital costs for motor-generator-flywheel and silicon controlled rectifier supplies can exceed \$100 M. These costs can be reduced by prolonging the dwell period. However, for long dwells we foresee a need to store thermal energy during the burn, in order to maintain steady steam turbine conditions when fusion ceases. Thermal storage costs (~\$1 $\times 10^{-3}$/J for high pressure water and ~\$5 $\times 10^{-4}$/J for liquid sodium) increase with dwell period and exceed \$100 M for dwells approaching 60 s. There is thus an optimum dwell period (~50 s) which minimizes the capital costs of the energy storage and transfer systems. We find a large variation in costs for the energy systems. The IT cycle costs ~\$200 M for $t_f \approx 300$ s and ~\$400 M for $t_f \sim 1.5 \times 10^3$ s, assuming water cooling and thermal storage. The OH cycle costs ~\$425 M for water storage and ~\$315 M for sodium, while the hybrid cycle requires ~\$325 M for water and ~\$250 for sodium storage. In all cases pulsed burn cycles have very expensive energy storage and transfer systems (≥\$200 M) compared to a CW cycle, which requires only ~\$10 M for such equipment.

Arrayed against these large capital costs for pulsed cycles is the capital cost of a noninductive current driver for the CW burn cycle. A \$200 M

savings for a CW burn cycle could easily be offset if a special 100-MW rf current drive system were needed to achieve CW operation. Based on crude projections for the cost of rf power we need noninductive current drive efficiencies of $\gamma \gtrsim 0.1$ A/W for CW operation or $\gamma \gtrsim 0.01$ A/W for the hybrid cycle in a reactor-size and -density plasma in order to be competitive with the conventional OH burn cycle. We expect $\gamma \gtrsim 0.01$ A/W is credible based on present-day experiments (e.g., in ALCATOR-C).

Finally, we can point to several fruitful areas for further research. Obviously, improved current drive efficiency (by a factor of ten) would be very desirable. In this regard, alternative drivers, such as the compressional Alfvén wave, need to be considered as well as the lower hybrid wave. The pulsed operating modes can become more attractive if ways can be found to reduce the frequency or damage from major disruptions. Likewise, we expect that cycles with external transformers become more appealing if plasma resistivity could be reduced below the Spitzer value, thereby prolonging the burn period, t_f. Sputtering is viewed as a major problem; control of the plasma edge temperature would be useful in prolonging component life. Technological innovation may likewise have large payoffs. For example, if the cost of rf equipment could be reduced by a large factor (to less than \$1/W) then the goals for current drive efficiency, γ, could be reduced appropriately. The cost of the TFC structure may be reduced by selecting cryogenic intercoil supports; the problem of eddy current heating and reduced access to the machine requires further study. Last of all, we mention that our thermal energy storage systems for pulsed burn cycles are designed to store the whole energy deficit of the dwell period and are required to deliver the power deficit with a fast time response. We need to study whether constant power to the turbine is a firm requirement; steam cycles with tolerance to small power variations could significantly reduce the costs of pulsed tokamak reactors.

Appendix A

MATERIALS PROPERTIES

This appendix details some of the physical and thermal properties used in this lifetime study. Many data are preliminary, especially considering the general lack of experiments with fusion neutron radiation.

The PCA steel referred to in this report is modeled by Type 316 stainless steel (20% cold worked). The vanadium alloy cited is actually vanadium base with 15% chromium and 5% titanium additions. Pure copper has relatively poor mechanical properties which can be improved by alloying; the data here represent typical properties of alloys such as AMAX-MZC (<1% chromium, zirconium, and magnesium) and copper-beryllium Alloy 25 (2% beryllium).

References for Appendix A

1. "U.S. FED/INTOR Activity: Critical Issues," USA FED-INTOR/82-1, Vol. i (1982); see Chap. 7.

2. R. F. MATTAS, "Fusion Component Lifetime Analysis," ANL/FPP/TM-160, Argonne National Laboratory (1982).

3. "Structural Materials for Superconducting Magnets (Preliminary Draft)," AISI 316 Stainless Steel, Handbook prepared by National Bureau of Standards (1982).

TABLE A-1

Cladding and First Wall/Limiter Structure*

Property	Beryllium	Tungsten	PCA	V-15Cr-5Ti	Copper
Thermal conductance, W/m-K	125 (300°C) 96 (600°C)	145 (227°C) 122 (727°C)	20.8 (427°C) 22.0 (500°C)	28.1 (500°C) 29.4 (600°C)	130 (200°C) 144 (300°C)
Thermal expansion coefficient (10^{-6} /K)	15.9 (500°C) 18.4 (1000°C)	4.3 (227°C) 4.6 (727°C)	16.1 (27°C) 17.7 (427°C)	10.4 (500°C) 10.6 (600°C)	17.0 (200°C) 17.8 (300°C)
Elastic modulus, GPa	200 (500°C) 150 (600°C)	398 (227°C) 379 (727°C)	208 (27°C) 182 (427°C)	118 (500°C) 116 (600°C)	116 (200°C) 111 (300°C)
Specific heat, J/kg-K	2250 (50°C) 2920 (1000°C)	138 (227°C) 146 (727°C)	503 (27°C) 557 (427°C)	558 (500°C) 580 (600°C)	423 (200°C) 425 (300°C)
Poisson's ratio	0.07	0.29	0.28	0.36	0.3
Density, g/cm^3	1.8	19.3	7.9	6.1	8.2
Electrical resistivity, μΩ-cm	15 (400°C)	----	97 (400°C)	57 (500°C)	4 (600°C)
Melting point, °C	1283	3410	1430	1888	865
Temperature limit, °C	700 (swelling)	600 (swelling)	500 (thermal creep)	600 (thermal creep)	250 (swelling ductility)
S_{mt}, MPa	----	----	215 (500°C)	200 (600°C)	----
Nuclear heating @ W_n = 1.0 MW/m^2, W/cm^3	7.8	23	10.8	7.4	14.7

*See Ref. 1.

TABLE A-2

Breeder Materials

Property	Li_2O	Lithium
Thermal conductance, W/m-K	3.4	48
Specific heat, J/kg-K	2763 (600°C)	4200 (400°C)
Density, g/cm^3	1.71 (85% TD)	0.495
Electrical resistivity, μΩ-cm	----	35 (500°C)

TABLE A-3

Magnet Structure: Stainless Steel

Property	Type 316 (Annealed)	Type 316 LN (Annealed)
Young's modules, GPa	206 (4 K) 194 (273 K)	215 (4 K) 185 (273 K)
Shear modulus, GPA	80 (4 K) 74 (273 K)	83 (4 K) 72 (273 K)
Poisson's ratio	0.29	0.29
Electrical resistivity, μΩ-cm	56 (4 K)	56 (4 K)
S_m, MPa	407 (4 K) 153 (300 K)	500 (4 K) 217 (300 K)
Fracture toughness, $MPa\sqrt{m}$	270 (4 K)	220 (4 K) 290 (300 K)

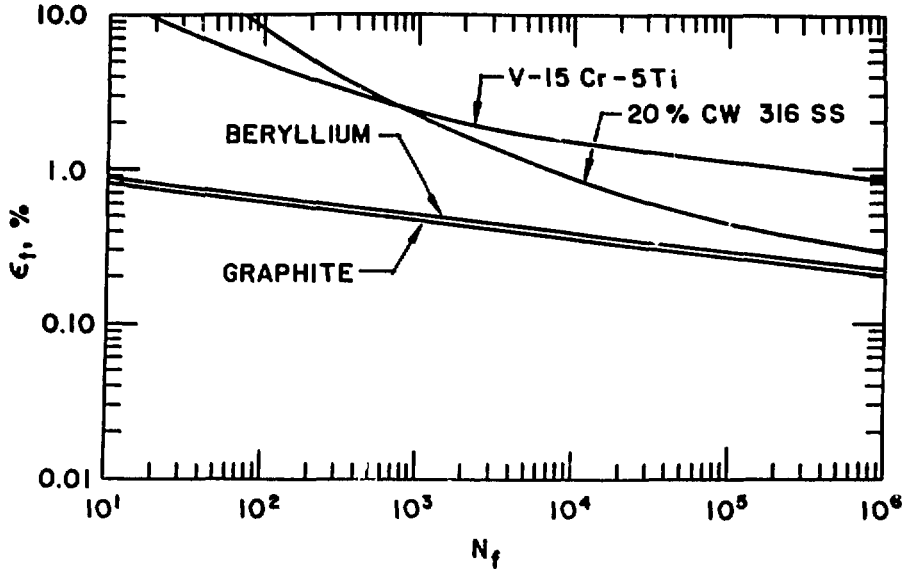

Fig. A-1. Fatigue life of first wall/limiter materials at 750 K.

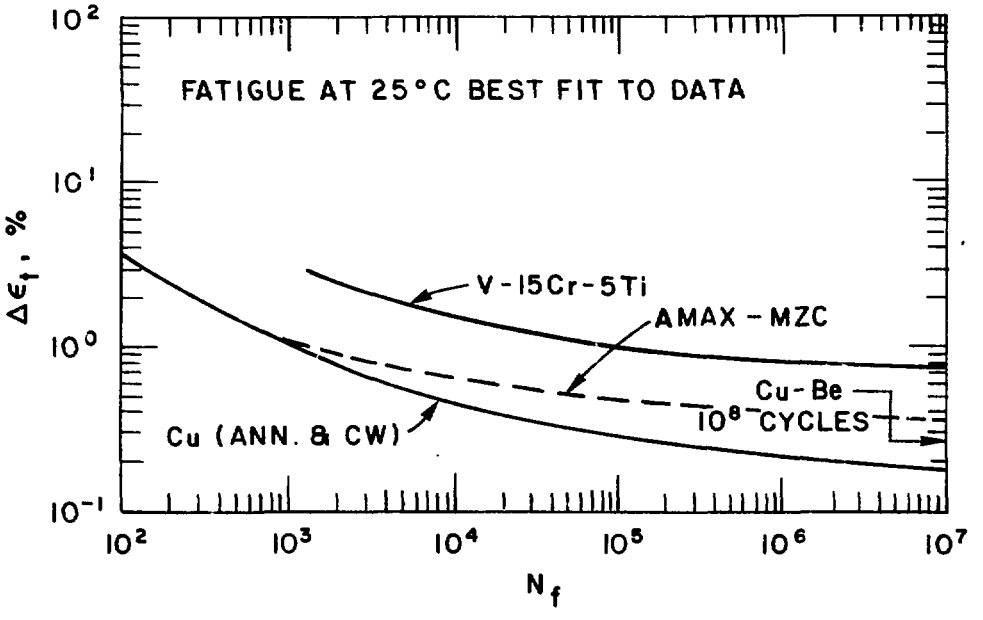

Fig. A-2. Fatigue life of limiter heat sink materials.

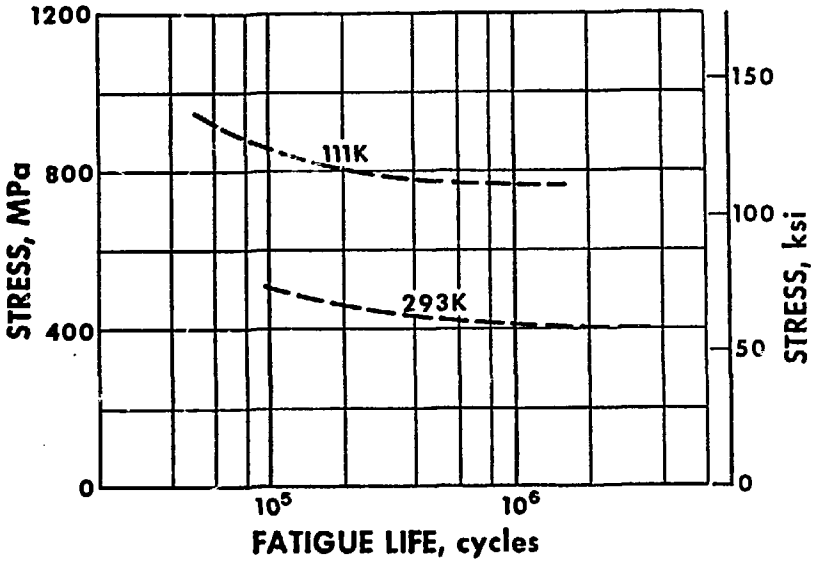

Fig. A-3. Stress controlled fatigue life of Type 316 LN (annealed)

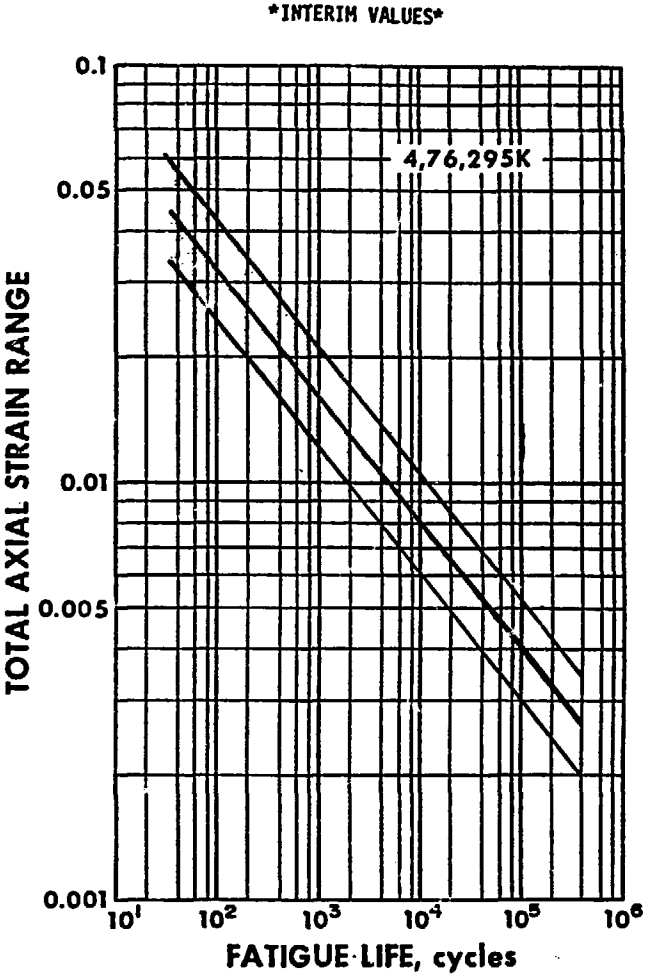

Fig. A-4. Strain controlled fatigue life of Type 316 stainless steel (annealed)

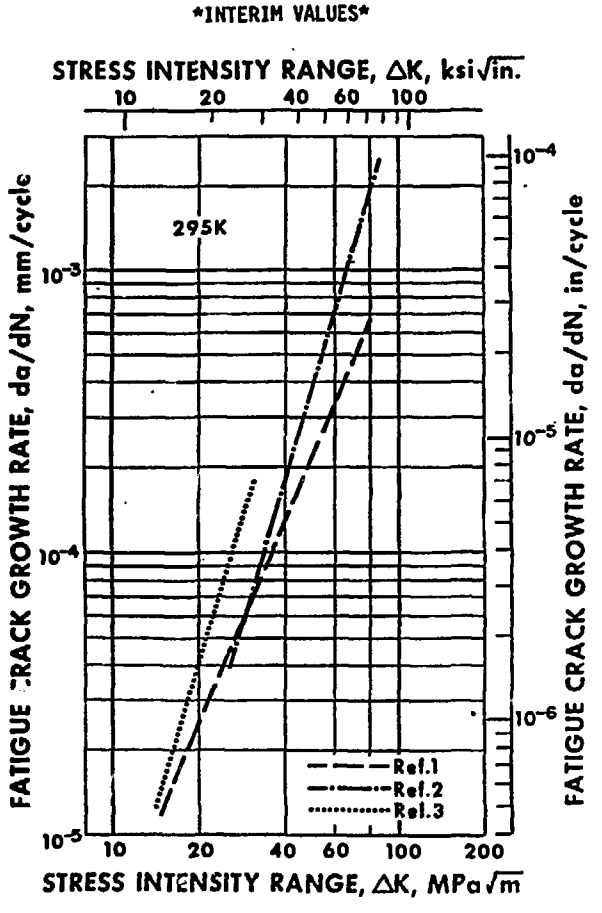

Fig. A-5. Fatigue crack growth rate of Type 316 LN (annealed), 295 K.

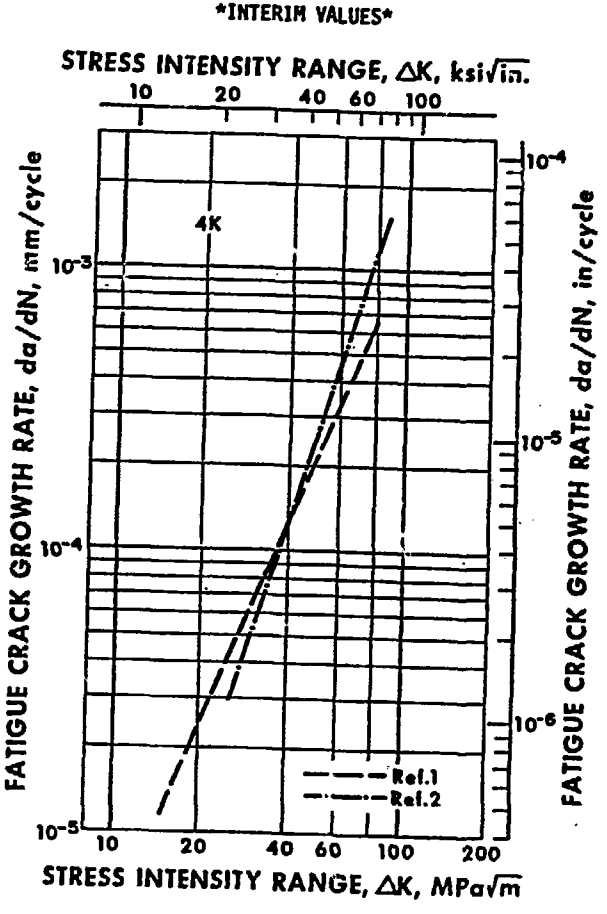

Fig. A-6. Fatigue crack growth rate of Type 316 LN (annaled), 4 K.

Appendix B

TEMPERATURE RESPONSES FOR DWELL TIMES OF 0, 30, AND 200 s

The computations for cyclic operation of the reactor assumes dwell times of 0, 30, 90, and 200 s. The data provided in Chap. IV utilizes temperature response for 90-s dwell time, since dwell times only of the order of 100 s appear practical based on the startup power and thermal storage requirements. For the sake ot completeness, analyses were extended to cover dwell times of 0, 30, and 200 s. The transient temperature response of all of the cases for the previously mentioned three regions are shown in Figs. B-1 through B-36. Thermal storage requirements for a few selected cases will be determined during the next phase of this study.

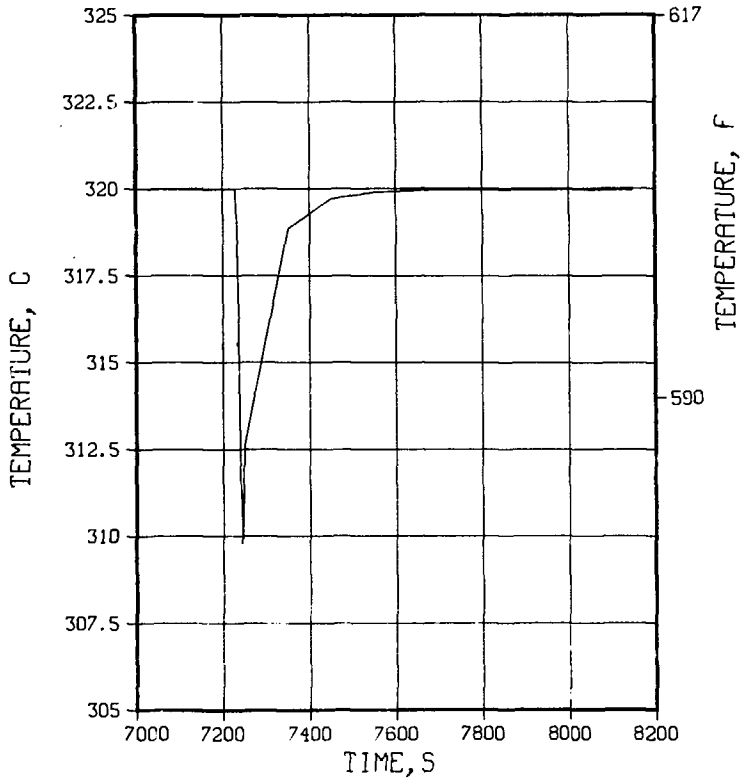

Fig. B-1. Coolant temperature response: 0-s dwell/Region 1.

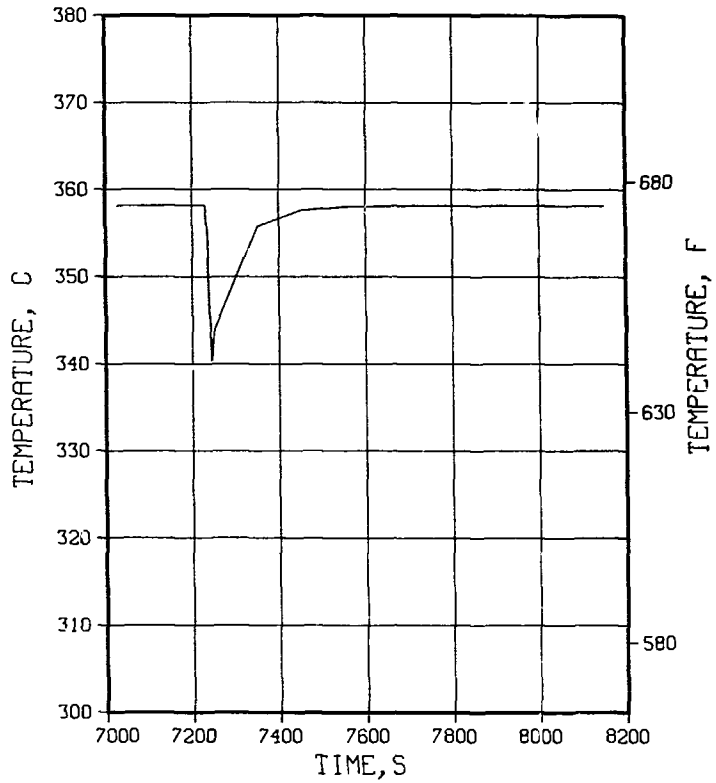

Fig. B-2. Cladding temperature response: 0-s dwell/Region 1.

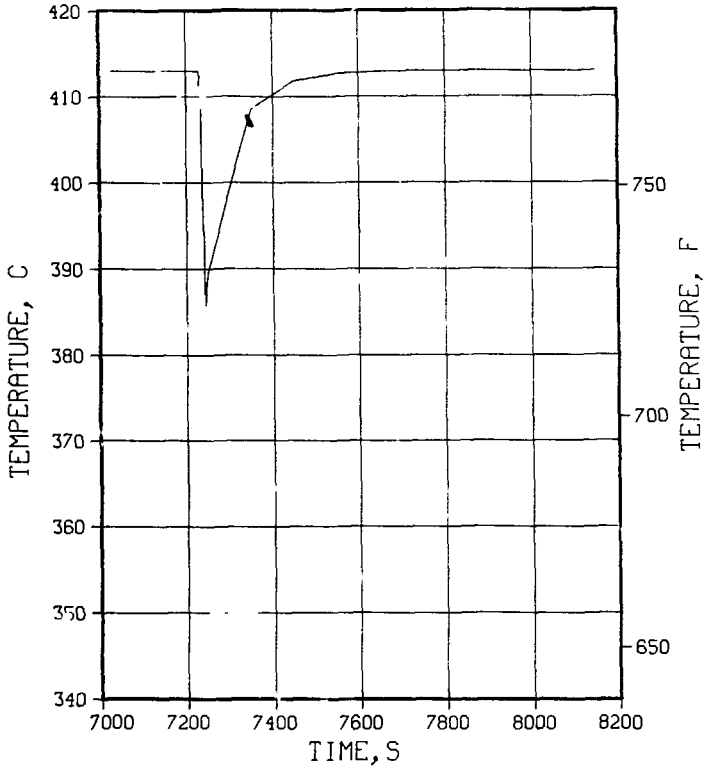

Fig. B-3. Breeder minimum temperature response: 0-s dwell/Region 1.

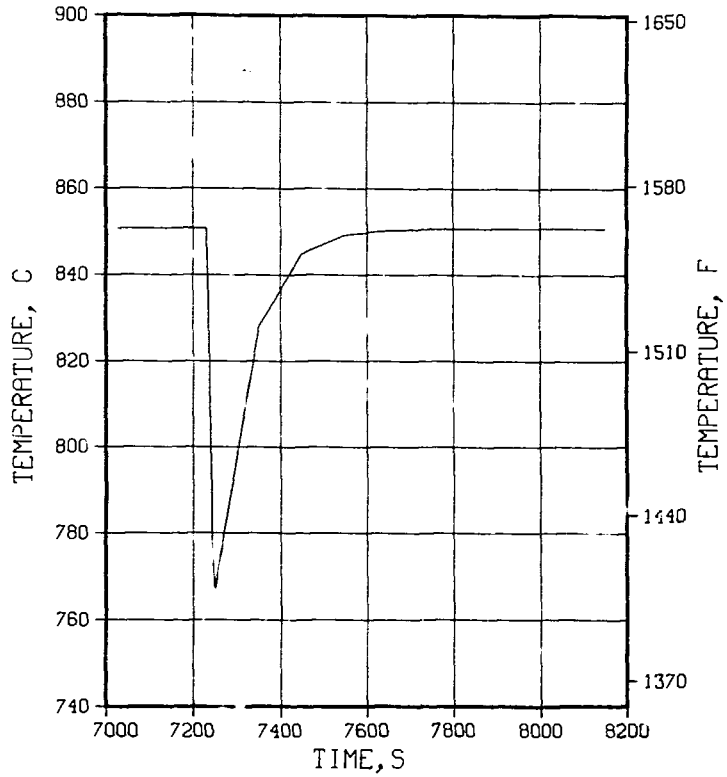

Fig. B-4. Breeder maximum temperature response: 0-s dwell/Region 1.

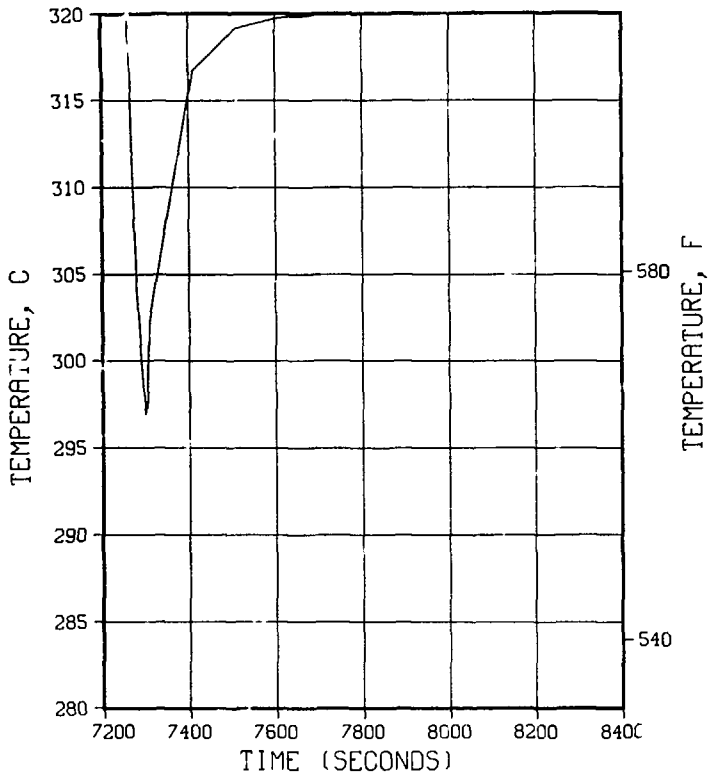

Fig. B-5. Coolant temperature response: 30-s dwell/Region 1.

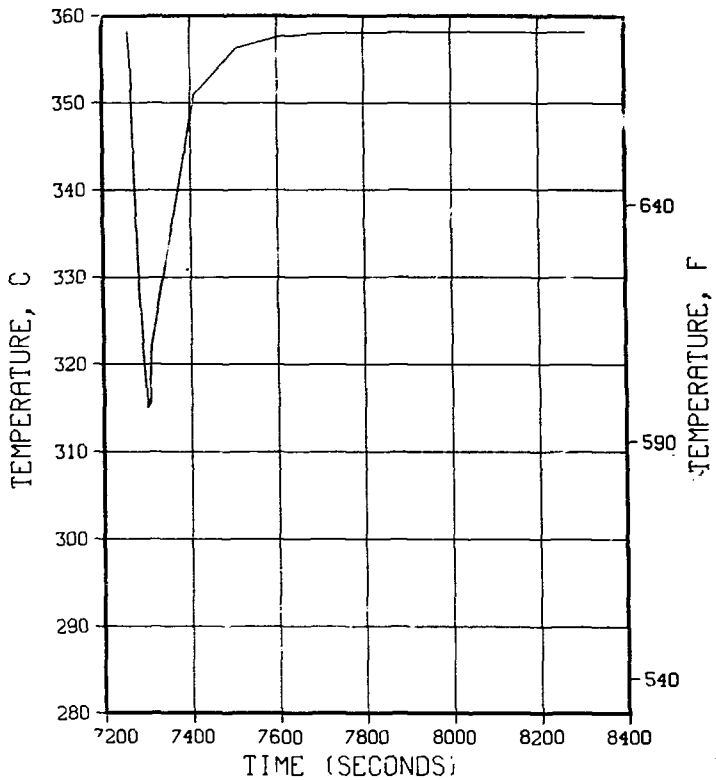

Fig. B-6. Cladding temperature response: 30-s dwell/Region 1.

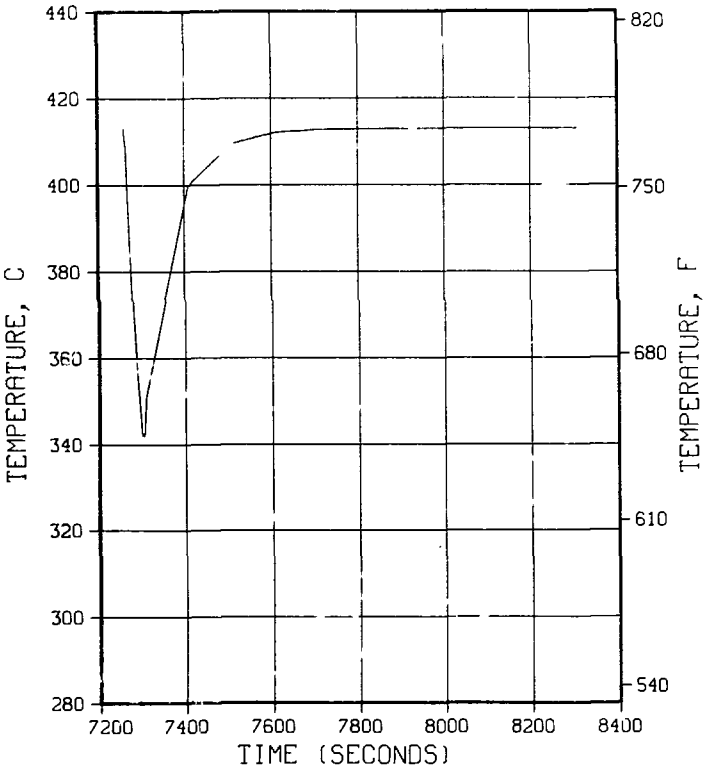

Fig. B-7. Breeder minimum temperature response: 30-s dwell/Region 1.

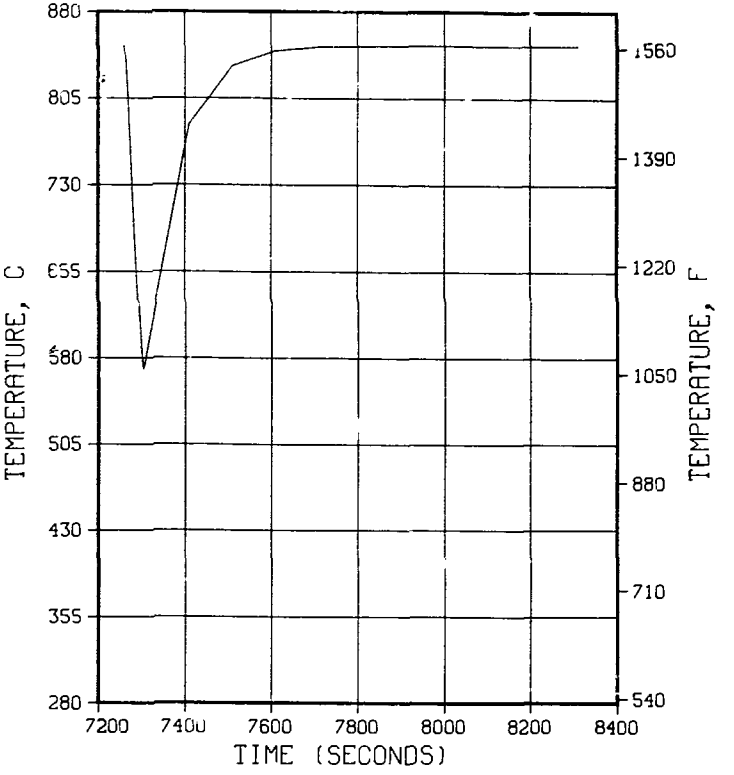

Fig. B-8. Breeder maximum temperature response: 30-s dwell/Region 1.

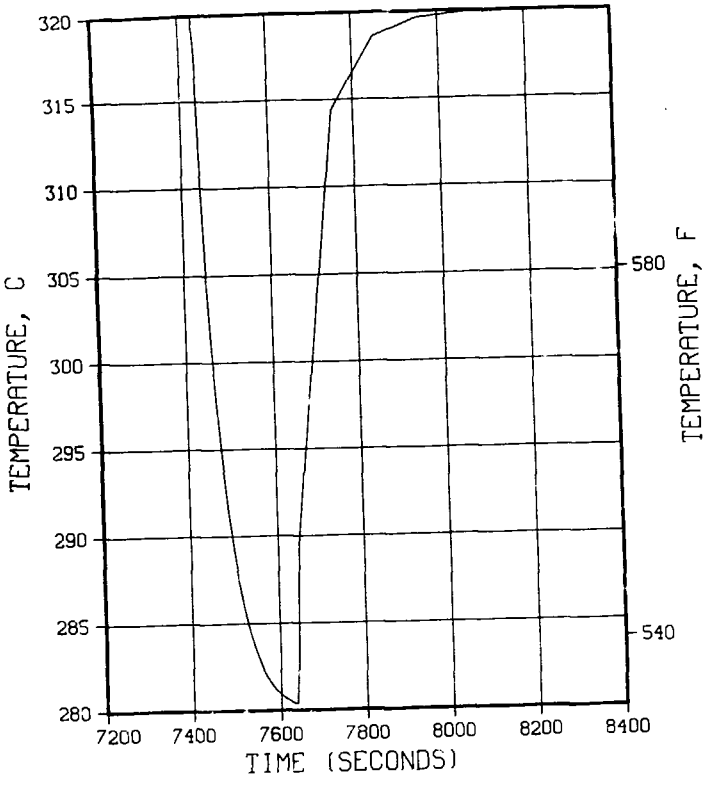

Fig. B-9. Coolant temperature response: 200-s dwell/Region 1.

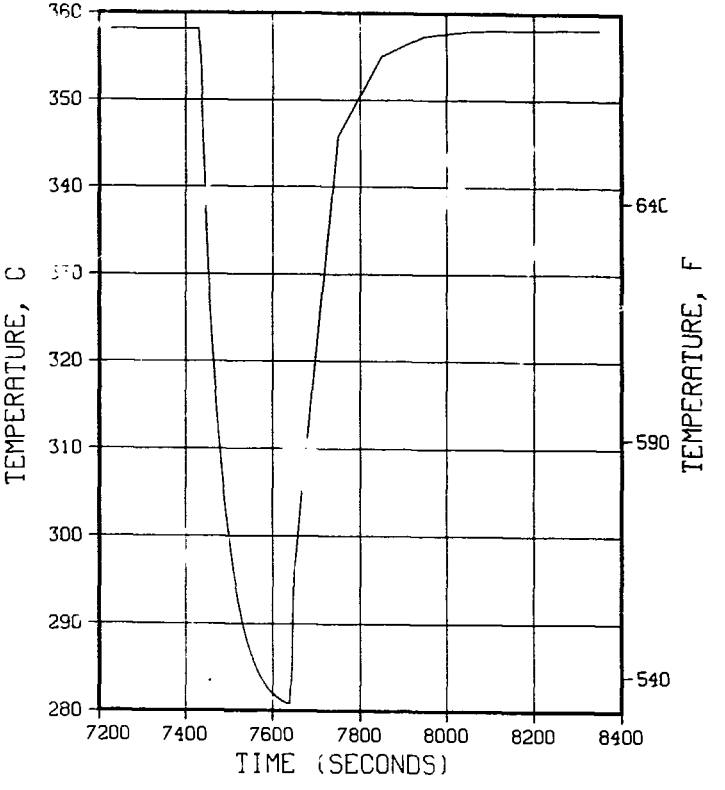

Fig. B-10. Cladding temperature response: 200-s dwell/Region 1.

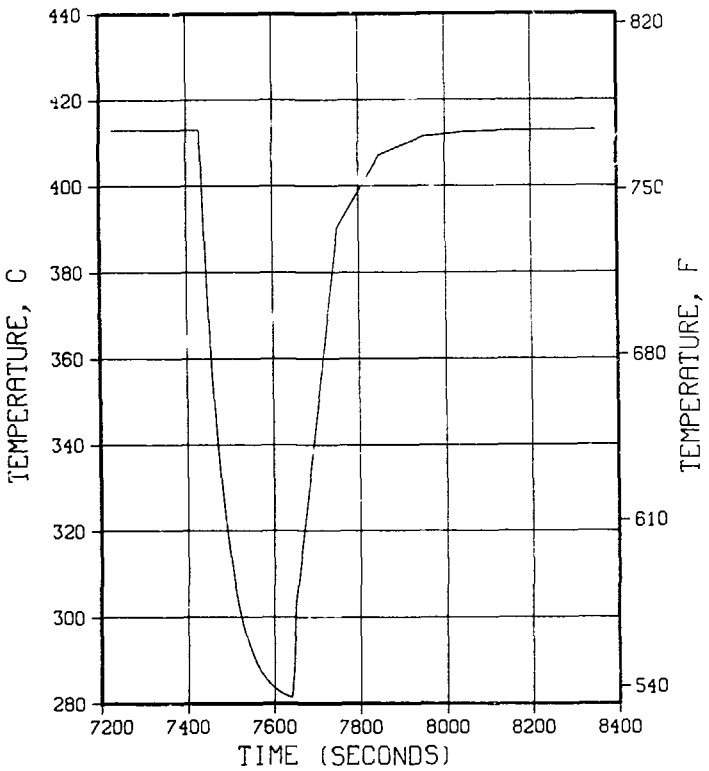

Fig. B-11. Breeder minimum temperature response: 200-s dwell/Region 1.

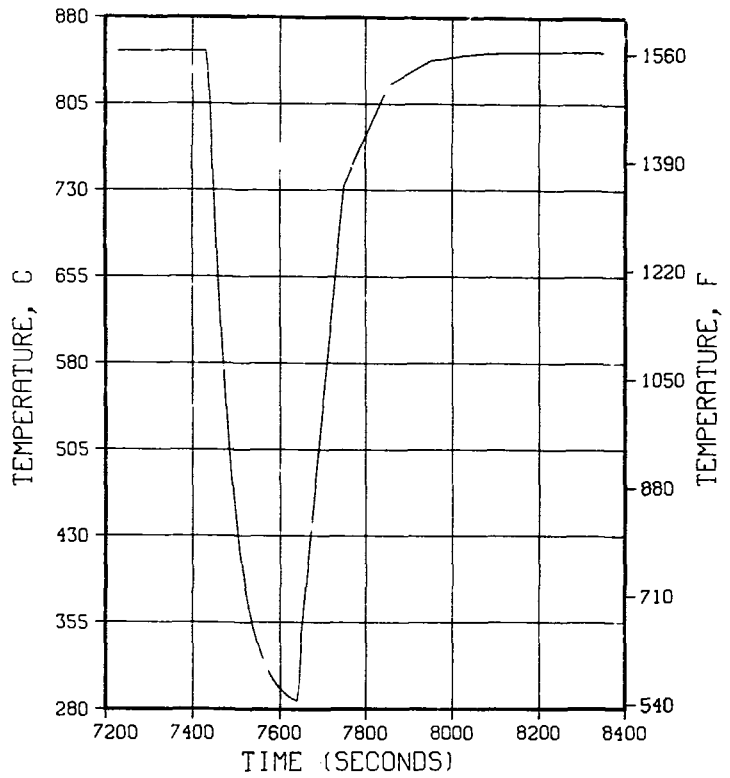

Fig. B-12. Breeder maximum temperature response: 200-s dwell/Region 1.

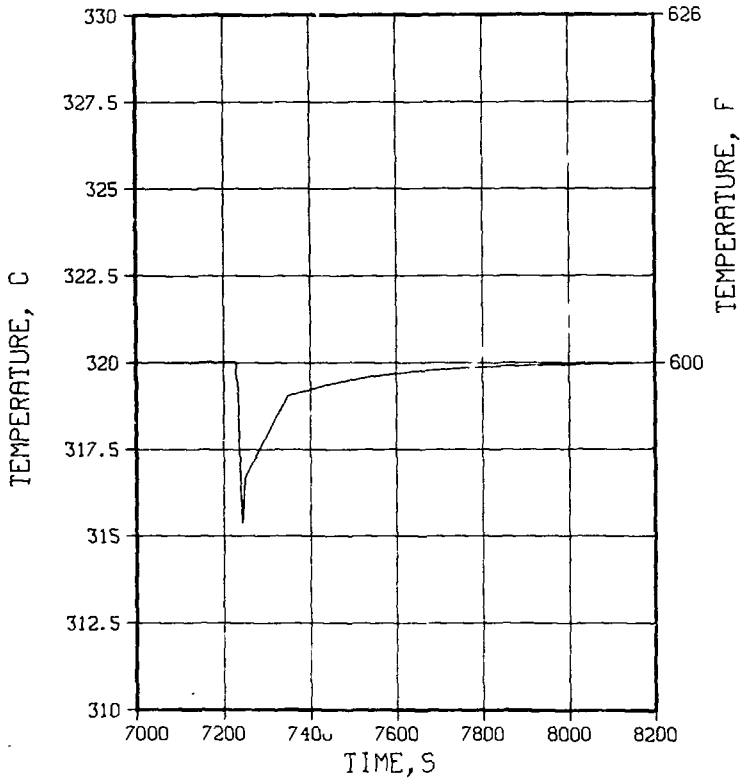

Fig. B-13 Coolant temperature response: 0-s dwell/Region 2.

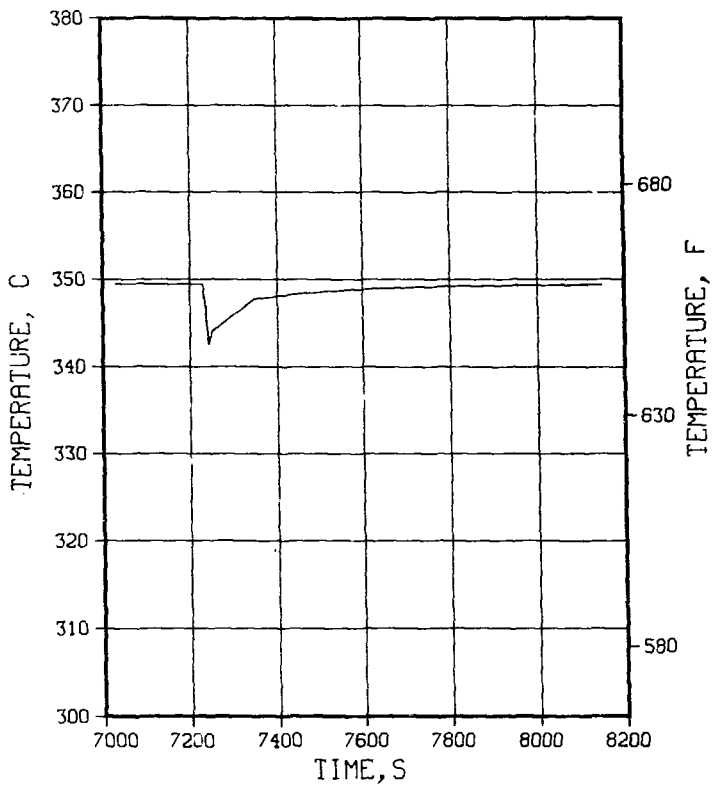

Fig. B-14. Cladding temperature response: 0-s dwell/Region 2.

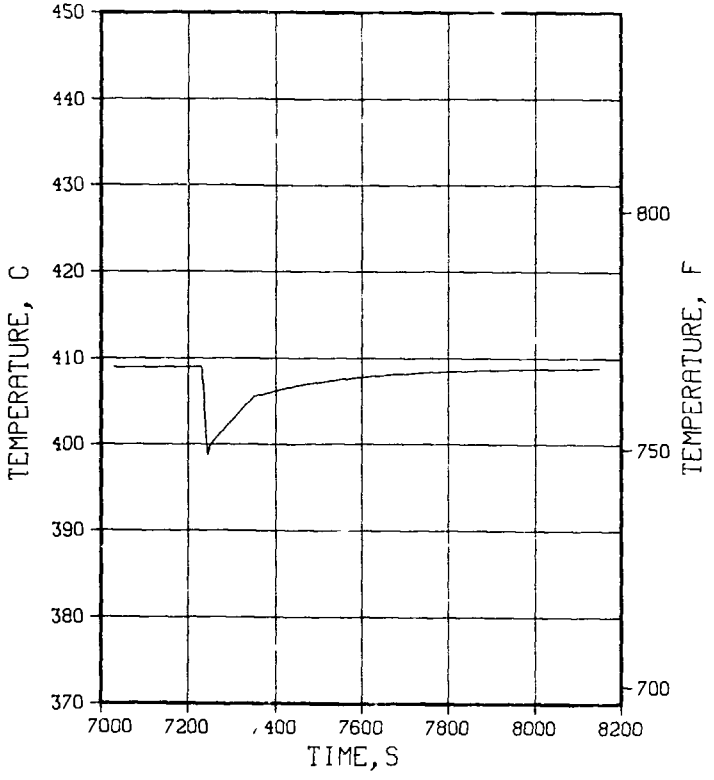

Fig. B-15. Breeder minimum temperature response: 0-s dwell/Region 2.

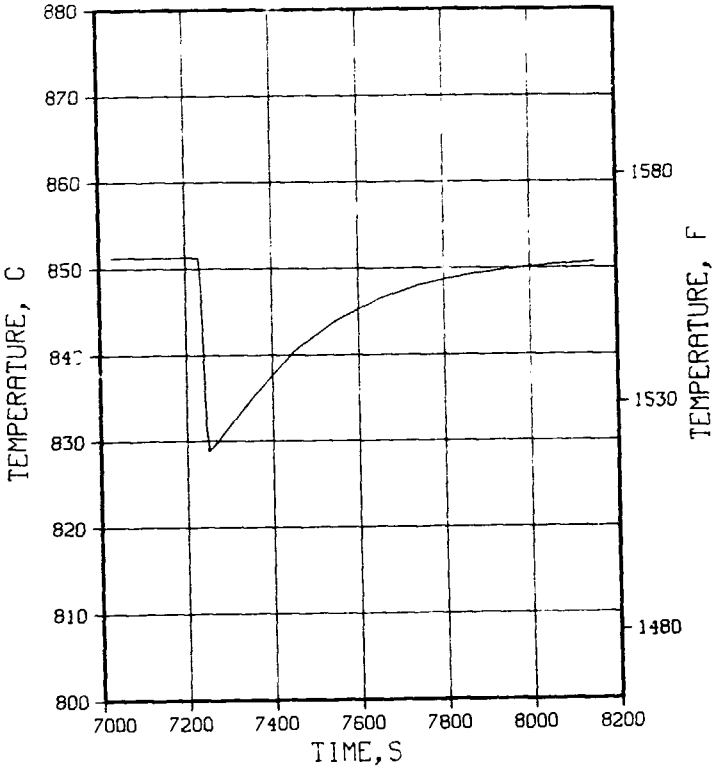

Fig. B-16. Breeder maximum temperature response: 0-s dwell/Region 2.

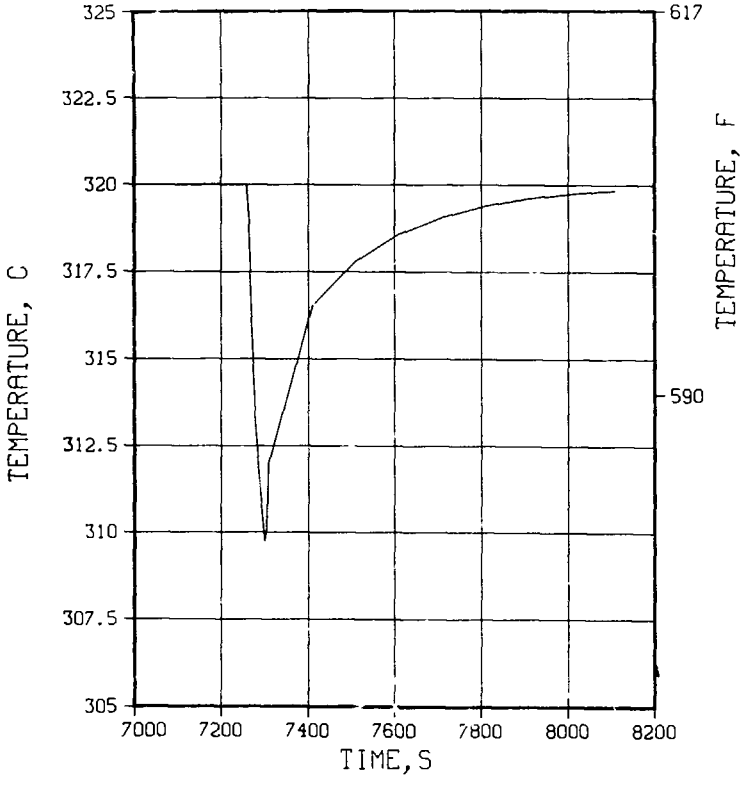

Fig. B-17. Coolant temperature response: 30-s dwell/Region 2.

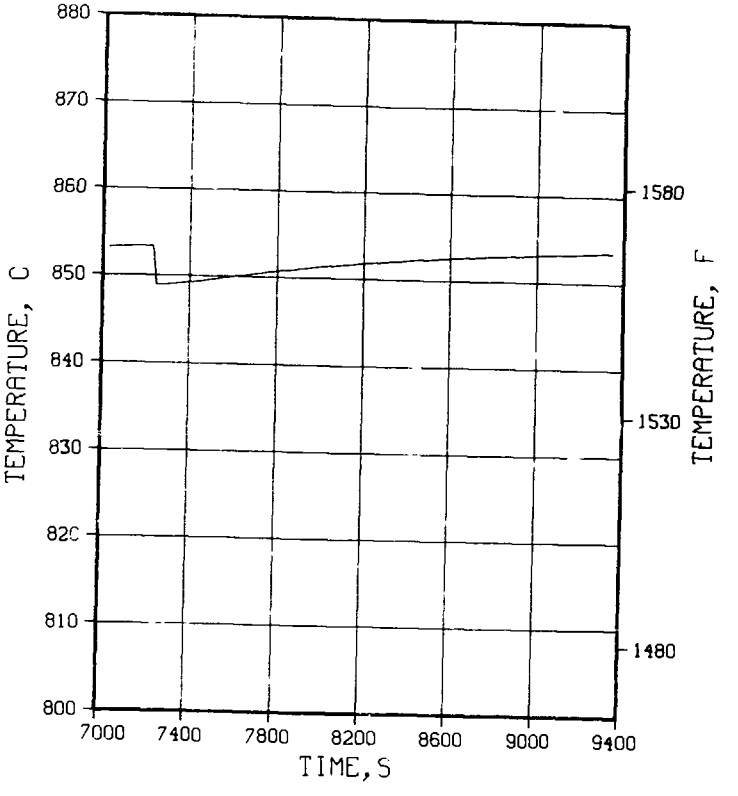

Fig. B-18. Cladding temperature response: 30-s dwell/Region 2.

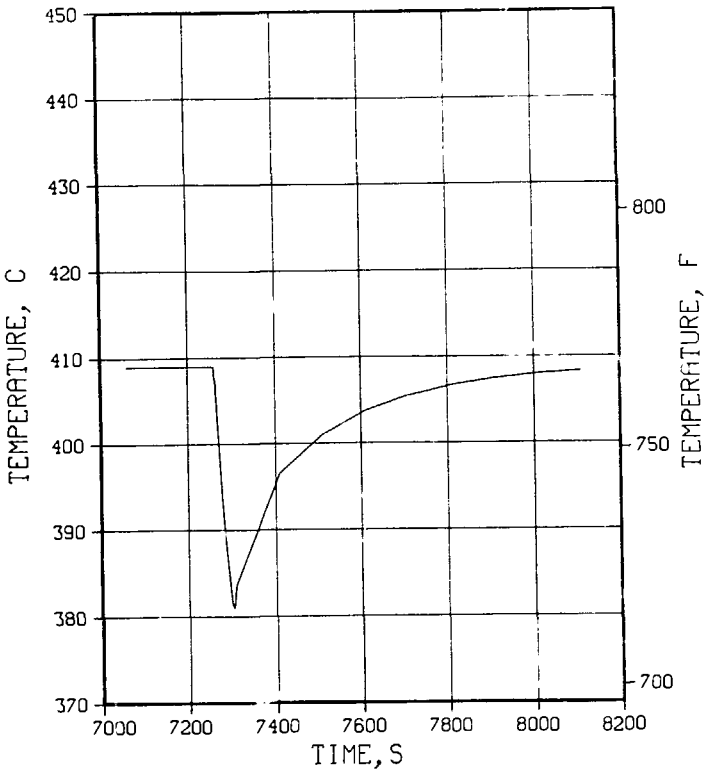

Fig. B-19. Breeder minimum temperature response: 30-s dwell/Region 2.

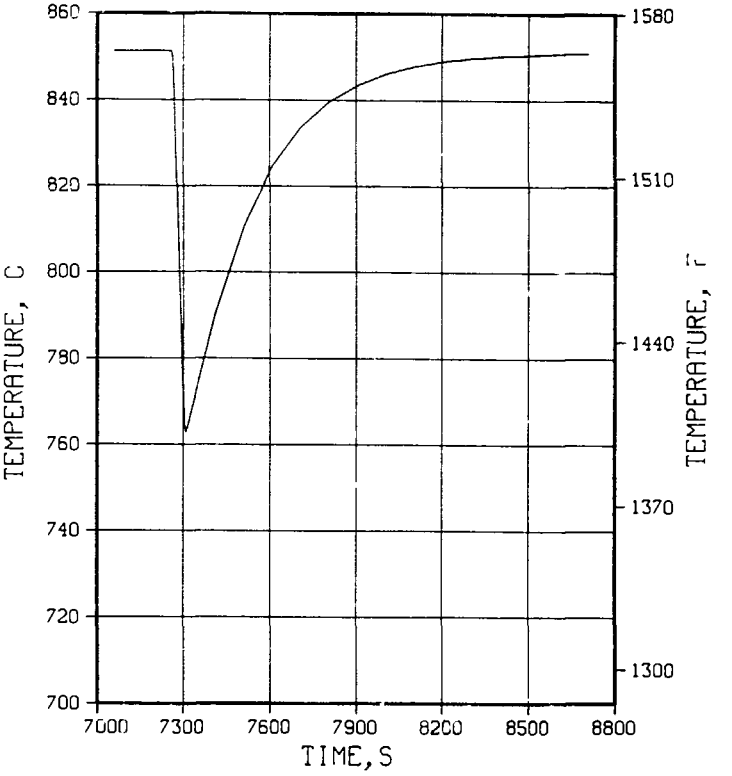

Fig. B-20. Breeder maximum temperature response: 30-s dwell/Region 2.

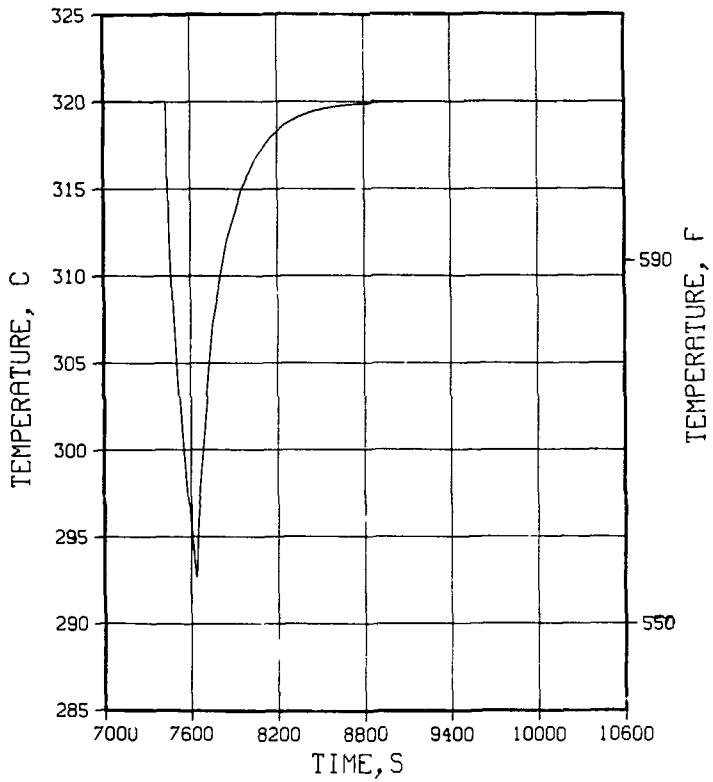

Fig. B-21. Coolant temperature response: 200-s dwell/Region 2.

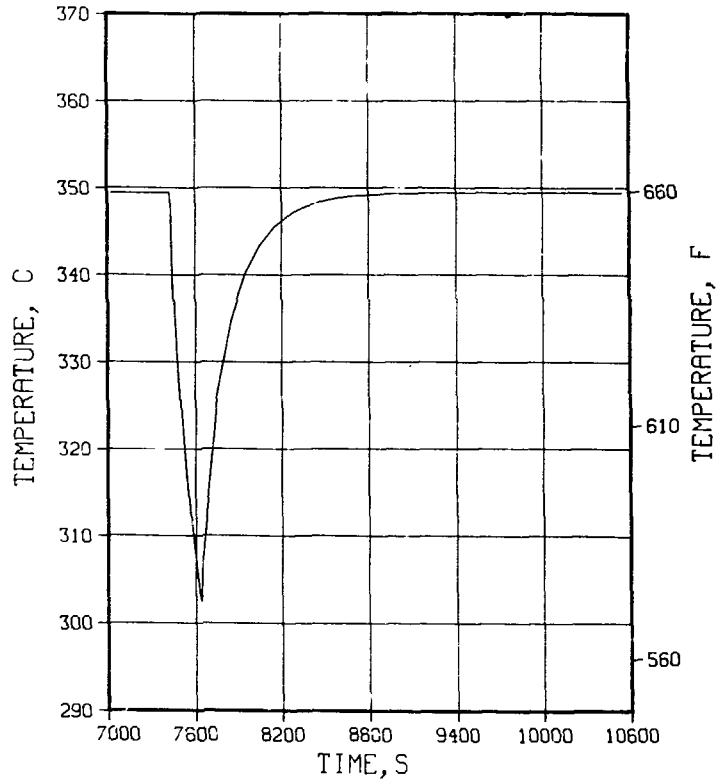

Fig. B-22. Cladding temperature response: 200-s dwell/Region 2.

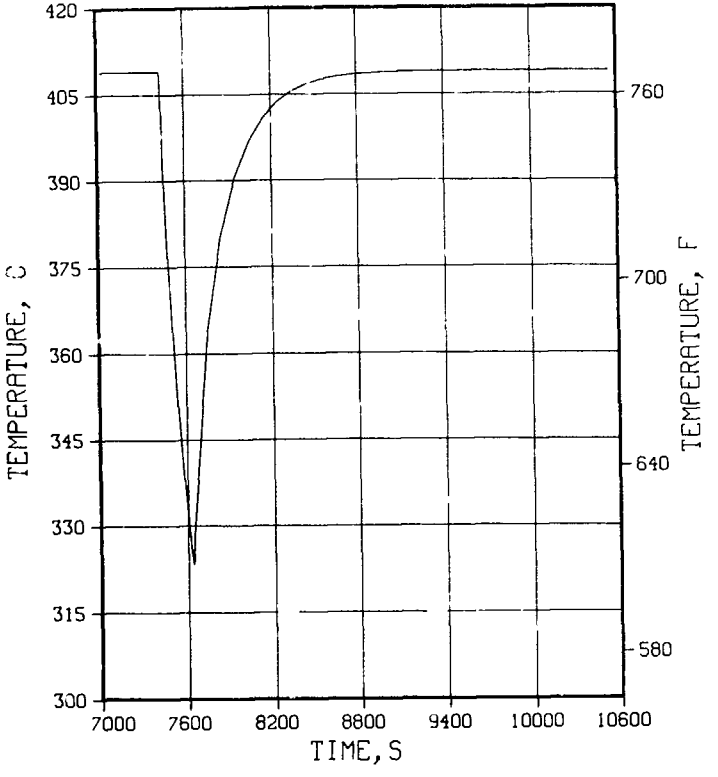

Fig. B-23. Breeder minimum temperature response: 200-s dwell/Region 2.

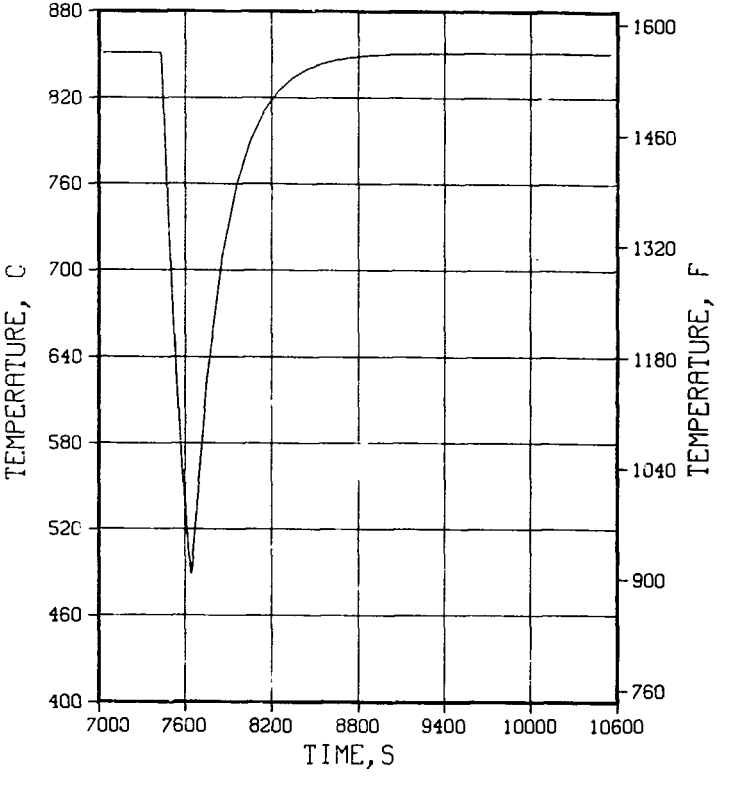

Fig. B-24. Breeder maximum temperature response: 200-s dwell/Region 2.

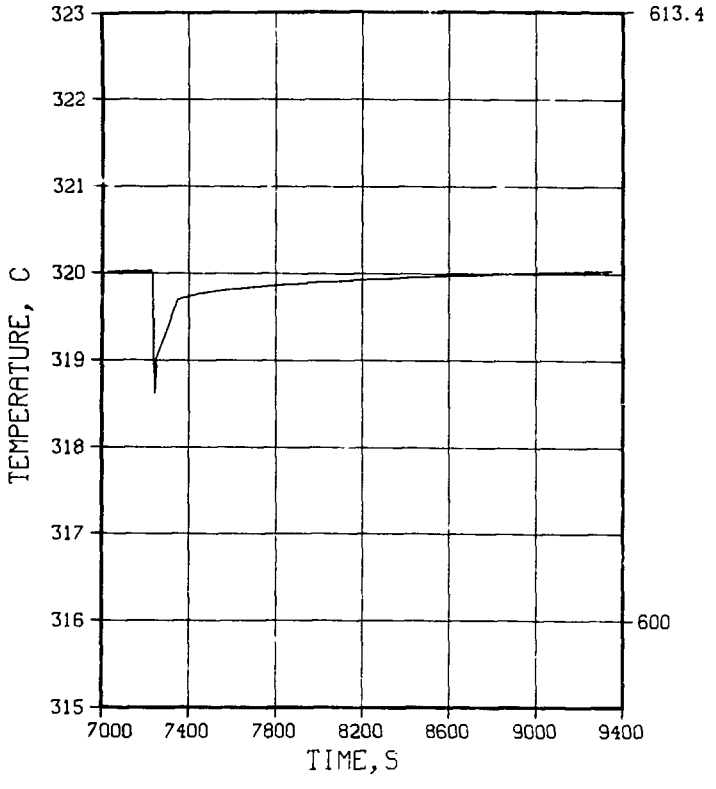

Fig. B-25. Coolant temperature response: 0-s dwell/Region 3.

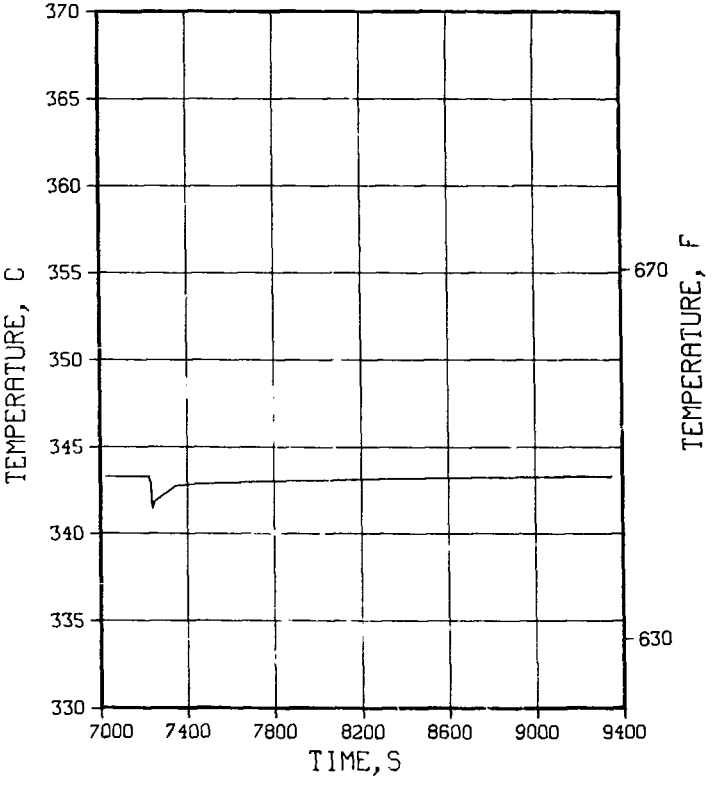

Fig. B-26. Cladding temperature response: 0-s dwell/Region 3.

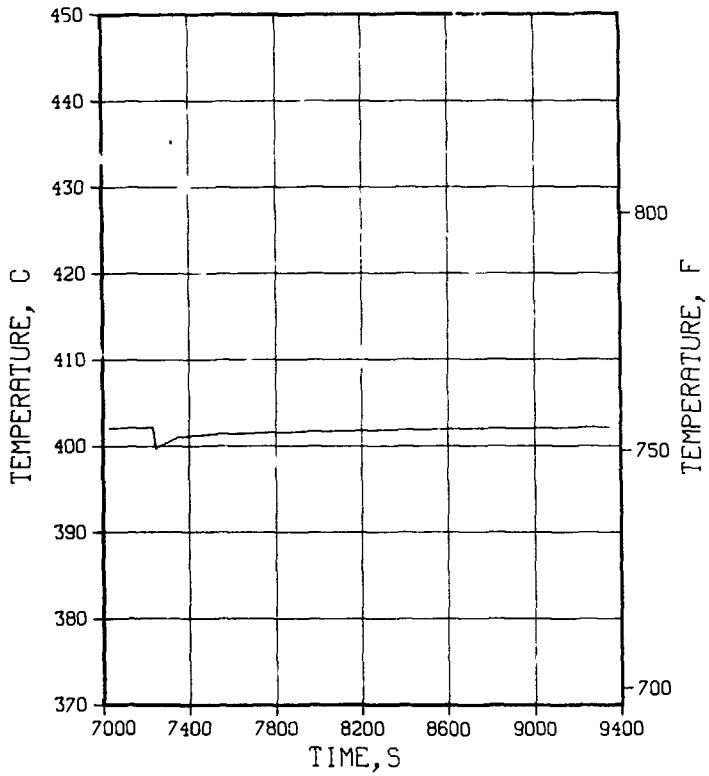

Fig. B-27. Breeder minimum temperature response: 0-s dwell/Region 3.

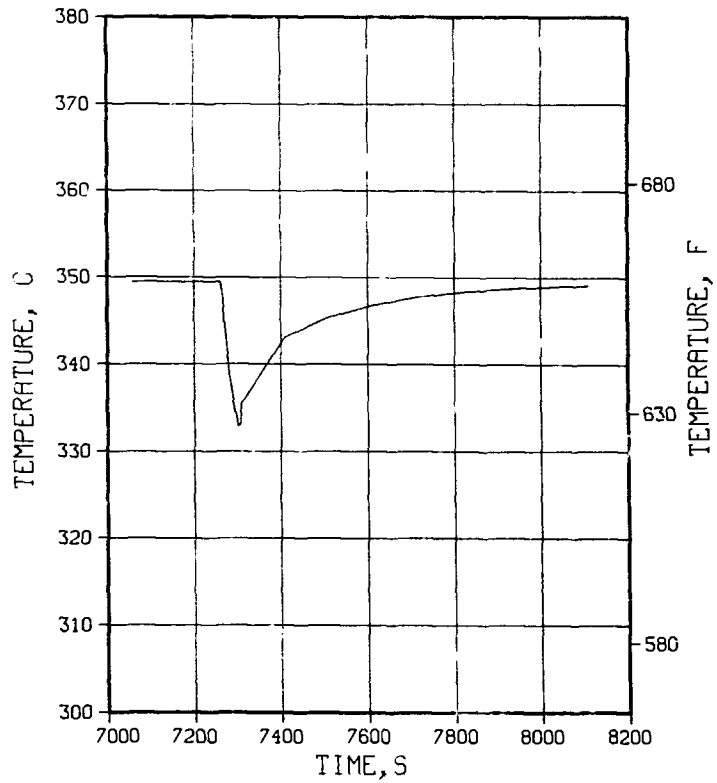

Fig. B-28. Breeder maximum temperature response: 0-s dwell/Region 3.

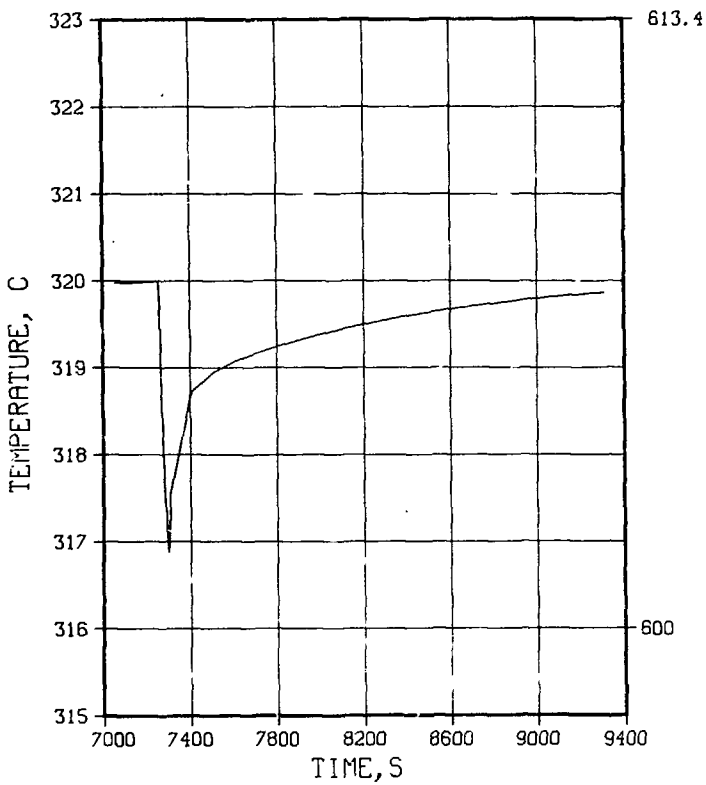

Fig. B-29. Coolant temperature response: 30-s dwell/Region 3.

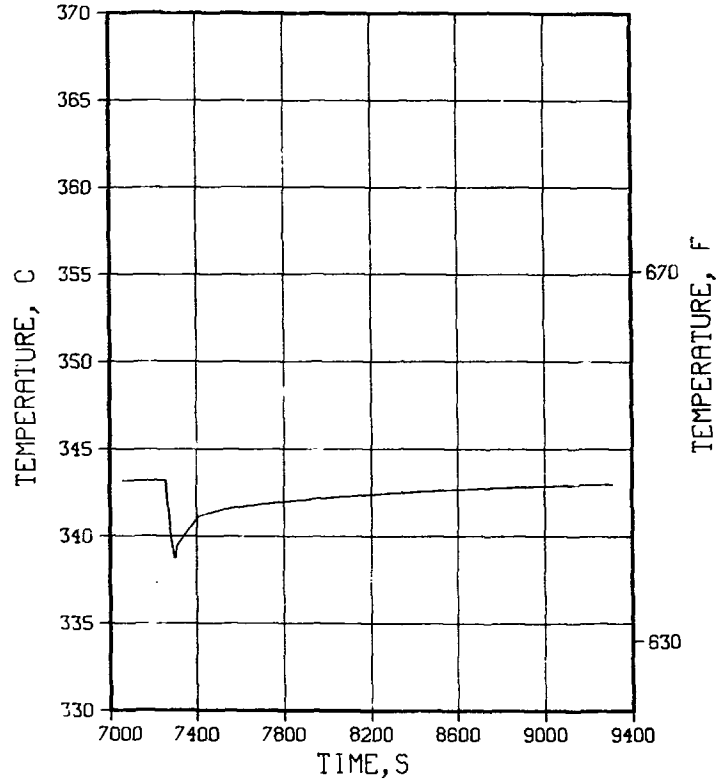

Fig. B-30. Cladding temperature response: 30-s dwell/Region 3.

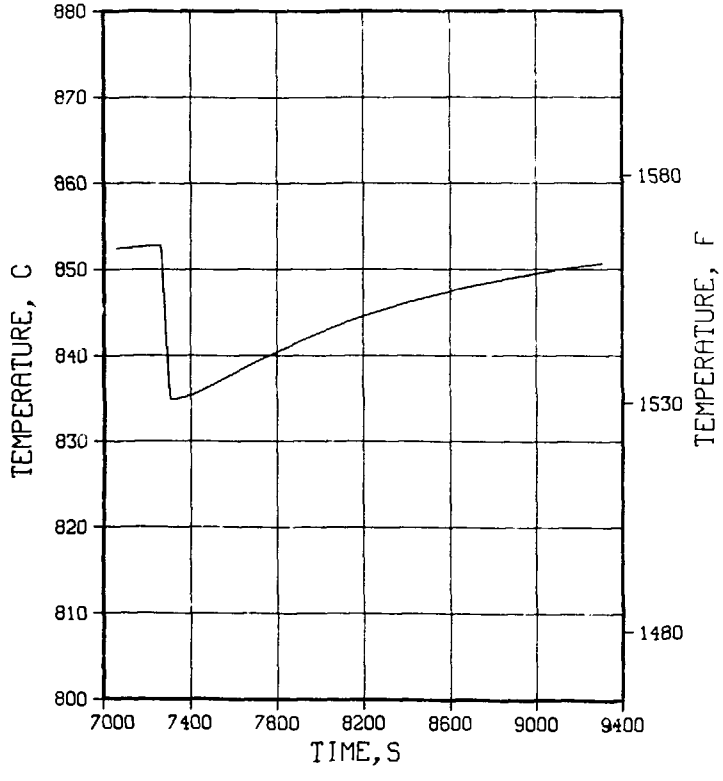

Fig. B-31. Breeder minimum temperature response: 30-s dwell/Region 3.

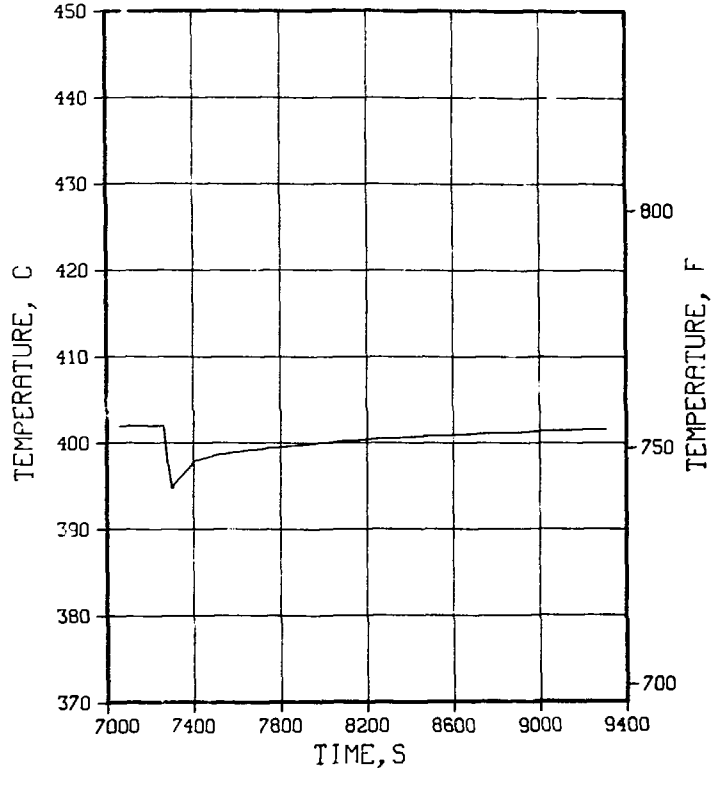

Fig. B-32. Breeder maximum temperature response: 30-s dwell/Region 3.

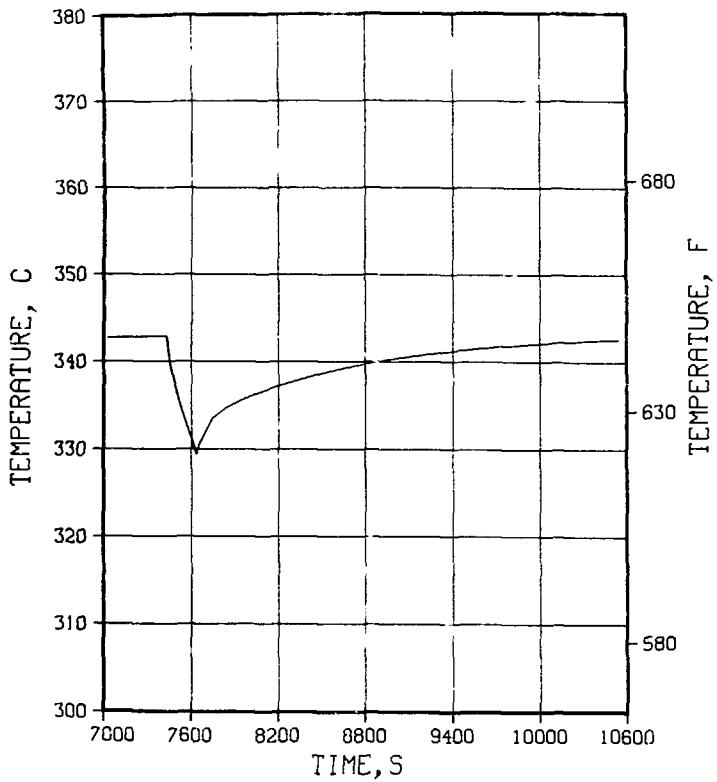

Fig. B-33. Coolant temperature response: 200-s dwell/Region 3.

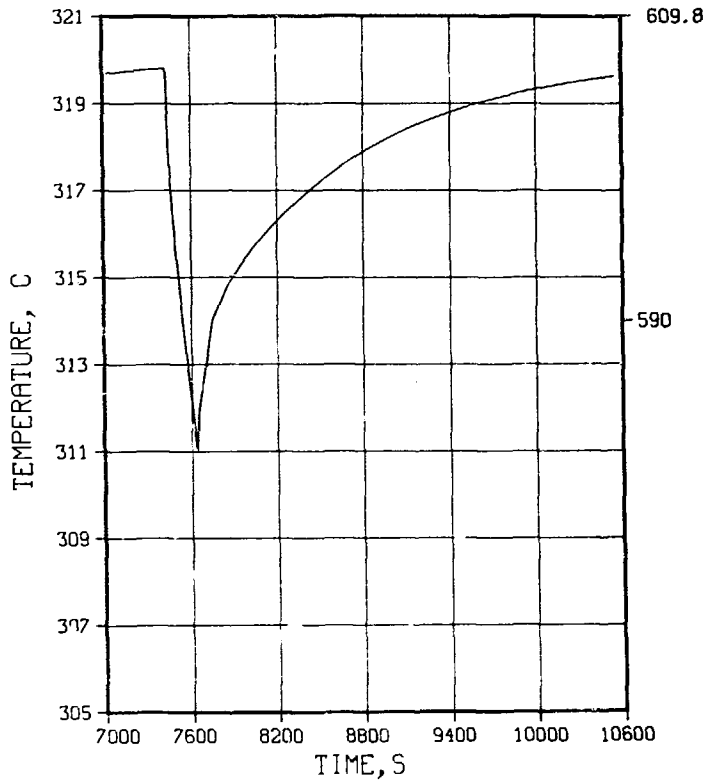

Fig. B-34. Cladding temperature response: 200-s dwell/Region 3.

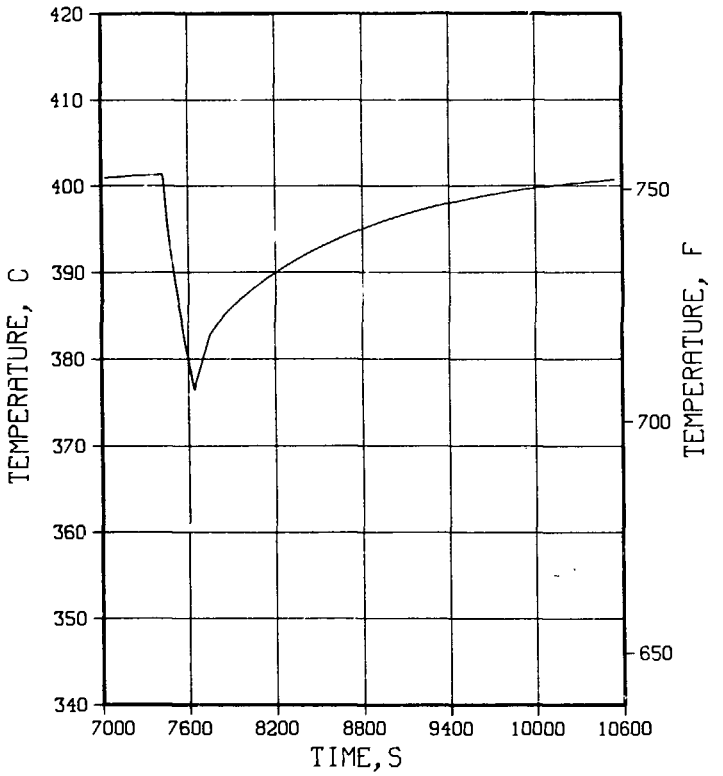

Fig. B-35. Breeder minimum temperature response: 200-s dwell/Region 3.

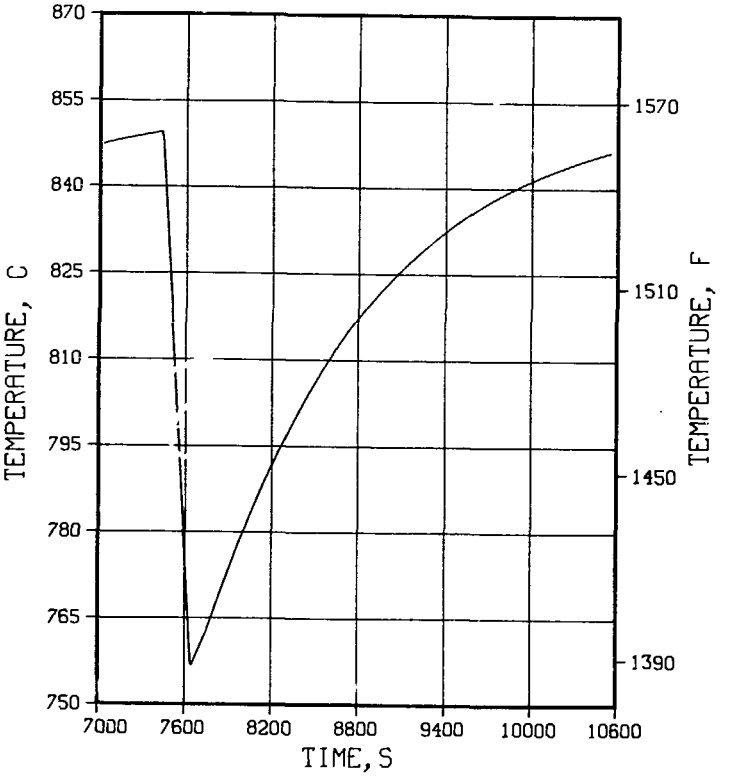

Fig. B-36. Breeder maximum temperature response: 200-s dwell/Region 3.

Distribution for ANL/FPP/TM-178

Internal:

C. Baker
M. Billone
C. Boley
J. Brooks
Y. Cha
R. Clemmer
D. Ehst (10)
K. Evans
P. Finn
Y. Gohar
D. Green
A. Hassanein
C. Johnson
J. Jung
S. Kim
L. LeSage
R. Leonard
B. Loomis
S. Majumdar
R. Mattas
B. Misra
R. Nygren
B. Picologou
J. Roberts
D. Smith
H. Stevens
D-K. Sze
L. Turner
S-T. Yang
ANL Patent Dept.
FP Program (10)
ANL Contract File
ANL Libraries (2)
TIS Files (6)

External:

DOE-TIC, for distribution per UC-20,20a,20b,20c,20d (237)
Manager, Chicago Operations Office, DOE
Special Committee for the Fusion Program:
S. Baron, Burns & Roe, Inc., Oradell, NJ
H. K. Forsen, Bechtel Group Inc., San Francisco, CA
J. Maniscalco, TRW, Inc., Redondo Beach, CA
G. H. Miley, University of Illinois, Urbana
P. J. Reardon, Brookhaven National Laboratory
P. H. Rutherford, Princeton Plasma Physics Laboratory
D. Steiner, Rensselaer Polytechnic Institute
K. R. Symon, University of Wisconsin-Madison
K. Thomassen, Lawrence Livermore National Laboratory
R. Aamodt, Science Applications, Inc.
M. Abdou, University of California-Los Angeles
R. Alsmiller, Oak Ridge National Laboratory
D. Anthony, General Electric Company
R. Balzheizer, Electric Power Research Institute
S. Bernabei, Princeton Plasma Physics Laboratory
A. Bers, Massachusetts Institute of Technology
W. Bjorndahl, TRW, Redondo Beach, CA
S. Bogart, Science Applications, Inc.
P. Bonoli, Massachusetts Institute of Technology
S. Buchsbaum, Bell Telephone Laboratories, Inc.
S. Burnett, GA Technologies
E. Canobbio, Max-Planck Institute für Plasmaphysik, West Germany
G. Casini, Joint Research Centre, Ispra Establishment, Italy
R. Challender, UKAEA, Risley, England
C-H. Chen, Institute of Plasma Physics, People's Republic of China
R. Cherdak, Burns & Roe
D. Cohn, Massachusetts Institute of Technology
P. Colestock, Princeton Plasma Physics Laboratory
R. Conn, University of California-Los Angeles
B. Coppi, Massachusetts Institute of Technology

J. Davis, McDonnell Douglas Astronautics Company
S. Dean, Fusion Power Associates, Gaithersburg, MD
J. DeVan, Oak Ridge National Laboratory
D. Dobrott, Science Applications, Inc., La Jolla, CA
N. Fisch, Princeton Plasma Physics Laboratory
K. Gentle, University of Texas-Austin
J. Gordon, TRW, Inc.
S. Gralnick, Grumman Aerospace Corporation
D. Graumann, GA Technologies
E. Greenspan, NRCN, Israel
R. Gross, Columbia University
R. Hagenson, Los Alamos National Laboratory
R. Hancox, Culham Laboratory, UKAEA, England
R. Harvey, GA Technologies
T. Hiraeoka, Japan Atomic Energy Research Institute, Japan
A. Husseiny, Iowa State University
W. Hooke, Princeton Plasma Physics Laboratory
J. Hosea, Princeton Plasma Physics Laboratory
D. Hwang, Princeton Plasma Physics Laboratory
R. Johnson, General Dynamics - Convair
T. Kammash, University of Michigan
C. Karney Princeton Plasma Physics Laboratory
R. Klima, Czechoslovak Academy of Sciences, Czechoslovakia
I. Knoblock, Max Planck Institute für Plasmaphysik, West Germany
H. Kouts, Brookhaven National Laboratory
R. Krakowski, Los Alamos National Laboratory
R. Langley, Sandia Laboratories
D. Leger, CEA-Saclay, Service DCAEA/SECF., France
R. Lengye, Max Plack Institute für Plasmaphysik, West Germany
S. Malang, University of Wisconsin-Madison
T. K. Mau, Univesity of California-Los Angeles
I. Maya, GA Technologies
D. Metzler, FEDC, Oak Ridge National Laboratory
R. Micich, Grumman Aerospace Corporation
D. Mikkelsen, Princeton Plasma Physics Laboratory
R. Mills, Princeton University
R. Moir, Lawrence Livermore National Laboratory
G. Morgan, McDonnell Douglas Astronautics Company
G. Moses, University of Wisconsin-Madison
R. Motley, Princeton Plasma Physics Laboratory
T. Nakakita, Toshiba Corporation, Japan
H. Nakashina, Kyushu University, Fukuoka, Japan
Y-K. Peng, FEDC, Oak Ridge National Laboratory
F. Perkins, Princeton Plasma Physics Laboratory
M. Porkolab, Massachusetts Institute of Technology
R. Post, Lawrence Livermore National Laboratory
J. Rawls, GA Technologies Inc.
D. Ross, University of Texas-Austin
R. Santoro, Oak Ridge National Laboratory
M. Sawan, University of Wisconsin
J. Schmidt, Princeton Plasma Physics Laboratory
P. Schmitter, Max Planck Institute für Plasmaphysik, West Germany
J. Schultz, Massachusetts Institute of Technology
K. Schultz, GA Technologies

R. Seale, University of Arizona
J. Shannon, FEDC, Oak Ridge National Laboratory
G. Shatalov, I. V. Kurchatov Institute of Atomic Energy, Moscow
J. Sheffield, Oak Ridge National Laboratory
C. Singer, Massachusetts Institute of Technology
W. M. Stacey, Jr., Georgia Institute of Technology
D. Start, Culham Laboratory, UKEA, Abingdon, England
M. Stauber, Grumman Aerospace Corporation
J. E. Stevens, Princeton Plasma Physics Laboratory
W. Stodiek, Princeton Plasma Physics Laboratory
K. Werner, Lawrence Livermore National Laboratory
L. Wittenberg, Monsanto Research Corporation
C. Wong, GA Technologies Inc.
G. Woodruff, University of Washington
D. Young, Jr., University of Texas-Austin
M. Youssef, University of California-Los Angeles
Library, Centre de Etudes Nucleaires de Fontenay, France
Library, Centre de Etudes Nucleaires de Grenoble, France
Library, Centre de Etudes Nucleaires de Saclay, France
Library, Centre de Recherches en Physique des Plasma, Lausanne, Switzerland
Library, FOM-Institute voor Plasma-Fysika, Jutphass, Netherlands
Library, Comitato Nazionale per l'Energia Nucleare, Rome, Italy
Library, Joint Research Centre, Ispra, Italy
Library, Japan Atomic Energy Research Institute, Ibaraki, Japan
Library, Max Planck Institute für Plasmaphytsik, Garching, Germany
Library, Culham Laboratory, UKAEA, Abingdon, England
Library, Laboratorio Gas Ionizati, Frascatti, Italy